INVESTIGATIONS ON PRESSURE INDUCED B1-B10-B2 PHASE TRANSITIONS IN BINARY SYSTEMS LaN, LiH AND MgO

By

DEBOJYOTI MUKHERJEE

Enrolment No.: PHYS012008003

Bhabha Atomic Research Centre, Mumbai, India

A thesis submitted to the

Board of Studies in Physical Sciences

In partial fulfillment of requirements

for the Degree of

DOCTOR OF PHILOSOPHY

of

HOMI BHABHA NATIONAL INSTITUTE

April, 2014

Homi Bhabha National Institute

Recommendations of the Viva Voce Committee

As members of the Viva Voce Committee, we certify that we have read the dissertation prepared by Debojyoti Mukherjee entitled “Investigations on pressure induced B1-B10-B2 phase transitions in binary systems LaN, LiH and MgO” and recommend that it may be accepted as fulfilling the thesis requirement for the award of Degree of Doctor of Philosophy.

Chairman – Prof. S. V. G. Menon **Date:** 29.12.2014

Guide / Convener – Prof. S. C. Gupta Satish C Gupta **Date:** 29.12.2014

Member 1 – Prof. S. L. Chaplot S. L. Chaplot **Date:** 29-12-2014.

Member 2 – Prof. P. Ch. Sahu P. Ch. Sahu **Date:** 29.12.2014

Examiner – Prof. G. D. Mukherjee **Date:** 29/12/2014

Final approval and acceptance of this thesis is contingent upon the candidate’s submission of the final copies of the thesis to HBNI.

I/We hereby certify that I/we have read this thesis prepared under my/our direction and recommend that it may be accepted as fulfilling the thesis requirement.

Date: 29.12.2014

Place:

Satish C Gupta

(Guide)

STATEMENT BY AUTHOR

This dissertation has been submitted in partial fulfillment of requirements for an advanced degree at Homi Bhabha National Institute (HBNI) and is deposited in the Library to be made available to borrowers under rules of the HBNI.

Brief quotations from this dissertation are allowable without special permission, provided that accurate acknowledgement of source is made. Requests for permission for extended quotation from or reproduction of this manuscript in whole or in part may be granted by the Competent Authority of HBNI when in his or her judgment the proposed use of the material is in the interests of scholarship. In all other instances, however, permission must be obtained from the author.

Debojyoti Mukherjee

DECLARATION

I, hereby declare that the investigation presented in the thesis has been carried out by me. The work is original and has not been submitted earlier as a whole or in part for a degree / diploma at this or any other Institution / University.

Debojyoti Mukherjee

List of Publications arising from the thesis

Journal

1. "Thermo-physical properties of LiH at high pressures by ab initio calculations", **D. Mukherjee**, B. D. Sahoo, K. D. Joshi, S. C. Gupta, and S. K. Sikka, *J. Appl. Phys.* **109**, 103515(2011).
2. "High pressure equation of state and ideal compressive and tensile strength of MgO single crystal: Ab-initio calculations", **D. Mukherjee**, K. D. Joshi, and S. C. Gupta, *J. Appl. Phys.* **113**, 233504(2013).
3. "Stabilization of tetragonal phase in LaN under high pressure via Peierls distortion", **D. Mukherjee,** B. D. Sahoo, K. D. Joshi and S. C. Gupta, *High Pres. Res.* **33**, 3 (2013).
4. "*Ab-initio* analysis of stability of ω-phase in Ti, Zr and Hf under high pressure", **D. Mukherjee,** K. D. Joshi and S. C. Gupta, *Trans Indian Inst. Metal* **64**, 245 (2011).
5. "On equation of state, elastic, and lattice dynamic stability of bcc bismuth under high pressure: *Ab-initio* calculations", **D. Mukherjee,** B. D. Sahoo, K. D. Joshi and S. C. Gupta, *J. Appl. Phys.* **115**, 053702 (2014).

Conferences

1. "Pressure induced phase transition in tin: *Ab-initio* calculations", **D. Mukherjee,** K. D. Joshi, and S. C. Gupta, *J. Phys.: Conf. Ser.* **215**, 012106 (2010)
2. "Shock Wave Induced Melting of Tin: *Ab-initio* Study", **D. Mukherjee**, K. D. Joshi, and S. C. Gupta, *AIP Conf. Proc.* **1349,** 821 (2011)
3. "On high pressure β → ω phase transition in Ta and Zr-Nb", **Debojyoti Mukherjee,** K.D. Joshi, and Satish C. Gupta, *J. Phys.: Conf. Ser.* **377**, 012072 (2012)
4. "Lattice dynamic calculations on LiH", **D. Mukherjee**, B.D. Sahoo, K.D. Joshi and Satish C. Gupta, *AIP Conf. Proc.* **1536**, 403 (2013)
5. "On Dynamic and Elastic Stability of Lanthanum Carbide", B.D. Sahoo, **D. Mukherjee,** K.D. Joshi and Satish C. Gupta, *J. Phys.: Conf. Ser.* **377**, 012087 (2012)

6. "On dynamic and elastic stability of group IIIB metal carbides: Ab-initio calculations", B.D. Sahoo, **D. Mukherjee**, K.D. Joshi and Satish C. Gupta, *AIP Conf. Proc.* **1447,** 803 (2012)
7. "Shock Induced Spall Fracture of Polycrystalline Copper", **D. Mukherjee**, Amit Rav, Amit Sur, K.D. Joshi and Satish C. Gupta, *AIP Conf. Proc.* **1591**, 608 (2014).

Debojyoti Mukherjee

To

SUP

ACKNOWLEDGEMENTS

I would like to thank all people who have helped me in different aspects and inspired me during my doctoral work.

I would like to express my sincere gratitude to my adviser Prof. Satish C. Gupta Sir, for his invaluable guidance, constant encouragement, inspiration, keen interest and good wishes. His wide knowledge and his logical way of thinking on critical scientific problems have been of great value for me.

I also like to thank Prof. S. K. Sikka Sir for his valuable suggestions and comments towards my research problems and explanations suggested from the outcome of these problems.

This thesis would not have been possible without the guidance, help, support, critical analysis and valuable suggestions from Dr. K. D. Joshi Sir who has been truly invaluable to me both on an academic and a personal level, for which I am extremely grateful. I am also thankful to him for sharing his excellent knowledge and scientific understanding with me.

It gives me immense pleasure to thank the members of the doctoral committee Prof. S. V. G. Menon (Chairman), Prof. S. L. Chaplot (Member), Prof. S. C. Sabharwal (Member) and Prof. P. Ch. Sahu (Member) for their critical review and suggestions during the progress review and pre-synopsis viva-voce.

I am grateful to all the members of Applied Physics Division. Specially, I would like to thank Rav Sir(Mr. Amit S. Rav), Amitda(Mr Amit Sur), Pandey Sir (Mr. Gaurav Pandey) who helped me in understanding the high pressure experiments and Ashokjee, Prakash, Kulbhushan, Bhaskar, Sarad, Siddhu for the technical support in conducting the experiments. I also acknowledge the assistance provided by Sahoo (Mr. B. D. Sahoo) for various fruitful discussions, preparation of the thesis.

I owe my heartfelt gratitude and indebtedness to my grandmother, my father, mother, father-in-law, mother-in-law for the constant appreciation and courage.

Finally, I would like to thank my life mate Suparna, for her continuous encouragement, care and constant support in every aspect of my life. She continuously supported me during my research work and writing thesis

Lastly, I beg apology to all the people whom I have missed to mention in this page.

CONTENTS

1. Introduction

2. Elastic, Lattice Dynamic and Structural Stability of Lithium Hydride under High Pressure: *Ab-initio* Calculations

3. *Ab-initio* Study of Equation of State and ideal compressive and tensile strength of MgO

4. B1 → B10 → B2 Structural Transition Sequence in LaN under High Pressure

5. Spall fracture and hardening of polycrystalline copper under shock loading

6. Summary and Future Scopes

Investigations on pressure induced B1-B10-B2 phase transitions in binary systems LaN, LiH and MgO

(SYNOPSIS)

Research on material properties under high pressure has attracted attention of scientific community since four decades and there are some fascinating results which enriches the basic and applied sciences [1-5]. Pressure is a thermodynamical variable which can be tuned in precise way to induce changes in materials properties similar to those brought by the application of temperature. The application of pressure can cause the reduction in volume of condensed matter by more than a factor of two and thus revealing many interesting changes in properties of materials under compression. The high pressures in the materials are generated either by static compression methods or by dynamic compression (shock compression) methods. The two methods of high pressure generation differ widely. In the static compression technique [4], material is squeezed slowly; hence, temperature inside the sample during the experiment remains constant *i.e.* the static compression is an isothermal process. To some extent, in static method one can compress the material hydrostatically by selecting a suitable (fluid or gas) pressure transmitting medium surrounding the sample [4,6]. In shock loading methods, on the other hand, materials are compressed uniaxially with very high rate of pressurization (rise times ~ few tens of nanoseconds), and the temperature and entropy of the materials always increase. Under static compression, the duration of the pressure on the material can be as long as we desire, however, in shock compression the duration of pressure pulse is very small (of order of few microseconds) depending upon the dimensions of the sample. Unlike the hydrostatic compression, the shock loading is always accompanied by the shear stresses which may induce phase transitions that are not observed under hydrostatic loading. For example, in tantalum (Ta) the body centered cubic (β) phase is found to be stable under hydrostatic compression up to 170 GPa whereas under shock loading it transforms to ω phase at ~ 45 GPa [7-9].

Phase transitions are examples of the striking changes that can be brought by application of pressure in materials. Some of the interesting pressure induced phase transitions are metallization of oxygen at ~ 96 GPa[10-11], metal to insulator transition in sodium at ~ 200 GPa [12], the hcp → three atom hexagonal (ω) → bcc (β) structural transformation in group IV transition metals Ti, Zr and Hf [13-16], the β to ω phase transition in tantalum and Zr-20%Nb alloy under transient loading to ~ 45 GPa and ~ 15 GPa, respectively [8-9, 17-18] etc. The discovery of such phase transformations in materials has added new dimensions to the understanding of behaviour of materials under high pressure. For example, the occurrence of hcp → ω → β structural phase transition in Ti, Zr and Hf under high pressure has been attributed to the transfer of electrons from filled *s*-band to the partially filled narrow *d*-bands and their distribution in various *d*-substates [19-21]. The knowledge of this structural sequence under pressure and its correlation with electron transfer from *s*-band to *d*-bands has added a new understanding in basic physics of transition metals and their alloys.

In addition to pressure induced phase transitions, the high pressure equation of state (EOS), *e.g.*, isotherm, isentrope and Hugoniot also play important role in characterization of state of a material under pressure. The knowledge of EOS serves as vital input to the computer codes for the hydrodynamic simulations which are related to the wave propagation in geological media, reactor accidents, fission/fusion energy systems and in the analysis of many problems pertaining to geophysics, astrophysics and planetology [1, 2]. Similarly, the pressure dependent elastic constants of materials play important role in determining the mechanical failure strength and various physical quantities such as Debye temperature, sound velocity, Gruneisen parameter, etc. The ultrasonic technique [22] is commonly used to measure the elastic constants of materials at ambient pressure. The Brillouin scattering is another method of measuring elastic constants at ambient conditions as well as at high pressures of few GPa [23-24]. Further, the high pressure x-ray diffraction measurements in diamond anvil cell (DAC) under non hydrostatic stress conditions have been used to evaluate elastic constants up to few tens of GPa [25-26].

The mechanical failure strength of materials is of practical interest. The failure strength of a material is governed by the binding energy and the defects and dislocation present in the material. In a perfect solid, the failure strength is solely dependent on its binding energy; however, in case of a practical solid the failure strength strongly depends upon the defects and dislocations present in it. Beside the defects and dislocation, the failure strength of materials also depends on the rate at which the strains are applied [27-28]. In fact, it has been observed experimentally that the failure strength of a material measured under quasistatic loading differs significantly from that measured under high strain rate conditions [27-30]. This suggests that the knowledge of strength properties merely at quasistatic loading conditions is not sufficient when the suitability of a material for applications involving high strain rates has to be decided. For example, analysis of structural response of a material subjected to high strain rate loading conditions occurring during the propagation of seismic waves through geological media and the fracture and fragmentation at high velocity impact needs the failure strength at high strain rate as input. The strength measurements at high strain rate conditions are quite challenging and need special techniques for generation and measurements of high strain rates [31-34]. The well configured shock wave experiments which not only can generate the high compressive stresses but also the high tensile stresses at strain rates ranging from 10^4/s to 10^9/s are ideal tool for measurement of failure strength at high strain rates [35].

Besides the advancement in high pressure experimental techniques, a significant progress has been made in theoretical front also in last few decades [14-15, 17, 19, 36-37]. With the advent of much enhanced computational power, the *ab-initio* theoretical methods based on density functional approach have been developed and employed for investigations of the phase transitions, equation of states, elastic properties, mechanical failure strength and pressure effect on melting point of materials [11, 14-15, 19, 36-40]. The present day theoretical methods are capable of not only reproducing the experimental results but also predicting the various new physical phenomena such as structural phase transitions, elastic and mechanical properties of the materials [37, 41-42]. For example, in calcium, the *ab-initio* calculations performed by Oganov *et al.* [37] predicted a β-tin type tetragonal structure (space group $I4_1/amd$) to be more favorable above 33 GPa. However, the high pressure x-ray diffraction measurements by Mao *et al.* [43] reported a phase transition around 32 GPa and indexed this as rhombohedral structure (space group R-3m) at 300 K and orthorhombic structure (space group C*mmm*) below 30 K. In view of this discrepancy between theory and experiment, Li *et al.* [44] repeated the high pressure experiment on this material and reported that the high pressure phase formed around 35 GPa is indeed a β-tin type tetragonal structure, consistent with theoretical prediction. In addition to predicting phase transitions, the *ab-initio* theoretical methods can be resorted as a tool to determine the ideal failure strength of materials under different deformation configurations and thus providing the information about the upper bound to the maximum stress that a given solid can withstand before failure under a particular deformation configuration. Further, the *ab-initio* theoretical methods have also been utilized to determine melting line of materials [39]. For example, molecular dynamic simulations or *ab-initio* static lattice calculations in conjunction with Lindemann melting criteria have been widely used to calculate the melting line and predict the melting of solids under shock loading [39, 45- 46].

The present thesis deals with theoretical studies carried out on binary compounds LiH, LaN and MgO to understand the high pressure behavior of these materials. The theoretical work includes the analysis of structural stability, determination of 300 K isotherm, elastic constants and phonon spectra as a function of hydrostatic compression. All these compounds exist in rocksalt structure (B1) at ambient conditions and have attracted attention of researchers due to their technical as well as academic importance. For example, in hydride and deuteride of lithium, the major interest is due to their importance as thermo nuclear materials and the potential hydrogen storage compound. The LaN is among the transition metal mononitrides that exhibit unique physical properties such as high hardness, brittleness and melting point. Apart from this, the LaN encounters many problems related to stoichiometry [47]. The MgO, however, has been subject of extensive study due to its geophysical implications as it constitutes the major part of the lower mantle of the earth. In various theoretical studies carried out in past [48-64] on these isostructural materials have predicted the B1 to a simple cubic CsCl type (B2) structural phase transition under hydrostatic compression. For example, in LiH, several theoretical studies predicted the B1 to B2 phase transition at the pressures ranging from 85 GPa to 660 GPa [48-54]. The experimental study performed up to ~ 250 GPa, however, shows no phase transition [65]. In LaN also, the theoretical studies [55-56] predicted the B1 to B2 phase transition and the transition pressure is put in the range of 25-27 GPa. The high pressure X-ray diffraction measurements carried out on this material in diamond anvil cell (DAC), however report the occurrence of a primitive tetragonal structure (B10, which can be viewed as distortion of B2 structure) with space group P_4/nmm at ~ 22.8 GPa [66]. Likewise in MgO also, the theoretical investigations predict the B1 to B2 structural phase transition under hydrostatic compression with transition pressures ranging from 116 GPa to 1050 GPa [57-64]. The static compression experiment [67] carried out up to maximum pressure of ~ 227 does not show any phase transition in this material. It may be noted that the most of the theoretical predictions on phase transition in these materials are based on the analysis of structural stability of B1 and B2 structures only. In light of the experimentally observed occurrence of B10 structure in LaN, the B10 structure also becomes one of the plausible structure to be considered for structural stability analysis of such isostructured binary compounds. In spite of a large body of research work available on these materials there are still useful aspects of high pressure behavior which required to be investigated. For example, in LiH, studies related to the pressure dependent of elastic properties, ambient condition thermophysical properties, *e.g.*, Gruneisen parameter, Debye temperature, and Hugoniot parameter were either limited or are not available. Similarly, in LaN, it is worth to investigate theoretically the existence of experimentally observed B10 structure and the cause for its occurrence. As far as MgO is concerned, no data are available on the mechanical stability of this material under uniaxial loading condition. Being a geophysically important material, the knowledge of its ideal strength for compression as well as for expansion under uniaxial loading condition will serve as an important input for simulation of wave propagations through geological media. The theoretical investigations on these binary compounds have been carried out mainly to address the above mentioned issues. Apart from the theoretical investigations on these compounds, the experimental work has been carried out in elemental solid copper also. The objective of the experimental work was to measure the tensile fracture strength of polycrystalline copper subjected to high strain rate loading in shock wave experiments and compare it with that measured under quasistatic loading condition. The whole work presented in the thesis has been classified in six chapters.

The first chapter gives an introduction to the basic concepts of the high pressure, the different methods to generate high pressure in materials, the effect of high pressure in materials, various diagnostic techniques utilized to understand the behavior of materials under high pressure. Also, a brief description of modern DFT based *ab-initio* electronic band structure method used for understanding the material response under high pressures has also been provided along with illustrations on the predictive capability of these theoretical tools.

The Second chapter deals with the theoretical calculations carried out on LiH. In LiH, the objective was to perform the studies to determine the pressure dependent elastic properties, ambient condition thermophysical properties e.g. Gruneisen parameter, Debye temperature, and Hugoniot parameter. For this purpose, first the *ab-initio* calculations at 0 K have been performed to analyze structural stability by choosing the three structures namely B1, B10 and B2 as plausible structures. The 0 K calculations have been utilized to derive the 300 K isotherm after adding finite temperature corrections. The bulk modulus and its pressure derivative at zero pressure as well as at higher pressures have been determined from theoretical isotherm. Additional calculations have been performed to determine the shear elastic moduli as a function of hydrostatic compression. Our structural stability analysis suggests that the B1 phase will transforms to B2 phase at ~ 327 GPa. The theoretical equation of state derived from these calculations agrees well with the experimental data [68]. The zero pressure equilibrium volume, bulk modulus and its pressure derivative has been found to be 17.26 Å^3/formula unit, 34.2 GPa, and 3.61 as compared to the experimental values [65] of 17.02 Å^3/formula unit, 32.2 GPa, 3.53, respectively. Other physical parameters such as bulk sound velocity of 6.48 km/s, the shock parameter of 1.15, the Debye temperature of 828 K and the Gruneisen parameter of 1.30 agree well with the experimental data of 6.43 km/s [69], 1.16 [70], 1.2 [69] and 810 K[71], respectively. The elastic constants C_{11}, C_{12} and C_{44} of B1 phase at zero pressure are calculated to be 77.0 GPa, 12.7 GPa and 48.2 GPa as compared to the experimental values of 74.06 GPa, 14.2 GPa and 48.43 GPa [69], respectively. The variation of elastic constants and elastic anisotropy with pressure was determined and the polycrystalline elastic moduli have also been calculated. Calculations are further extended to determine the phonon spectra of B1 phase of LiH as a function of compression up to 120 GPa [72]. The phonon spectrum calculated at zero pressure is in agrees reasonably with the experimentally measured data [65, 73-74]. The X-point phonon frequencies calculated at various pressures up to maximum of 120 GPa have been compared with the available experimental data [65].

The third chapter of the thesis is devoted to the analysis of structural stability, and determination of equation of state and elastic properties as a function of hydrostatic compression for MgO, a geophysically important material. To analyze the structural stability, the total energy calculations have been carried out on the B1, B10 and B2 structure of MgO and enthalpy has been determined as a function of pressure. The comparison of enthalpies of B1, B10 and B2 phases suggests the B1 to B2 structural transition at ~ 535 GPa, in line with the available theoretical findings [57-64]. The 0 K energy-volume relation in conjunction with thermal corrections has been utilized to derive the isotherm, isentrope and Hugoniot of this material. A good agreement has been found between the theoretically determined isotherm, isentrope and Hugoniot with the experimental data [75-80]. The theoretical investigations have been further extended beyond the hydrostatic conditions and the elastic moduli of MgO single crystal have been determined as a function of strain for uniaxial loading along [001] crystallographic direction under two deformation configurations "uniaxial stress condition" and "uniaxial strain conditions", respectively. The ideal failure strengths for compression and expansion under these two deformation configurations have been determined by examining the elastic stability conditions throughout the deformation path. It may be noted that the uniaxial stress condition is commonly encountered in quasistatic experiments, however, the uniaxial strain condition exists in high strain rate experiments *e.g.* uniaxial compression and expansion generated in shock wave experiments. The determination of elastic moduli as a function of [001] strain and examination of the elastic stability condition at each strain suggested that for [001] uniaxial expansion, the

MgO single crystal will fail due to vanishing of tensile modulus, whereas it will fail due to shear instability under uniaxial compressive loading. The ideal compressive strength and ideal tensile strength for compressive and tensile loading along [001] direction under uniaxial strain condition are determined to be ~ -283 GPa and ~ 20 GPa, respectively; the same under uniaxial stress condition are evaluated to be ~ -115 GPa and ~11 GPa, respectively. These findings suggest that the ideal compressive and tensile strength of MgO single crystal is higher for uniaxial strain condition than that for the uniaxial stress condition.

The fourth chapter presents the theoretical high pressure investigations on LaN. Unlike the LiH and MgO, this material is experimentally reported [66] to undergo pressure induced phase transition from B1 phase (high symmetry cubic structure) to a tetragonal (B10) phase (low symmetry structure named as HP-LaN by authors) at ~ 22.8 GPa. Whereas theoretical studies [55-56] prior to this experimental work have not included the tetragonal structure in their calculations and predicted the B1 to B2 phase transition in this material. We analyzed the structural stability of this material under hydrostatic compression by performing total energy calculations on B1, B2 and B10 (HP-LaN) structures. The present theoretical calculations suggest the B1 to HP-LaN transition at ~ 19 GPa as compared to the experimental value of 22.8 GPa [66]. Further, we predict that the HP-LaN phase transforms to B2 phase at ~ 169 GPa. While the B1 → HP-LaN transition is of first order in nature with 9% volume discontinuity, the HP-LaN → B2 transition is of second order in nature. To understand the cause for the existence of lower symmetry HP-LaN phase (a distortion of the B2 structure) prior to the stabilization B2 structure at higher pressures, we have analyzed the band structures of HP-LaN and B2 phase. Our analysis suggests that the low symmetry HP-LaN phase could be stabilized at lower pressure due to symmetry breaking lowering of total energy.

The fifth chapter reports the experimental measurements of the tensile fracture strength and yield strength of polycrystalline copper subjected to uniaxial loading at strain rates of ~ 10^4/s, generated in shock wave experiments carried out using single stage gas gun existing in our laboratory at BARC [81]. Additionally, the sample retrieved from peak shock loading of ~ 10 GPa are analyzed using nanoindentation technique to look for shock induced changes in its hardness and Young's elastic modulus. The yield strength and spall strength of 0.14 GPa and 1.32 GPa, measured at strain rates ~ 10^4/s from free surface velocity history measured using VISAR are higher by a factor of ~ 2.0 and 6, respectively, than the quasi static loading values. Further, the nanohardness and the Young's modulus have been determined to be 1.43 GPa and 239 GPa, respectively from the indentation method as compared to 1.21 GPa and 185 GPa for as-received sample. This signifies that the hardness and Young's modulus increases upon shock treatment on material.

The thesis will be concluded in the sixth chapter giving a discussion and summary of the overall work presented followed by further research scope open in the present field.

References

[1] F. R. Boyd, *Science*, **145**, 3627 (1964).
[2] D. J. Stevenson, *Annu. Rev. Earth Planet. Sci.*, **10**, 257 (1982).
[3] P. Ch. Sahu and N. V. Chandra Shekar, *Resonance*, General Article, August (2007).
[4] A. Jayaraman, *Rev. Mod. Phys.*, **55**, 65 (1983); *Rev. Sci. Instrum.,* **57**, 1013 (1986).
[5] P. W. Bridgman, *Proc. Am. Acad. Arts Sci.*, **47**, 321-43 (1911); *Proc. Am. Acad. Arts Sci.*, **47**, 441-558 (1911).
[6] N. Tateiwa and Y. Haga, *Rev. Sci. Instrum.,* **80**, 123901 (2009).
[7] H. Cynn and C. Yoo, *Phys. Rev. B*, **59,** 8526 (1998).
[8] L. M. Hsiung and D. H. Lassila, *Scripta Matter.*, **39,** 603 (1998).
[9] Luke L Hsiung, *J. Phys.: Condens. Matter*, **22,** 385702 (2010).
[10] Y. Akahama, H. Kawamura, D. Hausermann, M. Hanfland, and O. Shimomura, *Phys. Rev. Lett.*, **74**, 4690 (1995).
[11] S. Desgreniers, Y. K. Vohra, and A. L. Rouff, *J. Phys. Chem.*, **94**, 1117 (1990).
[12] Y. Ma, M. Eremets, A. R. Oganov, Y. Xie, I. Trojan, S. Medvedev, A. O. Lyakhov, M. Valle and V. Prakapenka, *Nature*, **458**, 182 (2009).
[13] S. K. Sikka, Y. K. Vohra and R. Chidambaram, *Prog. Mater. Sci.,* **27**, 245 (1982).
[14] H. Xia, G. Parthasarthy, H. Luo, Y. K. Vohra and A. L. Ruoff, *Phys. Rev. B*, **42**, 6736 (1990).
[15] J. S. Gyanchandani, Satish C Gupta., S. K. Sikka and R. Chidambaram, *High Press. Res*., **4**, 472 (1990); *J. Phys. Cond. Matter.*, **2**, 301 (1990).
[16] K. D. Joshi, G. Jyoti, Satish C. Gupta and S. K. Sikka, *Phys. Rev. B*, **65,** 052106 (2002).
[17] S. C. Gupta, K. D. Joshi and S. Banerjee, *Metal. and Materials Trans*, **39A**, 1593 (2008).

[18] G. K. Dey, R. Tewari, S. Banerjee, G. Jyoti, S. C. Gupta, K. D. Joshi, S. K. Sikka, *Acta Materialia*, **52,** 5243 (2004).

[19] K. D. Joshi, J. Gyanchandani, S. C. Gupta and S. K. Sikka, *J. Phys. Cond. Matter,* **14**, 1 (2002).

[20] J. S. Gyanchandani, S.K. Sikka and R. Chidambaram, in Recent Trends in High Press.

Res., Proceedings of XIII AIRAPT International Conference on High Press. Science and Technology (Ed: A.K. Singh), Oxford and IBH, New Delhi, **331** (1992).

[21] R. Ahuja J. M. Wills, B. Johansson and O. Eriksson, *Phys. Rev. B*, **48**, 16269 (1993).

[22] D. C. Hurley, R. S. Gilmore and W. F. Banholzer, *J. Appl. Phys.*, **76**, 7726 (1994).

[23] R. Vogelgesang A. K. Ramdas, and S. Rodriguez, M. Grimsditch, T. R. Anthony, *Phys. Rev. B*, **54**, 3989 (1996).

[24] E. S. Zouboulis, M. Grimsditch., A. K. Ramdas and S. Rodriguez, *Phys. Rev. B*, **57**, 2889 (1998).

[25] A. K. Singh, H. K. Mao, J. Shu, Russel J. Hemley, *Phys. Rev. Lett.,* **80**, 2157 (1998).

[26] T. S. Duffy, G. Shen, J. Shu, H. K. Mao, R. J. Hemley and A. K. Singh, *J. Appl. Phys*., **86**, 6729 (1999).

[27] G. I. Kanel, S. V. Razorenov, A. V. Utkin, V. E. Fortov, K. Baumung, H. U. Karow, D. Rusch, V. Licht, *J. Appl. Phys.*, **74**, 7162 (1993).

[28] E. Moshe, S. Eliezer, Z. Henis, M. Werdiger, E. Dekel, Y. Horovitz, S. Maman, I. B. Goldberg and D. Eliezer, *Appl. Phys. Lett.*, **76**, 1555 (2000).

[29] N. Eliaz, E. Moshe, S. Eliezer, and D. Eleizer, *Metall. Matter. Trans. A*, **31**, 1085 (2000).

[30] K. D. Joshi, Amit S. Rav, S. C. Gupta and S. Banerjee, *J. Phys. Conf. Series*, **215**, 012149 (2010).

[31] W. J. Nellis, J. A. Morarity, A. C. Mitchell and N. C. Holmes, *J. Appl. Phys.*, **82**, 2225 (1997).

[32] J. R. Asay, *Int. J. Impact Engg.*, **20**, 27 (1997).

[33] M. D. Furnish, L. C. Chhabildas, and W.D. Reinhart, *Int. J. of Impact Engg.*, **23**, 261 (1999).

[34] L. M. Barker and R. E. Hollenbach, *J. Appl. Phys.*, **43**, 4669 (1972).

[35] S. J. Turneaure and Y. M. Gupta, *Appl. Phys. Lett.*, **90**, 051905 (2007).

[36] K.D. Joshi and Satish C. Gupta, *High Press. Res.*, **27**, 259 (2007).

[37] A. R. Oganov, Y. Ma, Y. Xu, I. Erread, A. Bergarad, and A. O. Lyakhov, *PNAS*, **107**, 7646 (2010).

[38] D. Mukherjee, K. D. Joshi and S. C. Gupta, *J. Appl. Phys.*, **113,** 233504 (2013).

[39] L. Burakovsky, S. P. Chen, D. L. Preston, A. B. Belonoshko, A. Rosengren, A. S. Mikhaylushkin, S.I. Simak, and J.A. Moriarty, *Phys. Rev. Lett.*, **104**, 255702 (2010).

[40] B.D. Sahoo, K.D. Joshi and Satish C. Gupta, *J. Appl. Phys.*, **112**, 0935231-6 (2012).

[41] D. Mukherjee, B. D. Sahoo, K. D. Joshi, S. C. Gupta, and S. K. Sikka, *J. Appl. Phys.*, **109**, 103515 (2011).

[42] B.D. Sahoo, K.D. Joshi and Satish C. Gupta, *J. Appl. Phys.*, **113**, 1935121-7 (2013).

[43] W. L. Mao, L. Wang, Y. Ding, W. Yangd, W. Liu, D. Y. Kimg, W. Luo, R. Ahuja, *PNAS*, **107**, 9965 (2010).

[44] B. Li,Y. Ding, W. Yang, L. Wang, B. Zou, J. Shu, S. Sinogeikin, C. Park, G. Zou and H. Mao, *PNAS*, **109**, 16459 (2012).

[45] A. B. Belonoshko, L. Burakovsky, S. P. Chen, B. Johansson, A. S. Mikhaylushkin, D. L. Preston,S. I. Simak, and D. C. Swift, *Phys. Rev. Lett.*, **100**, 135701 (2008)

[46] D. Mukherjee, K. D. Joshi, and S. C. Gupta, *AIP Conf. Proc.,* **1349,** 821 (2011).

[47] F. Hulliger, *J. Magn. Magn. Mater.*, **8**, 183 (1978).

[48] R. Ahuja, O. Eriksson, and B. Johansson, *Physica B*, **265**, 87 (1999).

[49] Y. Wang, R. Ahuja, and B. Johansson, *Phys. Status Solidi* B, **235**, 470 (2003).

[50] J. L. Martins, *Phys. Rev. B*, **41**, 7883 (1990).

[51] Q. Gou, X. Wang, and J. Meng, *High Press. Res.*, **6**, 141 (1991).

[52] J. Y. Zhang, L. J. Zhang, T. Cui, Y. L. Niu, Y. M. Ma, Z. He and G. T. Zou, *Phys. Rev. B*, **75**, 104115 (2007).

[53] E. Zurek, R. Hoffmann, N. W. Ascroft, A. R. Oganov, and A. O. Lyakhov, *PNAS*, **106**, 17640 (2009).

[54] G Li, D. Wang, Q Jin and D. Ding, *Phys. Lett. A*, **143**, 9 (1990).

[55] G. Vaitheeswaran, V. Kanchana, M. Rajagopalan, *Solid State Commun.*, **124**, 97 (2002).

[56] Y. O. Ciftci, K. Colakoglu, E. Deligoz, H. Ozisik, *Mater. Chem. Phys.*, **108**, 120 (2008).

[57] K.J. Chang and Marvin L. Cohen, *Phys. Rev. B*, **30**, 4774 (1984).

[58] A.J. Cohen and R.G. Gordon, *Phys. Rev. B*, **14,** 4593 (1984).

[59] R.K. Singh and S.D. Sanyal, *Phys. Status Solidi B*, **113**, K23 (1982).

[60] J. Yamashita and S. Asano, *J. Phys. Soc. Jpn.*, **52,** 3506 (1983).

[61] B.B. Karki, L. Stixrude, S.J. Clark, M.C. Warren, G.J. Ackland and J. Crain, *Amr. Miner.*, **82**, 51 (1997).

[62] J. E. Jaffe, J. A. Synder, Z. Lin, and A. C. Hess, *Phys. Rev. B*, **62**, 1660 (2000).

[63] M. J. Mehl, R. E. Cohen, and H. Krakauer, *J. Geophys. Res.*, **93**, 8009 (1988).

[64] A. R. Oganov and P. I. Dorogokupets, *Phys. Rev. B*, **67**, 224110 (2003).

[65] A. Lazicki, P. Loubeyre, F. Occelli, R. J. Hemley, and M. Mezouar, *Phy. Rev. B*, **85**, 054103 (2012).

[66] S. B. Schneider, D. Baumann, A. Salamat, W. Schnick, *J. Appl. Phys.*, **111,** 093503 (2012).

[67] Thomas S. Duffy, Russell J. Hemley and Ho-Kwang Mao, *Phys. Rev. Lett.*, **74**, 1371 (1995).

[68] P. Loubeyre, R. Le Toullec, M. Hanfland, L. Ulivi, F. Datchi, and D. Hausermann, *Phys. Rev. B*, **57**, 10403 (1998).

[69] B. W. James and H. Kheyrandish, *J. Phys. C*, **15**, 6321 (1982).

[70] S. P. Marsh, LASL Report, "Hugoniot Equation of State of Li^{6}H, Li^{6}D, Li^{n}H, Li^{n}D" Report No.: LA-4942, **Copy No.: 29 A** (1974).

[71] R. Vacher, M. Biossier, and D. Laplaze, *Solid State Comm.*, **37**, 533 (1981).

[72] D. Mukherjee, B. D. Sahoo, K. D. Joshi and S. C. Gupta, *AIP Conf. Proc.*, **1536**, 403 (2013).

[73] G. Roma, C. M. Bertoni, and S. Baroni, *Solid State Commun.*, **98**, 203 (1996).

[74] M. G. Zemlianov, E. G. Brovman, N. A. Chernoplekov, I. L. Shitikov, *In Inelastic Scattering of Neutrons,* IAEA, Vienna, 431(1965).

[75] S. Speziale, C. S. Zha, T. S. Duffy, R. J. Hemley, and H. K. Mao, *J. Geophys. Res.*, **106**, 515 (2001).

[76] S. D. Jacobsen, C. M. Holl, K. A. Adams, R. A. Fischer, E. S. Martin, C. R. Bina, J. F. Lin, V. B. Prakapenka, A. Kubo, and P. Dera, *Am. Mineral.*, **93**, 1823 (2008).
[77] T. S. Duffy and T. J. Ahrens, *J. Geophys. Res.*, **100**, 529 (1995).
[78] B. Svendsen and T. J. Ahrens, *Geophys. J. Int.*, **91**, 667 (1987).
[79] L. Zhang, Z. Gong, and Y. Fei, *J. Phys. Chem. Solids,* **69**, 2344 (2008).
[80] T. S. Duffy, paper presented at DOE/SSAA Symposium, Washington, DC (2012).
[81] Satish C. Gupta, *Indian J Pure Appl. Phys.*, **34**, 651 (1996).

List of Figures

recovered sample and the as-received sample.

List of Tables

Chapter - 1

Introduction

1.1 Preface

Understanding the response of materials at high pressures is of interest not only from basic science point of view but also in applied sciences [1-6]. Pressure is a thermodynamical variable which can reduce the volume of condensed matter by more than a factor of two and thus can be taken as an independent parameter in the equation of state (EOS) of a material. The application of pressure on materials can bring various interesting changes such as the structural phase transformations, solid to liquid transitions, metal to insulator transitions, etc. Apart from these transitions sometimes the pressure induced mechanical instabilities can lead to simply fractures in the materials. Pressure can be applied on materials either isothermally or adiabatically. The isothermal pressurization condition is achieved in static compressions, *e.g.*, in experiments using diamond anvil cell, whereas, the adiabatic pressurization condition exists in high strain rate compressions (dynamic compressions), *e.g.*, in shock compression experiments using gas guns or lasers and in isentropic compressions employing lasers or magnetic flux compression technique. The above mentioned pressures driven changes in materials are not only dependent on the amplitude of the applied pressure but also on the rate of application of pressure or equivalently on the strain rates.

The above mentioned two methods of pressurization *i.e.*, static compression and shock compression differ significantly in nature. In the static compression technique [4], material is squeezed slowly; hence, temperature inside the sample during the experiment remains constant. To some extent, in static method one can compress the material hydrostatically by compressing the sample in the environment of a suitable (fluid or gas) pressure transmitting medium [4,7]. On the other hand, in shock compression methods, materials are compressed uniaxially with very high rate of pressurization (rise times ~ few tens of nanoseconds). The rapid compression increases the internal energy and temperature of the specimen. The irreversible sudden compression also increases the entropy of the system. Under static compression, the pressure can be held as long as we desire, however, in shock compression the duration of pressure pulse (of order of few microseconds) depends on the dimensions of the sample. Unlike the hydrostatic compression, the shock loading is always accompanied by the shear stresses which may induce phase transitions that are not observed under hydrostatic loading. For example, in tantalum (Ta) the body centred cubic (β) phase is found to be stable under hydrostatic compression up to 170 GPa whereas under shock loading it transforms to three atom hexagonal (ω) phase at ~ 45 GPa [8-10].

One of the important pressure induced changes in material behaviour observed is phase transitions. Some of the interesting pressure induced phase transitions under static compression are metallization of oxygen at ~ 96 GPa [11-12], metal to insulator transition in sodium at ~ 200 GPa [13], wide-bandgap, even-valence insulator to metal transition in silicon at ~ 90 GPa [14]. Apart from these pressure induced transitions, the hcp → three atom hexagonal (ω) → bcc (β) structural transformation in group IV transition metals Zr and Hf observed under static as well as shock compressions [15-22] are also interesting from applied as well as basic science point of view. The interesting high symmetry β to low symmetry ω phase transition in tantalum and Zr-20%Nb alloy has been reported to occur around ~ 45 GPa and ~ 15 GPa, respectively, under shock loading [9-10,23], whereas, the same transition does not occur under static compression [8, 23]. The discovery of such pressure induced phase transitions in materials has added new dimensions to the understanding of behaviour of materials under high pressure. For example, the occurrence of hcp → ω → β structural phase transition in Ti, Zr and Hf under high pressure has been attributed to the transfer of electrons from filled *s*-band to the partially filled narrow *d*-bands and their distribution in various *d*-substates [24-26]. The knowledge of this structural sequence under pressure and its correlation with electron transfer from *s*-band to *d*-band has added a new understanding in basic physics of transition metals and their alloys.

Apart from pressure induced phase transitions, the high pressure equation of state (EOS), *e.g.*, isotherm, isentrope and Hugoniot also play key role in complete characterization of material state under pressure. The knowledge of EOS is a vital input to the computer hydrodynamic codes used for the simulations various situations such as the wave propagation in geological media, reactor accidents, fission/fusion energy systems and in the analysis of many problems pertaining to geophysics, astrophysics and planetology [1, 2]. Similarly, knowledge of the pressure dependent elastic constants of materials can be utilized to examine mechanical stability as a function of pressure, to determine the pressure effect on melting, Debye temperature, sound velocity, Gruneisen parameter etc [27-29]

The mechanical failure strength especially the yield strength and the spall strength of materials is of practical interest. The failure strength of a material is dependent on the binding energy and the defects and dislocation present in the material. In a perfect solid, the failure strength is solely dependent on its binding energy; however, in case of a practical solid the failure strength strongly depends upon the defects and dislocations present in it. Beside the defects and dislocation, the failure strength of materials also depends on the rate at which the strains are applied [30-31]. In fact, it has been observed experimentally that the failure strength of a material measured under quasistatic loading differs significantly from that measured under high strain rate conditions [30-33]. This suggests that the knowledge of strength properties merely at quasistatic loading conditions is not sufficient when the suitability of a material for applications involving high strain rates has to be decided. For example, analysis of structural response of a material subjected to high strain rate loading conditions occurring during the propagation of seismic waves through geological media and the fracture and fragmentation at high velocity impact needs the failure strength at high strain rate as input.

In view of the key role played by pressure induced structural phase transitions, high pressure EOS, shock Hugoniot, pressure dependent elastic constants and strength of materials, it is important to determine these properties for understanding the several aspects of the material behavior under high pressures. The present thesis deals with such studies carried out on NaCl type structured (B1 Phase) binary compounds LiH, MgO and LaN. The thesis is planned as follows:

The present chapter provides the outline of the work to be presented in the subsequent chapters along with the current status of high pressure research including the basics of high pressure, the methods of generation of high pressure and various diagnostic techniques utilized for determining the behavior of the materials under pressure. Also discussed are the theoretical methods (*ab-initio* calculations) available to simulate the high pressure state of the materials.

The second chapter presents the detailed *ab-initio* theoretical investigations carried out on LiH under pressure. Under high pressure, because of the quantum influence of proton and increasing interaction of core electrons of neighboring atoms, this material is expected to display interesting behavior such as the transitions to low-symmetry phase, metal-insulator transition, etc [34]. Thus, *ab-initio* calculations at 0 K have been performed on the plausible phases of LiH and structural stability has been analyzed. The theoretical analysis predicts that the B1 phase of LiH will transform to CsCl type structure (B2 phase) at ~ 327 GPa. Various thermophysical properties *e.g.* Gruneisen parameter, Debye temperature, Hugoniot parameter etc., at ambient condition have been calculated and compared with available experimental and theoretical data. The variation of elastic constants and elastic anisotropy with pressure was determined and the polycrystalline elastic moduli have also been calculated. Calculations have further been extended to determine the phonon spectra of B1 phase of LiH as a function of compression up to 120 GPa [35]. The X-point phonon frequencies calculated at various pressures up to maximum of 120 GPa have been compared with the available experimental data [34].

The third chapter of the thesis provides the detailed account of the theoretical investigation on MgO. MgO having B1 structure at ambient conditions is a geophysically important material [36] and used as pressure standard in diamond anvil cell (DAC) based high pressure experiments. Apart from this, MgO is potentially suitable candidate for use as a window material in shock wave experiments [37]. Therefore, analysis of its structural stability, determination of equation of state and strength properties is of practical importance. The chapter presents the analysis of the structural stability under pressure followed by the determination of 300 K isotherm, isentrope and Hugoniot of this material and comparison with available experimental data [38-46]. The structural stability analysis predicts that the B1 phase of this material will transform to B2 structure at ~ 535 GPa. The calculations have been extended beyond the hydrostatic compression conditions and ideal failure strength has been determined for two different uniaxial loading conditions, *e.g.*, ‘uniaxial strain condition’ and ‘uniaxial stress condition’ along [001] crystallographic axis. For this purpose the elastic moduli of MgO single crystal as a function of compressive as well as tensile strain has been determined for two different loading conditions and ideal failure strength is determined by examining the elastic stability criterion at each strain for compression as well as in the expansion.

Another binary system chosen for theoretical investigation is rare earth mononitride LaN, which also like LiH and MgO exists in B1 phase at ambient conditions. Earlier theoretical investigations [47-48] have predicted B1 to B2 structural phase transition in material also under pressure, however, recent DAC based high pressure experimental study [49] has reported that at ~ 22.8 GPa, this material, instead of transforming to B2 phase goes to a lower symmetry primitive tetragonal structure (B10) named as HP-LaN by authors. The fourth chapter of the thesis presents the theoretical investigation on structural stability of LaN under high pressure. The comparison of total energies of B1, B2 and B10 (HP-LaN) structures as a function of hydrostatic compression suggests that the B1 phase will transform to B10 structure at ~ 25.8 GPa which will further transform to B2 structure at a pressure of ~ 169 GPa. The stability of B10 phase has been tested for LiH and MgO and it has been found that this structure remains unstable even up to a few Mbar pressures. To understand the cause for the existence of lower symmetry B10 phase (a distortion of the B2 structure) in LaN prior to the stabilization B2 phase at higher pressures, we have analyzed the band structures of B10 and B2 phase. Our analysis suggested that the low symmetry B10 phase could be stabilized at lower pressure due to lowering of total energy by symmetry breaking.

As already mentioned, in many applications, such as hypervelocity impacts and armor applications, the generated strains are dynamic in nature with very high strain rates ranging from ~ 10^4/s to 10^9/s. The yield strength and fracture strength are different for such high strain rates than those in static measurements. So, it is of practical importance to determine these properties under high strain rate conditions. Experimentally, it is possible to measure the dynamic yield strength (yield strength at high strain rates) and dynamic fracture strength (or spall strength) of materials using properly configured shock wave experiments [30, 50] in conjunction with interferometric technique known as velocity interferometer system for any reflector (VISAR) [51]. Shock wave experiments on polycrystalline copper have been performed to determine the dynamic yield strength; spall strength of this material at strain rates of ~ 10^4/s. Fifth chapter of thesis discusses the results of experimental measurements of these mechanical properties on polycrystalline copper.

The last chapter of the thesis will summaries and conclude the overall work presented in the thesis. The summary and conclusion will be followed by the further research scopes open in these areas.

With this outline of the work to be presented in the subsequent chapters of the thesis, the following sections of the this chapter give the present status of the high pressure research which includes the brief description of currently available experimental methods for generating high pressures in materials, various diagnostic techniques used to characterize the materials under high pressures and modern theoretical methods for understanding response of material under pressures.

1.2 Methods of High Pressure Generation

High pressures in materials can be generated experimentally in methods which can broadly be categorized into two types depending on the rate at which strain is generated in the sample, namely static compression and dynamic compression. As has already been stated, in static compression method, a very small sized sample along with a material used for measuring the pressure generated in the sample is encased in a gasket material and the whole system in compressed between two opposed diamonds (in DAC experiments) mechanically in very slow process so that the isothermal condition in the sample can be achieved. On the other hand, in dynamic compression method, a large amount of energy is imparted in the material in very short period of time using a sub-microsecond pressure pulse propagating through a material with super-sonic speed called shock wave. Here, evidently the material gets compressed adiabatically and temperature increases due to sudden deposition of large amount of energy in very short period of time. The following sub-sections give a brief account of these two techniques:

1.2.1 Static Compression

1.2.1.1 Methods of Static Compression

Static compression technique was first introduced by Nobel Laureate P. W. Bridgman. He built the piston-cylinder device where the sample is compressed in a cylinder by two opposed pistons [52]. This basic apparatus was improvised later. This was followed by the invention of Bridgman anvil cell where the material under examination is sandwiched between two anvils of tungsten carbide material. Electrical resistivity measurement and compressibility measurement can be carried as a function of pressure up to few GPa using this apparatus. The quest for still higher pressures led to the invention of the diamond anvil cell (DAC) [52-58] working with the same principle as the Bridgman cell; the only difference being the material used for the anvils is the hardest material known so far. The sample, here, is squeezed between two opposing single crystals of diamond. Various diagnostic techniques used to analyze the state of sample under high pressure include the measurement of electrical resistance, Mossbauer spectroscopy, x-ray diffraction, Raman and Brillouin spectroscopy, optical absorption spectroscopy etc.

The schematic diagram of DAC is shown in Fig. 1.1. As shown in figure the DAC set up consists of mainly four parts. The first component is the pressure generating

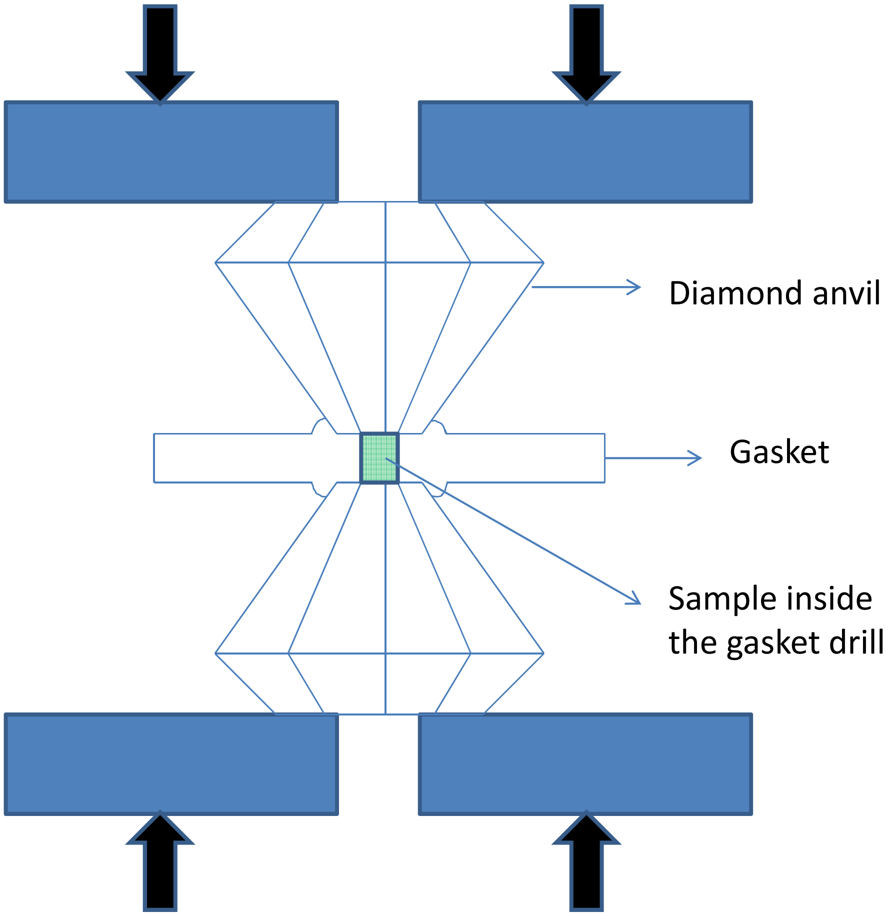

Figure 1.1: Schematic diagram of diamond anvil cell (DAC) with its basic components.

system which can be a lever arm, tightening screws or pneumatic or hydraulic pressure from a pressurized gas bottle applied to a membrane. For all cases the forces generated on the diamonds are of uniaxial type. Second component is the flawless, gem quality diamonds on which pressures are applied by the pressure generating devices. The culets of the diamonds face each other and they are adjusted to be parallel otherwise the triaxial strains will break the diamond. Third part of the system is the gasket which is a metallic plate on which first a small indent is made on it by pressurizing the gasket with diamonds. Then, a small drill of few micron diameters is made almost middle of the indent. This small hole is filled up with a pressure transmitting medium (fourth component of DAC) which is a fluid to generate hydrostatic pressure in the sample. A few microgram samples along with a small chip of pressure marker material are immersed in this pressure transmitting medium. When uniaxial load is applied over the diamonds, the pressure transmitting medium surrounding the sample produces hydrostatic pressure on the sample.

As pressure is increased the pressure transmitting medium starts getting solidified above certain pressure. As long as the shear strength of the solidified pressure transmitting medium is low enough, the compression is close to hydrostatic and named as quasi hydrostatic but when shear strength increased significantly the compression no longer remains to be hydrostatic. The commonly used pressure transmitting mediums in DAC are 4:1 methanol-ethanol mixture and some inert gases like Xe, Ar, He and H_2 [4]. The methanol-ethanol mixture remains hydrostatic up to 10.4 GPa; addition of small amount of water (methanol:ethanol:water :: 16:3:1) takes this hydrostatic range to 14.5 GPa, however, the gases Xe, Ar, He and H_2 are used upto higher pressures of ~ 100 GPa. Though it is believed that using Xe, He and H_2 as pressure transmitting media it is possible to maintain hydrostatic condition up to ~ 100 GPa [4], the recent high pressure work report that it not possible to maintain truly hydrostatic condition at pressures higher than ~ 15 GPa because none of the pressure transmitting medium remain fluid above this pressure [56]. The DAC developed by Mao and Bell can generate static pressure of about 200 GPa in samples [57-58]. Still higher pressures of more than 500 GPa are reported to be achieved by using improved DAC [59]. An advanced version of DAC where screw -

spring mechanism of conventional DAC is modified by attaching a motor driven gearbox to the system has been developed by Mao and Mao [60] and pressure of ~ 230 GPa has been generated in the Pt sample using this instrument. Recently, Evans *et al.* [61] have developed an apparatus named as dynamic DAC which applies a time dependent load to a sample. This instrument, which is a modified version of conventional DAC comprises a DAC coupled with piezoelectric actuators that derive a load supplementing the main load provided by the load screws of conventional DAC. It is capable of generating repetitive time dependent load/strain with loading rates of ~ 500 GPa/s and strain rates of ~ 0.16 /s in the sample. This instrument is useful for understanding the kinetics of phase transitions at such small strain rates which are inaccessible in shock wave experiments. Very recently, using the micro-semi-balls of nano-crystalline diamonds is used as second stage of conventional diamond anvil cell and this extends the achievable pressure in this device to above 600 GPa [62].

The measurement of pressure generated in the sample due to static compression is carried out using either the internal pressure markers or pressure dependence of ruby fluorescence. In first method the pressure generated in the sample is determined by adding internal pressure marker material (whose EOS is known) such as Cu, Mo, Pd or Ag with the sample in DAC [4]. The compression generated in the sample and pressure marker material is determined from collected x-ray diffraction data of sample and marker. The corresponding pressure in the sample is then inferred from the known EOS of marker material. In the second method the pressure dependence of the shift of the R1 (6927 Å) line of Ruby fluorescence is used to determine the pressure generated in the sample at a given compression [4]. The calibration of ruby fluorescence pressure scale for this purpose is carried out using isothermal EOS of standard substances derived from shock wave experiments [4]. The calibration so obtained relates the pressure and the shift in R1 line as follows [63]:

$$P(Mbar) = \frac{A}{B}\left\{\left[1+\frac{\Delta\lambda}{\lambda}\right]^{B} - 1\right\} \tag{1.1}$$

where $\Delta\lambda$ is the ruby R-line shift (= 0.365 Å/kbar) and A = 19.04 Mbar and B = 7.665.

The high pressure experiments using DAC can be conducted not only at room temperature but also at low as well as elevated temperatures. For low temperature experiments the DAC is immersed in the cryogenic fluid directly to gain the low temperature or cryogenically cooled system with the thermocouple arrangement are used [64]. To study high pressure behavior of materials at elevated temperatures, DACs are equipped with heating arrangements. Two techniques used to generate high temperature in the sample are resistive heating and laser heating [65-67]. The first laser heated DAC (LHDAC) introduced by Ming and Bassett had the capability to generate sustained temperature up to 2000º C and 3000º C using two different type of laser and pressures up to ~ 26 GPa [68]. New LHDAC can be used to understand the high pressure behavior of materials above 350 GPa in conjunction with temperature in excess of 5500 K [65]. This kind of LHDAC instrument is useful for understanding the state of material in the high pressure-high temperature conditions existing in the interior of the earth.

1.2.1.2 Diagnostic Techniques in Static High Pressure Experiments

In the high pressure experiments carried out using DAC set up the pressures in the sample can be held as long as one desires. This makes online characterization of pressurized sample in DAC easier than that in shock wave experiments. Various microscopic techniques such as x-ray diffraction [69], inelastic x-ray spectroscopy [70], extended X-ray absorption fine-structure (EXAFS) [71], X-ray fluorescence (XRF) [72], Mössbauer spectroscopy (SMS) [73], nuclear forward and inelastic scattering (NFS and NIS) [74], neutron diffraction, Raman scattering, IR scattering and Brillouin scattering [4, 75-81] are commonly used for online characterization of the pressurized sample in DAC.

The x-ray diffraction technique in DAC has made significant advancement in past few decades. As the sample size is very small (of the order of few microns) in DAC, for sufficient scattering from the sample high brilliance of x-ray is required. The birth of synchrotron radiation sources around the world has added new dimensions to the x-ray diffraction technique. The first synchrotron radiation beam was seen in General Electric Research Laboratory in Schenectady, New York on 1947 by Elder *et al.* [82]. Earlier, the synchrotron radiation generated by the moving particles in accelerators built for high energy particle physics was unwanted byproduct as more energy was needed to be pumped to overcome this leak and continue particle move with desired velocity(first generation of synchrotron source) [83]. Later, the analysis of this radiation revealed that it has very useful properties to be employed as probe for material research. These particle accelerators served as the second generation synchrotron sources. The second generation synchrotron sources produce dedicated x-rays by using bending magnets that keeps the electron beams moving in a circle. The third generation synchrotron sources were built by fitting second-generation sources with insertion devices such as undulator and wiggler magnets for optimization of the brightness. Wigglers can create a broad intense incoherent beam whereas; undulator can give narrower coherent beam. Fourth generation of synchrotron source is under construction for producing ultra brilliant, pulsed time-structured x-rays. The European Synchrotron Radiation Source (ESRF), Hamburger Synchrotronstrahlungslabor (HASYLAB), the Advanced Light Source (ALS) at Berkeley, the Japanese source SPRING-8 and National Synchrotron Light Source (NSLS) at Brookhaven National Laboratory are examples of some of the third generation synchrotron sources. The high brilliance (~ 10^3 -10^4 times more brilliant than the beams from conventional x-ray machines) along with tunability of wavelength of the x-rays, to control their polarization, and to choose between a single wavelength or a range of wavelengths makes this radiation an excellent probe for diverse systems such as normal and magnetic materials, biomolecules, polymers allowing to explore phase diagram, chemical reactivity, properties of elements and compounds [54]. The high brilliance of synchrotron radiation makes it a very powerful tool for characterizing the low Z elements (*e.g.* H_2, Li) or materials composed of low Z elements (*e.g.* hydrogen storage material $NaBH_4$) and quantitative analysis of phase composition specially for phases present in extremely low concentration < 1%. For example, in Li the occurrence of new rhombohedral phase and cubic polymorph with 16 atoms per unit cell under high pressure could be confirmed through sufficiently intense synchrotron radiation diffraction (SRD) [84]. In nominal high purity α-alumina ceramic, the SRD could clearly establish the presence of trace levels of β- alumina and anorthite ($CaAl_2Si_2O_8$), which was inconclusive from conventional x-ray diffraction [85]. Thus, now-a-days, the SRD has replaced the conventional x-ray diffraction for the on-line measurement in DAC. The synchrotron radiation has been used for Mossbauer spectroscopy also, e.g., detection of the antiferromagnetic to paramagnetic transition in $SrFe_2As_2$ at 4.2 GPa and 13 K of temperature could be done through Mossbauer spectroscopy using SRD [64]. Also for the same powder sample at 13 K temperature the angle dispersive synchrotron XRD shows orthorhombic phase below 4 GPa and tetragonal structure above 6 GPa.

The detection of pressure induced structural phase transitions and determination of their mechanisms is carried out by performing x-ray diffraction; Raman or IR spectroscopy in the compressed state, and electron diffraction and electron micrography measurements on samples retrieved after pressurization. The continuous monitoring of the evolution of the new structure in the sample material in DAC experiments through x-ray diffraction or Raman and IR spectroscopy is carried out in online mode as a function of applied pressure. On-line Raman measurement is also used to measure the ruby fluorescence and thereby measuring the stress on the diamonds and the sample. Vibrational spectroscopy gives vital information on the behavior of ice, in particular, the evolution of hydrogen bonds. Further, infrared reflectance spectra determined using synchrotron source have also been utilized to infer about phase transition in materials under pressure, e.g., Goncharov *et al.* [86] have reported a phase transition in ice at 60 GPa (70 GPa in D_2O ice) on the basis of infrared reflectance spectra determined employing synchrotron source. Further, the in-situ measurements are useful to detect the reversible phase transitions in the materials *e.g.* reversible cubic to amorphous phase transitions in negative thermal expansion materials $ZrMo_2O_8$ and $HfMo_2O_8$ [87], scheelite phase to fergusonite phase transition in $BaWO_4$ [88], etc. The electron microscopy measurements are useful for not only to detect the pressure induced irreversible phase transitions but also to determine the lattice correspondence between the parent and product phases, which in turn is used to understand the mechanism of the phase transition. For example, the lattice correspondence between the parent α (hcp) phase and product ω phase derived from electron diffraction patterns obtained from partially ω (three atom simple hexagonal) transformed samples of group IV transition elements and their alloys subjected to high static and dynamic pressures has been used to understand the mechanism of this transition [15, 89-95].

In addition to these microscopic techniques, the macroscopic method of electrical conductivity measurements is very useful in detecting the pressure induced phase transitions, *e.g.* in Ti and Yb through continuous monitoring of the electrical resistances under pressure, Singh [96-97] has not only detected the $\alpha \rightarrow \omega$ transition in Ti and fcc $\rightarrow$ bcc transition in Yb but also investigated the kinetics of these transitions.

Apart from determining structural phase transformations, phase diagram, reaction kinematics etc., experiments carried out on DAC in conjunction with synchrotron technique can map melting line by direct observation of melting as well as the dynamic insight of the melting phenomena. Melting can be probed in DAC using various methods: (a) observing changes in the sample surface by laser speckle technique [98]; (b) changes in the resistivity of the sample during heating [99]; (c) changes in the absorption of laser radiation [100]; (d) heating sample to a specific temperature and observation of visual changes after experiments [101]; (e) *in-situ* XRD technique to observe the diffuse scattering from liquid phase [102].

Using the high pressure-high temperature condition in the DAC, new materials have been synthesized many of which such as diamond and the cubic boron nitride (c-BN) have industrial importance [103]. Many noble metals nitrides such as PtN_2, IrN_2, and

OsN_2 have been synthesized by varying the pressure temperature condition and controlling the reaction pathways in the DAC [104-106].

1.2.2 Shock Compression Techniques

The shock compression methods of pressure generation which differ significantly from static compression method are also important as these are utilized to explore the different regimes of EOS surface which cannot be accessed in static compression experiments using DAC. The following subsections give the basic concepts of generating positive pressure (compressive stress) as well as negative pressures (tensile stress) in shock wave experiments. Also described are various methods of shock wave generation and diagnostic techniques used in shock experiments.

1.2.2.1 Basic Concepts of Shock Compression

A sudden deposition of high energy on a material by some means can generate an impulse of compression in the material which when traverses in the material with supersonic speed producing near-discontinuous changes in density and pressure across the wave front, a shock wave is said to be generated in the material. The shock front discriminates the material into two parts – the shocked and the un-shocked region across which various physical properties, such as density, pressure, temperature etc change abruptly. The temperature in dynamic compression can be tuned by varying the rise time of the pressure pulse. Highest temperature can be generated in the case of single-shock wave; whereas, the lowest temperature can be achieved in the isentropic process. The formation of shock wave in a medium can be understood as follows:

Consider a plate impact experiment where a moving plate (flyer) impacts a stationary plate (target) so that a linear shock wave travels through these plates. When the

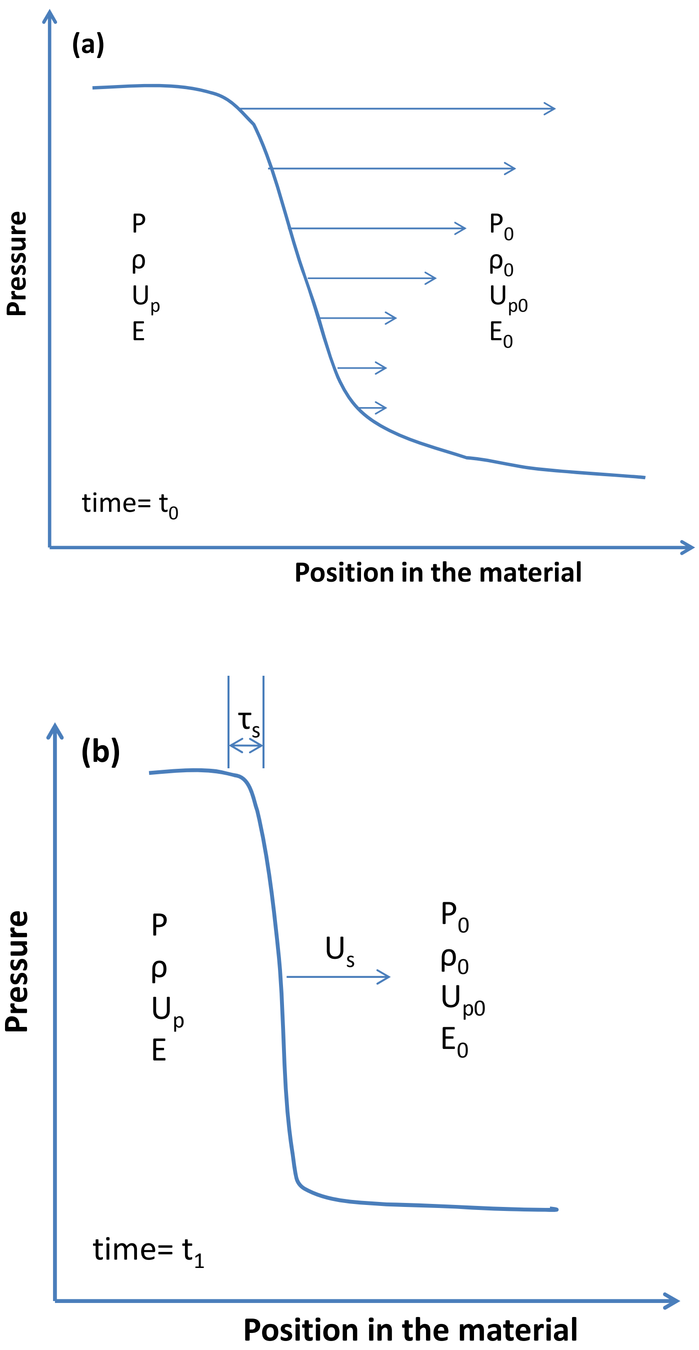

Figure 1.2: (a) Hypothetical broad stress wave profile at time = t_0. The length of the vector indicates the speed of the point in the profile, which increases with stress at that point. **(b)** At later time t_1 the wave front attains a finite constant width (τ_s) due to balancing of sharpening effect caused by non linearity and spreading effect from viscosity and thermal conductivity of material. Hence a steady shock wave with constant front width (τ_s) propagates into the material.

plates comes in contact of each other, a compressive disturbance propagates in the interior of the plates as a stress wave as shown schematically in Fig.1.2. Suppose that initially (at time $t = t_0$) the stress wave profile is broad as in Fig.1.2a. Every point in this profile travels with a velocity

$$\frac{dx}{dt} = C + U_p \tag{1.2}$$

where C and U_p denote the sound velocity and the material velocity, respectively, at pressure P. As, C and U_p are pressure dependent, the point near the crest will travel faster than the point far from the crest as the pressure increases towards crest. Thus, starting from foot to the crest of the profile the velocity goes on increasing (as shown by the vectors in Fig 1.2a) and with time this difference in velocity will sharpen the wave front. This sharpening effect arising due to dependence of sound speed on amplitude of pressure is opposed by the spreading effects due to viscosity and thermal conductivity of the material. Hence at some point of time $t = t_1$, when the two opposing effects start balancing each other the steady shock wave front with finite constant width (Fig. 1.2b) propagates in to the material.

For a steady shock wave the conservation of mass, momentum and energy across the shock wave front can be written as a set of differential equations [107-108], which lead directly to three Rankine-Hugoniot relationships between the specific volume V, the stress (shock pressure) P, the particle velocity U_p, the shock velocity U_s and the specific internal energy E (the zero subscript in these variables corresponds to the initial phase that is the unshocked state). These three conservation equation can be derived as follows:

Suppose a material is contained in a cylinder of cross-sectional area A. One end of the cylinder is open, but the other is closed by a piston that is in contact with the material. Initially, as shown in Fig. 1.3a, the system is at rest. Suppose that at time $t = 0$, the piston impulsively acquires the finite velocity U_p in the x-direction. Then it instantly begins to drive the material to the right at the same velocity U_p. This is accomplished by a shock wave that instantly appears on the face of the piston and propagates into the material with the finite velocity $U_s > U_p$ (see Fig. 1.3b). As U_s is finite, the material to the left of the shock wave moves at the velocity U_p, but the material to the right of it remains at rest. The equations for conservation for mass, momentum, and energy can now be derived as follows. It is assumed for simplicity that the system has adiabatic walls, that body forces such as gravity and electromagnetism are negligible and that there is no heat transfer by radiation across the shock.

Conservation of Mass

After unit time the piston has moved a distance U_p and the shock a distance U_s. During that time the shock compresses a mass of the material from its initial volume AU_s to $A(U_s - U_p)$. The density therefore increases from initial ρ_0 to ρ, so the conservation of mass demands that,

$$AU_s\rho_0 = A(U_s - U_p)\rho$$

$$or,\ U_s\rho_0 = (U_s - U_p)\rho \tag{1.3}$$

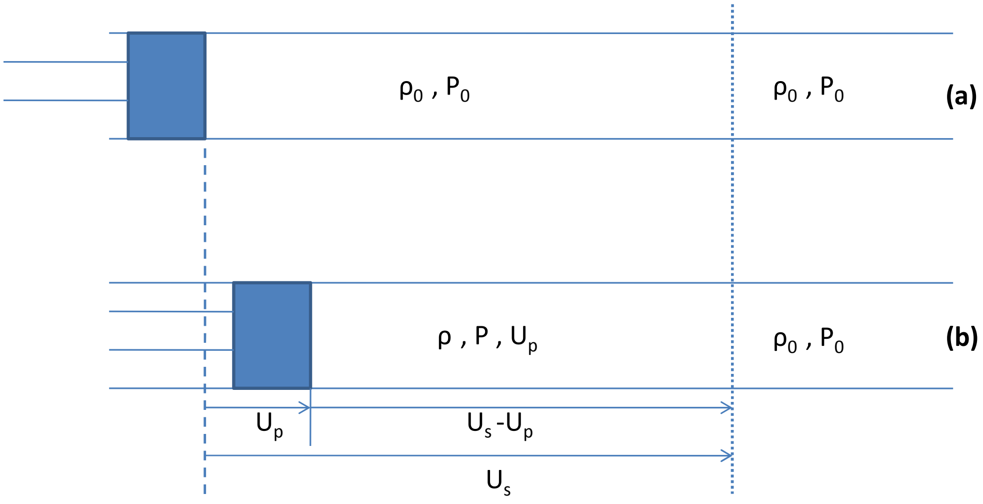

Figure 1.3: Shock wave generated by the impulsive motion of a piston. (a) Initial state at rest; (b) state in unit time after the piston had acquired velocity U_p impulsively.

Conservation of Momentum

The piston applies a driving force $(P - P_0)A$ to the material, causing it to acquire a momentum per unit time of $(\rho_0 U_s A)U_p$ Then from conservation of momentum,

$$P - P_0 = \rho_0 U_s U_p \tag{1.4}$$

Conservation of Energy

The compressive work that the piston does on the material in unit time is PAU_p. The energy gained by the material in unit time is the sum of the kinetic $\frac{1}{2}(\rho_0 U_s A)U_p^2$ and the internal energy $(\rho_0 U_s A)(E - E_0)$. Thus by conservation of energy

$$PU_p = \rho_0 U_s(\frac{1}{2}\, U_p^2 + E - E_0)$$

$$or,\ E - E_0 = \frac{1}{2}\,(P + P_0)(V_0 - V) \tag{1.5}$$

Further, the following useful relationships can be deduced from Eqns. (1.3) and (1.4):

$$(P - P_0) = \frac{U_S^2}{V_0^2}(V_0 - V) \tag{1.6}$$

$$U_p^2 = V_0^2\left[(P - P_0)(V_0 - V)\right] \tag{1.7}$$

Under compression the thermodynamic path followed by material while going from initial state (P_0, V_0) to final state (P, V) is Rayleigh line with slope U_S^2/V_0^2 as represented by Eqn. (1.6).

Fig. 1.4 displays the Hugoniot along with isotherm and isentrope from the same initial state. The blue, green and red curves represent the isotherm, isentrope and Hugoniot, respectively, starting from the same initial state (P_0, V_0). In the case of isotherm or isentrope, any final state is achieved following every point on the isotherm or isentrope curve from the initial state. In the case of Hugoniot, the situation is different. When a shock compresses a material, the material achieves a final pressure-volume state

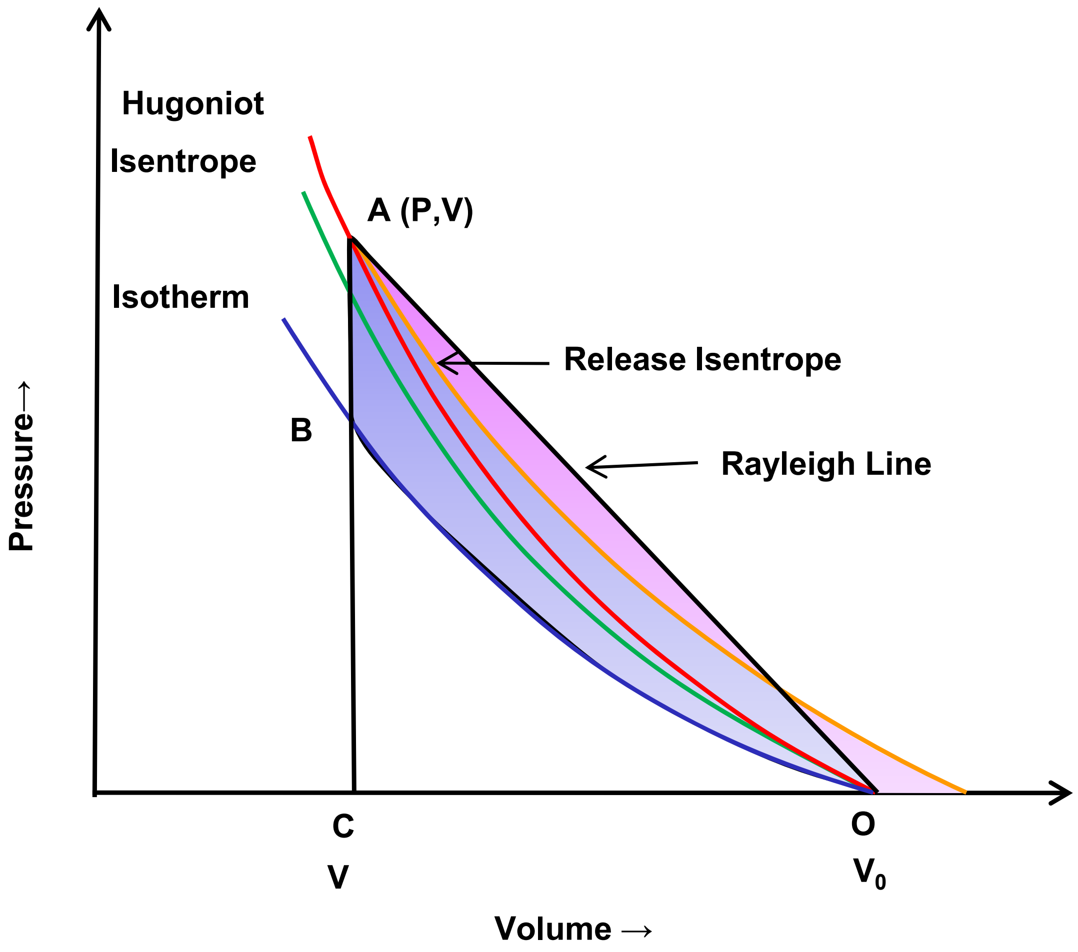

Figure 1.4: Schematic P-V diagram showing the compression curves. The Hugoniot lies above the isentrope which lies above the isotherm. For isentrope and isotherm, the thermodynamic path coincides with the locus of state. For Hugoniot which is the locus of shock states, the thermodynamic path is a straight line (Rayleigh line) from ($P = 0$, $V = 0$) to (P, V) state on the Hugoniot curve. The magenta colured curve is the release isentrope. The difference of the area of triangle OAC and curved triangle under release isentrope represents the heat deposited on the terminal material. In other words, the irreversible heating of the sample is equal to the difference between purple shaded areas below and above the Rayleigh line (Fig. 1.4). This irreversible heating of the material causes increase in its entropy.

A (P, V) from its initial state O (P_0, V_0) through the Rayleigh line as thermodynamic path (Fig. 1.4). Thus the successive states on the Hugoniot cannot be obtained one after another by a shock process. The Hugoniot is, thus, constructed from some initial state O (P_0, V_0) by carrying out different shock wave experiments to achieve different final pressure-volume state and then joining those final shocked states with the initial state. In other words, the Hugoniot of a material is the locus of all the equilibrium states that can be achieved from a given initial state, but the successive states along which cannot be achieved one from another by a shock process.

The process of shock compression is irreversible in nature and is accompanied by increase in entropy. Also, the temperature of the shock recovered sample is more than that of the initial unshocked state. Further, it is clear in Fig. 1.4 if the compression to volume V is carried out isothermally, then the increase in internal energy will be the area of the curved triangle OBC below the isotherm. However, under shock loading, the internal energy deposited on the compressed material is the area of the triangle OAC. The difference of the area OAC and OBC corresponds to the heat energy deposited by the shock on compressed material, which results in the thermal pressure. It may be noted that a small fraction of supplied energy goes in to generation of defects also. Fig. 1.4 clearly shows that with increasing compression, more and more energy goes into generation of thermal pressure. After passage of the shock, the material unloads through the release isentrope as shown in the Fig. 1.4 (orange line).

The relation between shock velocity (U_s) and particle velocity (U_p) also gives Hugoniot in the U_s - U_p plane as it can be drawn in the pressure – volume or pressure – density plane. An empirical relation between U_s and U_p is expressed as:

$$U_s = C_0 + sU_p + s^{'}U_p^2 + ... \qquad (1.8)$$

where C_0 is the bulk sound velocity of the material. It is experimentally observed that this relation is generally linear (Fig. 1.5a) for most of the materials which show no phase transition up to very high pressures *e.g.* normal metals like Li, Mo, Au, Os, Ba etc., or for

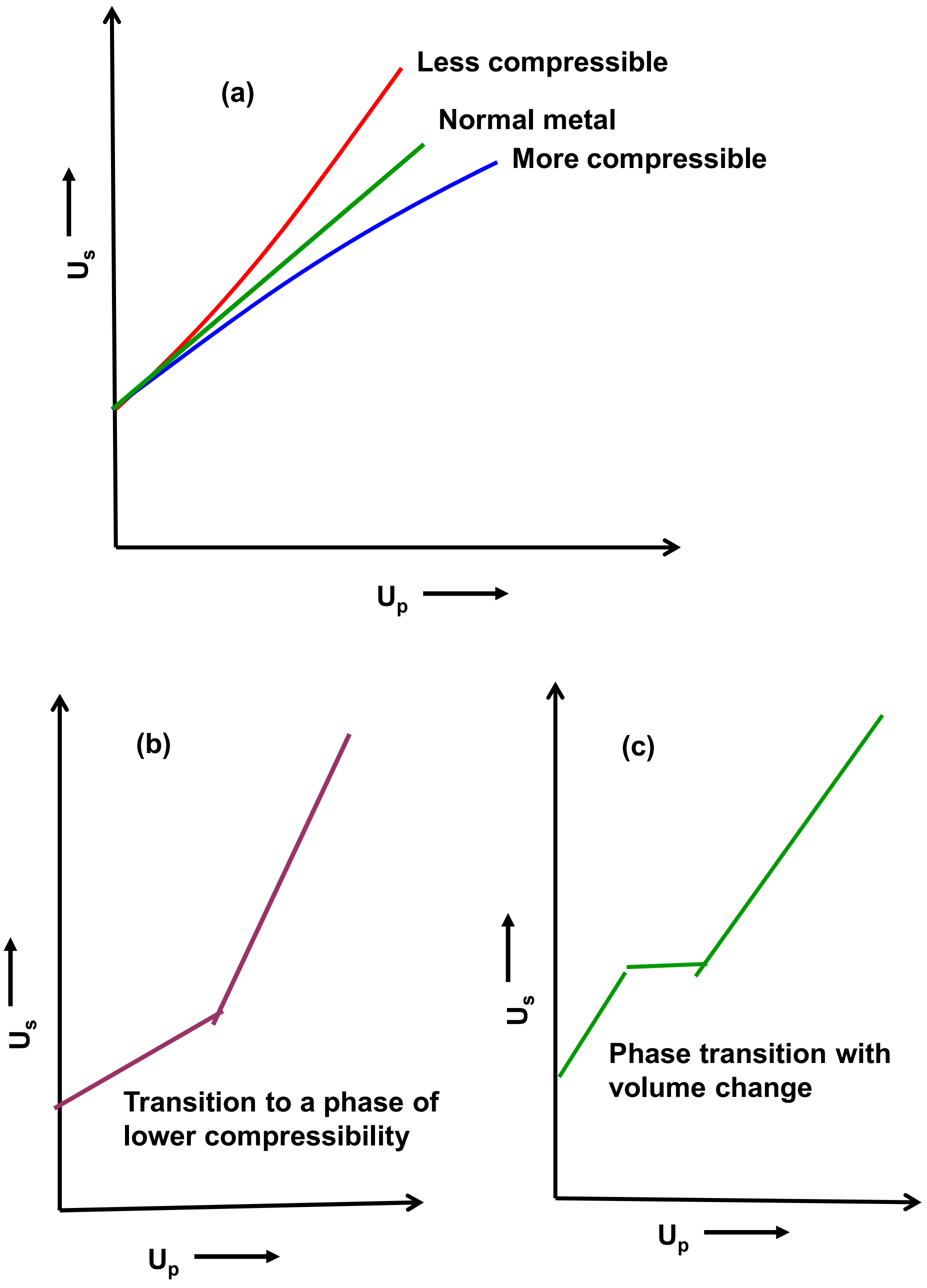

Figure 1.5: Representation of Shock Hugoniot in U_s-U_p plane for various conditions. The U_s –U_p relation for (a) normal material, material exhibiting decrease or increase in compressibility with shock compression, respectively; (b) a material undergoing a phase transition to a phase of lower compressibility (this situation can arise due to formation of a new electronic configuration of lower compressibility caused by transfer of outer electrons to partially filled inner shell at high pressure); (c) first order phase transition which are accompanied with volume change under shock compression.

those materials which undergo a phase transition to a new phase of same compressibility with negligible volume change *e.g.* thorium, [109-111, 27]. But as displayed in Fig. 1.5, in certain situations such as change in the compressibility, melting and first order polymorphic transitions under shock compression, U_s-U_p relation may deviate from linearity [109-113]. For example, for V, Nb, Co and Ta, the U_s-U_p relation is reported to be non linear with upward curvature however, the same for Al, Pb, Zn with a downward curvature [110-111]. These nonlinear relations between U_s and U_p with upward/downward curvature have been related to the decrease/increase in compressibility due to restructuring of energy spectra of electrons under high pressure and high temperature generated in shock compressions [110-111]. In some materials *e.g.* Gd, Nd, Y, Sc the U_s-U_p relation shows a break with two lines of different slopes (Fig. 1.5b). This break in U_s and U_p curve is attributed to the formation of compact electron configuration with reduced compressibility due to transfer of outer *s* electrons to the inner partially filled *d* shells at high shock compressions [110-111]. For a material undergoing first order phase transition the U_s-U_p relation exhibits two lines separated by a flat region (Fig. 1.5c)which is due to volume change occurring during transition [109-111, 113].

The complete characterization of state of material during shock compression needs knowledge of five unknowns namely pressure, shock velocity, particle velocity, density and internal energy. These five variables are interconnected by three Hugoniot relations (Eqn. 1.3 to 1.5) and thus measurement of any two variables suffices the complete characterization of state of shocked material. In plate impact experiments, the Hugoniot of any unknown target material generally determined using measured U_s and flyer plate velocity V_p in the impedance match method. The two types of impact configurations namely the symmetric impact and asymmetric impact can be used for this purpose. In the symmetric impact configuration the flyer plate and the target plate are made of same material; however, in asymmetric impact configuration the flyer plate material is different than the target material. In order to use asymmetric impact configuration for measurement of Hugoniot of unknown target material, the Hugoniot of the flyer plate material must be known. It may be noted that the Hugoniot of a material can be represented in P-U_p plane also by using the second shock jump condition (Eqn.

1.4). In the impedance match method this form of Hugoniot is used. The procedure of determination of Hugoniot by employing this method is explained below:

Suppose the experiment is carried out in asymmetric impact configuration. Consider that a flyer plate (impactor) of known Hugoniot, traveling at a velocity V_{p1} in right direction impacts the target at rest (Fig.1.6a). This impact introduces shock waves propagating in right direction in target plate and left direction in the flyer plate. Just before the impact, the pressure in the flyer plate is $P = P_0 = 0$ and particle velocity is V_{p1} in right direction, and after the impact, the left traveling compression wave reduces the forward motion (*i.e.* the motion in right direction) of the flyer *i.e.* with increasing compression the particle velocity in right direction reduces, therefore, as shown in Fig. 1.6b, its Hugoniot in P-U_p plane must be represented by a curve having a negative slope with origin at (0, V_{p1}) which is referred as reflected Hugoniot of flyer material also. The Hugoniot of the target which is initially at rest, must have its origin at $U_p = 0$ and $P = 0$ with a positive slope. It is evident from Eqn. (1.4) that the slope of a straight line joining this initial state to the final state (P_1, U_{p1}) in the target is just $\rho_0 U_{s1}$ (the slope of red line in the Fig 1.6b), where ρ_0 is the initial density of the target. The fundamental property of the impedance match method is that both the stress and the particle velocity must be continuous across the interface. Hence, the state achieved upon impact must be common to the Hugoniot's of the flyer and target as they are represented in the P-U_p plane. This common point can be found simply by extending a straight line of slope $\rho_0 U_{s1}$, of the target material, until it intersects the flyer Hugoniot. As shown in Fig. 1.6b, by performing experiments at several flyer velocities say V_{p2}, V_{p3} etc. the unknown Hugoniot of any material can be determined.

It may be noted that for a symmetric impact configuration as the material of flyer and target plate are identical, the Hugoniot of flyer is a mirror reflection of target Hugoniot about the pressure axis plus a translation by $U_p = V_{p1}$ (the velocity of flyer plate) along U_p axis. Therefore, the particle velocity U_{p1} corresponding to final state is simply equal to $\frac{1}{2} V_{p1}$. The shock pressure in target plate can be estimated just by substituting the measured U_{s1} and U_{p1} ($=\frac{1}{2} V_{p1}$) into Eqn. (1.4).

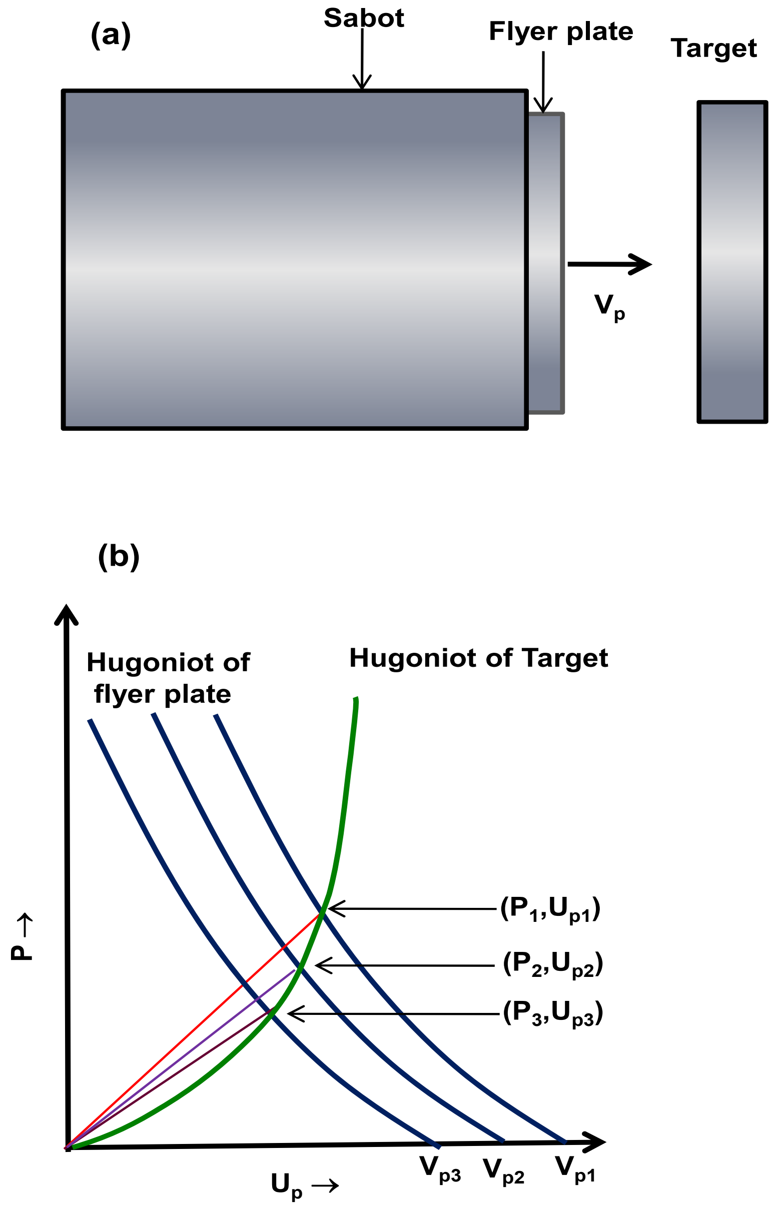

Figure 1.6: Impedance matching for Hugoniot determination. (a) A flyer plate attached with a sabot is moving at a speed V_{p1} strikes a target whose Hugoniot is to be determined. (b) Depending upon the impact velocity the origin of the flyer plate Hugoniot is displaced to V_{p1}, V_{p2} and $V_{p3,}$ and the curve is reflected to represent a left traveling shock wave. The several Hugoniot points of the target material can be determined from impedance match solutions for various impact velocities. The red, violet and brown lines are Rayleigh lines which are followed by the target material while going from a given initial state to final states achieved after the impact with flyer plates accelerated to velocities of V_{p1}, V_{p2} and V_{p3}.

1.2.2.2 Principle of Generation of Negative Pressure in Shock Wave Experiment

The shock compression experiments designed properly can generate not only the high compressive stresses but also high tensile stresses (negative pressure) in the materials [114]. The generation of high tensile stresses and occurrence of fracture in solids under shock loading is explained below:

Fig. 1.7 shows the state of the material during shock loading and unloading in a plate impact experiment for symmetric configuration (*i.e.* the target and flyer material are identical). In Fig. 1.7(a) (*x-t* diagram) the *x* and *t* are the distance from the impact surface and time after the impact, respectively. The right going shock wave in target takes the material from state 0 to state 1 as shown in the P-U_p diagram (Fig. 1.7(b)) and its propagation is represented by the line OB in the *x-t* diagram. Similarly, the left going shock wave in flyer takes the material from state 3 to state 1 in the P-U_p diagram and its propagation is represented by the line OA in the *x-t* diagram. The reflection of the shock wave in target at free surface produces a rarefaction wave represented by a rarefaction fan with C_{-h} and C_{-t} as the characteristic of head and tail, respectively. This rarefaction wave progressively unloads the material from state 1 to 3. Similarly, the reflection of the shock wave in the flyer at free surface results in a rarefaction wave, the propagation of which is represented by the family of C_+ characteristics. This rarefaction wave releases the pressure from state 1 to 0. The interactions of the right going and left going rarefaction waves result in various states in material represented by 6, 7, 8, 9, 10 and 11. It is clear that the interaction of these rarefaction waves results in negative pressure (tensile stress) states in the target material (for example states 7, 8, 9, 10 and 11 in P-U_p diagram). When the negative pressure exceeds the strength of the material, creation of new surface occurs parallel to the free surface. This process is called spalling and tensile stress at which the fracture of the material starts is known as spall strength (shown by point 9 in P-U_p diagram).

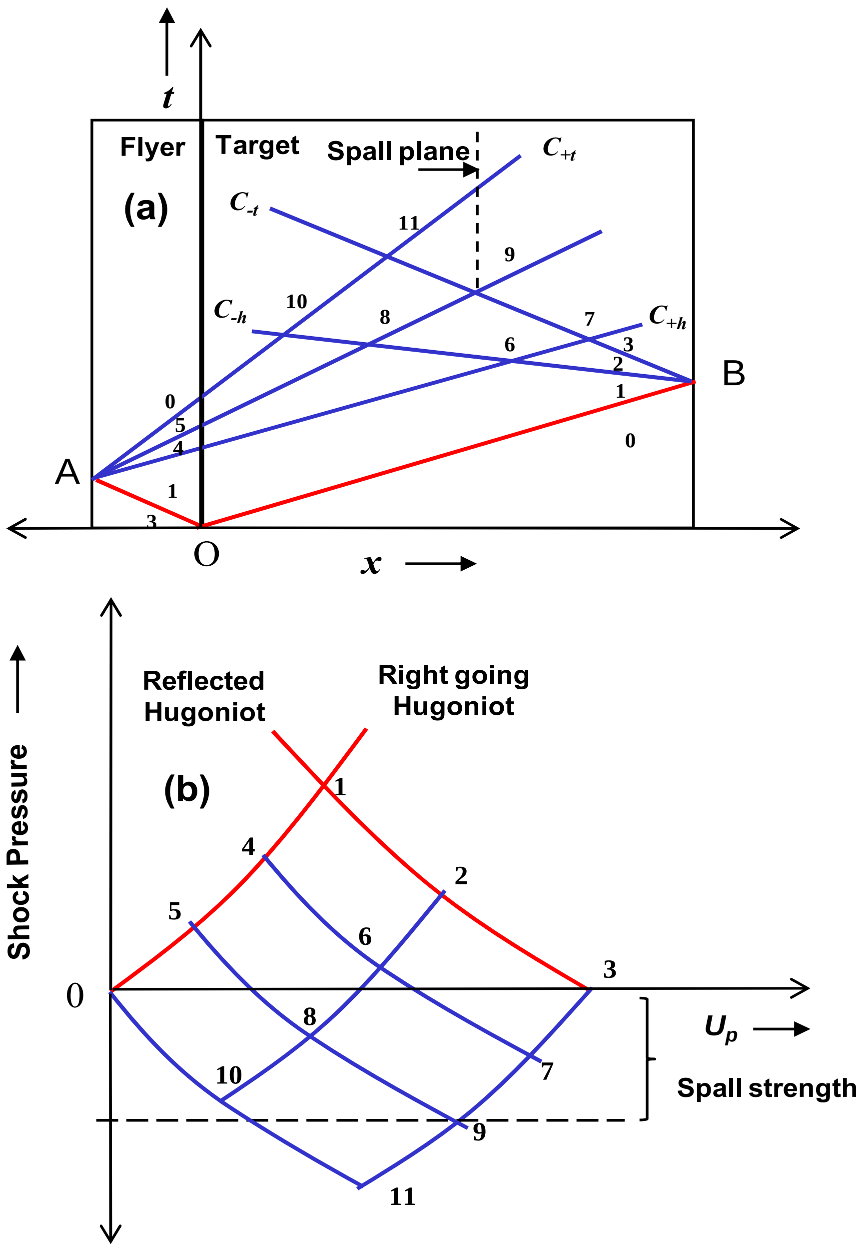

Figure 1.7: Generation of tensile stresses in material through plate impact experiment. The propagation of shock wave and release waves resulting from reflection of shock at target/ flyer free surface is shown in (a) x-t diagram (b) in P - U_p diagram. The shock wave through target and flyer takes their material to peak pressure state (labeled as '1') from initial states labeled as '0' and '3', respectively. The interactions of release waves produce various stress states labeled by '2' through '11'. As is clear from figure (b) many stress states lie in tensile regime. The tensile stress corresponding to state '9' is the maximum stress that solid can withstand before spall fracture.

1.2.2.3 Techniques of Shock Wave Loading

Shock wave in a material can be generated by impact or by rapid deposition of energy. Various forms of energy like chemical, mechanical, electrical, magnetic and radiation can be imparted in the material for producing shock waves. These can be classified as explosive driven systems, pulse radiation (laser, electron, X-ray, neutron, ion beam, photons etc.), gas guns, electric guns, rail guns and magnetic flux compression [108, 115-125].

For plate impact type experiments to generate shock wave in material, impact velocities are 15, 8, 5, 2 and 1 km/s for hemispherical explosively-driven systems, planar impactors accelerated with a two-stage light-gas gun, planar high-explosive systems, a powder gun and a single-stage gas gun, respectively[117-118,120]. Typically hydrogen, helium or nitrogen gases are used to drive the impactor in a two-stage and single-stage gas gun. Single stage light gas gun and powder gun drives a projectile with compressed gas and burned gunpowder, respectively. Shock transit time is few microseconds here. The advantage of gas-gun is that it is possible to perform experiments with well-defined initial conditions of the flyer and target materials (no temperature rise and density of projectile at the time of impact is that of ambient) with precisely controlled parallel and inclined impacts. Also it is possible to use large size samples of diameter of 25 mm and more which makes it easy to employ several diagnostic techniques simultaneously in a single experiment. In our laboratory at Bhabha Atomic Research Centre Mumbai, we have a single stage gas gun for studying the response of material to high stress and strain rates. The gun is capable of accelerating the flyer up to the velocity of 1 km/s, and generating the pressure of ~ 40 GPa in the target material [120]. In two stage light gas gun, burned gunpowder accelerates a piston which pumps the second stage. In the second stage, the piston compresses hydrogen gas upto ~ 100 MPa when rupture valve breaks and the compressed hydrogen gas drives the impactor along 10 m long launch tube. In the planar high-explosive systems, explosive kept on or ~ 1mm from the driver plate are burned and accelerated to 5 km/s. In hemispherical geometry the explosive driven system can generate about twice the impactor velocity of a two-stage gun.

Pulsed electrical currents can be used to launch impactor plates to velocities up to ~30 km s^{-1} or more using magnetic acceleration [123-125]. The electric gun developed in our laboratory at Bhabha Atomic Research Centre has capability of launching a 0.5 g flyer up to a velocity of 6.6 km/s [122]. High dynamic pressures are also achieved by rapid energy deposition, such as from lasers, and, in former times, underground nuclear explosives.

Extremely high shock pressures have been generated by direct irradiation of laser light with intensity of 10^{12} to 10^{14} Wcm^{-2}. The sample is less than ~ 1mm in diameter with a thickness of a few 100 μm. The temporal shape of the laser beam is often variable. For example, square pulses 10 ns long have been generated with 0.1 ns rise time [126].

The magnetic flux compressions can generate dynamic pressures in solids, where the process of pressurization is isentropic in nature. As Hugoniot of a material is a curve in EOS surface that is generated from a series of shock compression experiments, similarly, compression isentrope is a class of curves that explore another region of EOS surface. Unlike in shock compression experiments where only one datum is determined in one experiment, in isentropic compression experiment (ICE) one can generate a full isentrope in a single experiment. Magnetic pulse loading method is popular for ICE in solids [123-124]. Recently, Sandia National Laboratory has developed a Z accelerator facility to produce 0.5 Mbar isentropic compression in solids [125]. High magnetic fields (greater than 100 Tesla) are generally produced in pulsed form using capacitor banks. These fields may be further enhanced through compression of metallic liners (cylindrical shells) in which initial magnetic field may be trapped and then compressed using secondary energy source such as another capacitor bank or chemical explosives. The Z-accelerator of Sandia National Laboratory has been used to launch flyer plates of aluminium with thickness ~ 1 mm with ultrahigh velocities up to ~ 34 km/s not achievable with conventional gas guns [127]. Very recently, the static compressions have been combined with dynamic loading with laser irradiation to achieve terapascal pressure on a sample [128]. Here, a sample is compressed inside a diamond anvil cell and laser induced shock wave further pressurize this precompressed sample which can generate 10-100 TPa pressure.

1.2.2.4 Diagnostic Techniques in Shock Wave Experiments

Depending upon the nature of properties measured the diagnostic techniques used in shock wave experiments can be broadly classified in two categories namely macroscopic (continuum) measurement techniques and microscopic measurement techniques. The macroscopic measurement includes impact velocity measurement, shock arrival measurement and time resolved stress profile and particle/free surface velocity history measurements. The impact velocity can be measured using electrical pins or optical technique. The shock velocity in the target material is generally measured using electrical and optical transducers. For this purpose, the electrical sensors are placed at various known depths in the target from the impact surface and shock arrival timings at sensor locations is recorded, which is then used to determine the shock velocity in the target material [129-130]. The piezoresistive manganin gauges [131] have been widely used to record the time resolved stress profile [108,132-133]. The particle/free surface velocity history of the target plate after arrival of shock wave is measured using high precision laser interferometery techniques such as velocity interferometer system for any reflector (VISAR) [50-51] and optically recording velocity interferometer system (ORVIS) [134]. ORVIS employs a streak camera to record the interference data with subnanosecond time resolution. Later, line imaging variations on these techniques [135-137] has been extended to encode spatial information from streak camera detectors. Adapting these techniques to the context of laser-driven targets has enabled precise measurement of the motion of a variety of shock-related phenomena in laser-driven targets, including the motion of free surfaces, of shocked interfaces, and of ionizing shock fronts in a wide variety of transparent media. These macroscopic (continuum) techniques can provide quantitative information about shock induced phase transitions (both reversible and irreversible), mechanical failure (fracture strength, Hugoniot elastic limit (HEL) and yield strength) at high strain rates.

Though the in-situ microscopic measurements in shock wave experiments are difficult, there are few laboratories in the world that have recently developed capabilities of real time x-ray diffraction and Raman measurements in shock wave experiments [138-143]. They have carried out *in-situ* nanosecond lattice measurement that can determine reversible phase transition which is not possible to detect in the post shock analysis. For example, using online x-ray diffraction measurements Milathianaki et al. [138] have detected the hcp to bcc phase transformation in polycrystalline Mg subjected to laser shock. Similarly, in shock loaded iron the bcc to hcp structural transformation could be detected through in-situ x-ray diffraction measurements [139]. Nanosecond diffraction has been used to show that single crystal of silicon can sustain very high elastic strain [140]. More recently, time resolved optical transmission and imaging measurements have been reported on water samples subjected to multiple shock wave compressions up to peak pressures of 1–5 GPa in nanosecond time scales. The combination of optical transmission and imaging measurements provide the first consistent evidence for freezing on short time scales [143].

1.3 Electronic Band Structure Calculations

Apart from experimental techniques, there is a significant advancement in the theoretical methods used to calculate the electronic band structure of solids. The knowledge of electronic band structures in turn has been utilized to examine structural stability, to determine equation of state and elastic properties of materials as a function of pressure. The predictive capabilities of modern electronic band structure methods have facilitated the determination of structural phase transitions, equation of state and pressure dependent elastic and mechanical properties of materials prior to experiments.

Properties of a material *e.g.*, EOS, elastic moduli, strength etc. depend upon the crystal structure it adopts. Therefore, for proper understanding of material behavior under pressure it is essential first to analyze the structural stability. For a material, at a given thermodynamic condition (pressure, temperature and specific volume), the thermodynamically favourable structure is the one which has the lowest free energy and it is found by determining and comparing the free energies for various plausible structures. Depending upon the thermodynamic condition the different forms of free energy are used for structural stability analysis. For example, for constant volume and temperature condition the thermodynamically favorable structure is the one for which the Helmholtz free energy (*F*) is lowest. However, for constant pressure and temperature condition it is the Gibbs free energy (*G*) which is used to determine the possible stable crystal structure. These free energies are defined as follows:

The Helmholtz free energy, which is function of thermodynamic variables *T* and *V* is:

$$F = E - TS \tag{1.9}$$

With *E*, *T* and *S* are total internal energy, temperature and entropy, respectively. Further, the total internal energy is expresses as $E(V,T) = E_c(V) + E_T(V,T) + E_e(V,T)$, with E_c, E_T and E_e are 0 K energy, Lattice thermal energy and electronic excitation energy, respectively.

Similarly, the Gibbs free energy which is function of thermodynamic variables T and P is:

$$G = F + PV \tag{1.10}$$

With *P* and *V* are the pressure and volume thermodynamic variables.

It may be noted that for $T = 0$, the Helmholtz free energy reduces to total internal energy at 0 K and the Gibbs free energy reduces to $H = E_c + PV$, where H is defined as enthalpy. The term E_c can be determined through electronic band structure methods, however, the lattice thermal energy, electronic excitation energy and the entropy contribution can be determined by using the physical quantities such as elastic moduli and density of electronic states obtained from *ab-initio* calculations in the continuum model like Debye model.

The pressure from the total energy is determined as

$$P = -\frac{\partial E}{\partial V} \tag{1.11}$$

Thus the equation of state can be drawn by calculating the pressure at various compressions. The total energy calculations can be performed on specifically deformed lattice and by calculating the energy of the deformed lattice the elastic constants can be calculated.

There are several theories and approximations to calculate the electronic band structures of solids. For example, nearly free electron model, tight binding model, muffin-tin approximation, k-p perturbation theory and density functional theory. Brief outlines of these methods are provided below:

In the nearly free electron model, the interactions among electrons are completely ignored. The wavefunction is periodic in wavevector which is given by:

$$\Psi_{\mathrm{n},\mathbf{k}}(\boldsymbol{r}) = e^{i\boldsymbol{k}.\boldsymbol{r}} u_n(\boldsymbol{r}) \tag{1.12}$$

Where, n is the n$^{\text{th}}$ energy band, wavevector $\boldsymbol{k}$ is related to the direction of electron motion, $\boldsymbol{r}$ is the position in the crystal and the $u_n(\boldsymbol{r})$ is periodic over the lattice vector $\boldsymbol{R}$**:**

$$u_n(\boldsymbol{r}) = u_n(\boldsymbol{r} - \boldsymbol{R}) \tag{1.13}$$

Here the interaction between the ion cores and the conduction electrons are modelled as 'weak' perturbing potentials.

Other opposite extreme to this model is the tight binding model where the electrons stay most of the time to the constituent atoms. Here $\Psi(\boldsymbol{r})$ is approximated by a linear combination of atomic orbitals. $\psi_n(\boldsymbol{r})$

$$\Psi(\boldsymbol{r}) = \sum_{n,\boldsymbol{R}} \boldsymbol{b}_{n,\boldsymbol{R}}\, \psi_n(\boldsymbol{r} - \boldsymbol{R}) \tag{1.14}$$

Further improvement of the tight binding model is the well known Hubbard model, where the Hamiltonian of the interacting particles in the lattice consists of two terms: a kinetic energy term which describes the tunneling (hopping) of particles between sites of the lattice and a potential term for the on-site interaction. If interaction between particles of different sites of the lattice is considered, the model is referred as the extended Hubbard model.

Various electronic band structure methods such as Korringa-Kohn-Rostoker approximation (KKR), augmented plane wave (APW), linearized muffin-tin orbital (LMTO) and Green's function methods use the muffin-tin approximation. The muffin-tin approximation basically is shape approximation of the potential around an electron in the solid. In the methods using this approximation, the lattice is divided in two parts. Around the atom the potential is approximated to be spherically symmetric and electron wavefunction spanned as a linear combination of spherical harmonics multiplied by a radial wavefunction. Outside this spherically symmetric potential, the potential is assumed to be flat *i.e.* constant or zero, and linear combination of plane waves are used to span the wavefunction of the electron.

In the k.p perturbation theory the term ***k.p*** is taken as perturbation in the Hamiltonian. The total Hamiltonian is represented as:

$$H_T = H_0 + H'_K \tag{1.15}$$

Where $H_0 = \frac{p^2}{2m} + V$ is the unperturbed Hamiltonian and

$H'_K = \frac{\hbar^2 k^2}{2m} + \frac{\hbar\, \boldsymbol{k.p}}{m}$ is the perturbation term.

The perturb energy to the unperturbed Hamiltonian (which is the exact Hamiltonian for the ***k*** *= 0, i.e.,* at the Gamma point) is calculated. As all the theoretical analysis on various materials presented in the subsequent chapters of the thesis have used the band structure calculation methods based on the well established density functional approach, a separate section has been provided to describe the density functional theory.

1.3.1 Density Functional Theory

Density functional theory is a quantum mechanical description of the electronic band structure of many body system particularly atoms, molecules and the condensed phase. The theory deals with the calculation of total energy of the many body system from the first principle (*ab-initio*) or by solving the Schrodinger equation without taking any approximation on the potential of the system under consideration. With this theory the properties of the system under consideration can be determined from the total ground state energy functional i.e. the energy is a function of density which itself is a function of position co-ordinate. As it is not dependent on any particular parameters, these calculations are more reliable than any model calculations where many parameters are used to optimize the potential of the system and then predict the properties of the system. In the present thesis, the problems addressed stems ultimately from the calculations involving how matter behaves under pressure theoretically. A brief outline of the basic principle of the theory is given below.

Overview of DFT

The central concept of DFT is to describe the total energy of many-body interacting system via its particle density and not via its many-body wavefunction. Its main aim is to reduce the 3N degrees of freedom of the N-body system to only three spatial coordinates through its particle density. Its basis is the well known Hohenberg-Kohn (HK) theorem [148], which claims that all ground state properties of a system can be considered to be unique functionals of its ground state density and the exact ground state will be found when the exact density is found. Together with the Born-Oppenheimer (BO) approximation [149] and Kohn-Sham (KS) ansatz [150], practical accurate DFT calculations have been made possible via approximations for the so called exchange-correlation (XC) potential, which describes the effects of the Pauli principle and the Coulomb potential beyond a pure electrostatic interaction of the electrons. Since it is impossible to calculate the exact XC potential (by solving the many-body problem exactly), two common approximations are the so-called local density approximation (LDA) and generalized gradient approximations (GGA) are implemented to get the XC energy contribution towards the total energy.

In many cases the results of DFT calculations for condensed-matter systems agreed quite satisfactorily with experimental data, especially with better approximations for the XC energy functional since the 1990s. Also, the computational costs were relatively low compared to traditional ways which were based on the complicated many-electron wavefunction, such as Hartree-Fock theory [151-152] and its descendants.

1.3.1.1 The Many-Body System and Born-Oppenheimer (BO) Approximation

The Hamiltonian of a many-body condensed-matter system consisting of nuclei and electrons can be written as:

$$H_{tot} = -\sum_{I} \frac{\hbar^2}{2M_I} \boldsymbol{\nabla}^2_{\boldsymbol{R_I}} - \sum_{i} \frac{\hbar^2}{2m_e} \boldsymbol{\nabla}^2_{\boldsymbol{r_i}} + \frac{1}{2} \sum_{\substack{I,J \\ I\neq j}} \frac{Z_I Z_J e^2}{|\boldsymbol{R_I}-\boldsymbol{R_J}|} + \frac{1}{2} \sum_{\substack{i,j \\ i\neq j}} \frac{e^2}{|\boldsymbol{r_i}-\boldsymbol{r_j}|} - \sum_{I,i} \frac{Z_I e^2}{|\boldsymbol{R_I}-\boldsymbol{r_i}|} \tag{1.16}$$

where the indexes I, J run on all nuclei of the system, i and j on all the electrons, $\boldsymbol{R_I}$ and M_I are positions and masses of the nuclei, $\boldsymbol{r_i}$ and m_e of the electrons, Z_I the atomic number of nucleus I. The first two terms are the kinetic energies of the nuclei and the electrons respectively, the third term is the potential energy of nucleus-nucleus Coulomb interaction, the fourth term is the potential energy of electron-electron Coulomb interaction and the last term is the potential energy of nucleus-electron Coulomb interaction. The time-independent Schrödinger equation for the system reads:

$$H_{tot}\Psi(\{\boldsymbol{R}_{\mathrm{I}}\},\{\boldsymbol{r_i}\}) = E\,\Psi(\{\boldsymbol{R}_{\mathrm{I}}\},\{\boldsymbol{r_i}\}) \tag{1.17}$$

where $(\{\boldsymbol{R_I}\}, \{\boldsymbol{r_i}\})$ is the total wavefunction of the system. In principle, everything about the system is known if one can solve the above Schrödinger equation. However, it is impossible to solve it in practice as it is a partial differential equation entangled with large number of variables. A so-called Born-Oppenheimer (BO) approximation made by Born and Oppenheimer [149] in 1927 comes here for rescue. Since the nuclei are much heavier than electrons (the mass of a proton is about 1836 times the mass of an electron), the nuclei move much slower (about two order of magnitude slower) than the electrons. Therefore we can separate the movement of nuclei and electrons. When we consider the movement of electrons, it is reasonable to consider the positions of nuclei are fixed, thus the total wavefunction of the electrons and nuclei can be decoupled in the following way:

$$\Psi(\{\boldsymbol{R}_{\mathrm{I}}\},\{\boldsymbol{r_i}\}) = \Theta(\{\boldsymbol{R}_{\mathrm{I}}\})\phi(\{\boldsymbol{r_i}\};\{\boldsymbol{R}_{\mathrm{I}}\}) \tag{1.18}$$

where $\Theta(\{\boldsymbol{R}_I\})$ describes the nuclei and $\varphi(\{\boldsymbol{r}_i\} \; ; \; \{\boldsymbol{R}_I\})$ the electrons (depending parametrically on the positions of the nuclei). With the BO approximation, Eqn. (1.17) can be divided into two separate Schrödinger equations:

$$H_e \, \phi(\{\boldsymbol{r}_i\} \, ; \, \{\mathbf{R}_\mathrm{I}\}) = V(\{\mathbf{R}_\mathrm{I}\}) \, \phi(\{\boldsymbol{r}_i\} \, ; \, \{\mathbf{R}_\mathrm{I}\}) \tag{1.19}$$

where

$$H_e = -\sum_i \frac{\hbar^2}{2m_e} \boldsymbol{\nabla}_{r_i}^2 + \frac{1}{2} \sum_{\substack{I,J \\ I \neq j}} \frac{Z_I Z_J e^2}{|\boldsymbol{R}_I - \boldsymbol{R}_J|} + \frac{1}{2} \sum_{\substack{i,j \\ i \neq j}} \frac{e^2}{|\boldsymbol{r}_i - \boldsymbol{r}_j|} - \sum_{I,i} \frac{Z_I e^2}{|\boldsymbol{R}_I - \boldsymbol{r}_i|} \tag{1.20}$$

And

$$\left[- \sum_I \frac{\hbar^2}{2M_I} \boldsymbol{\nabla}_{\boldsymbol{R}_I}^2 + V(\{\boldsymbol{R}_\mathrm{I}\}) \right] \Theta(\{\boldsymbol{R}_\mathrm{I}\}) = E' \Theta(\{\boldsymbol{R}_\mathrm{I}\}) \tag{1.21}$$

Eqn. (1.19) is the equation for the electronic problem with the nuclei positions fixed. The eigenvalue of the energy $V(\{\boldsymbol{R}_I\})$ depends parametrically on the positions of the nuclei. After solving Eq. (1.19), $V(\{\boldsymbol{R}_I\})$ is known and by applying it to Eqn. (1.21), which has no electronic degrees of freedom, the motion of the nuclei is obtained. Eqn. (1.21) is sometimes replaced by a Newton equation, *i.e.*, to move the nuclei classically, equating $-\boldsymbol{\nabla}V$ with the forces.

The significance of the BO approximation is to separate the movement of electrons and nuclei. Now we can consider that the electrons are moving in a static external potential $V_{ext}(\boldsymbol{r})$ formed by the nuclei, which is the starting point of DFT. The BO approximation was extended by Bohn and Huang known as Born-Huang (BH) approximation [153] to take into account more non-adiabatic effect in the electronic Hamiltonian than in the BO approximation.

1.3.1.2 Thomas-Fermi-Dirac Approximation

The predecessor to DFT was the Thomas-Fermi (TF) model proposed by Thomas [144] and Fermi [145] in 1927. In this method, they used the electron density *n(**r**)* as the basic variable instead of the wave function. The total energy of a system in an external potential $V_{ext}(\mathbf{r})$ is written as a functional of the electron density *n(**r**)* as:

$$E_{TF}[n(\mathbf{r})] = A_1 \int n(\mathbf{r})^{5/3}\, d\mathbf{r} + \int n(\mathbf{r})\, V_{ext}(\mathbf{r})\; d\mathbf{r} + \frac{1}{2} \iint \frac{n(\mathbf{r})n(\mathbf{r}')}{|\mathbf{r}-\mathbf{r}'|}\, d\mathbf{r}\, d\mathbf{r}' \qquad (1.22)$$

where the first term is the kinetic energy of the non-interacting electrons in a homogeneous electron gas (HEG) with

$$A_1 = \frac{3}{10}\,(3\pi^2)^{2/3} \qquad (1.23)$$

in atomic units ($\hbar = m_e = e = 4\pi/\varepsilon_0 = 1$). The kinetic energy density of a HEG is obtained by adding up all of the free-electron energy state $\varepsilon_k = k^2/2$ up to the Fermi wave vector

$k_F = (3\pi^2 n(\mathbf{r}))^{1/3}$ as:

$$T_o[n(\mathbf{r})] = \frac{2}{(2\pi)^3}\int \frac{k^2}{2}\, 4\pi k^2\, dk \qquad (1.24)$$

$$= A_1 n(\mathbf{r})^{5/3}$$

The second term is the classical electrostatic energy of the nucleus-electron Coulomb interaction. The third term is the classical electrostatic Hartree energy approximated by the classical Coulomb repulsion between electrons. In the original TF method, the exchange and correlation among electrons was neglected. In 1930, Dirac

[146] extended the Thomas-Fermi method by adding a local exchange term $A_2 \int n(\boldsymbol{r})^{4/3}\, d\boldsymbol{r}$ to Eqn. (1.22) with $A_2 = -\frac{3}{4}\,(3/\pi)^{1/3}$, which leads Eqn. (1.22) to

$$E_{TFD}[n(\boldsymbol{r})] = A_1 \int n(\boldsymbol{r})^{5/3}\, d\boldsymbol{r} + \int n(\boldsymbol{r})\, V_{ext}(\boldsymbol{r})\, d\boldsymbol{r} + \frac{\mathbf{1}}{\mathbf{2}} \iint \frac{n(\boldsymbol{r})n(\boldsymbol{r}')}{|\boldsymbol{r}-\boldsymbol{r}'|}\, d\boldsymbol{r}\, d\boldsymbol{r}' + A_2 \int n(\boldsymbol{r})^{4/3}\, d\boldsymbol{r} \qquad (1.25)$$

The ground state density and energy can be obtained by minimizing the Thomas-Fermi-Dirac equation (1.25) subject to conservation of the total number (*N*) of electrons. By using the technique of Lagrange multipliers, the solution can be found in the stationary condition:

$$\delta\{E_{TFD}[n(\boldsymbol{r})] - \mu(\textstyle\int n(\boldsymbol{r})\, d\boldsymbol{r} - N)\} = 0 \qquad (1.26)$$

where μ is a constant known as a Lagrange multiplier, whose physical meaning is the chemical potential (or Fermi energy at T = 0 K). Eqn. (1.26) leads to the Thomas-Fermi-Dirac equation,

$$\frac{5}{3} A_1 n(\boldsymbol{r})^{2/3} + V_{ext}(\boldsymbol{r}) + \frac{1}{2} \int \frac{n(\boldsymbol{r}')}{|\boldsymbol{r}-\boldsymbol{r}'|}\, d\boldsymbol{r}' + \frac{4}{3} A_2 n(\boldsymbol{r})^{1/3} - \mu = 0 \qquad (1.27)$$

which can be solved directly to obtain the ground state density.

The approximations used in Thomas-Fermi-type approach are so crude that the theory suffers from many problems. The most serious one is that the theory fails to describe bonding between atoms, thus molecules and solids cannot form in this theory [147]. Although it is not good enough to describe electrons in matter, its concept to use electron density as the basic variable illustrates the way DFT works.

1.3.1.3 The Hohenberg-Kohn (HK) Theorems

DFT was proven to be an exact theory of many-body systems by Hohenberg and Kohn [148] in 1964. It applies not only to condensed-matter systems of electrons with fixed nuclei, but also more generally to any system of interacting particles in an external potential $V_{ext}(\mathbf{r})$. The theory is based upon two theorems.

The HK theorem I:

The ground state particle density $n(\mathbf{r})$ *of a system of interacting particles in an external potential* $V_{ext}(\mathbf{r})$ *uniquely determines the external potential* $V_{ext}(\mathbf{r})$*, except for a constant.*

Thus the ground state particle density determines the full Hamiltonian, except for a constant shift of the energy. In principle, all the states including ground and excited states (in case of density functional perturbation theory) of the many-body wavefunctions can be calculated. This means that the ground state particle density uniquely determines all properties of the system completely.

The HK theorem II:

There exists a universal functional $F[n(\mathbf{r})]$ *of the density, independent of the external potential* $V_{ext}(\mathbf{r})$*, such that the global minimum value of the energy functional* $E[n(\boldsymbol{r})] = \int n(\boldsymbol{r})\, V_{ext}(\boldsymbol{r})\ d\boldsymbol{r} + F[n(\boldsymbol{r})]$ *is the exact ground state energy of the system and the exact ground state density* $n_0(\mathbf{r})$ *minimizes this functional. Thus the exact ground state energy and density are fully determined by the functional* $E[n(\boldsymbol{r})]$.

The HK theorems can be generalized to spin density functional theory with spin degrees of freedom.[154] In this theory, there are two types of densities, namely, the particle density $n(\mathbf{r}) = n_{\uparrow}(\mathbf{r})+n_{\downarrow}(\mathbf{r})$ and the spin density $s(\mathbf{r}) = n_{\uparrow}(\mathbf{r}) - n_{\downarrow}(\mathbf{r})$ where ↑ and ↓ denote the two different kins of spins. The energy functional is generalized to $E\,[n(\mathbf{r}), s(\mathbf{r})]$. In systems with magnetic order or atoms with net spins, the spin density functional theory should be used instead of the original one-spin density functional theory. DFT can also be generalized to include temperature dependence [155] and time dependence known as time-dependent density functional theory (TD-DFT) [156].

Although HK theorems put particle density $n(\boldsymbol{r})$ as the basic variable, it is still impossible to calculate any property of a system because the universal functional $F[n(\boldsymbol{r})]$ is unknown. This difficulty was overcome by Kohn and Sham [150] in 1965, who proposed the well known Kohn-Sham ansatz.

1.3.1.4 The Kohn-Sham (KS) Ansatz

It is the Kohn-Sham (KS) ansatz [150] that puts Hohenberg-Kohn theorems into practical use and makes DFT calculations possible with even a single personal computer. This is part of the reason that DFT became the most popular tool for electronic structure calculations. The KS ansatz was so successful that Kohn was honored the Nobel Prize in chemistry in 1998.

The KS ansatz is to replace the original many-body system by an auxiliary independent-particle system and assume that the two systems have exactly the same ground state density. It maps the original interacting system with real potential onto a fictitious non-interacting system whereby the electrons move within an effective Kohn-Sham single-particle potential $V_{KS}(\boldsymbol{r})$ (Fig. 1.8). For the auxiliary independent-particle system, the auxiliary Hamiltonian is

$$\hat{H}_{KS} = -\frac{1}{2}\boldsymbol{\nabla}^2 + V_{KS}(\boldsymbol{r}) \tag{1.28}$$

in atomic units.

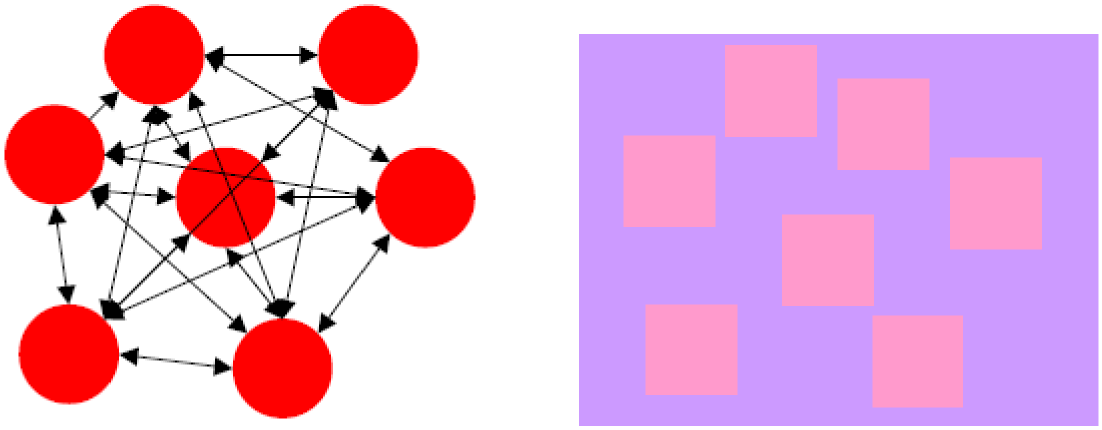

Figure 1.8: (Left) Interacting electrons + real potentials and (Right) non-interacting fictitious particles +effective potentials.

For a system with N independent electrons, the ground state is obtained by solving the N one-electron Schrodinger equations,

$$\left(-\frac{1}{2}\boldsymbol{\nabla}^2 + V_{KS}(\boldsymbol{r})\right)\psi_i(\boldsymbol{r}) = \varepsilon_i\,\psi_i(\boldsymbol{r}) \tag{1.29}$$

where there is one electron in each of the N orbitals $\psi_i(\boldsymbol{r})$ with the lowest eigenvalues ε_i. The density of the auxiliary system is constructed from:

$$n(\boldsymbol{r}) = \sum_{i=1}^{N} |\psi_i(\boldsymbol{r})|^2 \tag{1.30}$$

which is subject to the conservation condition:

$$\int n(\boldsymbol{r})\,d\boldsymbol{r} = N \tag{1.31}$$

The non-interacting independent-particle kinetic energy $T_S[n(\mathbf{r})]$ is given by,

$$T_S[n(\boldsymbol{r})] = -\frac{1}{2}\sum_{i=1}^{N}\int \psi_i^*(\boldsymbol{r})\, \boldsymbol{\nabla}^2\psi_i(\boldsymbol{r})\, d\boldsymbol{r} \tag{1.32}$$

Then the universal functional $F[n(\mathbf{r})]$ was rewritten as

$$F[n(\boldsymbol{r})] = T_S[n(\boldsymbol{r})] + E_H[n(\boldsymbol{r})] + E_{XC}[n(\boldsymbol{r})] \tag{1.33}$$

where $E_H[n(\mathbf{r})]$ is the classic electrostatic (Hartree) energy of the electrons,

$$E_H[n(\boldsymbol{r})] = \frac{1}{2}\iint \frac{n(\boldsymbol{r})n(\boldsymbol{r}')}{|\boldsymbol{r}-\boldsymbol{r}'|}\, d\boldsymbol{r}\, d\boldsymbol{r}' \tag{1.34}$$

and $E_{XC}[n(\mathbf{r})]$ is the XC energy, which contains the difference between the exact and non-interacting kinetic energies and also the non-classical contribution to the electron-electron interactions, of which the exchange energy is a part. Since the ground state energy of a many-electron system can be obtained by minimizing the energy functional $E[n(\boldsymbol{r})] = F[n(\boldsymbol{r})] + \int n(\boldsymbol{r})V_{ext}(\boldsymbol{r})d\boldsymbol{r}$, subject to the constraint that the number of electrons N is conserved,

$$\delta\{F[n(\boldsymbol{r})] + \int n(\boldsymbol{r})V_{ext}(\boldsymbol{r})d\boldsymbol{r} - \mu(\int n(\boldsymbol{r})\, d\boldsymbol{r} - N)\} = 0 \tag{1.35}$$

and the resulting equation is

$$\mu = \frac{\delta F[n(\boldsymbol{r})]}{\delta n(\boldsymbol{r})} + V_{ext}(\boldsymbol{r}) \tag{1.36}$$

$$\mu = \frac{\delta T_S n(\boldsymbol{r})}{\delta n(\boldsymbol{r})} + V_{KS}(\boldsymbol{r})$$

where μ is the chemical potential,

$$V_{KS}(\boldsymbol{r}) = V_{ext}(\boldsymbol{r}) + V_H(\boldsymbol{r}) + V_{XC}(\boldsymbol{r}) \tag{1.37}$$

$$= V_{ext}(\boldsymbol{r}) + \frac{\delta E_H[n(\boldsymbol{r})]}{\delta n(\boldsymbol{r})} + \frac{\delta E_{XC}[n(\boldsymbol{r})]}{\delta n(\boldsymbol{r})}$$

is the KS one-particle potential with the Hartree potential $V_H(\boldsymbol{r})$

$$V_H(\boldsymbol{r}) = \frac{\delta E_H[n(\boldsymbol{r})]}{\delta n(\boldsymbol{r})} \tag{1.38}$$

$$= \int \frac{n(\boldsymbol{r}')}{|\boldsymbol{r} - \boldsymbol{r}'|}\, d\boldsymbol{r}'$$

and the XC potential $V_{XC}(\boldsymbol{r})$

$$V_{XC}(\boldsymbol{r}) = \frac{\delta E_{XC}[n(\boldsymbol{r})]}{\delta n(\boldsymbol{r})} \tag{1.39}$$

Eqns. (1.29), (1.30), (1.37) together are the well-known KS equations, which must be solved self-consistently because $V_{KS}(\boldsymbol{r})$ depends on the density through the XC potential. In order to calculate the density, the N equations in Eqn. (1.29) have to be solved in KS theory as opposed to one equation in the TF approach. However an advantage of the KS method is that as the complexity of a system increases, due to N increasing, the problem becomes no more difficult, only the number of single-particle equations to be solved increases. Although exact in principle, the KS theory is approximate in practice because of the unknown XC energy functional $E_{XC}[n(\boldsymbol{r})]$. An implicit definition of $E_{XC}[n(\boldsymbol{r})]$ can be given as:

$$E_{XC}[n(\boldsymbol{r})] = T[n(\boldsymbol{r})] - T_S[n(\boldsymbol{r})] + E_{int}[n(\boldsymbol{r})] - E_H[n(\boldsymbol{r})] \tag{1.40}$$

where $T[n(\boldsymbol{r})]$ and $E_{int}[n(\boldsymbol{r})]$ are the exact kinetic and electron-electron interaction energies of the interacting system respectively. It is crucial to have an accurate XC energy functional $E_{XC}[n(\boldsymbol{r})]$ or potential $V_{XC}(\boldsymbol{r})$ in order to give a satisfactory description of a realistic condensed-matter system. The most widely used approximations for the XC potential are the local density approximation (LDA) and the generalized-gradient approximation (GGA).

1.3.1.5 Local (Spin) Density Approximation (L(S)DA)

The KS ansatz successfully maps the original interacting many-body system onto a set of independent single-particle equations and makes the problem much easier. On the other hand, without knowing the exact form of the XC energy functional $E_{XC}[n(\boldsymbol{r})]$, the KS equations are unsolvable. Although the exact XC energy functional $E_{XC}[n(\boldsymbol{r})]$ should be very complicated, simple but successful approximations to it have been made, which not only predict various properties of many systems reasonably well but also greatly reduce computational costs, leading to the wide use of DFT for electronic structure calculations. Of these approximations, the local density approximation (LDA) is the most widely used one. In LDA, the XC energy per electron at a point $\boldsymbol{r}$ is considered the same as that for a homogeneous electron gas (HEG) that has the same electron density at the point $\boldsymbol{r}$. The total exchange-correlation functional $E_{XC}[n(\boldsymbol{r})]$ can be written as,

$$E_{XC}^{LDA}[n(\boldsymbol{r})] = \int n(\boldsymbol{r})\epsilon_{XC}^{hom}(n(\boldsymbol{r}))d\boldsymbol{r} \tag{1.41}$$

$$E_{XC}^{LDA}[n(\boldsymbol{r})] = \int n(\boldsymbol{r})[\epsilon_X^{hom}(n(\boldsymbol{r})) + \epsilon_C^{hom}(n(\boldsymbol{r}))]d\boldsymbol{r}$$
$$= E_X^{LDA}[n(\boldsymbol{r})] + E_C^{LDA}[n(\boldsymbol{r})]$$

for spin unpolarized systems and

$$E_{XC}^{LDA}[n_\uparrow(\boldsymbol{r}), n_\downarrow(\boldsymbol{r})] = \int n(\boldsymbol{r})\epsilon_{XC}^{hom}(n_\uparrow(\boldsymbol{r}), n_\downarrow(\boldsymbol{r}))d\boldsymbol{r} \tag{1.42}$$

for spin polarized systems[14], where the XC energy density $\epsilon_{XC}^{hom}(n(\boldsymbol{r}))$ is a function of the density alone, and is decomposed into exchange energy density $\epsilon_X^{hom}(n(\boldsymbol{r}))$ and correlation energy density $\epsilon_C^{hom}\big(n(\boldsymbol{r})\big)$ so that the XC energy functional is decomposed into exchange energy functional $E_X^{LDA}[n(\boldsymbol{r})]$ and correlation energy functional $E_C^{LDA}[n(\boldsymbol{r})]$ linearly. The exchange energy functional $E_X^{LDA}[n(\boldsymbol{r})]$ employs the expression for a HEG by using it pointwise, which is known analytically as [9]

$$E_X^{LDA}[n(\boldsymbol{r})] = \int n(\boldsymbol{r})\epsilon_X^{hom}\big(n(\boldsymbol{r})\big)d\boldsymbol{r} \tag{1.43}$$
$$= -\frac{3}{4}\left({}^{3}/_{\pi}\right)^{1/3}\int n(\boldsymbol{r})^{4/3}\,d\boldsymbol{r}$$

Where

$$\epsilon_X^{hom}\big(n(\boldsymbol{r})\big) = -\frac{3}{4}\left({}^{3}/_{\pi}\right)^{1/3}n(\boldsymbol{r})^{1/3} \tag{1.44}$$

is the exchange energy density of the unpolarized HEG introduced first by Dirac.[146]. Analytic expressions for the correlation energy of the HEG are unknown except in the high and low density limits corresponding to infinitely weak and infinitely strong correlations. The expression of the correlation energy density of the HEG at high density limit has the form:

$$\epsilon_C = A\ \ln(r_s) + B + r_s(C\ \ln(r_s) + D) \tag{1.45}$$

and the low density limit takes the form

$$\epsilon_C = \frac{1}{2}\left(\frac{g_0}{r_s} + \frac{g_1}{{r_s}^{3/2}} + \cdots\right) \tag{1.46}$$

where the Wigner-Seitz radius r_s is related to the density as

$$\frac{4}{3}\pi {r_s}^3 = \frac{1}{n} \tag{1.49}$$

In order to obtain accurate values of the correlation energy density at intermediate density, accurate quantum Monte Carlo (QMC) simulations for the energy of the HEG are needed and have been performed at several intermediate density values [157] Most local density approximations to the correlation energy density interpolate these accurate values from QMC simulations while reproducing the exactly known limiting behavior.

The LDA is very simple and corrections to the exchange-correlation energy due to the inhomogeneities in the electronic density are ignored. However, it is surprisingly successful and even works reasonably well in systems where the electron density is rapidly varying. One reason is that LDA gives the correct sum rule to the exchange-correlation hole. That is, there is a total electronic charge of one electron excluded from the neighborhood of the electron at ***r***. In the meantime, it tends to underestimate atomic ground state energies and ionization energies, while overestimating binding energies. It makes large errors in predicting the energy gaps of some semiconductors. Its success and limitations lead to approximations of the XC energy functional beyond the LDA, through the addition of gradient corrections to incorporate longer range gradient effects (GGA), as well as LDA+U method to account for the strong correlations of the *d* electrons in transition elements and *f* electrons in lanthanides and actinides.

1.3.1.6 Generalized Gradient Approximation (GGA)

As mentioned above, the LDA neglects the in-homogeneities of the real charge density which could be very different from the HEG. The XC energy of inhomogeneous charge density can be significantly different from the HEG result. This leads to the development of various generalized-gradient approximations (GGA) which include density gradient corrections and higher spatial derivatives of the electron density and give better results than LDA in many cases.

The definition of the XC energy functional of GGA is the generalized form of Eqn. (1.42) of LSDA to include corrections from density gradient ∇ *n(**r**)* as

$$E_{XC}^{GGA}[n_\uparrow(\boldsymbol{r}), n_\downarrow(\boldsymbol{r})] = \int n(\boldsymbol{r})\epsilon_{XC}^{hom}(n_\uparrow(\boldsymbol{r}), n_\downarrow(\boldsymbol{r}), \nabla n_\uparrow(\boldsymbol{r}), \nabla n_\downarrow(\boldsymbol{r}))d\boldsymbol{r} \tag{1.50}$$

GGA generally works better than LDA, in predicting bond length and binding energy of molecules, crystal lattice constants, and so on, especially in systems where the charge density is rapidly varying. However GGA sometimes overcorrects LDA results in ionic crystals where the lattice constants from LDA calculations fit well with experimental data but GGA will overestimate it. Nevertheless, both LDA and GGA perform badly in materials where the electrons tend to be localized and strongly correlated such as transition metal oxides and rare-earth elements and compounds. This drawback leads to approximations beyond LDA and GGA.

1.3.1.7 LDA+U Approximation

Strongly correlated systems usually contain transition metal or rare-earth metal ions with partially filled *d* or *f* shells. Because of the orbital-independent potentials in LDA and GGA, they cannot properly describe such systems. For example, LDA predicts transition metal oxides to be metallic with itinerant *d* electrons because of the partially filled *d* shells. Instead, these transition metal oxides are Mott insulators and the *d* electrons are well localized. In order to properly describe these strongly correlated systems, orbital-dependent potentials should be used for *d* and *f* electrons.

There are several approaches available nowadays to incorporate the strong electron-electron correlations between *d* electrons and *f* electrons. Of these methods including the self-interaction correction (SIC) method [158], Hartree-Fock (HF) method [159], and GW approximation [160], LDA+U method [161] is the most widely used one.

In the LDA+U method, the electrons are divided into two classes: delocalized s, p electrons which are well described by LDA (GGA) and localized *d* or *f* electrons for which an orbital-dependent term $\frac{1}{2}\, U \sum_{i \neq j} n_i\, n_j$ should be used to describe Coulomb $d - d$ or $f - f$ interaction, where n_i are *d*- or *f*- orbital occupancies. The total energy in L(S)DA+U method is given as[161]:

$$E_{tot}^{LDA+U}[\rho_\sigma(\boldsymbol{r}), \{n_\sigma\}] = E^{LSDA}[\rho_\sigma(\boldsymbol{r})] + E^{U}[\{n_\sigma\}] - E_{dc}[\{n_\sigma\}] \qquad (1.51)$$

where σ denotes the spin index, $\rho_\sigma(\boldsymbol{r})$ is the electron density for spin- σ electrons and $\{n_\sigma\}$ is the density matrix of *d* or *f* electrons for spin-σ, the first term is the standard LSDA energy functional, the second term is the electron-electron Coulomb interaction energy [161]. The last term in Eqn. (1.51) is the double counting term which removes an averaged LDA energy contribution of these *d* or *f* electrons from the LDA energy.

1.3.2 Methods for Solving Kohn-Sham Equations

By using independent-particle methods, the KS equations provide a way to obtain the exact density and energy of the ground state of a condensed matter system. The KS equations must be solved consistently because the effective KS potential V_{KS} and the electron density $n(\mathbf{r})$ are closely related. This is usually done numerically through some self-consistent iteration. The process starts with an initial electron density, usually a superposition of atomic electron density, then the effective KS potential V_{KS} is calculated and the KS equation is solved with single particle eigenvalues and wavefunctions, a new electron density is then calculated from the wavefunctions. After this, self-consistent condition(s) is checked. Self-consistent condition(s) can be the change of total energy or electron density from the previous iteration or total force acting on atoms is less than some chosen small quantity, or a combination of these individual conditions. If the self-consistency is not achieved, the calculated electron density will be mixed with electron density from previous iterations to get a new electron density. A new iteration will start with the new electron density. This process continues until self-consistency is reached. After the self-consistency is reached, various quantities can be calculated including total energy, forces, stress, eigenvalues, electron density of states, band structure, etc. The most timing consuming step in the whole process is to solve KS equation with a given KS potential *VKS*. There are several different schemes to the calculation of the independent-particle electronic states in solids where boundary conditions are applied. They are basically classified into three types [162]:

1.3.2.1 Plane Waves

In this method, the wavefunctions (eigenfunctions of the KS equations) are expanded in a complete set of plane waves $e^{i\mathbf{k}.\mathbf{r}}$ and the external potential of nuclei are replaced by pseudopotentials which include effects from core electrons. Such pseudopotentials have to satisfy certain conditions. Most widely used pseudopotentials nowadays include norm-conserving pseudopotentials[163] (NCPPs) and ultrasoft pseudopotentials[164] (USPPs).

Plane waves have played an important role in the early orthogonalized plane wave (OPW) calculations [165-167] and are generalized to modern projector augmented wave (PAW) method [168-170]. Because of the simplicity of plane waves and pseudopotentials, computational load is significantly reduced in these methods and therefore it is most suitable for calculations of large systems. However, results from plane wave methods using pseudopotentials are usually less accurate than results from all-electron full potential methods. And great care should be taken when one generates pseudopotential and it should be tested to match results from all-electron calculations. The most widely used codes using plane waves and pseudopotentials are plane wave self-consistent field (now known as Quantum ESPRESSO)[171] (PWscf), ABINIT[172], VASP[173] (which uses PAW method too).

1.3.2.2 Localized Atomic(-like) Orbitals

The most well-known methods in this category are linear combination of atomic orbitals (LCAO) [174], also called tight-binding (TB) [174] and full potential non-orthogonal local orbital (FPLO) [175]. The basic idea of these methods is to use atomic orbitals as the basis set to expand the one-electron wavefunction in KS equations.

1.3.2.3 Atomic Sphere Methods

Methods in the class can be considered as a combination of plane wave method and localized atomic orbitals. It uses localized atomic orbital presentation near the nuclei and plane waves in the interstitial region. The most widely used methods are (full potential) linear muffin-tin orbital[176] (LMTO) as implemented in LMTART[177] by Savrasov and (full potential) linear augment plane wave[176, 178] (LAPW) as implemented in WIEN2K[179].

1.3.3 Lattice Dynamics and Phonons

To calculate the lattice dynamical properties, we have linear response method [180] and density functional perturbation theory (DFPT) [181], which are closely related. In both methods, it is essential to calculate the second-order perturbation of DFT total energy, i.e., $\delta^2 E$, in the framework of density functional theory. The perturbation is induced by small displacements δR of the nuclei from their equilibrium positions, which result in changes in the external potential V_{ext}, the wave functions of the KS equations and hence the electron charge density. $\delta^2 E$ is obtained by expanding the DFT total energy with respect to the changes in the wave functions to first order and external potentials up to second order. Detailed expressions can be found in Ref [180-181].

Phonon spectra can be obtained by first calculating the dynamical matrix

$$D_{ij}(\boldsymbol{q}) = \sum_{R'} e^{-i\,\boldsymbol{q}.\boldsymbol{R}'} \frac{\partial^2 E}{\partial u_i(\boldsymbol{R}+\boldsymbol{R}')\partial u_j(\boldsymbol{R})} \tag{1.52}$$

with respect to the atomic displacements $u(\boldsymbol{R})$ for each atom in each direction, (i,j=1, 2, 3, corresponding to x, y and z directions), and then by solving the equation

$$D(\boldsymbol{q})\boldsymbol{\epsilon} = M\, \omega_{\boldsymbol{q}}^2 \boldsymbol{\epsilon} \tag{1.53}$$

which gives the phonon frequencies $\omega_{\boldsymbol{q}}$of the phonons with wave vector $\boldsymbol{q}$, where M is a diagonal matrix with the atomic masses on the diagonal.

1.4 Summary

In this chapter a brief description of the work to be presented in the subsequent chapters of the thesis is provided. This description is followed by an overview of the available experimental techniques for carrying out high pressure experiments and various diagnostic techniques used to understand the response of the material to high pressures. Also, the basic principle of the modern electronic band structure theoretical methods used for analyzing the high pressure behaviour of materials has been introduced.

References

1. F. R. Boyd, *Science* **145**, 3627 (1964).
2. D. J. Stevenson, *Annu. Rev. Earth Planet. Sci.* **10**, 257 (1982).
3. P. Ch. Sahu and N. V. Chandra Shekar, *Resonance*, General Article, August (2007).
4. A. Jayaraman, *Rev. Mod. Phys.* **55**, 65 (1983); *Rev. Sci. Instrum.* **57**, 1013 (1986).
5. P. W. Bridgman, *Proc. Am. Acad. Arts Sci.* **47**, 321 (1911); *Proc. Am. Acad. Arts Sci.* **47**, 441 (1911).
6. R. J. Hemley and N. W. Ashcroft, *Physics Today* **51**, 8 (1998).
7. N. Tateiwa and Y. Haga, *Rev. Sci. Instrum.* **80**, 123901 (2009).
8. H. Cynn and C. Yoo, *Phys. Rev. B*, **59,** 8526 (1998).
9. L. M. Hsiung and D. H. Lassila, *Scripta Matter.* **39,** 603 (1998).
10. L. L. Hsiung, *J. Phys.: Condens. Matter* **22,** 385702 (2010).
11. Y. Akahama, H. Kawamura, D. Hausermann, M. Hanfland, and O. Shimomura, *Phys. Rev. Lett.* **74**, 4690 (1995).
12. S. Desgreniers, Y. K. Vohra, and A. L. Ruoff, *J. Phys. Chem.* **94**, 1117 (1990).
13. Y. Ma, M. Eremets, A. R. Oganov, Y. Xie, I. Trojan, S. Medvedev, A. O. Lyakhov, M. Valle and V. Prakapenka, *Nature* **458**, 182 (2009).
14. H Luo, S. Desgreniers, Y. K. Vohra, and A. L. Ruoff, *Phys. Rev. Lett.* **67**, 2998 (1991).
15. S. K. Sikka, Y. K. Vohra and R. Chidambaram, *Prog. Mater. Sci.* **27**, 245 (1982).
16. H. Xia, G. Parthasarthy, H. Luo, Y. K. Vohra and A. L. Ruoff, *Phys. Rev. B* **42**, 6736 (1990).
17. J. S. Gyanchandani, S. C Gupta., S. K. Sikka and R. Chidambaram, *High Press. Res*. **4**, 472 (1990); *J. Phys. Cond. Matter.* **2**, 301 (1990).
18. K. D. Joshi, G. Jyoti, S. C. Gupta and S. K. Sikka, *Phys. Rev. B* **65,** 052106 (2002).
19. M. P. Usikov and V. A. Zilbershtein, *Phys. Stat. Sol.(a)* **19**, 53 (1973).
20. S. Song and G.T. Gray III, *Phil. Mag. A* **71**, 275 (1995).

21. G. Jyoti, K. D. Joshi, S. C. Gupta, S. K. Sikka, G. K. Dey and S. Banerjee, *Phil. Mag. Lett.* **75**, 291 (1997); J. S. Gyanchandani, *Ph.D. Thesis*, Bombay University, India (1995).
22. C. W. Greeff, D. R. Trinkle, and R. C. Albers, *J Appl. Phys.* **90**, 2221 (2001).
23. G. K. Dey, R. Tewari, S. Banerjee, G. Jyoti, S. C. Gupta, K. D. Joshi, S. K. Sikka, *Acta Materialia* **52,** 5243 (2004).
24. K. D. Joshi, J. Gyanchandani, S. C. Gupta and S. K. Sikka, *J. Phys. Cond. Matter* **14**, 1 (2002).
25. J. S. Gyanchandani, S.K. Sikka and R. Chidambaram, in Recent Trends in High Press. Res., Proceedings of XIII AIRAPT International Conference on High Press. Science and Technology (Ed: A.K. Singh), Oxford and IBH, New Delhi, **331** (1992).
26. R. Ahuja J. M. Wills, B. Johansson and O. Eriksson, *Phys. Rev. B* **48**, 16269 (1993).
27. S. C. Gupta, K. D. Joshi and S. Banerjee, *Metall. Mater. Trans. A* **39A**, 1585 (2008).
28. B. W. James and H. Kheyrandish, *J. Phys. C: Solid State Phys.* **15**, 6321 (1982).
29. A. R. Oganov and P. I. Dorogokupets, *Phys. Rev. B* **67**, 224110 (2003).
30. G. I. Kanel, S. V. Razorenov, A. V. Utkin, V. E. Fortov, K. Baumung, H. U. Karow, D. Rusch, V. Licht, *J. Appl. Phys.* **74**, 7162 (1993).
31. E. Moshe, S. Eliezer, Z. Henis, M. Werdiger, E. Dekel, Y. Horovitz, S. Maman, I. B. Goldberg and D. Eliezer, *Appl. Phys. Lett.* **76**, 1555 (2000).
32. N. Eliaz, E. Moshe, S. Eliezer, and D. Eleizer, *Metall. Matter. Trans. A* **31**, 1085 (2000).
33. K. D. Joshi, A. S. Rav, S. C. Gupta, S. Banerjee, *J. Phys. Conf. Series* **215**, 012149 (2010).
34. A. Lazicki, P. Loubeyre, F. Occelli, R. J. Hemley, and M. Mezouar, *Phys. Rev.B.* **85**, 054103-1 (2012).
35. D. Mukherjee, B. D. Sahoo, K. D. Joshi and S. C. Gupta, *AIP Conf. Proc.* **1536**, 403 (2013).

36. F. Coppari, R. F. Smith, J. H. Eggert, J. Wang, J. R. Rygg, A. Lazicki, J. A. Hawreliak, G. W. Collins, and T. S. Duffy, *Nat. Geosci.***6**, 926 (2013).
37. G. D. Stevens, L. R. Veeser, P. A. Rigg, and R. S. Hixson. (2005). “SUITABILITY OF MAGNESIUM OXIDE AS A VISAR WINDOW”. Retrieved from http://www.osti.gov/scitech/servlets/purl/935049
38. T. S. Duffy, R. J. Hemley and H. Mao, *Phys. Rev. Lett.* **74**, 1371 (1995).
39. S. Speziale, C. Zha, T. S. Duffy, R. J. Hemley and H. Mao, *J. Geophy. Res.* **106,** 515 (2001).
40. S. D. Jacobsen, C. M. Holl, K. A. Adams, R. A. Fischer, E. S. Martin, C. R. Bina, J.-F. Lin, V. B. Prakapenka, A. Kubo and P. Dera, *Amer. Miner.* **93**, 1823 (2008).
41. T. S. Duffy and T. J. Ahrens, *J. Geophys. Res.* **100**, 529 (1995).
42. T. S. Duffy and T. J. Ahrens, *High Pressure Science and Technology* (Ed: S. C. Schmidt, J. W. Shaner, G. A. Samara and M. Ross, Amer. Inst. Phys., NY 1107) (1993).
43. B. Svendsen and T. J. Ahrens, *Geophys. J. R. Astr. Soc.* **91**, 667 (1987).
44. L. Zhang, Z. Gong and Y. Fei, J. Phys. Chem. Solids **69**, 2344 (2008).
45. E. A. Perez-Albuerne and H. G. Drickamer, *J. Chem. Phys.* **43**, 1381 (1965).
46. T. S. Duffy, presentation in 2012 DOE/SSAA Symposium, Washington D.C. (2012).
47. G. Vaitheeswaran, V. Kanchana, M. Rajagopalan, *Solid State Commun.* **124**, 97 (2002).
48. Y. O. Ciftci, K. Colakoglu, E. Deligoz, H. Ozisik, *Mater. Chem. Phys.* **108**, 120 (2008).
49. S. B. Schneider, D. Baumann, A. Salamat, W. Schnick, *J. Appl. Phys.* **111,** 093503 (2012).
50. G. I. Kanel, S. V. Razorenov and V. E. Fortov, *J. Phys Cond. matter* **16**, S1007 (2004).
51. L. M. Barker and R. E. Hollenbach, *J. Appl. Phys.* **43**, 4669 (1972).
52. P. W. Bridgman, Collected Experimental Papers, seven volumes (1964) (Cambridge, MA: Harvard University Press).
53. P. W. Bridgman, *The Physics of High Pressure*, (Bell, London, 1952).

54. F. P. Bundy, in *Modern High Pressure Research*, (Ed: R.H. Wentorf Jr. Butterworths, Washington, DC, 1962), Vol. 1.
55. H. T. Hall, *Rev. Sci. Instr.* **33**, 1278 (1962).
56. M. B. Weinberger, S. H. Tolbertand A. Kavner, *Phys. Rev. Lett.* **100**, 045506 (2008).
57. H. K. Mao and P. M. Bell, *Science* **200**, 1145, (1978);.K. A. Goettel, H. K. Mao and P. M. Bell, *Rev. Sci. Instrum.* **56**, 1420 (1985).
58. H. K. Mao, P. M. Bell, J. W. Shaner and D. J. Steinberg, *J. Appl. Phys*. **49**, 3276 (1978).
59. L. Ruoff and H. Luo, in Recent Trends in High Pressure Research, Proceedings of XIII AIRAPT Int. Conf. On High Pressure Sciences and Technology(Ed: A.K. Singh, Oxford and IBH New Delhi 1992), p. 779.
60. W. Mao and H.-k. Mao, *J. Phys. Cond. Matt*. **18**, S1069 (2006).
61. W. J. Evans, C.-S. Yoo, G. W. Lee, H. Cynn, M. J. Lipp, and K. Visbeck, *Rev. Sci. Instrum.* **78**, 073904 (2007).
62. L. Dubrovinsky, N. Dubrovinskaia, V. B. Prakapenka, and A. M. Abakumov, *Nat. Commun.* **3**, 1163 (2012). http://dx.doi.org/10.1038/ncomms2160.
63. H. K. Mao, J. Xu, and P. M. Bell, *J Geophys. Res.* **91**, 4673 (1986).
64. J. J. Wu et al., *Scientific Reports* **4,** 3685 (2014).
65. S. Tateno, K. Hirose, Y. Ohishi, Y. Tatsumi, Science **330**, 359 (2010).
66. N. Dubrovinskaia, and L. Dubrovinsky, *Advances in High-Pressure Techniques for Geophysical Applications*, pp. 487–501, New York: Elsevier (2005).
67. A. Salamat, et al., *Coord. Chem. Rev.* (2014), http://dx.doi.org/10.1016/j.ccr.2014.01.034
68. L. C. Ming and W. A. Bassett, *Rev. Sci. Instrum.*, 45, 1115 (1974).
69. M. Murakami, K. Hirose, K. Kawamura, N. Sata, Y. Ohishi, *Science* **304**, 855 (2004).
70. J. F. Lin, W. Sturhahn, J. Y. Zhao, G. Y. Shen, H. K. Mao, R. J. Hemley, *Science* **308**, 1890 (2005).
71. D. Andrault, M. Munoz, N. Bolfan-Casanova, N. Guignot, J.P. Perrillat, G. Aquilanti, S. Pascarelli, *Earth Planet. Sci. Lett.* **293**, 90 (2010).

72. D. Andrault, S. Petitgirard, G. Lo Nigro, J. L. Devidal, G. Veronesi, G. Garbarino, M. Mezouar, *Nature* **487**, 354 (2012).
73. V. Potapkin, C. McCammon, K. Glazyrin, A. Kantor, I. Kupenko, C. Prescher, R. Sinmyo, G. V. Smirnov, A. I. Chumakov, R. Ruffer, L. Dubrovinsky, *Nat. Commun.* **4**, 1427 (2013).
74. C. McCammon, L. Dubrovinsky, O. Narygina, I. Kantor, X. Wu, K. Glazyrin, I. Sergueev, A. I. Chumakov, *Phys. Earth Planet. Inter.* **180**, 215 (2010).
75. A. K. Singh, H. K. Mao, J. Shu, R. J. Hemley, *Phys. Rev. Lett.* **80**, 2157 (1998).
76. T. S. Duffy, G. Shen, J. Shu, H. K. Mao, R. J. Hemley and A. K. Singh, *J. Appl. Phys*. **86**, 6729 (1999).
77. A. K. Singh and T. Kenichi, *J. Appl. Phys*. **90**, 3269 (2001).
78. D. C. Hurley, R. S. Gilmore and W. F. Banholzer, *J. Appl. Phys*. **76**, 7726 (1994).
79. R. Vogelgesang A. K. Ramdas, and S. Rodriguez, M. Grimsditch, T. R. Anthony, *Phys. Rev. B* **54**, 3989 (1996).
80. E. S. Zouboulis, M. Grimsditch., A. K. Ramdas and S. Rodriguez, *Phys. Rev. B* **57**, 2889 (1998).
81. M. Grimsditch, E.S. Zouboulis, A. Polian, *J. Appl. Phys.* **76**, 832 (1994).
82. F. Elder, A. M. Gurewitsch, R. V. Langmuir, H. C Pollock, *Phys. Rev.* **71**, 829 (1947).
83. G. **S.** Knapp, M. A. Beno, and H. You, *Annu. Rev. Mater. Sci*. **26**, 693 (1996).
84. M. Hanfland, K. Syassen, N. E. Christensen and D. L. Noviko, *Nature* **408**, 174 (2000).
85. L. A. Bruno and O' Connor H. Brian, *J. Am. Ceram. Soc*. **80**, 2941 (1997).
86. A. F. Goncharov *et al.*, Science **273**, 5272 (1996)
87. C. Lind, D. G. VanDerveer, A. P. Wilkinson, J. Chen, M. T. Vaughan, and D. J. Weidner, *Chem. Mater.* **13**, 487 (2001).
88. V. Panchal, N. Garg, A. K. Chauhan, Sangeeta, S. M. Sharma, *Solid State Comm.* **130**, 203 (2004).
89. Y. K. Vohra, S. K. Sikka, E. S. K. Menon and R. Krishnan, *Acta. Metall.* **28***,* 683 (1980).

90. H. Xia, S. J. Duclos, A. L. Ruoff and Y. K. Vohra, *Phys. Rev. Lett.* **64**, 204 (1990).
91. H. Xia, G.Parthsarthy, H. Luo, Y. K. Vohra and A. Ruoff, *Phys. Rev.* B **42**, 6736 (1990).
92. M. P. Usikov and V. A. Zilbershtein, *Phys. Stat. Sol.(a)* **19**, 53 (1973).
93. A. R. Kutsar, I. V. Lyasotski, A. M. Podurits and A. F. Sanches-Bolinches, *High Press. Res.* **4**, 475 (1990).
94. S. Song and G.T. Gray III, *High Pressure Science and Technology* (Eds: S.C. Schmidt, J.W. Fowles, G.S. Samara and M. Ross), AIP Press, New York, 251 (1994).
95. Y. K. Vohra, S. K. Sikka R. Chidambaram, *Bull. Mater. Sci.* **2**, 109 (1981).
96. A. K. Singh, *Bull. Mater. Sci.* **5**, 219 (1983).
97. A. K. Singh, *Mater. Sci. Forum* **3**, 291 (1985).
98. D. Errandonea, B. Schwager, R. Ditz, C. Gessmann, R. Boehler, M. Ross, *Phys. Rev. B* **63**, 132104 (2001).
99. S. T. Weir, M. J. Lipp, S. Falabella, G. Samudrala, Y. K. Vohra, *J. Appl. Phys.* **111**,123529 (2012).
100. A. Zerr, R. Boehler, *Nature* **371**, 506 (1994).
101. J. Ruiz-Fuertes, A. Karandikar, R. Boehler, D. Errandonea, *Phys. Earth Planet. Inter.* **181**, 69 (2010).
102. A. Dewaele, M. Mezouar, N. Guignot, P. Loubeyre, *Phys. Rev. B* **76**, 144106 (2007).
103. L. Vel, G. Demazeau, J. Etourneau, *Mater. Sci. Eng. B* **10**, 149 (1991).
104. E. Gregoryanz, C. Sanloup, M. Somayazulu, J. Badro, G. Fiquet, H. K. Mao, R. J. Hemley, *Nat. Mater.* **3**, 294 (2004).
105. J. C. Crowhurst, A. F. Goncharov, B. Sadigh, C. L. Evans, P. G. Morrall, J. L. Ferreira, A. J. Nelson, *Science* **311**, 1275 (2006).
106. A. F. Young, C. Sanloup, E. Gregoryanz, S. Scandolo, R. J. Hemley, H. K. Mao, *Phys.Rev. Lett.* **96**, 155501 (2006).
107. L. Davison, *Fundamentals of shockwave propagation in solids*, Springer Verlag, 2008, p. 38.

108. G. E. Duval and R. A. Graham, *Rev. of Modern Phys*. **49**, 523 (1977); G. E. Duvall and G. R. Fowles, *Shock Waves in High Pressure Physics and Chemistry* Vol 2, (Ed: R S Bradley) New York(1963): Academic, p. 2.
109. S. K. Sikka, B. K. Godwal and R. Chidambaram, *Bull. Mater. Sci*. **7**, 370 (1985).
110. L. V. Al'tshuler, A. A. Bakanova, I. P. Dudoladov, E. A. Dynin, R. F. Trunin and B. S. Chekin, *J. Appl. Mech. Tech. Phys*. **22** 145 (1981).
111. R. F. Trunin, *Phys. Uspekhi* **44**, 371 (2001).
112. R. G. McQueen, S. P. Marsh, J. W. Taylor, J. N. Fritz and W. J. Carter, in High Velocity Impact Phenomena (Ed. R. Kinslow), Academic, New York, 293 (1971).
113. A. A. Bakanova, I. P. Dudoladov and Y. N. Sutulov, *Sov. Phys. Sol. State* **11**, 1515 (1970).
114. K. D. Joshi and S. C. Gupta, *High Press. Res.* **27**, 259 (2007).
115. W. J. Nellis, J. A. Morarity, A. C. Mitchell and N. C. Holmes, *J. Appl. Phys*. **82**, 2225 (1997); A. Benuzzi *et al.*, *Phys. Rev. E* **54**, 2162 (1996).
116. Y. M. Gupta, *Shock Compression of Condensed Matter*, (Eds. M. D. Furnish, L. C. Chhabildas and R. S. Hixson, AIP, 2000) p. 3.
117. L. V. Al'tshuler *et al*, *Phys.-Usp.* **39**, 539 (1996)
118. J. R. Asay, *Int. J. Impact Engg*. **20**, 27 (1997).
119. M. D. Furnish, L. C. Chhabildas, and W. D. Reinhart, *Int. J. Impact Engg*. **23**, 261 (1999).
120. S. C. Gupta, R. G. Agarwal, J. S. Gyanchandani, S. Roy, N. Suresh, S. K. Sikka, A. Kakodkar and R. Chidambaram, *in Shock Compression of Condensed Matter* (Ed. S.C Schmidt, R.D. Dick, J.W. Forbes and D.G. Tasker), 839 (1991).
121. J. Osher, R. Gathers, H. Chau, R. Lee, G. Pomykal, and R. Weingart, *Int. J. Impact Eng*. **10**, 439 (1990).
122. T. C. Kaushik *et al*, *IEEE Transaction in Plasma Science* **30(6)**, 2133 (2002).
123. C. A. Hall, J. R. Asay, M. D. Knudson, W. A. Stygar, R. B. Spielman, T. D. Pointon, D. B. Reisman, A. Toor and R. C. Cauble, *Rev. Sci. Instrum*. **72**, 3587 (2001).
124. M. D. Knudson, D. L. Hanson, J. E. Bailey, C. A. Hall, and J. R. Asay, *Phys. Rev. Lett*. **87**, 225501-1 (2001).

125. D. B. Reisman et al., *J. Appl. Phys*. **89**, 1625 (2001).

126. L. D. Da Silva *et al.*, *Phys. Rev. Lett.* **78**, 483(1997).

127. R. W. Lemke, M. D. Knudson, C. A Hall, and T. A. Haill, P. M. Desjarlais, J. R. Assay and T. A. Mehlhorn, *Phys. Plasmas* **10**, 1092 (2003).

128. R. Jeanloz et al., *PNAS* **104**, 22 (2007).

129. G. Jyoti, N. Suresh, K. D. Joshi and S. C. Gupta, *Solid State Physics, India* (Ed: R. Mukhopadhyay, B.K. Godwal and S.M. Yusuf), vol. 42, p. 272(1999).

130. A. S. Rav, K. D. Joshi and S. C. Gupta, in 12th National Seminar on Physics and Technology of Sensors, 2007.

131. S. C. Gupta and Y. Gupta, *J. Appl. Phys.***57**, 2464 (1985).

132. S. C. Gupta, *Indian J. of Pure & App. Phys.* **34**, 651 (1996).

133. S. C. Gupta and S. K. Sikka, *Shock Waves* **6**, 345 (1997).

134. D. D. Bloomquist and S. A. Sheffield, *J. Appl. Phys.* **54**, 1717 (1983).

135. W. Hemsing, A. Mathews, R. Warnes, M. George, and G. Whittemore, in Shock Compression of Condensed Matter, edited by S. Schmidt, R. Dick, J. Forbes, and D. Tasker (Elsevier, New York),pp. 767(1992).

136. K. Baumung, J. Singer, S. Razorenov, A. Utkin, in Shock Compression of Condensed Matter, edited by S. Schmidt and W. Tao (AIP, Woodbury, NY), p. 1015(1996).

137. P. Celliers, G. Collins, L. DaSilva, D. Gold, and R. Cauble, *Appl. Phys. Lett.* **73**, 1320 (1998)

138. D. Milathianaki et al., *Phys. Rev. B* **86**, 014101(2012).

139. D. H. Kalantar et al., *Phys. Rev. Lett.* **95**, 075502 (2005).

140. A. Loveridge-Smith, A. Allen, J. Belak, T. Boehly, A. Hauer, B. Holian, D. Kalantar, G. Kyrala, R. W. Lee, P. Lomdahl, M. A. Meyers, D. Paisley, S. Pollaine, B. Remington, D. C. Swift, S. Weber, J. S. Wark, *Phys. Rev. Lett*. **86**, 2349 (2001).

141. G. I. Pangilinan and Y. M. Gupta, *High Pressure Shock Compression of Solids III*, ed. L. Davison and M. Shahinpoor (Springer Verlag–New York 1998) p. 81.

142. K. G. Nakamura, K. Wakabayashi, Y Hironaka and K Kondo, *J. Phys. Cond. Matter* **14**, 10817 (2002).

143. D. H. Dolan and Y. M. Gupta, *J. Chem. Phys*. **121**, 9050 (2004).

144. L. H. Thomas, *Proc. Cambridge Phil. Roy. Soc.* **23**, 542 (1927).

145. E. Fermi, *Rend. Accad. Naz. Lincei* **6**, 602 (1927).

146. P. A. M. Dirac, *Proc. Cambridge Phil. Roy. Soc.* **26**, 376 (1930).

147. E. Teller, *Rev. Mod. Phys.* **34**, 627 (1962).

148. P. Hohenberg and W. Kohn, *Phys. Rev.* **136**, B864 (1964).

149. M. Born and R. Oppenheimer, *Annalen der Physik* **84**, 457 (1927).

150. W. Kohn and L. J. Sham, *Phys. Rev.* **140**, A1133 (1965).

151. D. R. Hartree, *Proc. Cam. Phil. Soc.* **24**, 89 (1928).

152. V. Z. Fock, *Z. Phys.* **61**, 209 (1930).

153. M. Born and K. Huang, *Dynamic Theory of Crystal Lattices.* Oxford: Oxford University Press (1954).

154. R. O. Jones and O. Gunnarsson, *Rev. Mod. Phys.* **61**, 689 (1989).

155. N. D. Mermin, *Phys. Rev.* **137**, A1441 (1965).

156. E. Runge and E. K. U. Gross, *Phys. Rev. Lett.* **52**, 997 (1984).

157. D. M. Ceperley and B. J. Alder, *Phys. Rev. Lett.* **45**, 566 (1980).

158. A. Svane and O. Gunnarsson, *Phys. Rev. Lett.* **65**, 1148 (1990).

159. S. Massida, M. Posternak and A. Baldereschi, *Phys. Rev. B* **48**, 5058 (1993).

160. L. Hedin, *Phys. Rev.* **139**, A796 (1965).

161. V. I. Anisimov, F. Aryasetiawan and A. I. Lichtenstein, *J. Phys. Cond. Matter* **9**, 767 (1997).

162. R. M. Matrin, *Electronic Structure - Basic Theory and Practical Methods*, Cambridge University Press (2004).

163. D. R. Hamann, M. Shluter, and C. Chiang, *Phys. Rev. Lett.* **43**, 1494 (1979).

164. D. Vanderbilt, *Phys. Rev. B* **41**, 7892 (1990).

165. W. C. Herring, *Phys. Rev.* **57**, 1169 (1940).

166. W. C. Herring and A. G. Hill, *Phys. Rev.* **58**, 132 (1940).

167. F. Herman, *Rev. Mod. Phys.* **30**, 102 (1958).

168. P. E. Blochl, *Phys. Rev. B* **50**, 17953 (1994).

169. G. Kresse and D. Joubert, *Phys. Rev. B* **59**, 1758 (1999).

170. N. A. W. Holzwarth, G. E. Matthews, A. R. Tackett, and R. B. Dunning, *Phys. Rev. B* **55**, 2055 (1997).

171. http://www.quantum-espresso.org/

172. http://www.abinit.org/

173. http://cms.mpi.univie.ac.at/vasp/

174. J. C. Slater and G. F. Koster, *Phys. Rev.* **94**, 1498 (1954).

175. K. Koepernik and H. Eschrig, *Phys. Rev. B* **59**, 1743 (1999).

176. O. K. Anderson, *Phys. Rev B* **12**, 3060 (1975).

177. S. Y. Savrasov, *Phys. Rev. B* **54**, 16470 (1996);S. Y. Savrasov, D. Y. Savrasov, *ibid* **54** 16487 (1996).

178. D.J. Singh, *Plane Waves, Pseudopotentials and the LAPW Method*, Kluwer Academic Publishers, Boston, Dordrecht, London (1994).

179. P. Blaha, K. Schwarz, G. K. H. Madsen, D. Kvasnicka and J. Luitz, WIEN2K, (K. Schwarz, Techn. Univ. Wien, Austria, 2001).

180. S. Y. Savrasov, *Phys. Rev. Lett.* **69**, 2819 (1992).

181. X. Gonze, D. C. Allan, and M. P. Teter, *Phys. Rev. Lett.* **68**, 3603 (1992).

Chapter - 2

Elastic, Lattice Dynamic and Structural Stability of Lithium Hydride under High Pressure: *Ab-initio* Calculations

2.1 *Introduction*

Lithium hydrides (LiH) having NaCl structure (B1) at ambient condition is a good hydrogen storage material. Under high pressure, because of the quantum influence of proton and increasing interaction of core electrons of neighboring atoms, this material is expected to display interesting behavior such as the transitions to low-symmetry phase, metal-insulator transition, etc [1]. These expectations have attracted attention of many researchers [1-16] in this compound to understand its solid state properties. Many of these studies are also related to high pressure behavior of LiH, which include analysis of its phase stability [1-11], determination of equation of state [3,4,8-13], understanding the effect of pressure on electronic charge density [13], band structure [9,13,14] and melting point [16] etc. As far as structural stability of this compound under high pressure is concerned, widely differing results have been reported in literature [2,3,17,18]. On the basis of psuedopotential calculations within local density approximation (LDA), Martins [17] predicted NaCl type (B1 phase) to CsCl type (B2 phase) structural phase transition at ~ 450 GPa, whereas, theoretical calculations by Gou *et al.* [18] using ionic overlap compression model found this transition to occur at ~ 85 GPa. In contrast to this, the x-ray diffraction measurements in DAC carried out by Loubeyre *et al.* [11] do not show any phase transition up to 94 GPa. Subsequent theoretical studies by Ahuja *et al.* [2] using full potential LMTO and Wang *et al.* [3] using full potential LAPW (WIEN97 package) put this transition at ~ 400 GPa and 313 GPa, respectively. However, using pseudopotential technique Zhang *et al.* [19] and Zurek *et al.*[20] found the transition pressure as ~ 200 GPa and 300

GPa, respectively. The recent high pressure x-ray diffraction measurements carried out in DAC [1] confirm that LiH will remain in B1 phase even up to ~ 252 GPa.

In addition to the direct total energy calculations for determining the structural stability, it is also worth to examine the elastic and lattice dynamic stability as a function of pressure or temperature, which can give additional insight into the mechanism of the phase transition or simply the mechanical failure of the LiH. In spite of so much importance of knowledge of the elastic and lattice dynamic stability, there are very few theoretical and experimental work published on this aspect of LiH [15, 19, 21-23]. For instance, there exists one theoretical study by Zhang *et al.* [19], where on the basis of theoretically calculated pressure dependent elastic constants and the lattice dynamical study at high pressure, the B1 to B2 transition has been associated to the softening of TA phonon at the zone boundary. In experimental front, the measurements of phonons as a function of pressure have also been reported on this compound by Ho *et al.* [24] up to 15 GPa and by Lazicki *et al.* [1] up to 120 GPa using Raman scattering.

In view of limited studies on the elastic and lattice dynamic stability of LiH as a function of pressure, the present theoretical work focuses on the structural, elastic and lattice dynamic stability of LiH under hydrostatic compression up to several Mbar. Unlike previous theoretical studies, in the present work the structural stability has been analyzed by not only considering B1 and B2 structures but also including B10 (primitive tetragonal structure P*4/nmm*) structure for analysis. The equation of state up to several Mbar has been derived from the 0 K calculations. Further, these calculations have been utilized to derive various thermophysical properties, *e.g.*, equilibrium volume, bulk modulus, its pressure derivative, Debye temperature, Grüneisen parameter etc. Moreover, the single crystal elastic constants have been employed to get the elastic properties of polycrystalline LiH.

2.2 Theoretical Procedure of Calculations

The total energy calculations required for carrying out structural stability analysis, and for determination of 0 K isotherm and elastic moduli have been performed using WIEN2K package [25] based on FP-LAPW method. The exchange correlation part of the total energy is evaluated using generalized gradient approximation (GGA) [26]. In order to test the applicability of different exchange-correlation functional, some calculations have also been done with LDA. It is found that the equation of state parameters obtained from GGA calculations are in better agreement with the experimental data. A grid of 5000 k points has been used for sampling the Brillouin zone. The plane wave cutoff parameter $R_{MT}\,K_{MAX}$ is fixed at 7 with muffin tin radius R_{MT} chosen to be 1.3 a.u. for Li and 1.0 a.u. for H. The variation in R_{MT} around these values does not affect the results. The self consistent cycle was run until the energy convergence criterion of 0.1 mRy was met.

2.2.1 Structural stability analysis and determination of equation of state

To analyze the structural stability under hydrostatic compression, the total energy for B1, B2 and B10 phases of LiH at 0 K have been computed as a function of volume up to about 450 GPa. The B10 phase is a primitive tetragonal structure having space group P*4/nmm.* The atomic species Li and H of two units of LiH are located at 2c (0 ½ z, ½ 0 -z) and 2a (0 0 0, ½ ½ 0) sites (international table of Crystallography, Vol. 2) [27]. As shown in Fig. 2.1, the B10 structure is a distortion of B2 structure and one can go from B10 structure to B2 structure by changing the c/a ratio to $1/\sqrt{2}$ and the z value to 0.5. Therefore, the total energy calculations required for structural stability analysis of B10 and B2 phases have been performed on this tetragonal cell and at each volume the *c/a* ratio and internal parameter ‘z’ are optimized. Finally, to examine the structural stability under pressure, the total energy of the tetragonal cell at various volumes for optimized *c/a* ratio and internal parameter ‘z’ is compared with that of the B1 phase. Further, the total energy at 0 K is used to generate pressure-volume relation for each phase and which finally is utilized to determine the enthalpies of these phases at various pressures. In order to derive the pressure-volume relation, a polynomial fit of total energy with volume is used and the pressure is determined using the expression (1.11). The enthalpies have been compared at various pressures and the stable structure is obtained. After examining the structural stability at various pressures, the 0K isotherm of the LiH is determined and a 300K isotherm is obtained after adding the lattice thermal corrections as follows:

The 0K theoretical P-V data are fitted to the third order Birch-Murnaghan (B-M) equation of state:

$$P = \frac{3}{2}B_0\left[\left(\frac{V}{V_0}\right)^{-7/3} - \left(\frac{V}{V_0}\right)^{-5/3}\right]\left[1 + \frac{3}{4}\left(B_0^{'} - 4\right)\left\{\left(\frac{V}{V_0}\right)^{-2/3} - 1\right\}\right] \tag{2.1}$$

where, V and V_0 are volume at a compressed state and volume at zero pressure, respectively. The bulk modulus at zero pressure (B_0) and the pressure derivative of bulk modulus at zero pressure ($B_0^{'}$) is derived from the above fit. The bulk modulus B and its pressure derivative B' at different pressures are then determined as follows:

$$B = V\frac{\partial^2 E_c}{\partial V^2} = -V\frac{\partial P}{\partial V} \text{ and } B^{'} = \frac{\partial B}{\partial P} = -\frac{V}{B}\frac{\partial B}{\partial V} \tag{2.2}$$

The total energy $E(V,T)$ and pressure $P(V,T)$ at given temperature T and volume V can be expressed as [28-29]:

$$E(V,T) = E_c(V) + E_T(V,T) + E_e(V,T) \tag{2.3}$$

$$P(V,T) = -\frac{\partial F(V,T)}{\partial V} = -\frac{\partial F_c}{\partial V} - \frac{\partial F_T(V,T)}{\partial V} - \frac{\partial F_e(V,T)}{\partial V} \tag{2.4}$$

Here $F(V,T)$ is the Helmholtz free energy at temperature T and volume V with F_c, denoting the free energy at 0 K, and $F_T(V,T)$ and $F_e(V,T)$ are the free energies corresponding to the thermal lattice vibrations and thermal electronic excitations contributions, respectively.

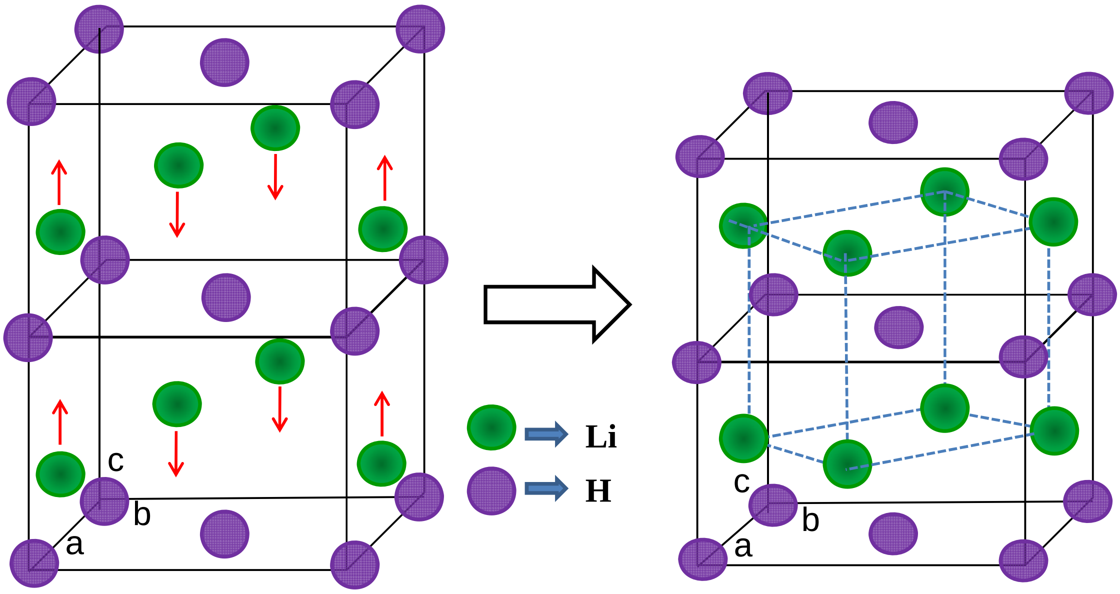

Primitive Tetragonal (B10) structure **Simple cubic (B2) structure**

Figure 2.1: A relationship between B10 (tetragonal with space group P*4/nmm)* and B2 structure in LiH. The atomic shuffle needed for B10 structure to transform to B2 structure. In the B10 structure, the hydrogen atoms occupy the 2a (0 0 0, ½ ½ 0) site and lithium atoms occupy the 2c (0 ½ z, ½ 0 -z) location (for B10 structure, z is a free internal parameter). The B10 structure becomes identical to the B2 phase for z = 0.5 and $c/a = 1/\sqrt{2}$. The cell formed by dotted lines in the right hand side figure is the B2 unit cell formed from the B10 structure.

The Eqn. (2.4) can equivalently be put in different way as [28-30]

$$P(V,T) = -\frac{\partial E_c(V)}{\partial V} + \frac{\gamma E_T}{V} + \gamma_e \frac{E_e}{V} \tag{2.5}$$

where E_T is vibrational energy of the ions contribution including zero point vibration energy and E_e thermal electronic contribution to the total energy. γ and γ_e are the thermal and electronic Grüneisen parameters, respectively. At 300 K the electronic excitation energy contributions are very small (of order of 10^{-2} mRy/atom) hence to determine the 300 K isotherm these terms in Eqn. (2.3) and (2.5) are neglected. The thermal Grüneisen parameter is determined using the definition:

$$\gamma = -\frac{\partial \ln \theta_D}{\partial \ln V} \tag{2.6}$$

The volume dependent Debye temperature θ_D in the above equation has been calculated using following expression [28]:

$$\frac{1}{\theta_D^3} = \frac{1}{3}\left(\frac{1}{\theta_L^3} + \frac{2}{\theta_T^3}\right) \tag{2.7}$$

Here the Debye temperatures θ_L and θ_T associated with longitudinal and transverse polarization, respectively are determined as a function of volume from the theoretically calculated elastic constants using the expression [28,31]:

$$\theta_L = 251.45\sqrt{\frac{B+\frac{4}{3}G}{\rho}V_{mol}^{-\frac{1}{3}}} \quad ; \quad \theta_T = 251.45\sqrt{\frac{G}{\rho}V_{mol}^{-\frac{1}{3}}} \tag{2.8}$$

Where the G is the polycrystalline shear modulus determined from average of the shear modulus calculated using single crystal elastic constants C_{11}, C_{12} and C_{44} in Voigt and Reuss approximations as discussed in next section [32-33].

The E_T per atom is approximated using the high temperature limit of Debye model of lattice vibrations [28]:

$$E_T = 3k_BT\left[1+\left(\frac{1}{20}\right)\left(\frac{\theta_D}{T}\right)^2 - \left(\frac{1}{1680}\right)\left(\frac{\theta_D}{T}\right)^4\right] \tag{2.9}$$

Where, k_B is the Boltzmann constant.

Finally the 300 K isotherm is evaluated by substituting the value of γ, E_T at 300 K calculated using Eqn. (2.6) through Eqn. (2.9) in Eqn. (2.5).

2.2.2 Elastic Constants and Phonons

For the LiH single crystal having cubic structure, there are only three independent elastic constants, C_{11}, C_{12} and C_{44} or equivalently three independent elastic moduli namely bulk modulus (*B*) and two shear moduli *C'*= (C_{11} - C_{12})/2 and C_{44}. To determine the shear moduli *C'* and C_{44} at a particular volume, the total energy is calculated as a function of different kinds of distortions and the shear elastic moduli are then calculated from the second order derivative of the total energy with respect to strain e_i (with *i*= 1to 6) as described below:

Total energy of the strained lattice is related to the deformation tensor by the following relation [34]:

$$E_c(V,\underline{\varepsilon}) = E_c(V,0) + \frac{1}{2}V\sum_i\sum_j C_{ij}e_ie_j \tag{2.10}$$

Where e_i are the components of the deformation tensor $\underline{\varepsilon}$ represented in matrix notation as follows:

$$\underline{\varepsilon} = \begin{bmatrix} e_1 & \frac{1}{2}e_6 & \frac{1}{2}e_5 \\ \frac{1}{2}e_6 & e_2 & \frac{1}{2}e_4 \\ \frac{1}{2}e_5 & \frac{1}{2}e_4 & e_3 \end{bmatrix} \tag{2.11}$$

The total energy variation of the lattice is calculated using volume conserving deformation [29, 35]. The volume conserving deformations used for the calculations of the shear elastic moduli C' and C_{44}, respectively are (in matrix notation):

$$\begin{bmatrix} e & 0 & 0 \\ 0 & -e & 0 \\ 0 & 0 & \frac{e^2}{1-e^2} \end{bmatrix} \quad \text{and} \quad \begin{bmatrix} 0 & e & 0 \\ e & 0 & 0 \\ 0 & 0 & \frac{e^2}{1-e^2} \end{bmatrix} \tag{2.12}$$

When these two deformation matrices (Eqn. 2.12) are used in Eqn. (2.10), the relation between the total energies of the strained lattice and the elastic constants becomes:

$$E_c(V, \underline{\varepsilon}) = E(V,0) + V(C_{11} - C_{12})e^2 + O(e^4) \tag{2.13}$$

$$E_c(V, \underline{\varepsilon}) = E(V,0) + 2VC_{44}e^2 + O(e^4) \tag{2.14}$$

At each unit cell volume V, the total energy of the strained lattice $E_c(V, \underline{\varepsilon})$ is computed and then Eqn. (2.13) and Eqn. (2.14) are used to determine the moduli C_{11} - C_{12} and C_{44}. Again, the bulk modulus (B) calculated using equation of state (Eqn. 2.2) is related to the C_{11} and C_{12} elastic constants by the following relation

$$B = \frac{1}{3}(C_{11} + 2C_{12}) \tag{2.15}$$

The independent elastic constants C_{11} and C_{12} are evaluated by solving Eqn. (2.15) and Eqn. (2.13).

These three independent elastic moduli are used to calculate the shear elastic constant for polycrystalline LiH containing randomly oriented crystallites. For this purpose, two different averaging procedures are implemented – first one is based on the strain continuity across the grain boundaries suggested by Voigt and the other is based on the stress continuity across the grain boundaries suggested by Reuss. These two averaging is the upper and lower limit of the isotropic polycrystalline shear modulus. The expression for the polycrystalline shear modulus G_V and G_R for the Voigt and Reuss approximations for cubic system (LiH) are given as:

$$G_V = \frac{1}{5}(C_{11} - C_{12} + 3C_{44}) \tag{2.16}$$

$$G_R = \frac{5C_{44}(C_{11} - C_{12})}{3(C_{11} - C_{12}) + 4C_{44}} \tag{2.17}$$

Finally, the polycrystalline shear modulus G is found from the Voigt-Reuss-Hill approximation [36] which is the arithmetic average of G_V and G_R.

The bonding nature of a material is analyzed phenomenologically by the Cauchy's pressure $P_c = (C_{12} - C_{44})$ [37]. Similarly, the brittle or ductile behavior has an empirical linking with the Pugh's relationship (G/B ratio) [38]. For covalent or metallic bonding, the directionality of bonds and thus the angular character of atomic bonding must be taken into account which could be described by the Cauchy's pressure. For covalent material the material's resistance to shear (C_{44}) is much higher than the volume change (C_{12}) resulting the Cauchy pressure to be negative (for metallic material vice-versa). Another empirical relation is to measure the ductility of a material through its G/B ratio. If G/B ratio is greater than 0.5 the material may be considered as brittle, while if $G/B < 0.5$ the material is ductile.

Apart from static lattice calculations, the lattice dynamic calculations, have also been performed using plane wave pseudopotential method as implemented in the Quantum ESPRESSO software package [39] and phonon spectra at various volumes have been determined. The lattice dynamical calculations have been carried out within the framework of self consistent perturbation theory with 4×4×4 q points and 8×8×8 k-mesh used for integration over the Brillouin zone. The calculations are carried out within GGA and the electronic wave functions are expanded in a plane wave (PW) basis set with energy cut off of 60 Ry and charge density is represented in PWs with energy cut off of 600 Ry.

2.3 *Results and Discussions*

2.3.1 *Structural stability and equation of state*

In order to determine equation of state, the knowledge of structural stability as a function of pressure is necessary. Therefore we have analyzed structural stability of LiH under hydrostatic pressure. For this purpose the total energy at 0 K has been calculated at various unit cell volumes for the B1, B2 and B10 structures. In order to test the structural stability of B10 and B2 phases the calculations have been performed on the tetragonal cell and at each volume the *c/a* ratio and internal parameter 'z' are optimized. Fig. 2.2 shows the optimized *c/a* ratio and *z* as a function of volume. Also plotted is the total energy of tetragonal cell corresponding to the optimized parameters at each volume. It is clear from the figure that at zero pressure the optimum value of *c/a* and z parameter of the tetragonal cell is ~0.7598 and 0.2863, respectively, indicating that at zero pressure, the B10 structure has lower energy than the B2 phase. Upon compression, the optimum *c/a* ratio decreases, whereas, the z parameter increases monotonically with increasing pressure and approach to a value of ~ 0.707 and 0.5, respectively, at volume of 10.053 Å^3/ formula unit with corresponding pressure of ~ 31 GPa. Beyond this pressure the two parameters remain fixed at these values, indicating that the B2 structure becomes a low energy structure as compared to B10 phase beyond this pressure. Further, in the same figure, the total energy of the B1 structure has also been displayed. The comparison of total energy of B1, B10 and B2 structures, clearly suggests that up to volume/formula unit of $\leq$ 4.8 Å^3 with corresponding pressure of $\leq$ 327 GPa, the B1 structure has lowest energy among these three phases and beyond this pressure LiH stabilizes in B2 phase. B10 structure does not stabilize at any compression. Further, shown is the enthalpy of B2 phase relative to B1 phase in Fig. 2.3. The comparison of enthalpies (Fig. 2.3) puts this transition at ~ 323 GPa *i.e.* slightly lower side. The transition pressure predicted in the present work is in accord with the predictions of Wang *et al.* [3] and Zurek *et al.* [20] and not with Gou *et al.* [18] and Zhang *et al.* [19]. The calculated 300 K isotherm is plotted in

Fig. 2.4 along with the experimental data [1, 11]. The agreement between theory and experiment is excellent and is better than with some other theoretical predictions. Further, it is clear from the figure that 300 K isotherm is better described by GGA as compared to LDA.

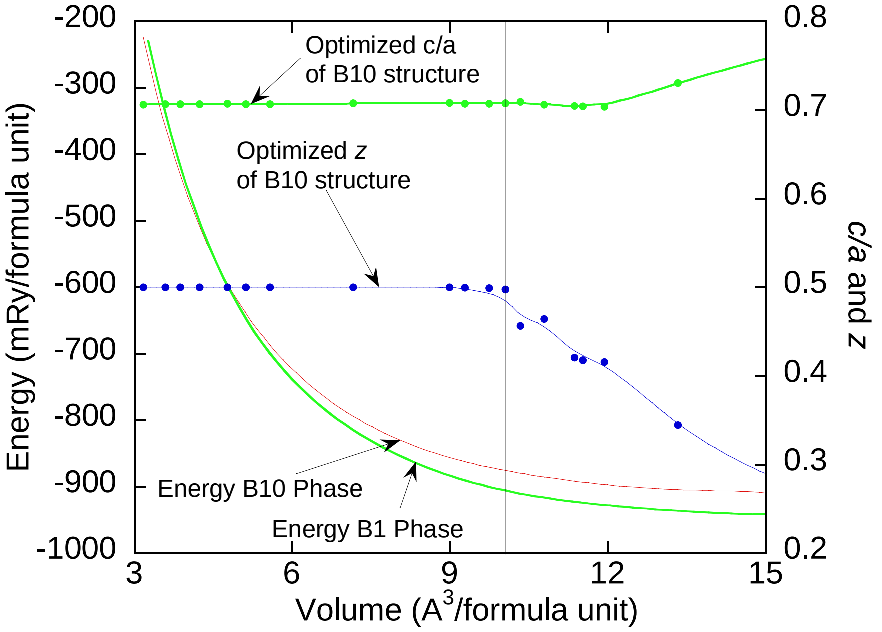

Figure 2.2: The total energy of the B1 phase and tetragonal structure (B10). The total energy at each volume for the tetragonal structure is plotted for optimum *c/a* and *z*. For clarity, the optimized *c/a* and fractional coordinate *z* of tetragonal structure as a function of volume are also plotted. It may be noted that for $V \leq 10.053$[Å^3/formula unit], *i.e.* pressure ≥ 31 GPa, the optimum *c/a* and *z* of the tetragonal structure saturate at a value of ~ 0.707 and 0.5, respectively.

In Table 2.1, we compare various physical quantities for B1 phase derived from our calculations with the experimental data and theoretical values available from other sources [6-9, 11, 12, 19, 21-23, 40-41]. The calculated zero pressure volume, bulk modulus and its pressure derivative at zero pressure volume obtained from GGA (LDA) calculations agree within 1.4(8.3), 1.4(19.4) and 2.3(1.4) %, respectively with experimental values[11, 21]. The experimental data agree better with the GGA results. This is consistent with the theoretical study by Lebegue *et al.* [4] using projector - augmented - wave method under GGA. Further, as depicted in the Table 2.1, our theoretical zero pressure bulk modulus of 34.2 GPa from GGA and 40.3 GPa from LDA calculations at 0 K agrees well with GGA and LDA values of 36.2 GPa and 40.5

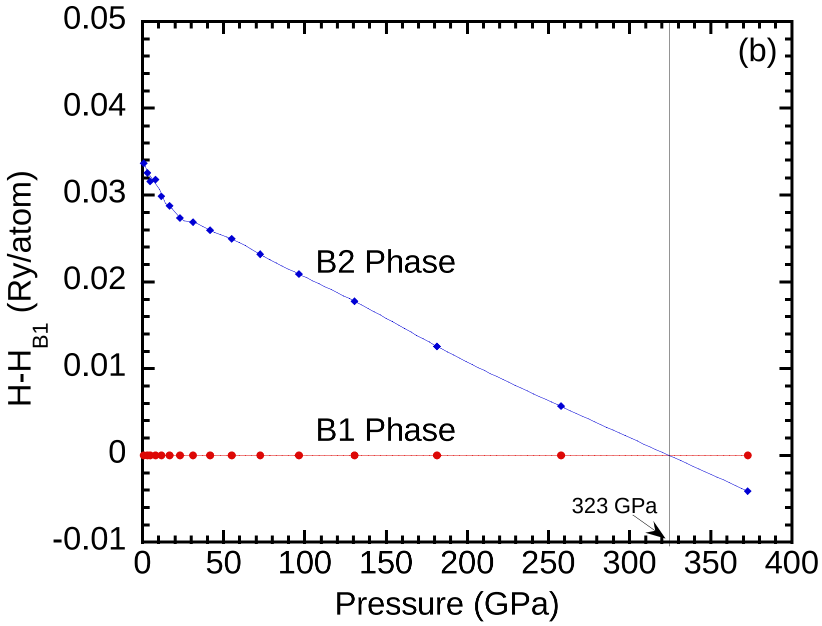

Figure 2.3: The differential enthalpy (*H*) of B1 and B2 phases of LiH with respect to B1 phase as a function of pressure (*P*). In this $H - P$ plot, the crossover of the energies for these two phases occurs at ~ 323 GPa of pressure as pointed out with black line.

GPa reported by Barrera *et al.*[6] from pseudopotential calculations at 0 K. However,the room temperature value of B_0 by these authors under quasi harmonic approximation is ~ 29 GPa for GGA and ~ 33 GPa for LDA, suggesting that the value determined from LDA is closer to the experiment (32.2 GPa). We find that, if instead of quasi harmonic approximation, the experimentally measured temperature derivative of bulk modulus (~ -0.0083 GPa/K) [21] is used, the 0 K value reported by Barrera *et al.* [6], becomes ~ 34 GPa for GGA and ~38 GPa for LDA at the room temperature. Interestingly, as shown in the Table 2.1, we find that though, the zero pressure volume and bulk modulus are different for GGA and LDA, the pressure derivative of bulk modulus is almost the same for both the approximations. This is consistent with the argument by Knuc and Syassen [42] that the third order derivative of total energy with respect to volume is nearly independent of the approximation used for the exchange-correlation functional. Additionally, we have also made contact with the available shock data by evaluating the parameters for the linear shock velocity (U_s) versus particle velocity (U_p) relation:

$$U_s = C_b + sU_p \tag{2.18}$$

here, the constant C_b is approximately related to the bulk modulus and the *s* parameter to pressure derivative of the bulk modulus through following expressions:

$$C_b = \sqrt{\frac{B_0}{\rho_0}} \tag{2.19}$$

$$B_0^{'} = 4s - 1 \tag{2.20}$$

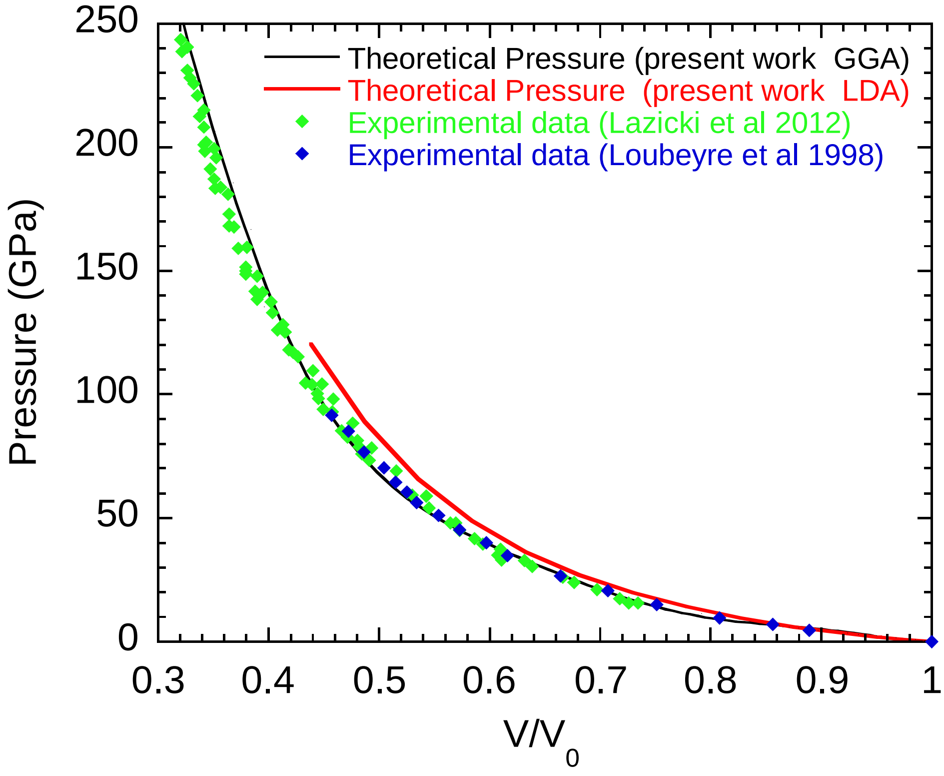

Figure 2.4: The pressure-volume relation or the equation of state of LiH at room temperature. The experimental data (filled diamond) of Loubeyre *et al.* [11] and Lazicki *et al.* [1] has also been shown for comparison.

The theoretical bulk modulus and its derivative is further utilized to derive the Grüniesen parameter (γ), the bulk sound speed and the Hugoniot parameter 's'. The Grüniesen parameter is estimated from $B_0^{'}$ using the well known Dugdale MacDonald relation [43]. The value of Grüneisen parameter so determined, turns out to be 1.30 as compared to 1.2 obtained at 140 K by James and Kheyrandish [21] using experimental measured value of thermal expansion coefficient, compressibility and heat capacity. The bulk sound velocity of 6.48 km/s determined from theoretical bulk modulus using Eq. (2.19) exhibits a good agreement with 6.43 km/s derived from experimentally measured adiabatic elastic constants [21] at 140 K. The value of '*s*' determined employing theoretically calculated $B_0^{'}$ in Eq. (2.20) is 1.15, in good agreement (within 0.8 %) with the experimental value of 1.16 determined from experimentally measured shock velocity vs particle velocity plot [40]. These values are listed in Table 2.1 also.

Table 2.1. Comparison of theoretical and experimental values of various physical properties of LiH at zero pressure.

Properties	*Present Theoretical Work	Theoretical (Other sources)	Experimental
V_0 (300K) ($Å^3$/atom)			
GGA	17.26	17.76[6],16.15[7], (15.18-16.24)[8], 15.24[19]	17.02[11], 16.85[12]
LDA	15.60	16.46[6],(14.87-15.18)[8], 16.0[9]	
B_0 (GPa)			
GGA	34.2	36.2[6] ,36.07[7], (34.03-39.99) [8],34.30[19]	32.2[11], 33.74[21], 32.35[22]
LDA	40.3	40.5[6], 36.6[9], (41.33-42.8) [8]	
B_0'			
GGA	3.61	3.49[7], 3.40[19]	3.53[11]
LDA	3.58	3.40[9]	(3.8±0.15) [22]
C_b (km/s)	6.48	--	6.43[21]
s	1.15	--	1.16[37]
γ	1.30	0.85[9]	1.2[21]
C_{11} (GPa)	77.0	82.7[19], 69.28[23]	74.06[21], 72.83[21] , 67.2 [22]
C_{12} (GPa)	12.7	10.7[19], 17.14[23]	14.2[21], 14.93[22]
C_{44} (GPa)	48.2	52.5[19], 58.25 [23]	48.43[21], 48.0[21], 46.37[22]
θ_0 (K)	828	1246[9]	1128±10[21],810[41]

[*] All the quantities are at zero pressure and zero temperature except the volume which is at zero pressure and room temperature.

2.3.2 *Elastic Properties*

In Table 2.1, we have also compared the theoretically determined elastic constants at ambient pressure with the experimental data measured through ultrasonic technique [21-22] and other theoretical values calculated using a periodic *ab-initio* (HF and DFT) code "CRYSTAL" based on an atom-centered (Gaussian) basis set program [23] and *ab-initio* pseudopotential plane wave method [19]. The presently determined values are closer to the values measured in ultrasonic experiments [21] at the temperature of ~ 60 K and 140 K. A further confirmation comes from the calculation of the Debye temperature (θ_0) from these elastic constants. The value of θ_0, turns out to be 828 K, which is near the value 810 K derived through the experimentally measured specific heat [41]. Further, the pressure dependence of the Debye temperature is also determined which is shown in Fig. 2.5. As shown in the figure, the Debye temperature increases monotonically with pressure.

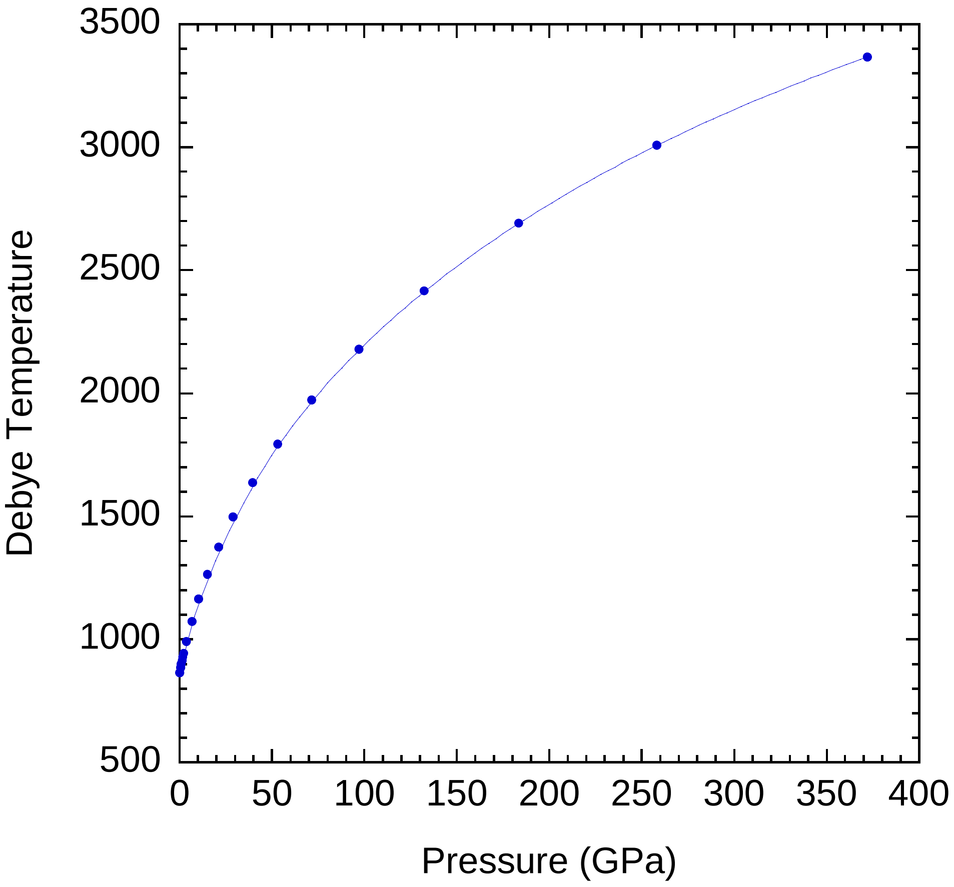

Figure 2.5: Debye temperature as a function of pressure.

After finding that our calculated elastic constants at zero pressure and the experimental data are in good agreement, we have performed further calculations for determinations of elastic constants as a function of compression for B1 phase. As shown in Fig. 2.5b (Fig. 2.5a is the *E*-*V* plot for comparison), the bulk modulus and shear modulus C' of B1 phase increase monotonically with increasing compression, which is similar to the trend found by Zhang *et al.* [19]. However, the shear modulus C_{44} determined from our calculations initially increases monotonically with compression and reaches its maximum value of ~ 109 GPa at a volume of ~ 5.97 $(A^0)^3$/atom (corresponding pressure ~196 GPa), thereafter, starts softening upon further compression. However, it does not soften completely at the B1 → B2 transition pressure. This softening is unlike that reported by Zhang *et al.* [19], where C_{44} increases monotonically upto to the pressure of 600 GPa. It was predicted by Zhang *et al.* [19] that LiH is different in this respect from NaH, KH and CsH. We do not support this conclusion. The numerical values of elastic constants are shown in Table 2.2. No experimental data are available for comparison at higher pressures. Additionally, Fig 2.6 shows the elastic anisotropy ($A= 2C_{44}/(C_{11}-C_{12})$) parameter as a function of pressure. The parameter "*A*" at zero pressure is found to be ~ 1.48 as

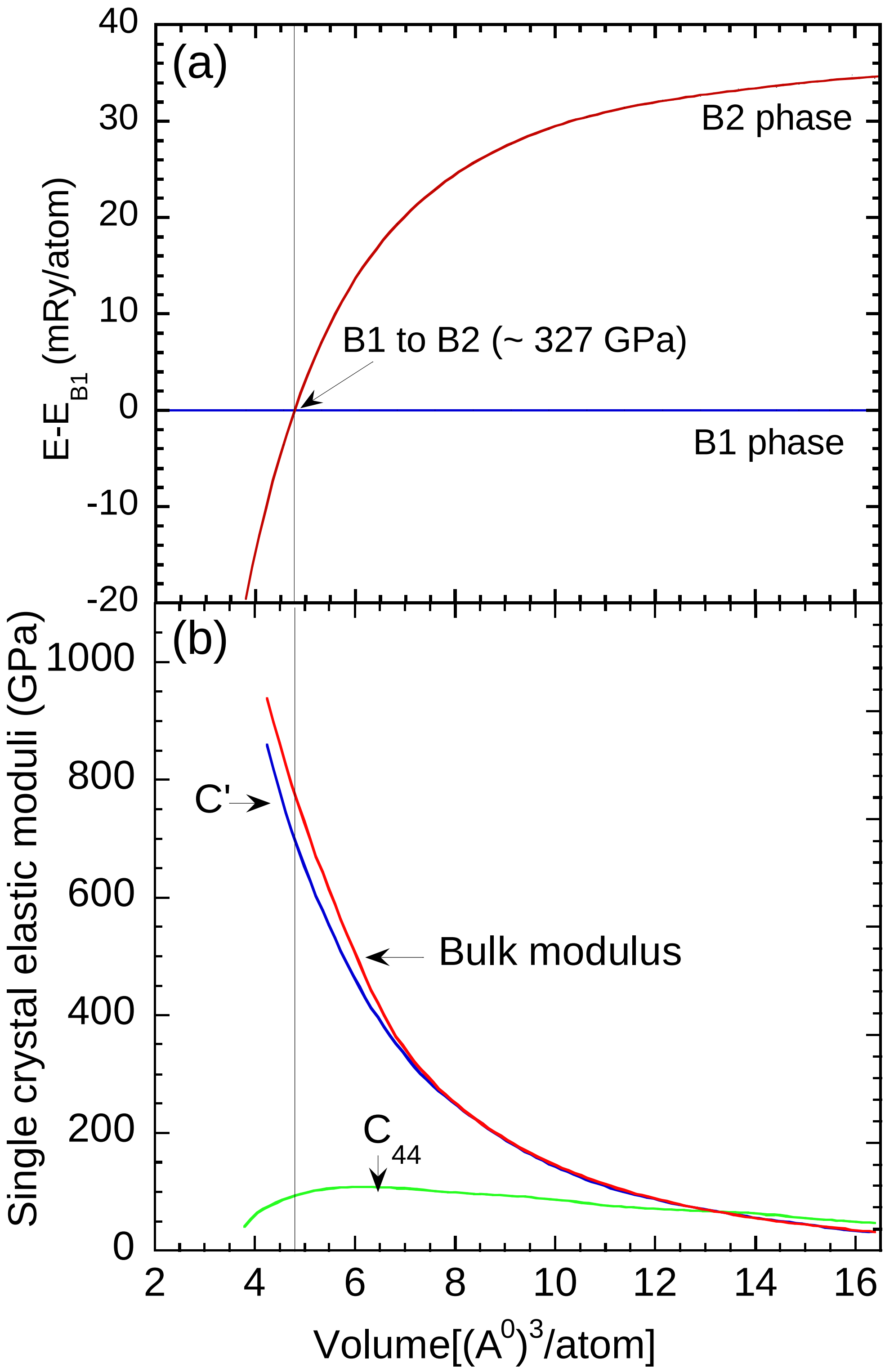

Figure 2.5: (a) Total energy of B2 phase with respect to B1 phase. This energy-volume plot indicates the transition corresponding to volume of 4.8 Å^3/formula unit (~ 327 GPa of pressure). (b) Single crystal elastic constants as a function of volume of LiH.

compared to the 1.603 (at 4.2 K of temperature) determined from the adiabatic elastic constants measured experimentally. As pointed out by James and Kheyrandish [21], this is the largest among the alkali halides in the NaCl structure. Its value becomes near to that of the heavier alkali halides only at higher pressures.

Table 2.2. Theoretically calculated single crystal elastic constants of B1 phase of LiH at various unit cell volume and corresponding hydrostatic pressures.

Volume ($Å^3$/atom)	Pressure (GPa)	C11 (GPa)	C12(GPa)	C44(GPa)
15.94	0.39	79.9	13.4	49.1
14.87	3.17	107.2	14.2	55.7
14.42	4.67	118.2	16.0	61.4
13.66	7.67	139.3	19.7	65.1
12.90	11.43	166.1	23.4	67.2
12.14	16.12	197.0	28.8	70.4
11.38	22.05	233.9	35.9	73.9
10.62	29.66	281.9	43.7	80.3
9.87	39.64	346.8	50.7	88.5
9.11	52.94	421.8	63.3	93.4
8.35	70.87	528.7	73.7	97.0
7.59	95.14	643.0	98.9	101.4
6.83	127.93	813.7	120.7	107.7
5.97	196.10	1125.8	203.6	109.1
5.16	281.25	1485.1	269.9	104.9
4.85	323.75	1662.4	306.2	99.2

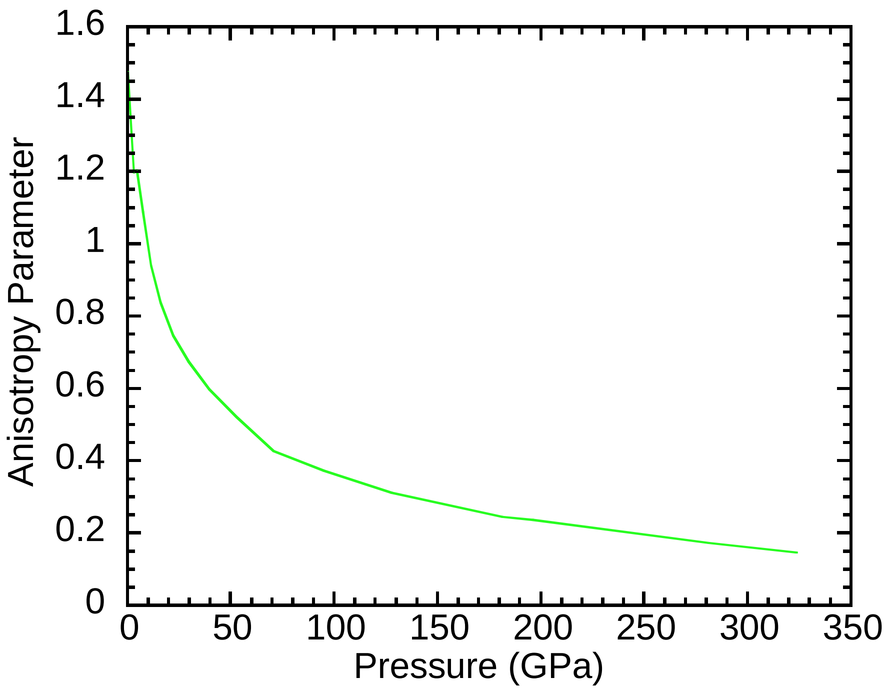

Figure 2.6: Elastic anisotropy parameter (*A*) of LiH as a function of pressure. '*A*' starts from 1.48 at zero pressure and decreases monotonically with pressure.

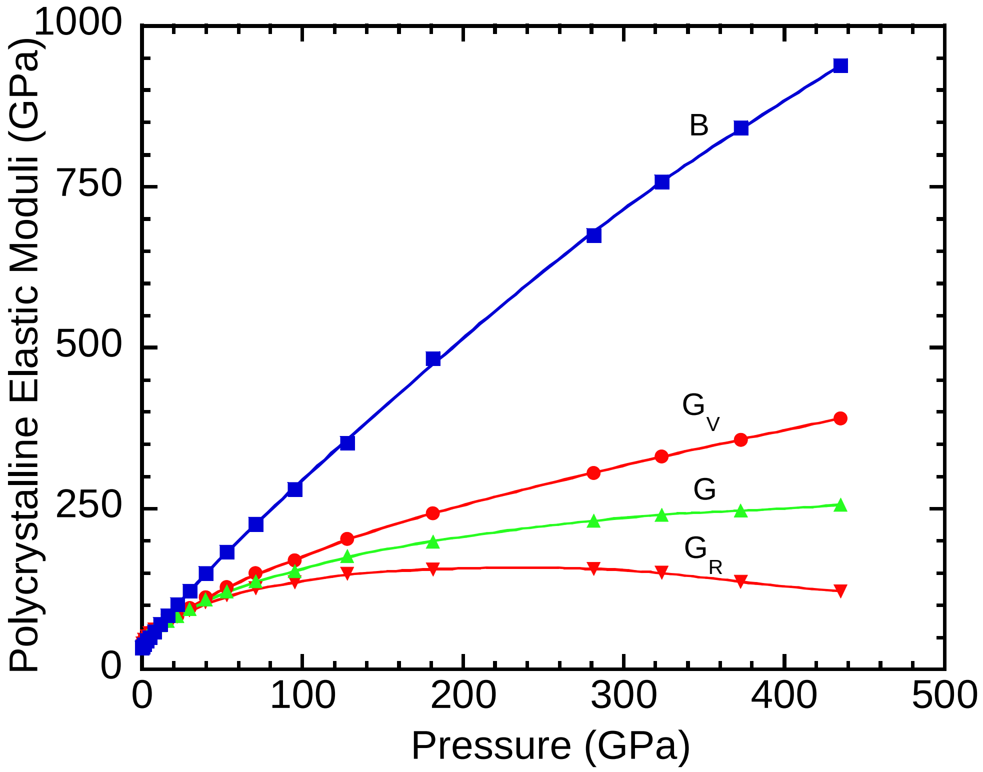

Figure 2.7: Polycrystalline shear elastic modulus (*G*) and bulk modulus (*B*) as a function of pressure.

Fig. 2.7 shows the polycrystalline elastic moduli in the Voigt (G_v) and Reuss (G_R) approximation as a function of pressure. In Voigt approximation, the elastic stiffness constants over all lattice orientations of polycrystalline material are averaged using the assumption that the strain is uniform throughout a grain. Whereas, in Reuss approximation the elastic compliances are averaged assuming the stress uniformity throughout a grain. As is plotted in the figure, G_V and G_R determine the upper and lower bounds of the shear modulus. The Voigt-Reuss-Hill approximated value of shear modulus G which is the average of the G_R and G_V is also shown in the figure. The zero pressure shear modulus and the Poisson ratio of polycrystalline LiH is determined to be 41.7 GPa and 0.14, respectively. Like C_{44}, initially, the G_R also increases with increasing pressure and reaches to a maximum value of ~ 158.3 GPa at 238.89 GPa, it decreases monotonically thereafter upon further increase of pressure.

In the figure 2.8, the Cauchy's pressure $C_{12} - C_{44}$ and the G/B ratio has been plotted as a function of pressure. As is evident from the figure, for the pressure below ~ 100 GPa, the Cauchy's pressure has negative value and also, the G/B ratio is greater than 0.5 which suggest that LiH may display the brittle nature up to this pressure. According to these phenomenological relations, above this pressure, the LiH may behave as a ductile material.

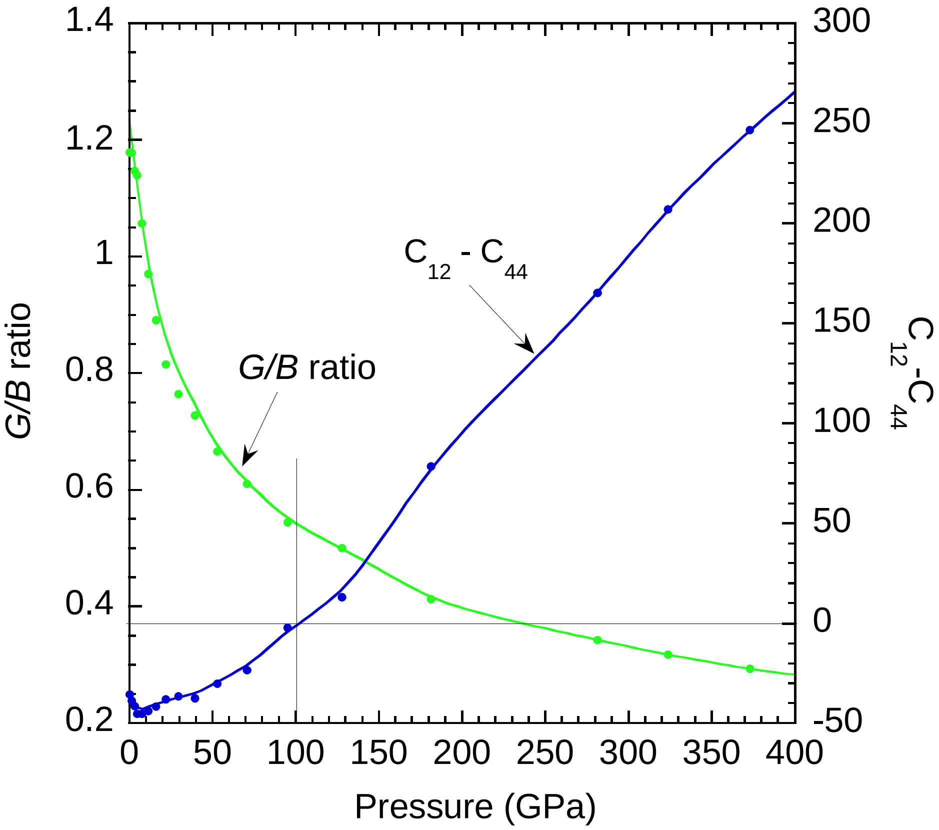

Figure 2.8: Cauchy's pressure and the Pugh's relation *G/B* as a function of pressure.

2.3.3 The electronic band structure and density of states

The electronic density of states (DOS) as well as band structure for B1 and B2 phases of LiH has also been calculated at ambient pressure (Fig. 2.8a and 2.8b) and at the transition pressure (Fig. 2.9a and 2.9b). It is evident from both the DOS and band structure plot that there exists a band gap in the B1 phase at ambient pressure implying that it is insulator at normal pressure in agreement with experiments [44]. At the transition pressure, though the band gap for B1 phase almost vanishes, the DOS at Fermi energy is still almost zero, indicating that the B1 phase is still non-conducting. However, the situation for B2 phase is different and the DOS at the Fermi energy around the transition pressure is non-zero, implying that the LiH becomes metallic in nature at the transition pressure which is consistent with the earlier theoretical findings [3].

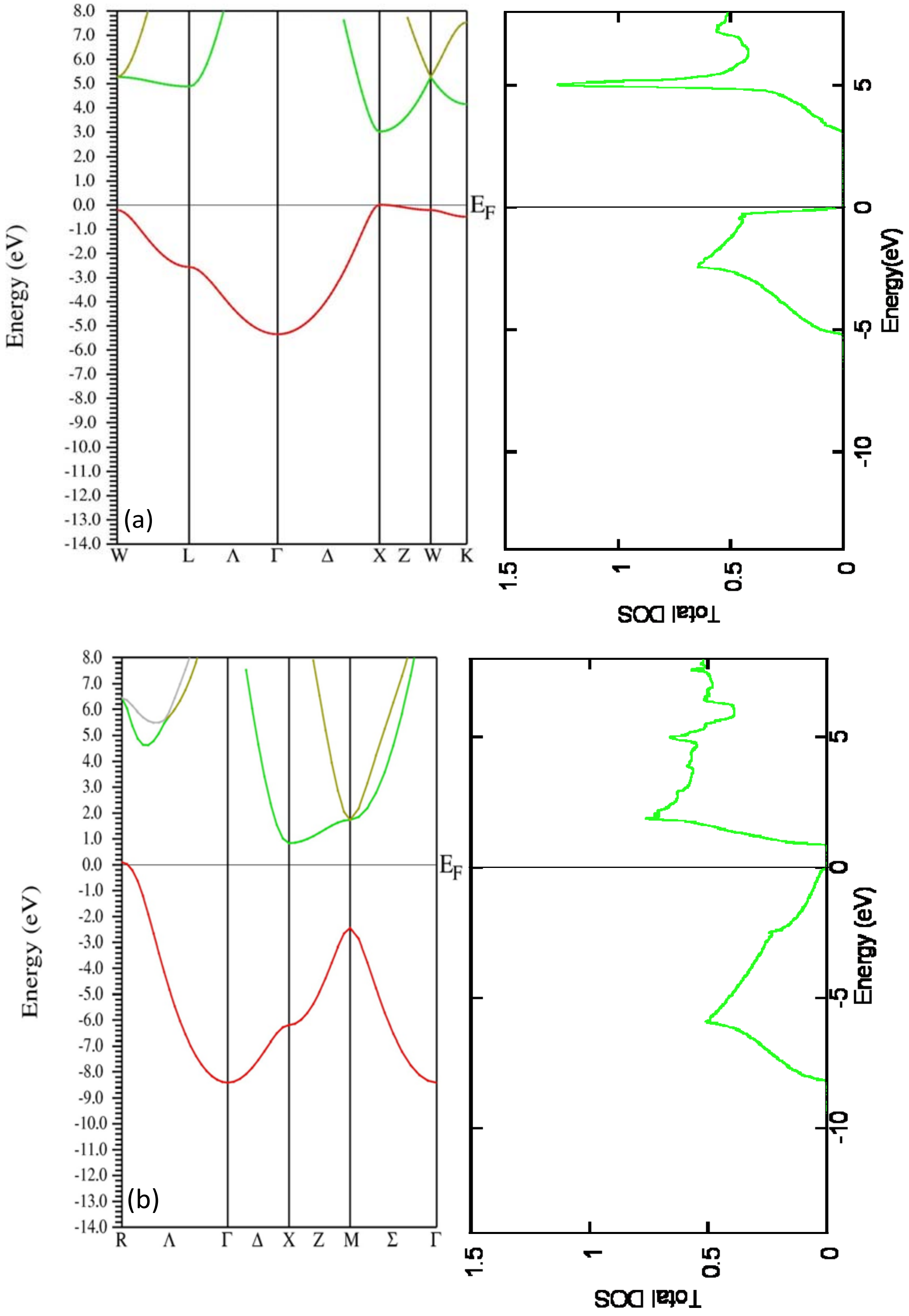

Figure 2.8: Band structure and total density of states of (a)B1 phase of LiH at ambient pressure and (b) B2 phase of LiH at ambient pressure.

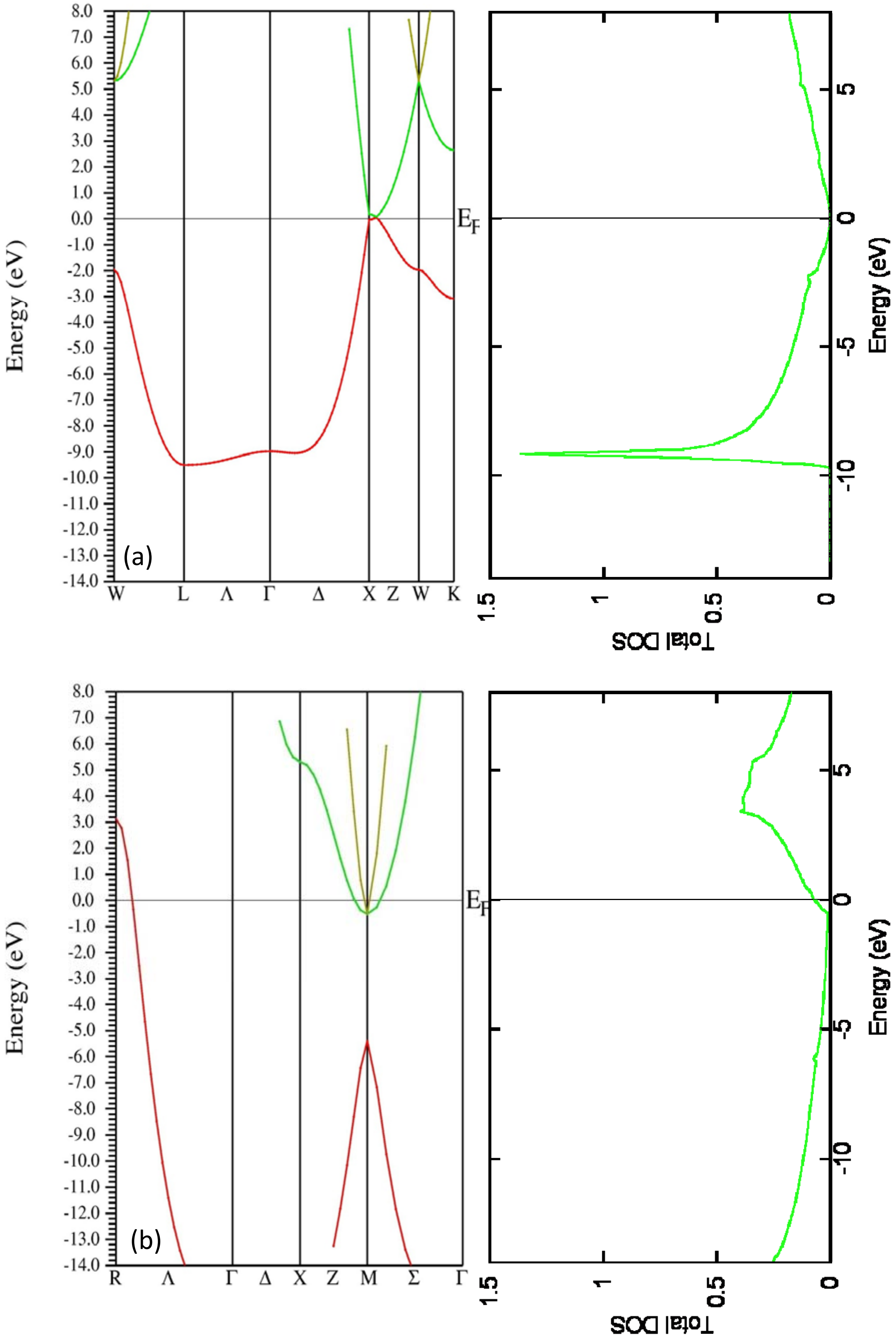

Figure 2.9: Band structure and total density of states of (a) B1 phase of LiH at the B1→B2 transition pressure and (b) B2 phase of LiH at transition pressure.

2.3.4 Lattice dynamics of LiH

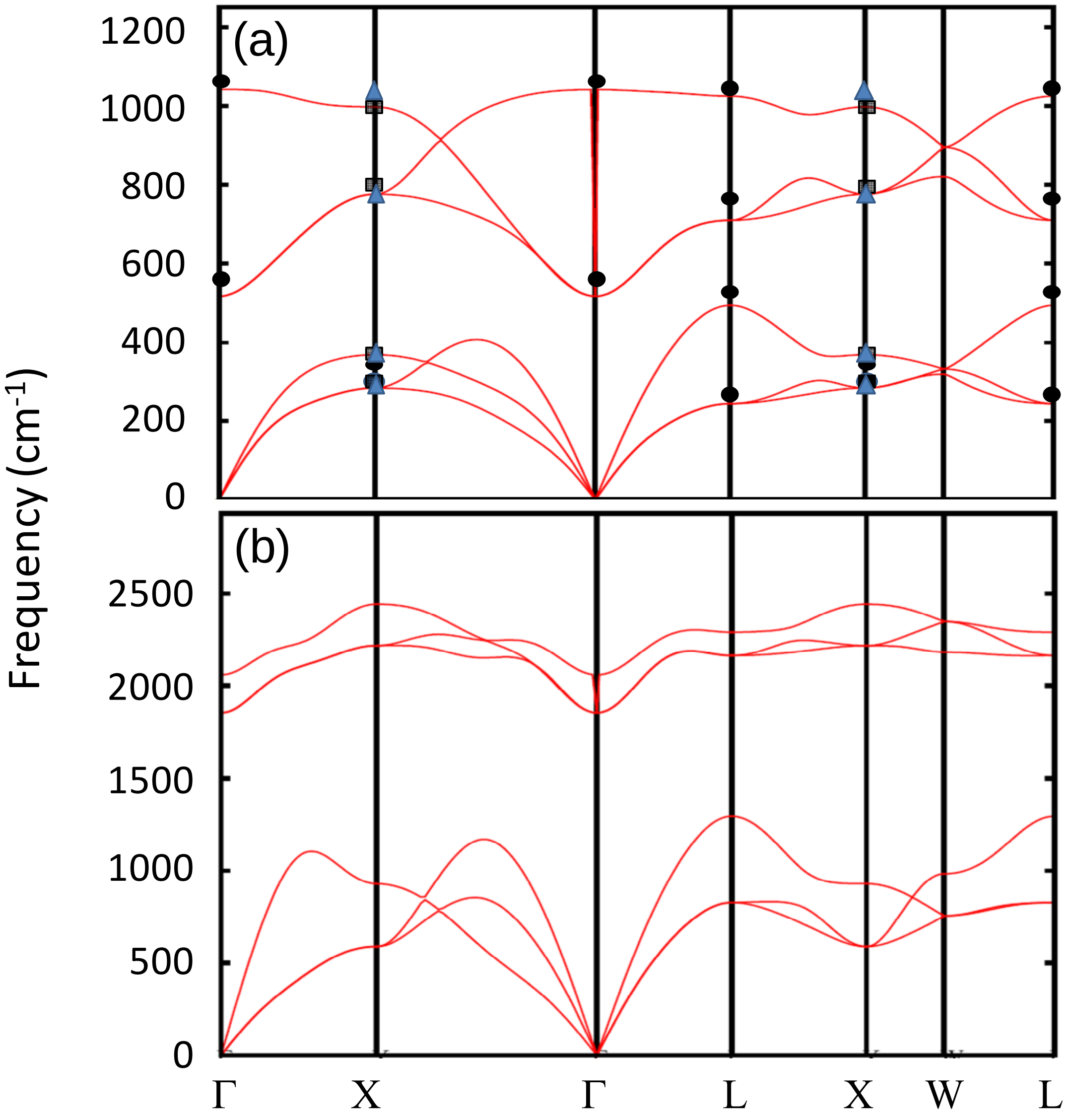

Figure 2.10: (a) Phonon spectra of LiH in the B1 phase at ambient pressure. Symbol ■ corresponds to experimental data of Lazicki *et al.* [1], ● displays data of ref. [45-46] and Δ corresponds to data of Anderson *et al.*[49]. (b) Phonon spectra of LiH in the B1 phase at 300 GPa.

The phonon spectrum of a solid is useful to get insight into lattice dynamical stability of the material which in turn is related to structural stability of the material. Additionally, it is useful for evaluating various thermodynamic quantities such as specific heat, thermal expansion coefficients etc. Due to the low atomic mass of hydrogen the phonon frequencies in the alkali hydrides are high and the contribution of the ionic zero-point motion to the enthalpy of the crystal is not negligible. Roma *et al.* [45] using density functional perturbation theory implemented in plane-wave pseudopotential method with the inclusion of non-linear core correction for the exchange-correlation potential calculated the phonon dispersion relation in LiH. They found that this self-consistent linear response calculation of lattice dynamics successfully reproduced the experimental data.

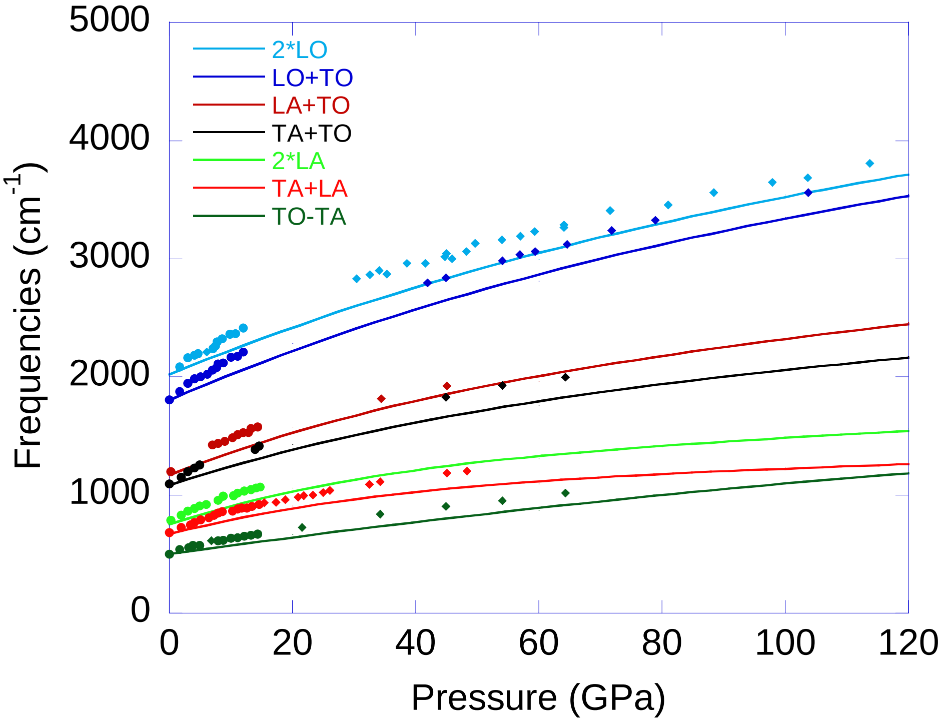

Figure 2.11: Combination of different acoustic and optical phonon frequencies at X-point compared with the experimental data of Lazicki *et al.* [1] and Ho *et al.* [24]. The circular dots correspond to Ho *et al.* [24] data points and the diamond dots are of Lazicki *et al.* [1].

In the present calculations, the phonon spectra of LiH have been calculated in the B1 phase at various pressures. The phonon spectra calculated at zero pressure has been compared with the available experimental data at the Γ, X and L points of the Brillouin zone [1, 45-46, 49] (Fig. 2.10a). The theoretically determined optical as well as acoustic phonon frequencies at these points show reasonably good agreement with the experimental data [1, 45-46, 49]. In Fig. 2.10b, the phonon spectra at 300 GPa for the B1 phase of LiH is also shown. At zero pressure, the gap between longitudinal acoustic (LA) and transverse optical (TO) phonon branches is significantly small (~ 40 cm^{-1}) and upon compression this gap widens monotonically with increasing pressure. For example, at 300 GPa (Fig. 2.10b) the gap between LA and TO branch increases to 576 cm^{-1} from zero pressure value of 40 cm^{-1}. Additionally, in Fig. 2.11 the theoretically calculated X-point phonon frequencies (combination of different acoustic and optical phonon modes) of LiH in B1 have been compared with experimental data at various pressures [1, 24]. The maximum deviation of theoretically determined frequencies for TA and LA phonons is found to be within ~ 16% and 11%, respectively, from the experimental data. The same for TO and LO phonons is evaluated to be within ~ 8.7% and 7.0%, respectively. It is worth to mention here that using *ab-initio* linear response calculation Zhang *et al.* [19] have predicted softening of TA(X) mode around ~ 200 GPa of pressure and reported that this could be indicative of a possible B1 → B2 phase transition. However, our calculations do not show softening of any of the phonon branches at X-point up to 300 GPa. Finally, Table 2.3 gives a comparison of the X-point phonon frequencies and the microscopic Grüneisen parameter corresponding to particular LA, TA and LO, TO branches at ambient pressure with the available experimental and theoretical values. As is clear from the Table 2.3, the acoustic phonon frequencies TA(X) and LA(X) of 289 cm^{-1} and 369 cm^{-1} calculated at X point at ambient pressure in the present work agree reasonably (maximum within ~ 7.9 % and ~ 6.5 %, respectively) with experimental values 298-312 cm^{-1} and 393 – 379 cm^{-1}, respectively [1,24,48-49]. Similarly for the zero pressure optical phonon frequencies TO(X) and LO(X) of 776.77 cm^{-1} and 998.46 cm^{-1} calculated at X point in the present work agree within ~ 3.7 % and ~ 5.6 %, respectively with experimental values 777.5-806 cm^{-1} and 1003-1054.5 cm^{-1}, respectively [1,24,48-49].

Table 2.3: The equilibrium X-point phonon frequencies and the corresponding Grüneisen parameters for that particular vibrational mode have been compared with the previous literature.

	LO(X)		TO(X)		LA(X)		TA(X)	
	ω_0(cm^{-1})	γ	ω_0(cm^{-1})	γ	ω_0(cm^{-1})	γ	ω_0(cm^{-1})	γ
Present Calculation	998.46	0.61	776.77	0.91	369.00	1.08	289.00	0.85
Experimental Data								
Lazicki *et al.*[1]	1003	0.75	805	0.93	379	1.6	298	0.78
Ho *et al.*[24]	1015	0.69	806	0.88	393	1.10	299	0.90
Laplaze *et al.*[48]					379		312	
Anderson *et al.*[49]	1054.5		777.5		385		300	
Theoretical Other sources								
Hex *et al.*[50]		1.2		1.15		1.88		0.77
Ho *et al.*[24]	1408	0.7	793	1.01	443	1.36	303	0.65
Anderson *et al.*[49]	937		821		392		286	
Zhang *et al.*[19]	1041		821		404		312	
Yu *et al.*[47]	1039		857		457		349	

2.4 Summary

Ab-initio total energy calculations have been performed on the plausible phases (B1, B2 and B10 structures) of LiH as a function of hydrostatic compression to examine the structural stability. Apart from this, the calculations have been carried out to determine the equation of state and pressure dependent elastic constants and lattice dynamic stability of LiH. Various thermo physical parameters have been determined from theoretical equation of state and elastic constants.

The structural stability analysis suggests that B1 phase of LiH will transform to B2 phase at a compression of ~ 0.29 with corresponding transition pressure of ~ 327 GPa. The 300 K isotherm determined theoretically after adding the lattice thermal energies to the cold energies agrees closely with experimental P-V data. The equation of state derived from calculations within GGA agrees better with experimental data than that obtained from the LDA approximation. Calculated equilibrium lattice parameter, bulk modulus and pressure derivative of bulk modulus at zero pressure derived from theoretical equation of state are in good agreement with the experimental findings. Various physical quantities such as elastic modulus at ambient pressure, the Debye temperature, the Grüneisen parameter, bulk sound speed, the Hugoniot parameter ‘s’ compare well with the available experimental data.

The ambient pressure elastic constants C_{11}, C_{12} and C_{44} of 77 GPa, 12.7 GPa and 48.2 GPa of the B1 phase of LiH determined in the present work are in reasonable agreement with experimental data lying in the range 82.7-69.28 GPa, 10.7-17.14 GPa and 52.5-58.25 GPa, respectively measured in different works [19, 23]. The C_{11} and C_{12} increase monotonically with increasing pressure, whereas, the C_{44} modulus first increases with increasing pressure and reaches to maximum value of ~ 109 GPa at a pressure of~ 196 GPa, it decreases thereafter upon further compression. The elastic anisotropy parameter ($A=2C_{44}/(C_{11}-C_{12})$) at zero pressure is found to be ~ 1.48. Further, this parameter has been found to decrease monotonically with increasing pressure. The single crystal elastic constants as a function of pressure have been further utilized to determine the polycrystalline elastic constants using Voigt-Reuss-Hill approximation. Further, the Cauthy's pressure and Pugh's relationship between elastic moduli has been calculated as a function of pressure and an attempt has been made to understand the ductile or brittle nature of LiH as a function of pressure. Based on this analysis LiH will behave as a brittle material below 100 GPa and above this pressure it is expected to exhibit the ductile nature.

The DOS and band structure plots LiH suggest that at ambient pressure LiH will be insulating, whereas above the transition pressure it will be metallic in B2 phase. The phonon spectra of this material at zero pressure determined from lattice dynamics calculations display good agreement (the maximum deviation being ~ 16 % of the present theoretical finding for TA branch) with the available experimental data. The X-point phonon frequencies of different optical and acoustic branches of LiH has been calculated as a function of pressure and the maximum deviation of the calculated phonon frequencies has been found to be ~ 16 %, 11 %, 8.7 %, and 7.0 % for TA, LA, TO, and LO respectively with the experimental data of Lazicki *et al.* [1] and Ho *et al.* [24].

References

1. A. Lazicki, P. Loubeyre, F. Occelli, R. J. Hemley, and M. Mezouar, *Phys. Rev.B.* **85**, 054103-1 (2012).
2. R. Ahuja, O. Eriksson, B. Johansson, *Physica B* **265**, 87 (1999).
3. Y. Wang, R. Ahuja, and B. Johansson, *Phys. stat. sol.(b)* **235**, 470 (2003).
4. S. Lebegue, M. Alouani, B. Arnaud, W. E. Pickett, *Europhysics Lett.* **63**, 562 (2003).
5. L. Guangwei, D. Wang, J. Qinghuai and D. Ding, *Phys. Lett. A* **143**, 473 (1990).
6. G. D. Barrera, D. Colognesi, P. C. H. Mitchell, A. J. Ramirez-Cuesta, *Chem. Phys.* **317**, 119 (2005).
7. Y. Bouhadda, A. Rabehi and S. Bezzari-Tahar-Chaouche, *Revue des Energies Renouvelables* **10**, 245 (2007).
8. J. Y. Zhang, L. J. Zhang, T. Cui, Y. L. Niu, Y. M. Ma, Z. He and G. T. Zou, *J. Phys.: Cond. Matter* **19**, 425218 (2007).
9. J. Hama, K. Suito and N. Kawakami, *Phys. Rev. B* **39**, 3351 (1989).
10. J. Zhang, Y. Zhao, Y. Wang, and L. Daemen, *J. Appl. Phys.* **103**, 093513 (2008).
11. P. Loubeyre, R. L. Toullec, M. Hanfland, L. Ulivi, F. Datchi and D. Hausermann, *Phys. Rev B* **57**, 10403 (1998).
12. G. Vidal-Valat and J. P. Vidal, *Acta Crystallog. Sect. A: Found. Crystallogr.* **48**, 46 (1992).
13. C. O. Rodriguez and K. Kunc, *J. Phys.: Cond. Matter* **1**, 1601 (1989).
14. H. F. Zhang, Y. Yu, Y. N. Zhao, W. H. Xue, T. Gao, *J. Phys And Chem. Solids* **71**, 976 (2010).
15. J. I. Verble, J. L. Warren, J. L. Yarnel, *Phys. Rev.* **168**, 980 (1968).
16. T. Ogitsu, E. Schwegler, F. Gygi, and G. Galli, *Phys. Rev. Lett.* **91**, 1755021 (2003).
17. J. L. Martins, *Phys. Rev. B* **41**, 7883(1990).
18. Q. Gou, X. Wang and J. Meng, *High Press. Res.* **6**, 141 (1991).
19. J. Zhang, L. Zhang, T. Cui, Y. Li, Z. He, Y. Ma and G. Zou, *Phys. Rev. B* **75**, 1041151 (2007).
20. E. Zurek, R. Hoffmann, N. W. Ascroft, A. R. Oganov and A. O. Lyakhov, *PNAS* **106**, 17640 (2009).
21. B. W. James and H. Kheyrandish, *J. Phys. C: Solid State Phys.* **15**, 6321 (1982).

22. D. Gerlich and C. S. Smith, *J. Phys.: Chem. Solids* **35**, 1587 (1974).
23. W. F. Perger, J. Criswell, B. Civalleri, R. Dovesi, *Comp. Phys. Comm.* **180**, 1753 (2009).
24. A. C. Ho, R. C. Hanson, and A. Chizmeshya, *Phys. Rev. B* **55**, 14818 (1997).
25. P. Blaha, K. Schwarz and J. Luitz, WIEN2K (Technical University of Vienna).
26. J. P. Perdew, S. Burke and M. Ernzerhof, *Phys. Rev. Lett.* **77**, 3865 (1996).
27. www.cryst.ehu.es/cgi-bin/cryst/programs/nph-wp-list
28. B. K. Godwal and R. Jeanloz, *Phys. Rev. B* **40**, 7501 (1989).
29. S. C. Gupta, K. D. Joshi, S. Banerjee, *Metall. Materials Trans. A* **39**, 1593 (2008).
30. G. Valentin, *ArXiv: Cond-Matt/*99114072-v2 [Cond-mat.mtrl-sci], 1999.
31. C. Kittel, *Introduction to Solid State Physics* (John Wiley & Sons, NewYork 1996).
32. W. Voigt, *Lehrbuch der Kristallphysik* (Taubner, Leipzig, 1928).
33. A. Reuss, Z. Angew. *Math. Mech.* **9**, 49 (1929).
34. J. F. Nye, *Physical Properties of Crystals*, Oxford University Press, London (1957).
35. R. E. Cohen, L. Sixtrude and E. Wasserman, *Phys. Rev B* **56**, 8575 (1997).
36. G.Grimvall, Thermophysical Properties of Materials, *1st Edition. Elsevier*, (1999)
37. D. Pettifor, Theoretical predictions of structure and related properties of intermetallics, *Mater. Sci. Tech.* **8** (1992) 345.
38. S. F. Pugh, Relations between the elastic moduli and the plastic properties of polycrystalline pure metals, *Philos. Mag.* **45** (1954) 823.
39. S. Baroni et al.,Quantum ESPRESSO package, 2005, www.pwscf.org/
40. S. P. Marsh, LASL Report, "*Hugoniot Equation of State of* Li^6H*,* Li^6D*,* Li^nH*,* Li^nD" (1974).
41. R. Vacher, M. Biossier and D. Laplaze, *Soild State Comm.* **37**, 533 (1981).
42. K. Kunc and K. Syassen, *Phys. Rev. B* **81**, 1341021 (2010).
43. J. S. Dugdale and D. K. MacDonald, *Phys. Rev.* **85**, 832 (1953).
44. Y Kondo and K Asaumi, *J. Phys. Soc. Jpn.* **57**, 367 (1988).
45. G. Roma, C. M. Bertoni, and S. Baroni, *Solid State Comm.* **98**, 203 (1996).
46. M. G. Zemlianov, E. G. Brovman, N. A. Chernoplekov, I. L. Shitikov, In Inelastic Scattering of Neutrons, IAEA, Vienna, p. 431(1965).
47. W. Yu, C. Jin and A. Kohlmeyer, *J. Phys.: Cond. Matt.* **19,** 086209(2007).

48. D. Laplaze, *J. Phys. (Paris)* **37**, 1051 (1976).

49. A. Anderson and F. Lüty, *Phys. Rev. B* **28**, 3415 (1983).

50. H. Jex, *J. Phys. Chem. Solids* **35**, 1221 (1974).

Chapter - 3

Ab-initio Study of Equation of State and ideal compressive and tensile strength of MgO

3.1 Introduction

Magnesium oxide or magnesia (periclase) having NaCl-type structure (B1 phase) at ambient conditions, is one of the major constituent of the earth-forming materials. Also, it is used as a basic end-member of refractory ceramics material for its physical and chemical stability under high pressure and high temperature. Apart from its geophysical importance, the structural stability under very high pressure makes it a suitable candidate for the pressure standard in the diamond anvil cell (DAC) experiments. Also, in the shock compression experiments, MgO can be used as a window material due to its optical transparency up to shock pressure of ~ 23 GPa and high shock impedance (more than that of LiF). For all these applications, it is important to understand the structural and elastic stability, equation of state (EOS) of this material under high pressure. In addition to these investigations, the determination of ideal tensile and compressive strength of this material under various loading conditions will also be of practical interest.

As far as behavior of MgO under hydrostatic compression is concerned, a large body of literature exists on structural stability analysis, determination of equation of state and lattice dynamical and elastic stability [1-9]. In a high pressure x-ray diffraction experiment using DAC, Duffy *et al.* [1] have demonstrated that the B1 phase remains stable up to ~ 227 GPa, the maximum pressure achieved in their experiment. Speziale *et al.* [2], from energy dispersive x-ray diffraction measurements carried out in diamond anvil cell experiments up to 52 GPa at room temperature, have determined the pressure-volume EOS of MgO at room temperature. Further, using the measured room temperature isotherm in conjunction with the third order Birch-Murnaghan EOS and Debye model for thermal pressure contribution, the authors have developed a model that satisfactorily describes the experimental data from room pressure and room temperature to 203 GPa and 3663K. Garcia *et al.* [3] also have determined high pressure–high temperature isotherms of MgO up to 1273 K and 6 GPa by compressing this material in tungsten carbide anvils. In recent past, Jacobsen *et al.* [4] have measured the EOS of MgO single crystal up to ~ 118 GPa under quasi hydrostatic environment using helium as pressure transmitting medium, and up to ~ 87 GPa in non-hydrostatic conditions using KCl powder as pressure transmitting medium in DAC experiments. In addition to the measurements of equation of state, the studies on the effect of pressure on compressive strength and grain size [5], and behavior of elastic constants as a function of temperature from 4.2 K to 1300 K [6, 7] at room pressure have also been reported in past. The pressure and temperature dependence of elastic constants upto ~ 8 GPa and 1600 K has been studied by Chen *et al.* [8] using ultrasonic interferometric technique. Ghose *et al.* [9] using inelastic x-ray scattering have measured the phonon dispersion relation for both the optical and acoustic branches along Γ-X direction as a function of pressure up to ~ 35 GPa.

Apart from these static high pressure experimental studies, MgO has been investigated under shock compression also. The shock compression experiments on this material mainly include generation of P-V data along Hugoniot and in-situ measurement of shock temperature [10-17]. Duffy and Ahrens [10] have measured the Hugoniot of the polycrystalline MgO, in the pressure range of 14 to 233 GPa using propellant and light gas gun facility. Fat'yanov *et al.* [15] carried out shock wave experiments on MgO using two stage light gas gun and used optical pyrometry to measure shock temperature in the pressure range of 102 to 203 GPa. Based on their measurements, these authors suggested that that MgO does not undergo melting transition up to the highest pressure of ~ 203 GPa with corresponding temperature of ~ 6.53×10^3 K. Using two-stage light gas gun facility Zhang *et al.* [16] carried out two experiments, one at ~ 114 GPa and other at ~

192 GPa. They have plotted their data along with those available from Duffy *et al.* [10], Marsh [14], and Vassiliou *et al.* [17] in both the pressure-volume as well as in the U_s (shock velocity) - U_p (particle velocity) plane. On the basis of the U_s-U_p plot these authors have reported a volume discontinuity by ~1.9 % (increase in volume) at the shock pressure of ~ 170 GPa. This volume discontinuity has been associated with the transition of B1 phase to another solid high pressure phase [16]. Very recently, laser shock compression experiments have been carried out up to 1400 GPa [18]. According to this new study, MgO under shock compression, transforms from B1 phase to B2 structure (CsCl type structure) above 360 GPa [18].

In theoretical front also, MgO has attracted the attention of many high pressure researchers [19-26]. For instance, Cohen and Gordon [19] using modified electron gas theory predicted a B1 to B2 phase transformation at ~ 256 GPa or 372 GPa, depending upon the two different kinds of the wavefunctions chosen for the oxygen ion. Subsequent to this work, Chang and Cohen [20] on the basis of the *ab* initio pseudopotential calculations within local density approximation (LDA) have predicted the B1 to B2 structural phase transition at ~ 1050 GPa. However, in another pseudopotential calculation, the same transition has been put ~ 451 GPa by Karki *et al.* [23]. Further, using density functional theory (DFT) within both LDA and generalized gradient approximation (GGA) Jaffe *et al.* [24] predicted this transition to occur at ~ 515 GPa. In yet another all electron total energy calculations Mehl *et al.* [25] placed this transition at ~ 510 GPa, close to ~ 509 GPa and 489 GPa that predicted by Oganov and Dorogokupets [26] later using PAW and ECP potentials, respectively, implemented in the more accurate modern code VASP.

Apart from structural stability aspects, theoretical studies to examine the lattice dynamic and elastic stability of MgO under pressure have also come into existence in past [26-28]. For example, Karki *et al.* [27] have performed a detailed calculation of elastic constants of B1 and B2 phases of MgO as a function of pressure. Their calculations correctly show that at ambient conditions, the B1 phase is elastically stable whereas the B2 phase is unstable. Further these authors have suggested that the shear instability might not be solely responsible for possible B1 to B2 phase transformation in MgO. This is because the shear modulus C_{44} though starts decreasing with pressure beyond 350 GPa, it still remains non zero even at predicted B1 to B2 transition pressure of 451 GPa and vanishes at ~ 1400 GPa, much beyond the transition pressure. In another study employing density functional perturbation theory (DFPT), Karki *et al.* [28] have determined the temperature variation of elastic constants of B1 phase and also calculated the phonon dispersion relation for B1 phase at ambient as well as at high pressures. The monotonous reduction in theoretical elastic constants with increasing temperature has been reported to display fair agreement with experimental measurements of Isaak *et al.* [29]. Based on the phonon dispersion relations calculated as a function of pressure, the authors have predicted the dynamic stability of B1 phase up to 150 GPa (the maximum pressure up to which the study has been carried out). The pressure variation of elastic constants of B1 phase has been studied by Oganov and Dorogokupets [26] also, using calculations based on VASP code. In addition to these studies, the pressure dependence of elastic constants have also been investigated by Gueddim *et al.* [30] using FP-LAPW method, and Lu *et al.*[31] using pseudopotential method. Further, through molecular dynamic simulations, the pressure–temperature phase diagram and pressure effect on melting temperature of MgO has also been determined by various researchers [32-34]. The onset of melting of MgO along Hugoniot predicted has been predicted to be ~ 430 GPa with corresponding temperature of ~ 11000 K from the molecular dynamic simulations [32]. This theoretical shock pressure for onset of melting of MgO is lower by ~28% as compared to the experimental value of ~ 600 GPa, reported recently by laser shock experiments [17].

In spite of so much of research work done on high pressure-high temperature behavior of MgO, the strength properties of MgO under uniaxial compression or expansion is, to our knowledge, yet to be explored. The uniaxial compression or expansion can be achieved under two different loading configurations namely uniaxial strain condition and uniaxial stress condition. The uniaxial strain condition is encountered in shock experiments where materials are subjected to high strain rates (~10^4/s to 10^9/s), whereas the uniaxial stress condition exists in quasi static loading of materials where the material gets sufficient time for the lateral dimension to relax. With the advancements in the shock wave experimental techniques and development of new sophisticated diagnostic techniques it has been possible to realize the ideal failure strength for tension under uniaxial strain condition at strain rates as high as 10^9/s, on many materials such as Mo, Al and Cu [35, 36]. Apart from experiments, the *ab-initio* studies pertaining to determination of ideal strength under pure uniaxial stress condition as well as under uniaxial stress combined with biaxial compression/tension have also been reported in the past [37-40]. The ideal failure strength under quasi-static loading conditions derived from such studies play an important role in providing correct description of the hardness of a material as the material deformations during hardness measurements occur at finite strains where the knowledge of elastic moduli at the equilibrium structure only is not sufficient to give stringent evaluation of hardness [41]. The MgO being a geophysically important material, the knowledge of its ideal strength for compression and expansion under uniaxial strain condition will serve as one of the useful inputs required for analysis of structural response of this material subjected to high strain rate loading conditions occurring during the propagation of seismic waves through geological media and the fracture and fragmentation at high velocity impact. Similarly, the knowledge of ideal strength of MgO single crystal under uniaxial stress condition will be an important input for more stringent evaluation of the hardness of this material.

The main purpose of this chapter is to present the results on theoretical determination of the ideal failure strength of MgO single crystal subjected to uniaxial compression and expansion along [001] crystallographic direction. For this purpose, the elastic moduli of MgO single crystal subjected to uniaxial compression and expansion along [001] crystallographic direction under two different deformation conditions namely “uniaxial strain condition” and “uniaxial stress condition” have been determined and elastic stability conditions have been tested at various compressive and tensile strains. The examination of elastic stability along the entire deformation path for the above mentioned deformation conditions yielded ideal failure strengths of the MgO single crystal for [001] compressive and tensile loading under these two conditions. Before proceeding for these calculations, we have determined the isotherm, isentrope and Hugoniot of MgO; and compared these with the experimental data which provided the proof of the reliability of the present calculations.

3.2 Methodology Employed for Present Calculations

The full potential linearised augmented plane wave (FP-LAPW) [42] method within the generalized gradient approximations [43] has been utilized to carry out the detailed calculations. These total energy calculations are performed in the B1, B2 and B10 (The detailed description of B10 structure and its relationship with the B2 phase has already been discussed in chapter 2) structure of the MgO to analyze its structural stability under hydrostatic compression. The total energy calculations required for structural stability analysis of B10 and B2 phases have been performed on the tetragonal cell and at each volume the *c/a* ratio and internal parameter ‘z’ are optimized. Finally, to examine the structural stability under pressure, the total energy of the tetragonal cell at various volumes for optimized *c/a* ratio and internal parameter ‘z’ is compared with that of the B1 phase. Further, the total energy at 0 K is used to generate pressure-volume relation for each phase and which finally is utilized to determine the enthalpies of these phases at various pressures. It has been found that the B1 phase remains stable up to ~ 535 GPa. The total energy calculations required for determination of equation of state and elastic moduli of B1 phase under hydrostatic compression has been carried out using the NaCl type fcc cell. However, to examine elastic stability of B1 structure under uniaxial compression and expansion along [001] direction, it is represented as a bct cell with $c/a = \sqrt{2}$ (Fig. 3.1) and the strains are applied along c-axis of this cell. For all the calculations, a grid of 7000 k points is used for sampling of full Brillouin zone. The plane wave cutoff parameter $R_{MT} K_{MAX}$ is fixed at 7 with muffin tin radius R_{MT} chosen to be 1.4 a.u. for Mg and 1.3 a.u. for O. The variation in R_{MT} around these values does not affect the results.

The self consistent cycle was run until the energy convergence criterion of 0.01 mRy was met.

3.2.1 Determination of Isotherm at 300 K, Isentrope and Hugoniot

As a first step of our theoretical study, we performed total energy calculations on B1 phase as a function of hydrostatic compression and determined its 0 K isotherm, which after adding thermal corrections as described in chapter 2, is converted to 300 K isotherm. The 0 K isotherm is further utilized to generate isentrope and Hugoniot of MgO in B1 phase using the procedure described below:

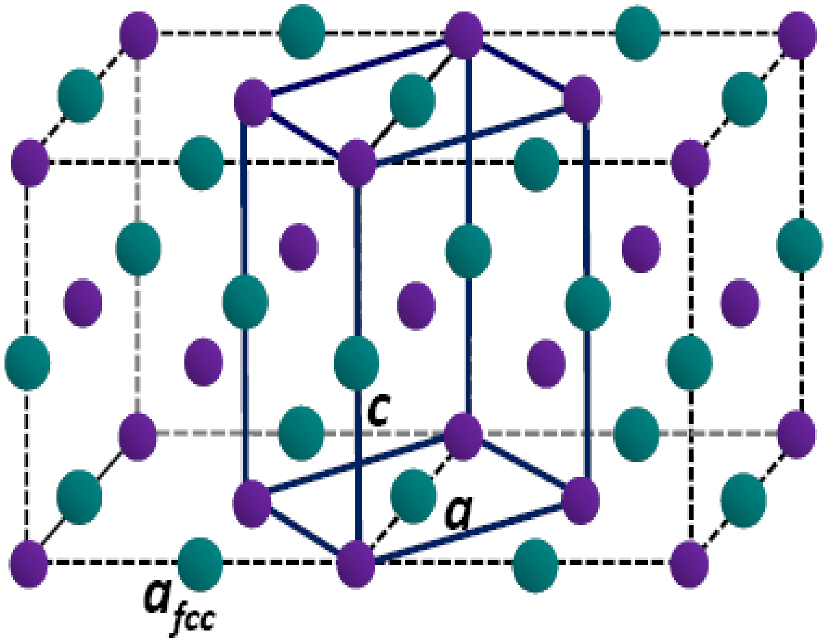

Figure 3.1: The representation of fcc cell (B1) of MgO as bct cell (cell bounded by dark solid lines). The small spheres (purple coloured) and big spheres (green coloured) show the oxygen and magnesium atoms, respectively.

To determine the isentrope, we have first calculated temperature rise along the isentropic compression. For this purpose**,** the entropy *S(T,V)* is expressed by the following thermodynamic relation:

$$TdS = T\left(\frac{\partial S}{\partial T}\right)_V dT + T\left(\frac{\partial S}{\partial V}\right)_T dV \tag{3.1}$$

which upon using Maxwell relations reduces to

$$TdS = C_V dT + T\left(\frac{\partial P}{\partial T}\right)_V dV \tag{3.2}$$

Where, C_V is specific heat at constant volume. Eqn. (3.2) under isentropic condition *i.e.* for $dS = 0$, further reduces to

$$\frac{dT}{T} = -\frac{\gamma(V)}{V} dV \tag{3.3}$$

with $\frac{1}{C_V}\left(\frac{\partial P}{\partial T}\right)_V = \left(\frac{\partial P}{\partial E}\right)_V = \frac{\gamma(V)}{V}$**,** $\gamma(V)$ being the Gruneisen parameter for the material under consideration. The Eqn. (3.3) upon integration yields following expression for temperature rise along isentrope:

$$\ln\left(\frac{T_S}{T_0}\right) = -\int_{V_0}^{V}\left[\frac{\gamma(V)}{V} dV\right] \tag{3.4}$$

Where $\gamma(V)$ is calculated at various volumes using Eqn. (2.6) and a polynomial fit of this in volume is obtained. The T_S calculated from Eqn. (3.4) is then substituted in Eqn. (2.5) to evaluate the pressure along isentrope.

The shock Hugoniot is determined using Eqn. (2.3) and (2.5) in conjunction with the Rankine–Hugoniot relation (the energy conservation equation for a shock-wave travelling through a material) [44-45]:

$$E(V,T_H)-E(V_0,T_0)=\frac{1}{2}\left[P(V,T_H)+P(V_{0,}T_0)\right]\left[V_0-V\right] \tag{3.5}$$

Here T_H is the temperature rise along shock Hugoniot and T_0 is the room temperature.
At high temperatures generated during shock compression the ratio $\theta_D/T << 1$, the expression for E_{lT} reduces as

$$E_{lT}=3k_BT \tag{3.6}$$

As temperatures generated during shock compressions are high so contribution of electronic excitations also becomes significant. The electronic contributions to energy and pressure are evaluated from β and γ_e determined theoretically using following expressions [46-47]:

$$\beta=\pi^2k_B^2N(E_f)/3 \tag{3.7}$$

Where $N(E_f)$ is the density of states at Fermi level, which is determined at various unit cell volume from FP-LAPW calculations, and

$$\gamma_e=\frac{\partial\ln\beta}{\partial\ln V}. \tag{3.8}$$

Finally, using the expression of energy $E(V,T)$ and the corresponding pressure $P(V,T)$ calculated according to Eqn. (2.3) and (2.5), the Hugoniot point for a particular compression is evaluated by finding the temperature (T_H) for which the Rankine –

Hugoniot relation (Eqn. 3.5) is satisfied. Putting the value of T_H in the expression of *P(V,T)* the Hugoniot pressure is calculated.

3.2.2 Ideal failure strength under uniaxial compression and expansion

The determination of isotherm, isentrope and Hugoniot of MgO is followed by calculation of ideal failure strength of MgO single crystal in B1 phase subjected to uniaxial compressive loading as well as tensile loading along [001] crystallographic direction. For this purpose, the undeformed B1 cell (which is fcc) is represented as a bct cell with *c/a* ratio = √2 and strains along c-axis *i.e.* the axis oriented along [001] direction are applied on this cell (Fig. 3.1). Both compression and tension were carried out under two types of deformation configurations namely "uniaxial strain condition" (*i.e.* the condition where $e_i = e \neq 0$ for $i = 3$ and $e_i = 0$ for $i \neq 3$, e_i are the components of strain matrix) and "uniaxial stress condition" (*i.e.* the condition where $\sigma_i = \sigma \neq 0$ for $i = 3$ and $\sigma_i = 0$ for $i \neq 3$, σ_i are the components of stress matrix).

To simulate the [001] compression/expansion under uniaxial strain condition, the compressive/tensile strains (e) are applied along the c axis of the bct cell keeping the lateral dimension fixed. At each [001] strain the total energy is calculated and the stress along [001] direction is evaluated using following expression:

$$\sigma = \frac{2}{a_0^2 c_0} \frac{\partial E}{\partial e} \tag{3.9}$$

With a_0 and c_0 are the lattice parameters normal to and along the loading axis of undeformed bct cell. E is the total energy per formula unit of MgO. A factor of 2 is multiplied as bct cell contains two units of MgO. The ideal failure strength (σ_c), for uniaxial compression/expansion along [001] direction under uniaxial strain condition is defined as the maximum uniaxial stress which the MgO single crystal can withstand prior to mechanical failure. To evaluate this (i) the elastic moduli K_L, $C'=(C_{11}-C_{12})/2$, C_{44} and C_{66} of bct cell have been determined as a function of [001] strain and (ii) the following stability conditions are examined along the entire deformation path:

$$K_L = \frac{2}{a_0^2 c_0}\left(\frac{\partial^2 E}{\partial e^2}\right) > 0\ ;\ C' > 0\ ;\ C_{44} > 0\ ;\ C_{66} > 0 \tag{3.10}$$

The stress corresponding to the minimum strain at which any one of the above mentioned stability criteria gets violated is considered as the ideal failure strength of MgO single crystal subjected to uniaxial compression/expansion along [001] direction under “uniaxial strain condition”. The C', C_{66} and C_{44} at a given [001] strain are determined using following volume conserving distortions as described in ref. [48, 49]

$$\begin{bmatrix} \delta & 0 & 0 \\ 0 & -\delta & 0 \\ 0 & 0 & \dfrac{\delta^2}{(1-\delta^2)} \end{bmatrix} \quad \begin{bmatrix} 0 & \delta & 0 \\ \delta & 0 & 0 \\ 0 & 0 & \dfrac{\delta^2}{1-\delta^2} \end{bmatrix} \quad \begin{bmatrix} \dfrac{\delta^2}{1-\delta^2} & 0 & 0 \\ 0 & 0 & \delta \\ 0 & \delta & 0 \end{bmatrix}$$

As the strains are volume conserving no stress term comes into the energy equations of the strained lattice used to evaluate the shear moduli at a given volume [48-51].

For simulation of the [001] compression/expansion under uniaxial stress condition (i) a strain (e) is applied along the c axis; (ii) and at this fixed strain the total energy is calculated as a function of lateral lattice parameter. The total energy is then plotted as a function of lateral lattice parameter to find the minimum energy and corresponding lateral lattice parameter. A typical example is given in Fig. 3.2 for e = 0.093. The above procedure is repeated for several strains along c- axis. The stress is determined from a polynomial fit of total energy to strain along c-axis using the expression:

$$\sigma = \frac{2}{a^2 c_0}\frac{\partial E}{\partial e} \tag{3.11}$$

Where a is the relaxed lateral parameter. The ideal compressive or tensile strength is determined same way as described for "uniaxial strain condition" except the longitudinal modulus K_L in the stability conditions of Eqn. (3.10) is replaced by the Young's modulus defined as:

$$Y = {}^{2}\!\!\diagup_{a^2 c_0}\left({}^{\partial^2 E}\!\!\diagup_{\partial e^2}\right) \tag{3.12}$$

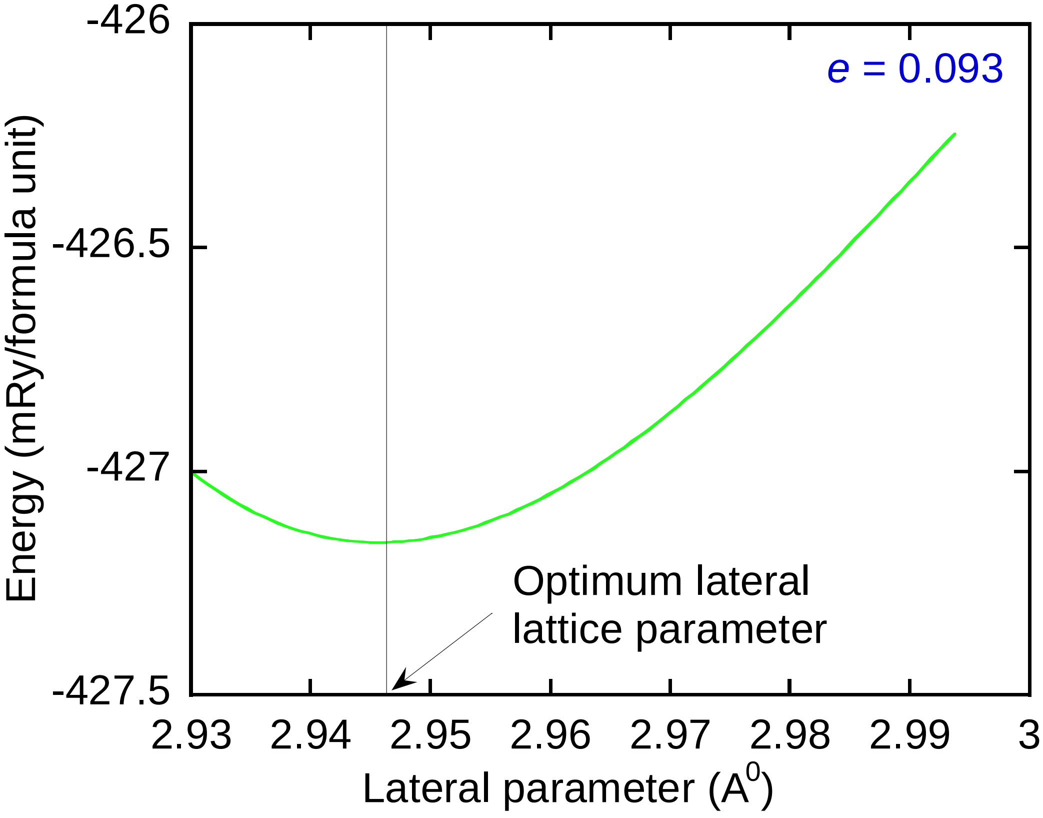

Figure 3.2: Total energy as a function of lateral lattice parameter of bct cell strained along [001] direction by e = 0.093. The thin vertical line marks the minimum energy and corresponding lateral lattice parameter.

3.3 Results and Discussions

3.3.1 Structural stability and equation of state

In order to determine equation of state of a material the knowledge of its structures at various pressures is necessary. Therefore we have analyzed structural stability of MgO under hydrostatic pressure. For this purpose the total energy at 0 K has been calculated at various unit cell volumes for the B1, B2 and B10 structures. In order to test the structural stability of B10 and B2 phases the calculations have been performed on the primitive tetragonal cell and at each volume the *c/a* ratio and internal parameter 'z' are optimized. Fig. 3.3 shows the optimized *c/a* ratio and *z* as a function of volume. Also plotted is the total energy of tetragonal cell corresponding to the optimized parameters at each volume. It is clear from the figure that at zero pressure the optimum value of *c/a* and z parameter of the tetragonal cell is ~ 0.74 and ~ 0.28, respectively, indicating that at zero pressure, the B10 structure has lower energy than the B2 phase. Upon compression, the optimum *c/a* ratio decreases, whereas, the z parameter increases monotonically with increasing pressure and approach to a value of ~ 0.707 and 0.5, respectively, at volume of 16.078 $Å^3$/ formula unit with corresponding pressure of ~ 25 GPa. Beyond this pressure the two parameters remain fixed at these values, indicating that the B2 structure becomes a low energy structure as compared to B10 phase beyond this pressure. Further, in the same figure, the total energy of the B1 structure has also been displayed. The comparison of total energy of B1, B10 and B2 structures, clearly suggests that up to volume/formula unit of $\leq$ 8.90 $Å^3$ with corresponding pressure of $\leq$ 535 GPa, the B1 structure has lowest energy among these three phases and beyond this pressure MgO stabilizes in B2 phase. B10 structure does not stabilize at any compression. Further, the enthalpy (*H*) of B1 and B2 phases are determined using theoretically calculated total energy in conjunction with the 0 K isotherms. The plot of enthalpy of B2 phase relative to that of B1 structure is given in the Fig. 3.4. The comparison of enthalpies puts the B1 to B2 transition pressure at ~ 535 GPa, which is in line with other theoretical predictions [23-25].

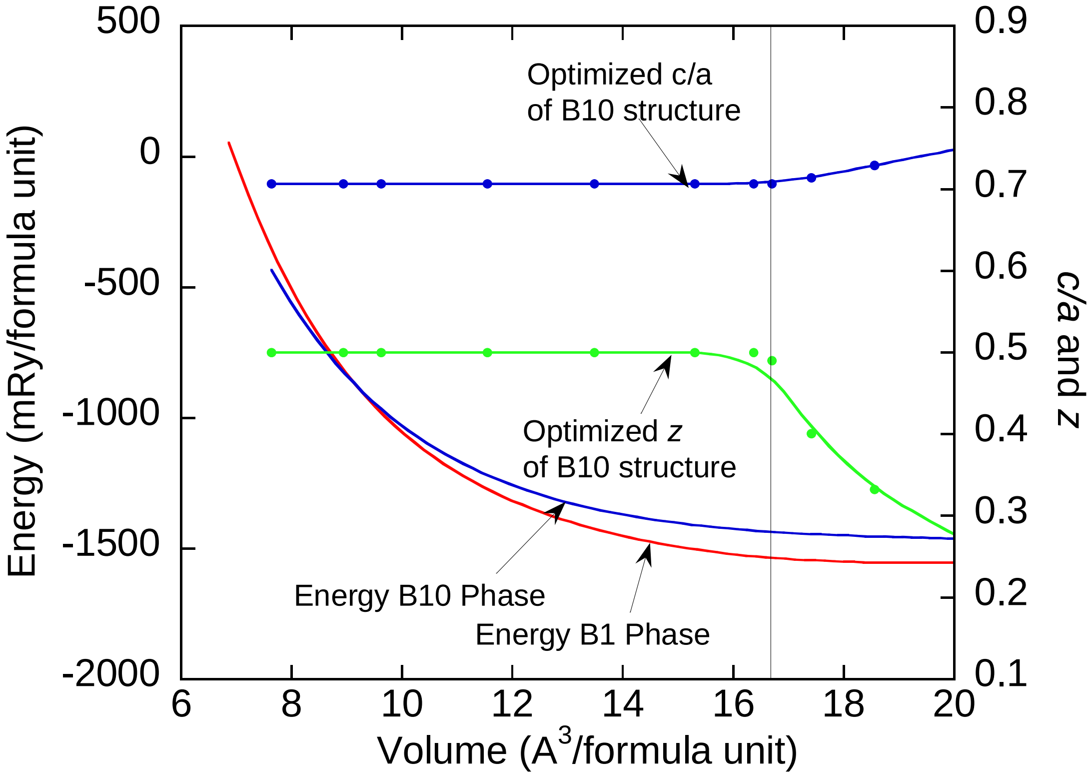

Figure 3.3: The total energy of the B1 phase and tetragonal structure (B10). The total energy at each volume for the tetragonal structure is plotted for optimum *c/a* and *z*. For clarity, the optimized *c/a* and fractional coordinate *z* of tetragonal structure as a function of volume are also plotted. It may be noted that for $V \leq 16.078$[Å^3/formula unit], *i.e.* pressure ≥ 25 GPa, the optimum *c/a* and *z* of the tetragonal structure saturate at a value of ~0.707 and 0.5, respectively.

Additionally, the activation barrier between the B1 and B2 structures has been determined at various compressions. For this purpose, the total energy calculations at a given compression have been carried out on a rhombohedral cell as a function of rhombohedral angel (α). It may be noted that the B1 and B2 structures are special cases of rhombohedral cell *i.e.* for α = 60° the rhombohedral cell reduces to B1 structure and for α = 90° it corresponds to B2 structure [52]. Fig. 3.5 shows the total energy of rhombohedral cell as a function of angle α relative to that for the α = 60. The figure correctly depicts that at ambient pressure the B1 phase is stable structure, whereas, the B2 structure is metastable. At the pressure of ~ 535 GPa (the transition pressure predicted from the comparison of the total energy), both B1 and B2 have same energy and are separated by a barrier of height ~ 23 mRy/formula unit. Above this pressure, the B2 phase displays the global minima and B1 phase emerges as a metastable structure.

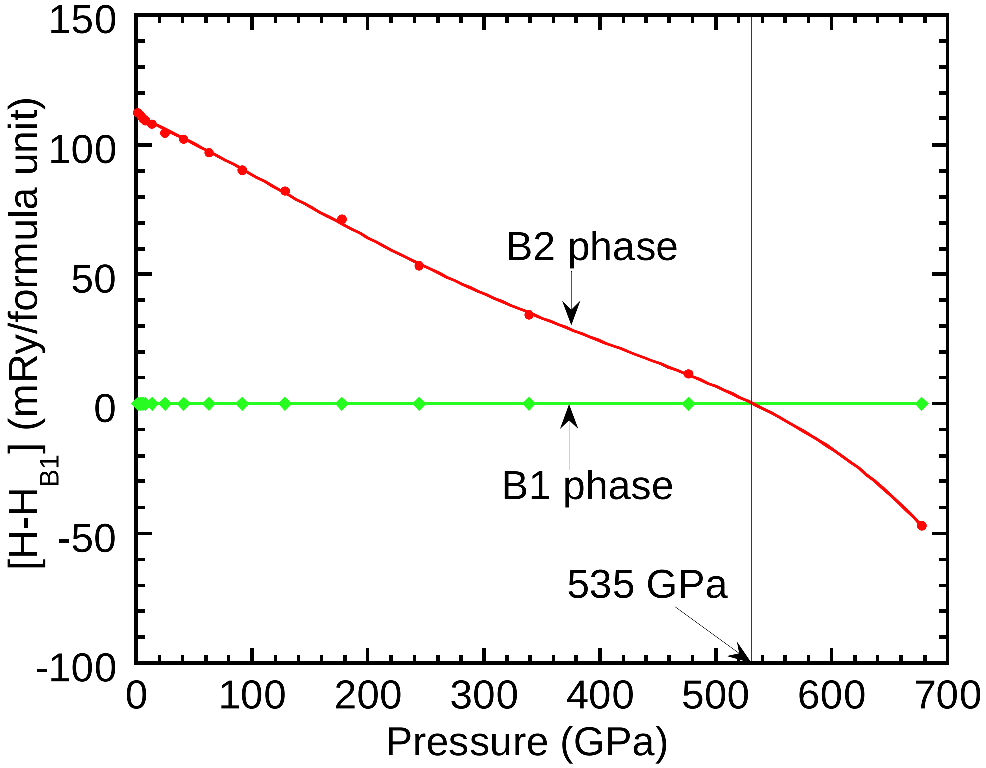

Figure 3.4: The enthalpy of B2 phases relative that of B1 phase as a function of pressure.

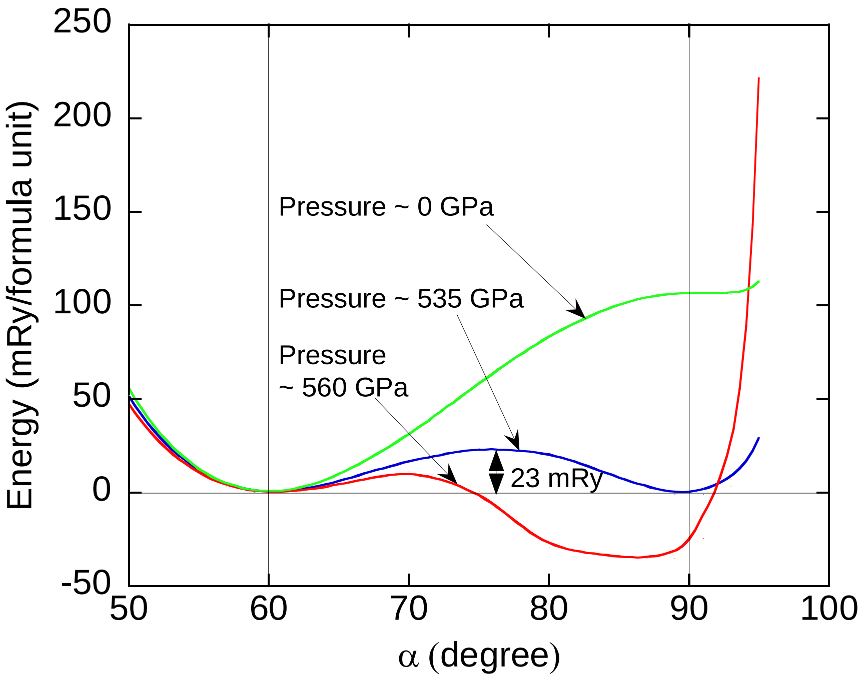

Figure 3.5: Total energy of rhombohedral cell relative to that of B1 phase as a function of α at various compressions.

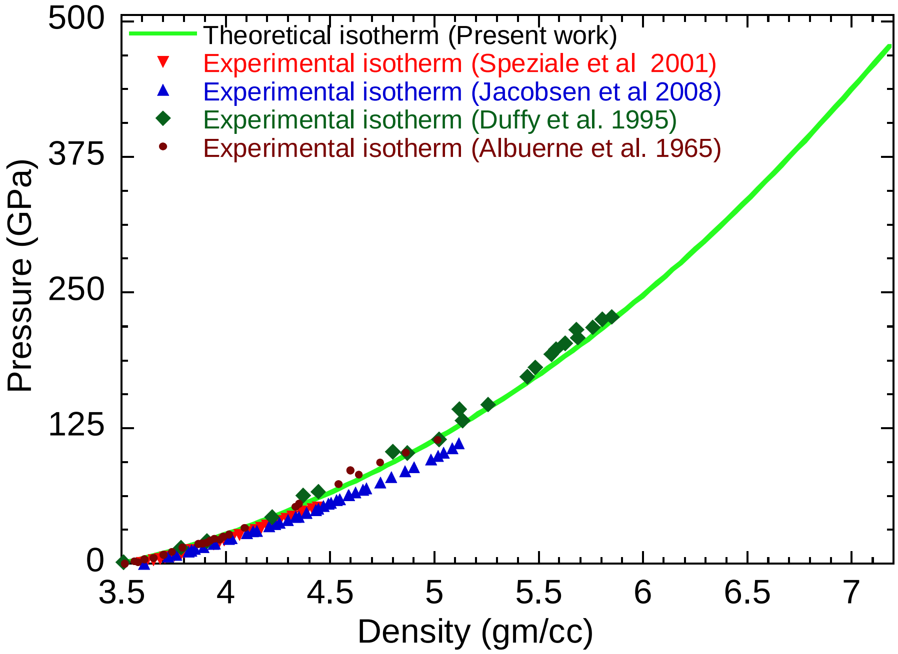

Figure 3.6: The comparison of theoretically determined 300 K isotherm of B1 phase of MgO with experimental data [1, 2, 4, 53].

Table 3.1: Comparison of theoretical and experimental values of physical properties of MgO at ambient condition.

Properties at Equilibrium Volume	Present Theoretical Work	Theoretical (Other sources)	Experimental
V_0 (Å^3/formula unit)	19.11	18.40[20], 18.65[19] 24.01 [21], 18.52[22] 19.19 [23, 26],18.81 [28] 18.06 [29], 17.54 [31]	18.67 [2,4,55,56], 18.69 [54], 18.65 [3],
B_0 (GPa)	157.2	159.7 [23], 153.9 [26] 159 [28], 171 [29] 160.9 [31], 163 [30]	160.2 [2], 153[55] 160 [54], 161 [56], 159.6 [4]166.2 [7]
B_0'	3.97	4.26 [23], 4.05 [26] 4.30 [28], 4.29 [29] 4.12 [31]	3.99 [2], 4.1 [55], 4.15 [54], 3.94 [56], 3.74 [4]
γ	1.43	1.52 [26], 1.54 [28]	1.49[2], 1.6* [7]
C_{11}(GPa)	276.0	291 [23], 280 [26] 338 [29], 299.9 [31] 302 [30]	295.9 [6], 286 [58] 296 [7]
C_{12}(GPa)	87.0	91[23, 26]], 91 [29] 94.9 [31], 94 [30]	95.4 [6], 87 [58] 95.9 [7]
C_{44} (GPa)	154.4	139 [23], 142.5 [26] 118 [29], 146 [31], 144 [30]	153.9 [6], 148 [58] 156 [7]
θ_0 (K)	732	910 [26]	773 [57], 946 [6] 962 [7]

After predicting the structural stability, the theoretical 300 K isotherm of MgO in B1 phase has been determined (Fig. 3.6) and compared with the available experimental data [1-2, 4, 53]. The Theoretical isotherm shows good agreement with the experimental data of Duffy *et al.* [1] and Perez-Albuerne and Drickamer [53], however it is somewhat overestimated as compared to that of Speziale *et al.*[2] and Jacobsen *et al.* [4]. In Table 3.1, various physical quantities derived from present all-electron calculations are compared with previous experimental findings [2-4, 6-7, 54-58] and theoretical values available from other sources [19-23, 26-31]. The calculated zero pressure volume, bulk modulus and its pressure derivative at this volume agree within 2.4%, 5.4% and 4.3 %, respectively, with experimental values [2-4, 6-7, 54-58]. The Gruniesen parameter (γ)

turns out to be 1.43 as compared to 1.49 measured at 300 K by Speziale *et al.* [2] and 1.6 measured by Sumino *et al.*[7] at 80 K.

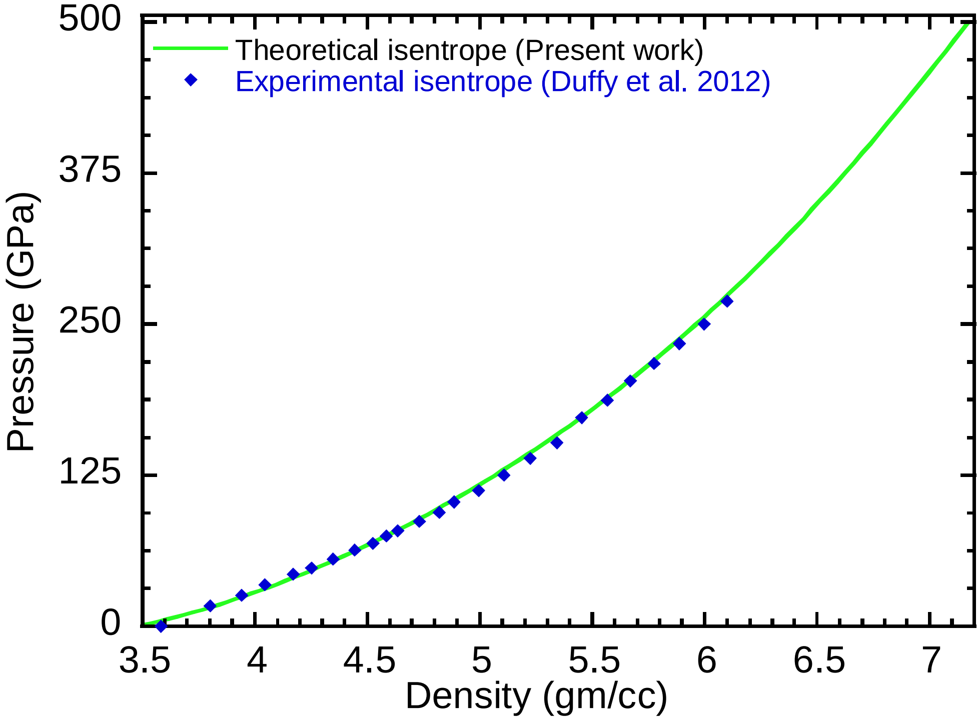

Figure 3.7: The comparison of theoretically determined isentrope of B1 phase of MgO with experimental data [59].

The theoretical isentrope of MgO is plotted in Fig. 3.7 along with the experimental isentrope data generated recently by Duffy *et al.* [59] by conducting ramp compression experiments on MgO. The agreement between the theoretical isentrope and experimental data is quite good. Fig. 3.8 shows Hugoniot of B1 phase of MgO in P-V (Fig. 3.8a) and U_s-U_p (Fig. 3.8b) plane, where U_s is the shock velocity and U_p is the particle velocity. Our theoretical Hugoniot agrees reasonably well with experimental data generated in various studies [10-12, 16, 59]. As is clear from the figure, the U_s and U_p display a linear relationship of type $U_s = C_0 + s\ U_p$ with C_0 approximately equal to the bulk sound velocity. The value of C_0 and s evaluated from linear fit of theoretical U_s with U_p is 6.74 km/s and 1.23, respectively, in good agreement with 6.87 km/s and 1.24 measured experimentally [10].

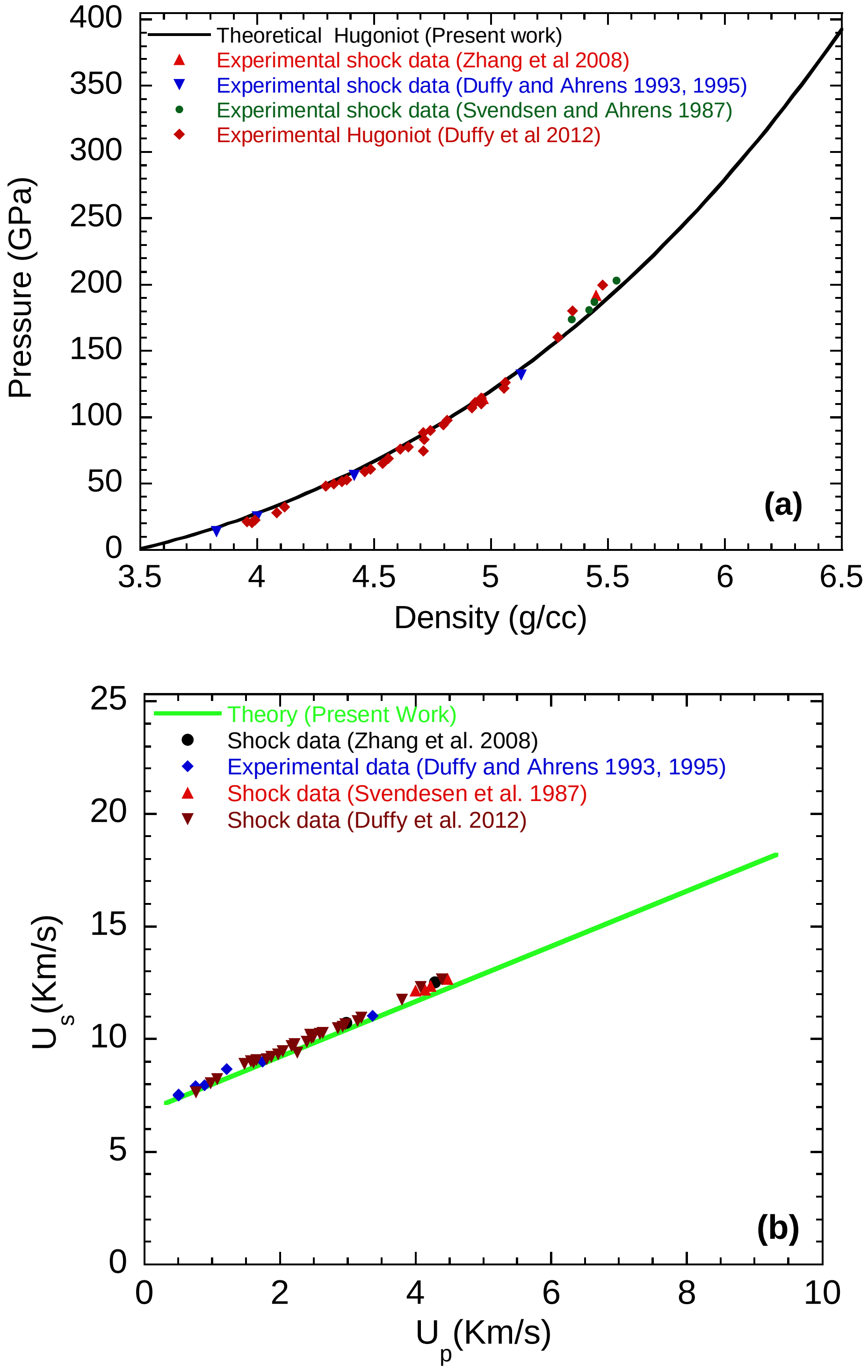

Figure 3.8: The theoretical Hugoniot of MgO for B1 phase plotted in (a) pressure-density and (b) U_s - U_p plane. Experimental data [1, 10-12, 16, 57] has also been plotted for to check the matching of the present theoretical data with the available experimental findings.

After finding the isothrerm, isentrope and Hugoniot of MgO, the elastic constants C_{11}, C_{12} and C_{44} of B1 phase at ambient pressure are determined and compared with the experimental data [6, 7, 58] measured through ultrasonic and rectangular parallelepiped resonance techniques, and other theoretical values[23, 26, 29-31]. Presently determined values of C_{11}, C_{12} and C_{44} agree within 6.7%, 9.3% and 4%, respectively with the experimental data [6, 7, 58]. The value of Debye temperature (θ_0) calculated from these elastic constants is 732 K as compared to the 773 K determined using experimentally measured specific heat [57] in the low temperature Debye approximation. Though our theoretical value of θ_0 shows a good agreement with that determined using experimentally measured specific heat in the low temperature Debye approximation it deviates significantly from the values determined using experimental elastic constants [6-7] and theoretical value of Oganov *et al.* [25].

3.3.2 Ideal Compressive and tensile strength

Having demonstrated that the various ground state properties and equation of state derived from present theoretical calculations agree reasonably well with the available experimental data, we have extended the total energy calculations to determine the ideal compressive and tensile strength of MgO single crystal subjected to uniaxial compressive and tensile loading along [001] crystallographic direction. As mentioned earlier, the compressive and tensile loadings have been carried out in two deformation configurations *i.e.* uniaxial strain condition and uniaxial stress condition. It may be noted that the uniaxial strain condition is encountered in experiments where materials are subjected to rapid loading with strain rates ranging from 10^4/s to 10^9/s. Such high strain rates in materials can be achieved in shock wave experiments. In fact, a suitably configured shock wave experiment not only generates high compressive stresses but also high tensile stresses at such strain rates [35-36, 60] which may cause spall fracture in material. The uniaxial stress condition prevails when materials are subjected to quasistatic loading with strain rates of order of 10^{-3}/s.

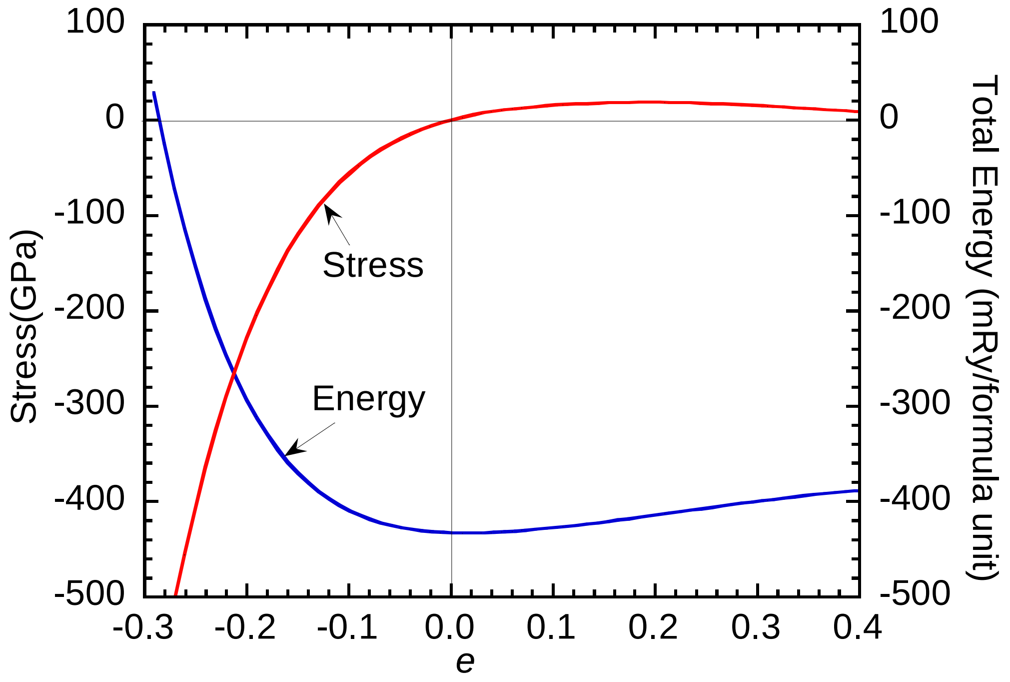

Figure 3.9: Total energy versus strain plot of MgO single crystal strained along [001] direction under uniaxial strain condition. Also displayed is the corresponding uniaxial stress along [001] direction.

Fig. 3.9 displays the total energy and corresponding uniaxial stress as a function of strain along [001] direction for uniaxial strain condition. As is clear from the figure, for compression, the stress along [001] direction increases monotonically with increasing *e*, however, for tension, it first increases and reaches to maximum value of ~ 20 GPa at *e* ~ 0.19 corresponding to the inflection point in total energy, thereafter it decreases monotonically with increasing *e*. To identify the minimum strain and corresponding stress at which MgO single crystal fails mechanically upon [001] compression and expansion under uniaxial strain condition, various elastic moduli of bct MgO have been calculated as a function of *e* and plotted in Fig. 3.10. As depicted in the figure for [001] compression, the shear modulus C' vanishes first at strain *e* ~ - 0.218 with corresponding stress σ ~ - 283 GPa. However, for tension the longitudinal modulus vanishes first at the strain *e* ~ 0.19 with corresponding stress of σ_c ~ 20 GPa. These results suggest that for compressive [001] loading the MgO single crystal fails mechanically due to shear instability whereas for tensile loading it fails due to vanishing of tensile modulus. Thus, the ideal compressive strength and ideal tensile strength of MgO single crystal subjected to compressive and tensile loading along [001] direction under uniaxial strain condition is determined to be ~ -283 GPa and ~ 20 GPa, respectively.

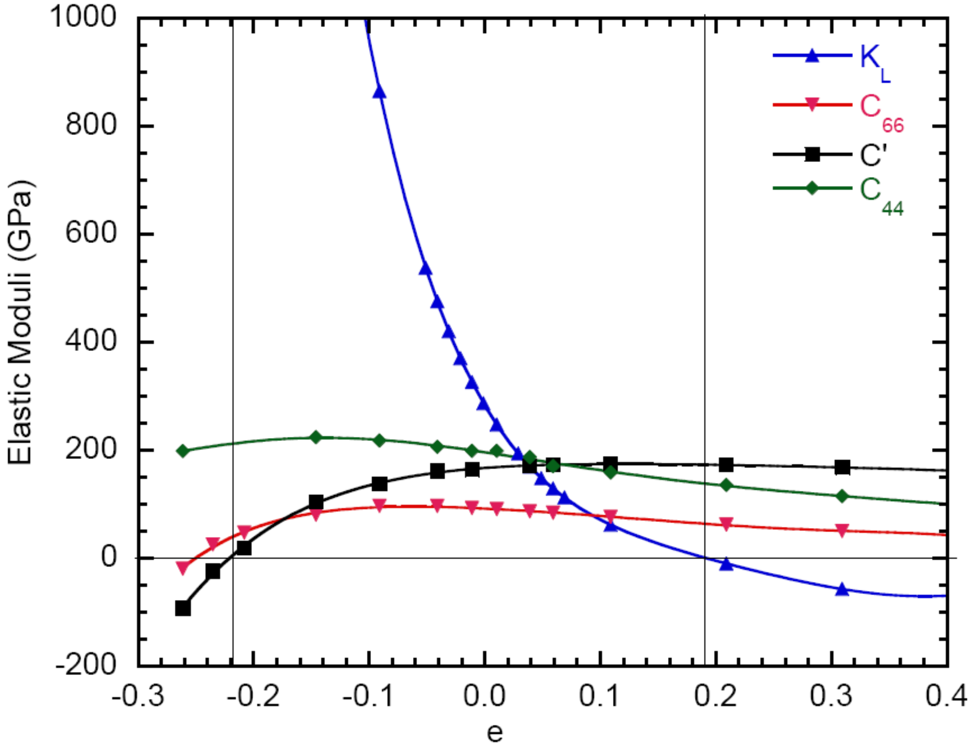

Figure 3.10: Various elastic moduli as a function of strain for MgO single crystal strained along [001] direction under uniaxial strain condition. Application of strain distorts the fcc lattice to fct or equivalently to a bct lattice. The elastic moduli at various strains have been calculated for bct lattice. The two thin vertical lines intercepting the strain axis at -0.218 and 0.19 displays the strains at which mechanical failure occurs under compression and tension, respectively. The stresses corresponding to these strains as shown in Fig. 3.9 are -283 GPa and 20 GPa, respectively.

In Fig. 3.11, the total energy and corresponding stress is displayed as a function of strain along [001] direction for uniaxial stress condition. Like for first type of deformation configuration, here also, for compression, the stress along [001] direction increases monotonically with increasing strain, however, for expansion it first increases with increasing strain and reaches to a maximum value of ~ 11 GPa at *e* ~ 0.13 corresponding to the inflection point in total energy - strain curve. Again to identify the minimum strain for which any one of the stability conditions gets violated, we determined various elastic moduli of bct MgO as a function of strain *e*. These are plotted against *e* in Fig. 3.12. As is clear from figure, for compression the shear modulus C_{66} vanishes first at the strain *e* ~ -0.17 with corresponding stress of ~ -115 GPa. For expansion, however, it is the Young's modulus which vanishes first at a strain of ~ 0.13 with corresponding stress of ~ 11 GPa. Like uniaxial strain condition, in the uniaxial stress condition also, for compression the mechanical failure of MgO single crystal occurs due to shear instability, however, that for expansion is due to vanishing of Young's modulus. On the basis of these results the ideal compressive strength and ideal tensile strength for uniaxial loading along [001] direction under uniaxial stress condition is evaluated to be ~ -115 GPa and ~ 11 GPa, respectively.

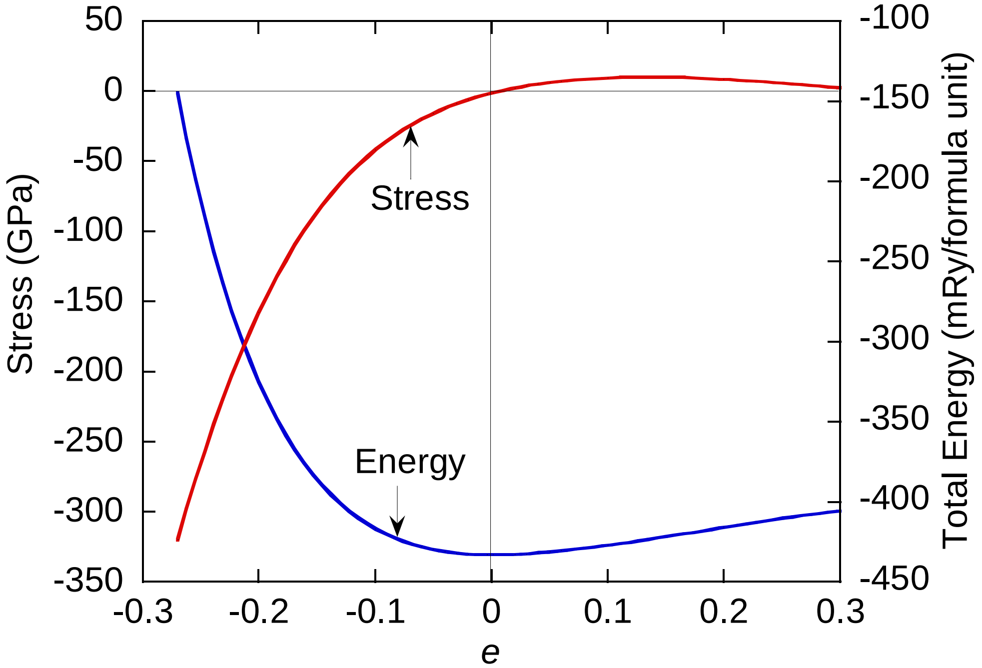

Figure 3.11: Total energy versus strain plot of MgO single crystal strained along [001] direction under uniaxial stress condition. Also displayed is the corresponding uniaxial stress along [001] direction.

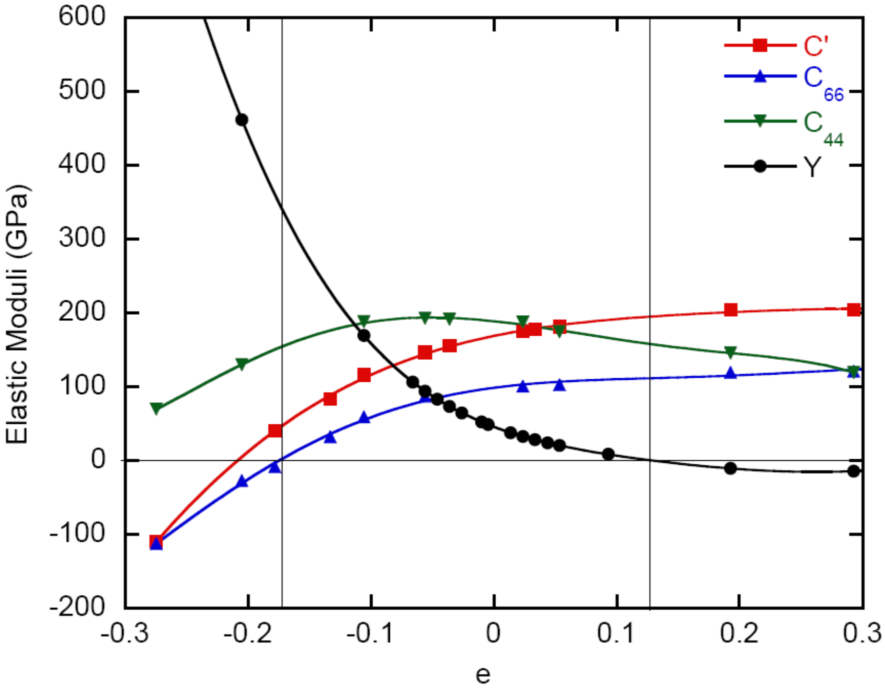

Figure 3.12: Various elastic moduli as a function of strain for MgO single crystal strained along [001] direction under uniaxial stress condition. The two thin vertical lines intercepting the strain axis at -0.17 and 0.12 displays the strains at which mechanical failure occurs under compression and tension, respectively. The stresses corresponding to these strains as shown in Fig. 3.11 are -115 GPa and 11 GPa, respectively.

These findings suggest that the ideal compressive and tensile strength of MgO single crystal is higher for “uniaxial strain condition” than that for the “uniaxial stress condition”. The higher failure strength under uniaxial strain condition than that under unaxial stress condition determined from present theoretical work in MgO is in accordance with the findings of Chatterbuck *et al.* [39] and Černý and Pokluda [40] in various elemental solids such as Fe, Mo, W, Cu, Pt and Au, where these authors have determined the tensile strength along [001] direction in two conditions, the uniaxial stress condition and the triaxial stress condition (lateral strains superimposed over [001] uniaxial strain). It has been demonstrated that the tensile strength increases when the lateral tension is superimposed over [001] uniaxial tension. The reason for this is associated with the presence of transverse stress (or strain) which prevents the Poisson contraction, making the structure to reach the inflection point at a larger uniaxial strain as compared to that under uniaxial stress condition [39, 40]. This argument is equally valid in our case also, where the uniaxial strain condition under compression/expansion is achieved by keeping the lateral dimension of MgO single crystal fixed at zero stress value, *i.e.* by not allowing the Poisson expansion/contraction, which is equivalent to adding transverse stresses.

The higher values of failure strengths under "uniaxial strain condition" (which can be generated in shock wave experiments) than that under "uniaxial stress condition" (which exists in quasi static loading experiments) have also been observed experimentally [35-36]. For example, in Al and Cu foil the tensile fracture strength measured in shock wave experiment [36] at strain rate of ~ 10^4/s are reported to be ~ 1 GPa and ~ 2 GPa, as compared to the typical quasi-static fracture strength values of ~ 0.12 GPa and ~ 0.4 GPa, respectively. Similarly, Mo single crystal subjected to shock loading along [001] crystallographic direction at strain rate of ~ 10^4/s (ref. 35) shows tensile fracture strength of ~ 3.3 GPa as compared to the quasi-static value of ~ 0.55 GPa [61]. Additionally, in these experiments, it has also been found that the tensile fracture strength increases with increasing strain rate and approaches to ideal value at strain rate of ~ 10^8/s [35-36]. The reason for this is attributed to the competition between two mechanisms causing the fracture in materials. In the first mechanism it is the movement of defects and dislocation present in the material which cause fracture in the materials, i.e. the strength of the material is controlled by nucleation and movement of dislocation and microcracks. However, in second mechanism it is the binding energy of the solid which decides the fracture strength. Thus, if the material is defect free, it will fail only when the any one of the elastic stability condition gets violated. It is argued that the first type of mechanism is operative up to strain rates ~ 10^7/s [35-36, 61], however, at ultrahigh strain rates of ≥ 10^8/s, due to inertia, the defects and dislocations of the material could not respond to the rapidly increasing stress, thereby making the binding energy completely responsible for the fracture process at such high strain rates [35-36, 61]. Hence, the ideal compressive and tensile strength calculated in present work give upper bound to fracture strength of MgO.

Additionally, it may also be noted that (i) the [001] compressive strength of MgO under uniaxial stress condition is much higher than that of ductile copper and aluminium and (ii) the failure in MgO under compression is due to shear instability whereas that in Cu and Al is due to vanishing of Young's modulus[37, 38]. The reason for this could be associated to the relatively small Poisson ratio (~ 0.18) of MgO as compared to that of Cu (~ 0.34) and Al (~ 0.35), which has caused the bcc saddle point and hence the inflection point to occur at a very large strain (the inflection point in MgO has not reached even at e = -0.3) before which the structure has already failed due to shear instability. In contrast to this, in Cu and Al the inflection point has reached at very low strains of ~- 0.09 and - 0.1, respectively, causing the failure to occur due to vanishing of Young's modulus [37, 38]. Moreover, under tension, the MgO fails due to vanishing of Young's modulus whereas the Cu and Al fail due to shear instability [37, 38].

3.4 Summary

To summarize, the *ab-initio* calculations at 0K have been performed on MgO and the structural stability has been examined as a function of hydrostatic compression. The 0K calculations in conjunction with Debye model for thermal corrections have been utilized to generate 300K isotherm, isentrope and Hugoniot of MgO. The structural stability analysis suggests that MgO will transform from B1 phase to B2 phase at ~ 535 GPa in line with other theoretical predictions. The theoretical isotherm, isentrope and Hugoniot compare well with the available experimental data. The activation barrier calculated between B1 and B2 phases at transition pressure is ~ 23 mRy/formula unit. Various physical quantities such as zero pressure equilibrium volume, bulk modulus, its pressure derivative, Gruneisen parameter and Debye temperature determined at zero pressure are 19.11 $Å^3$/formula unit, 157.2 GPa, 3.97, 1.43 and 732 K respectively, as compared to the experimental values of 18.65-18.69 $Å^3$/formula unit, 166.2-153GPa, 4.15-3.74, 1.49 and 773-962K. The shock parameter C_0 and s of 6.74 km/s and 1.23 show a good agreement with the experimental data of 6.87 km/s and 1.24, respectively.

Apart from these studies the ideal strength of MgO single crystal subjected to two deformation conditions namely uniaxial stress condition and uniaxial strain condition along [001] crystallographic direction has also been determined. For both the deformation configurations present calculations suggest that under compression the MgO single crystal will fail due to shear instability, whereas, under expansion it will fail due to vanishing of tensile modulus. The ideal [001] compressive strength under “uniaxial strain condition” and “uniaxial stress condition” is determined to be -283 GPa and -115 GPa, respectively. However, ideal tensile strength is evaluated to be 20 GPa and 11 GPa, respectively, for the above mentioned two deformation conditions. These results suggest that the MgO single crystal will offer higher resistance against failure for compression as well as expansion under “uniaxial strain condition” than that for the “uniaxial stress condition”. The understanding of the strength properties under these loading conditions will provide useful input to codes developed for analysis of the structural response of MgO.

References

1. T. S. Duffy, R. J. Hemley and H. Mao, *Phys. Rev. Lett.* **74**, 1371 (1995).
2. S. Speziale, C. Zha, T. S. Duffy, R. J. Hemley and H. Mao, *J. Geophy. Res.* **106,** 515 (2001).
3. D. M. Garcia, Y. L. Godec, M. Mezouar, G. Syfosse, J. P. Itie and J. M. Besson, *High Press. Res.* **18**, 339 (2000).
4. S. D. Jacobsen, C. M. Holl, K. A. Adams, R. A. Fischer, E. S. Martin, C. R. Bina, J.-F. Lin, V. B. Prakapenka, A. Kubo and P. Dera, *Amer. Miner.* **93**, 1823 (2008).
5. A. K. Singh, H. P. Liermann and S. K. Saxena, *Solid State Comm.* **132**, 795 (2004).
6. K. Marklund and S.A. Mahmoud, *Phys. Scripta* **3**, 75 (1971).
7. Y. Sumino, O. L. Anderson and I. Suzuki, *Phys. Chem. Minerals.* **9**, 38 (1983).
8. G. Chen, R. C. Liebermann and D. J. Weidner, *Science* **280**, 1913 (1998).
9. S. Ghose, M. Krisch, A. R. Oganov. A. Beraud, A. Bosak, R. Gulve, R. Seelaboyina, H. Yang and S. K. Saxena, *Phys. Rev Lett.* **96**, 035501-1 (2006).
10. T. S. Duffy and T. J. Ahrens, *J. Geophys. Res.* **100**, 529 (1995).
11. T. S. Duffy and T. J. Ahrens, *High Pressure Science and Technology* (Ed: S. C. Schmidt, J. W. Shaner, G. A. Samara and M. Ross, Amer. Inst. Phys., NY 1107) (1993).
12. B. Svendsen and T. J. Ahrens, *Geophys. J. R. Astr. Soc.* **91**, 667 (1987).
13. T. J. Ahrens, and R. K. Linde, *Behaviour of Dense Media under High Dynamic Pressures*, (Gordon and Breach, New York, 325) (1968).
14. S. P. Marsh, *LASL Shock Hugoniot Data*, (University of California Press, Berkeley, 658) (1980).
15. O. V. Fat'yanov, P. D. Asimow and T. J. Ahrens, *Shock Compression of Condensed Matter*, (Ed: M. L. Elert, W. T. Buttler, M. D. Furnish, W. W. Anderson and W. G. Proud, 855) (2009).
16. L. Zhang, Z. Gong and Y. Fei, *J. Phys. Chem. Solids* **69**, 2344 (2008).
17. M. S. Vassiliou, T. J. Ahrens, *Geophys. Res. Lett.* **8**, 729 (1981).
18. R. S. McWilliams, D. K. Spaulding, J. H. Eggert, P. M. Celliers, D. G. Hicks, R. F. Smith, G. W. Collins, R. Jeanloz, *Science* **338**, 1330 (2012).
19. A. J. Cohen and R. G. Gordon, *Phys. Rev. B* **14,** 4593 (1976).

20. K. J. Chang and M. L. Cohen, *Phys. Rev. B* **30**, 4774 (1984).
21. R. K. Singh and S. D. Sanyal, *Phys. Status Solidi B* **113**, K23 (1982).
22. J. Yamashita and S. Asano, *J. Phys. Soc. Jpn.* **52,** 3506 (1983).
23. B. B. Karki, L. Stixrude, S. J. Clark, M. C. Warren, G. J. Ackland and J. Crain, *Amr. Miner.* **82**, 51 (1997).
24. J. E. Jaffe, J. A. Synder, Z. Lin and A. C. Hess, *Phys. Rev B* **62**, 1660 (2000).
25. M. J. Mehl, R. E. Cohen and H. Krakauer, *J. Geophys. Res.* **93**, 8009 (1988).
26. A. R. Oganov and P. I. Dorogokupets, *Phys. Rev. B* **67**, 224110-1 (2003).
27. B. B. Karki, G. J. Ackland and J. Crain, *J. Phys. Cond. Matter* **9**, 8579 (1997).
28. B. B. Karki, R. M. Wentzcovitch, S. de Gironcoli and S. Baroni, *Phys. Rev. B* **61**, 8793 (2000).
29. D. G. Isaak, O. L. Anderson, and T. Goto, *Phys. Chem. Miner.* **16**, 704 (1989).
30. A. Gueddim, N. Bouarissa and A. Villesuzanne, *Comp. Material Sci.* **48**, 490 (2010).
31. L.-Y. Lu, Y. Cheng, X.-R. Chen, J. Zhu, *Physica B* **370**, 236 (2005).
32. A. B. Belonoshko, S. Arpan, R. Martonak and R. Rosengren, *Phys. Rev. B* **81**, 054110-1 (2010).
33. Z. J. Liu, X. W. Sun, Q. F. Chen, L. C. Cai, X. M. Tan and X. D. Yang, *Phys. Lett. A* **353**, 221 (2006).
34. D. Alfe, *Phys. Rev. Lett.* **94**, 235701-1 (2005).
35. G. I. Kanel, S. V. Razorenov, A. V. Utkin *et al.*, *J. Appl. Phys.* **74**, 7162 (1993).
36. E. Moshe, S. Eliezer, Z. Henis, M. Werdiger, E. Dekel, Y. Horovitz, S. Maman, I. B. Goldberg and D. Eliezer, *Appl. Phys. Lett.* **76**,1555 (2000).
37. M Cerny, M Šob, J Pokluda and P Šandera, *J. Phys.: Condens. Matter* **16**, 1045 (2004).
38. W. Li and T. Wang, *J. Phys.: Cond. Matter* **10,** 9889 (1998).
39. D. M. Clatterbuck, D. C. Chrzan, J. W. Morris Jr., *Scripta Mater.* **49**, 1007 (2003).
40. M. Černý and J. Pokluda, *Phys. Rev. B* **82**, 174106 (2010).
41. Y. Zhang, H. Sun and C. Chen, *Phys. Rev. Lett.* **93,** 195504-1 (2004).
42. P. Blaha, K. Schwarz and J. Luitz, WIEN2K (Technical University of Vienna).
43. J. P. Perdew, S. Burke and M. Ernzerhof, *Phys. Rev. Lett.* **77**, 3865 (1996).
44. W. Band and G. E. Duvall, *Am. J. Phys.* **29**, 780 (1961).

45. G. E. Duvall and G. R. Fowles, *Shock Waves in High Pressure Physics and Chemistry*, vol 2, (ed R. S. Bradley, New York: Academic) 209 (1963).
46. F. Birch, *J. Geophys. Res.* **83**, 1257 (1978).
47. K. D. Joshi, S. C. Gupta and S. Banerjee, *J. Phys. Cond. Matter* **21**, 415402 (2009).
48. R. E. Cohen, L. Sixtrude, and E. Wasserman, *Phys. Rev. B* **56**, 8575 (1997).
49. S. C. Gupta, K. D. Joshi and S. Banerjee, *Metall. Materials Trans. A* **39**, 1593 (2008).
50. M. J. Mehl, *Phys. Rev. B* **47**, 2493 (1993).
51. G. Steinle-Neumann and R. E. Cohen, *J. Phys. Cond. Mater.* **16**, 8783 (2004).
52. M. J. Mehl and D. Finkenstadt, *Phys. Rev. B* **77**, 052102 (2008).
53. E. A. Perez-Albuerne and H. G. Drickamer, *J. Chem. Phys.* **43**, 1381 (1965).
54. Y. Fei, *Am. Miner.* **84**, 272 (1999).
55. W. Utsumi, D. J. Weinder and R. C. Libermann, *Properties of earth and planetary Materials at High pressure and High Temperature,* Geophys. Monogr., Ser., vol. 101, edited by M. H. Manghnani and T. Yagi, pp. 327-333, AGU, Washington, D.C. (1998).
56. A. Dewaele, G. Fiquet, D. Andrault and D. Hausermann, *J. Geophysical Res.* **105**, 2869 (2000).
57. H. Watanabe, *Thermophysical properties of synthetic high pressure compounds relevant to Earth's mantle*, in High Pressure Research in Geophysics, Adv. Earth Planet Sci, Vol. 12, edited by S. Akimoto and M.H. Manghnani, pp. 441, Cent. for Acad. Publ., Tokyo, (1982).
58. S. Baghavantam, *Pro. Indian. Acad. Sci. (Paris)* **54**, 23 (1961).
59. T. S. Duffy, presentation in 2012 DOE/SSAA Symposium, Washington D.C. (2012).
60. K. D. Joshi and S. C. Gupta, *High Press. Res.* **27**, 259 (2007).
61. G. S. Burkhanov, V. M. Kirillova, A. R. Kadyrbaev, V. V. Sdobyrev and V. A. Dement'ev, in proceedings of 16th International Metallurgical & Material Conference (METAL 2007) held on 22-24 May 2007, Czech Republic.

Chapter - 4

B1 → B10 → B2 Structural Transition Sequence in LaN under High Pressure

4.1 Introduction

The transition metal mononitrides are frequently used as refractory material as they exhibit unique mechanical properties such as high hardness, brittleness, elastic moduli and melting point [1-4]. These properties ensure an extensive and growing application of nitrides of *d*- and *f*- metals in modern technology, e.g., the basis for development of various corrosion and wear-resistant coatings (in cutting tools and magnetic storage devices). These materials also have unique combination of chemical characteristics with the above mentioned physical or mechanical properties; namely interesting optical, electronic, magnetic and vibrational properties [1-4]. A small deviation from the stoichiometry of these compounds can change the physical and chemical properties of these materials drastically. Several of these nitrides show superconducting behaviour with relatively high superconducting temperature. These properties of transition metal mononitrides make them suitable for various technological and scientific applications such as producing solid solution of improved physic-chemical properties, new composite materials. For example, nanocrystalline hard transition metal nitrides (TiN, VN, W_2N, CrN_x and others) can be embedded in amorphous Si_3N_4, BN to produce novel nanocomposite superhard materials [5]. The cubic δ-NbN has been found to posses high hardness (a Vickers hardness of 20 GPa) as well as superconducting behavior for possible applications at extreme conditions [2] and thus have attracted attention of scientific community.

LaN, a mononitride of *5d* transition element La, possessing rocksalt type structure (B1) at ambient conditions, is one of the important transition metal nitrides, which has been studied by researchers in recent past [6-11], with the aim to determine the ground state properties and understand the structural stability under high pressure.

Some of the high pressure theoretical studies have concentrated mainly on B1 to B2 structural phase transition. For example, Vaitheeswaran *et al.* [7] through first principles total energy calculations predicted the rocksalt type to CsCl type (B2) structural phase transition in this material at ~ 26.9 GPa. The same transition has been predicted to occur at ~ 25 GPa by Ciftci *et al.* [8] on the basis of augmented plane wave pseudopotential calculations using VASP package. Stampfl *et al.* [6] have investigated ground state bulk properties of *3d*, *4d* and *5d* transition metal mononitrides using full potential linearized augmented plane wave (FP-LAPW) method within both the local density approximation (LDA) and generalized gradient approximation (GGA). The main physical properties determined by these authors from their *ab-initio* calculations are lattice constants, bulk moduli, heat of formation, cohesive energy, band structure and density of states of these mononitrides in B1 phase. Based on the comparison of results obtained from GGA and LDA calculations, as expected, these authors reported that the GGA yields 1%–2% larger lattice constants, 10%–20% smaller bulk moduli, and 10%–30% lower heats of formation compared to the LDA. The structural and electronic properties of LaN have been investigated by Ghezail *et al.* [9] also using full potential linearized muffin tin (FP-LMTO) and FP-LAPW method within both the LDA and GGA. These authors report that the structure of the stable phase of LaN predicted using *ab-initio* calculations is sensitive to the kind of approximation used for treating exchange correlation interactions. Apart from these static lattice calculations, the lattice dynamic studies of LaN has also been reported in recent past [10].

In experimental front, recently, in a high pressure X-ray diffraction measurements carried out on LaN powder in diamond anvil cell (DAC), occurrence of a new phase at ~ 22.8 GPa has been reported by Schneider *et al.* [10]. This high pressure phase has been identified as a primitive tetragonal structure with space group P*4/nmm* and is named as HP-LaN [11] phase by the authors. In the present thesis, following the literature, we have named this structure as B10 phase. This experimental finding is in contrast with the earlier theoretical predictions [7-8].

The material with rocksalt type structure at the ambient condition transforms generally to the CsCl type structure. There are large numbers of compounds showing this transition sequence under pressure. For example, alkali halides (except CsCl, CsBr and CsI), thorium chalcogenides and pnictides ThX (X=S, Se, P, As, and Sb) [12], barium chalcogenides and pnictides BaX (X= S, Se and Te) [13] follows this phase transition sequence. Thus the occurrence of high pressure B10 structure in LaN is rather unusual in nature. However, Iron monoxide (FeO) exists in the B1 structure under ambient conditions and transforms to the nickel arsenide-type (B8) structure under high pressure [14-15]; but above 3850 K temperature B1 to B2 transition is observed [16]. As the existence of high pressure B10 phase is bit unusual, we attempted to investigate the reason behind its stability by performing the detailed analysis of the electronic band structure.

Motivated with this experimental study, we have attempted to theoretically investigate the pressure induced B1 to B10 structural phase in LaN. For this purpose, we have performed first principles electronic band structure calculations on B1, B10 and B2 phase of LaN using FP-LAPW method implemented in the WIEN2K package [17-18]. The theoretical study presented in this chapter includes the analysis of the relative stability of these phases of LaN as a function of hydrostatic compression and the possible mechanism behind the occurrence of low symmetry phase B10 under high pressure before the B2 phase gets stabilized at still higher pressures.

4.2 Theoretical Method

The structural stability and equation of state of LaN has been determined from first principles total energy calculations using FP-LAPW method [17-18]. To analyze the structural stability we have considered three plausible phases of LaN namely B1, B10 and B2 structures. For the total energy calculations, the unit cell of these structures is divided into two regions, the one consisting of non overlapping atomic spheres centered at the atomic site and the other an interstitial region as discussed in the first chapter. The muffin tin radius for atomic sphere of La was chosen to be 2.2 a.u. while the same for nitrogen was kept to be 1.5 a.u. The parameter $R_{MT}K_{MAX}$ that determines the number of basis functions (size of matrices) is chosen to be 7; here R_{MT} is muffin tin radius and K_{MAX} is the magnitude of the largest K vector (reciprocal lattice vector) used in plane wave expansion. The dimension of K^2_{max} is that of energy. The magnitude of the largest vector (G_{max}) used in charge density Fourier expansion was set to be 12. A grid of 5000 k-points was used for sampling of the Brillouin zone. The exchange correlation interaction was treated within generalized gradient approximation (GGA) [19] for all the calculations. For B10 and B2 phases the calculations have been performed on the tetragonal cell as described in chapter 2.

The HP-LaN or B10 structure, which, has been found to occur in LaN under high pressure has also been reported to exist in BaO at high pressures [20]. The atomic species La and N of the two units of LaN contained in the tetragonal cell of the B10 structure were located at 2c (0 ½ z, ½ 0 -z) and 2a (0 0 0, ½ ½ 0) sites (international table of Crystallography, Vol. 2). The value of z determined experimentally at 39 GPa is 0.3450, which increases to 0.3586 at ~ 60 GPa [11]. At 39 GPa, the experimentally measured c/a ratio of B10 phase is reported to be 0.75412, which shows a slight variation with pressure and reaches to ~ 0.7415 at ~ 60 GPa [11]. As already discussed in chapter 2, the B10 structure becomes identical to B2 phase for c/a =1/√2 and z = ½. In our calculations we have optimized both the c/a ratio and the z for B10 structure for all volumes. For this purpose, at each volume, we have chosen several c/a ratios ranging from 0.76 to 0.69 (which include the c/a corresponding to B2 structure also) and optimized the value of z for each c/a. The optimum c/a and z at a given volume is the one for which the total energy is minimum. This procedure was repeated at various volumes and optimum c/a and z as a function of volume has been obtained. The structural stability as a function of hydrostatic compression has been analyzed by comparing the total energies of B1, B10 and B2 phases as a function of volume.

The 0 K pressure-volume (P-V) data for LaN have been determined by finding the negative volume derivative of total energy calculated at various unit cell volumes. The 300 K isotherm is derived by adding the thermal contributions to the 0 K isotherm. The zero pressure bulk modulus (B_0) and its pressure derivative at zero pressure (B_0') were obtained by fitting the isotherm to the third order Birch-Murnaghan equation of state [21] as described in section 2.2.1. Further, the elastic constants of B1 phase of LaN have also been determined as a function of hydrostatic compression following the procedure described in the chapter 2.

4.3 Results and Discussions

4.3.1 Structural Phase Transition Sequence and the EOS

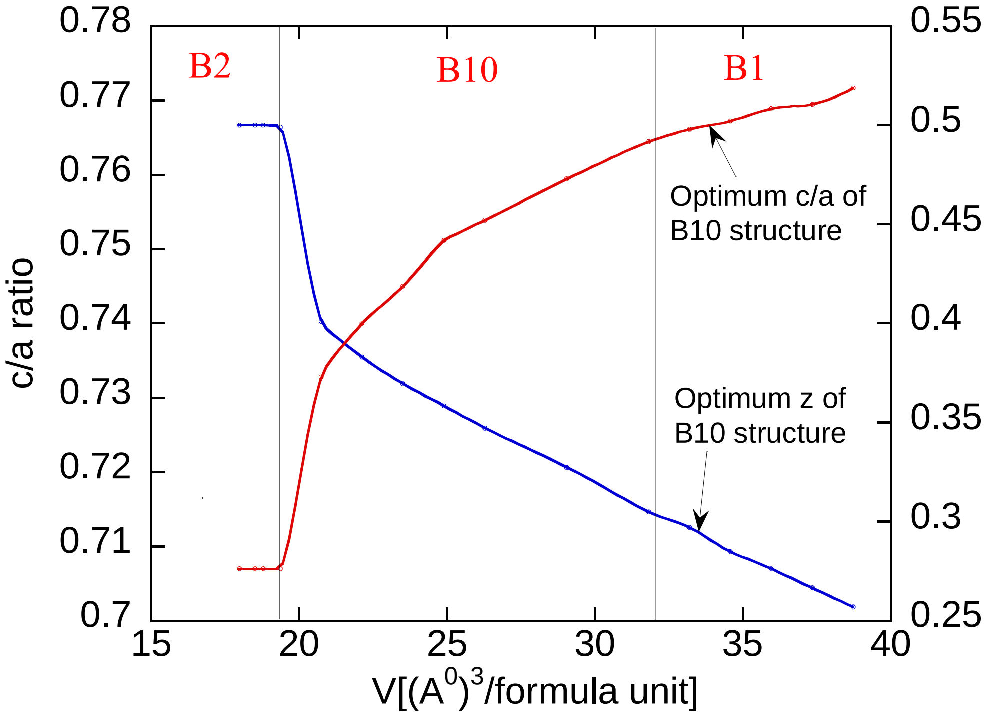

Figure 4.1: The optimized c/a and fractional coordinate z as a function of volume for tetragonal structure. The regions marked as B1, B10 and B2 represent the regime of stability of B1, B10 and B2 structures, respectively. It may be noted that the tetragonal structure with $0.707 < c/a \leq 0.7597$ and $0.3271 \leq z < 0.5$ represents the B10 phase, however, the $c/a = 0.707$ and $z = 0.5$ corresponds to B2 phase.

The structural stability of B1, B10 and B2 phases has been examined as a function of hydrostatic compression. As one can go from B10 structure to B2 structure by changing the c/a ratio to $1/\sqrt{2}$ and the z value to 0.5, for these two structures the calculations have been performed in primitive tetragonal cell only and at each volume the c/a ratio and z value is optimized. In Fig. 4.1, we have plotted the optimum *c/a* and z value as a function of volumes/formula unit of tetragonal cell. The optimum value of *c/a* ratio and z at the zero pressure equilibrium volume of tetragonal cell *i.e.* V_{0t}= 35.87 Å^3/formula unit is ~ 0.7687 and ~ 0.2791, respectively. The c/a ratio decreases monotonically with increasing compression and approaches a constant value of ~ $1/\sqrt{2}$ at V = 19.44 Å^3/formula unit (V/V_{0t} ~ 0.542 with corresponding pressure ~ 169 GPa), whereas, the z parameter increases with increasing compression and reaches a constant value of ~ 0.5 at above mentioned compression. This indicates that beyond 169 GPa the B2 structure becomes lower in energy than the B10 Phase. Further, in Fig. 4.2, we have compared the theoretically determined optimum lattice parameters of B10 structure with the experimental values of Schneider *et al.* [11] at various pressures. The theoretical lattice parameters are found to agree with the experimental values within ~ 2.5%.

The total energies of B1 and optimized primitive tetragonal cell are compared in Fig. 4.3 as a function volume. Also, for sake of clarity, the optimum c/a and z values for tetragonal cell are also plotted. It is clear from the figure that the B1 phase which is a stable structure at ambient conditions transforms to a tetragonal structure (B10) at V = 32.01 Å^3/formula unit with V/V_0 ~ 0.852 and corresponding pressure of ~ 25.83 GPa. This is in agreement with the experimental findings of Schneider *et al* [11], where authors have reported this transition to occur at ~ 22.8 GPa. Further, the c/a ratio of ~ 0.7541 and z ~ 0.3416, determined theoretically for B10 phase at ~ 40 GPa (V ~ 27.01 Å^3/formula unit) are in good agreement with the experimental values of 0.7522 and 0.3450, respectively. Similarly, at ~ 60 GPa the theoretical c/a and z are found to be ~ 0.7500 and ~ 0.3583 as compared to the experimental values of 0.7415 and 0.3586, respectively [11]. Additionally, present calculations predict that upon further compression the B10 phase will transform to B2 structure at V ~ 19.44 Å^3/formula unit with corresponding pressure of ~ 169 GPa.

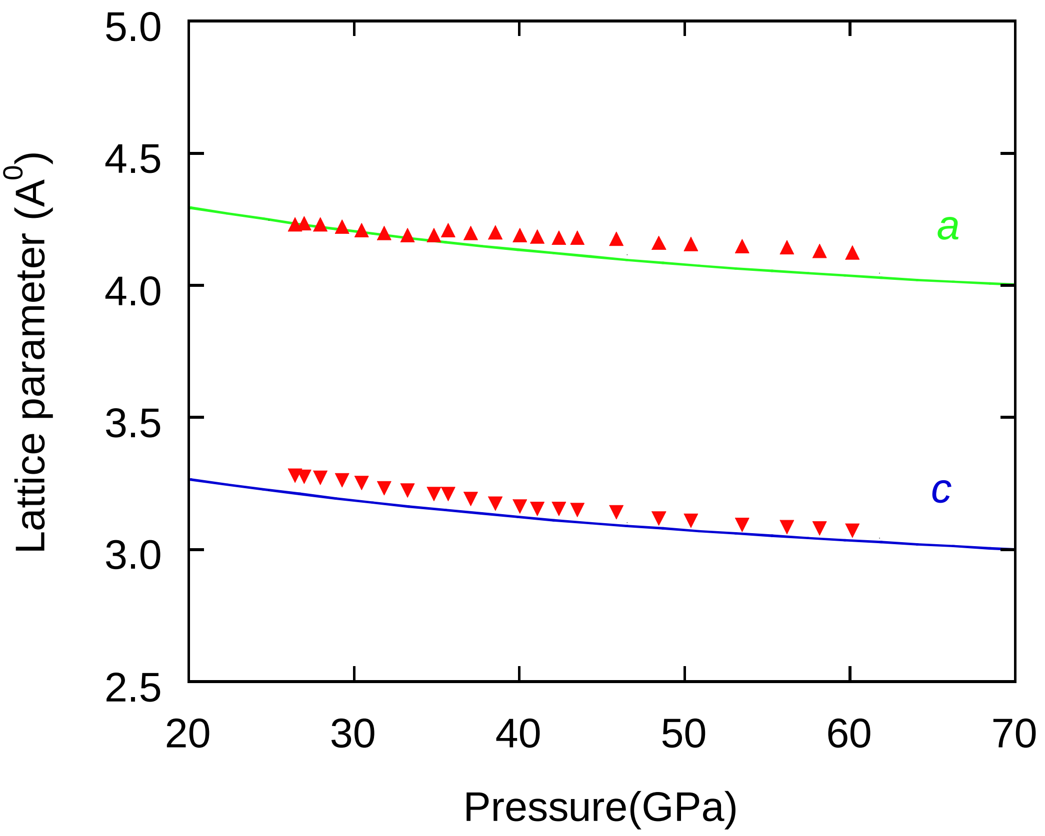

Figure 4.2: The comparison of theoretically optimized lattice parameters of B10 structure with the experimental values of Schneider *et al.* [11] at various pressures.

Further, using calculated total energies and pressures, we have determined the enthalpy of B1, B10 and B2 structures at various pressures. The Fig. 4.4 displays the enthalpies of these structures relative to that of B2 phase. As is clear from the figure, the comparison of enthalpies puts the B1 to B10 transition pressure at ~19 GPa as compared to 25.8 GPa obtained from the comparison of total energy. This is expected as this transition is of first order in nature (as a volume discontinuity occurs at the transition pressure). The B10 to B2 transition is of second order in nature (as no volume discontinuity is associated with this transformation) and thus, the transition pressure determined from the enthalpy comparison is identical to that obtained from the total energy comparison *i.e.* ~ 169 GPa. Table 4.1 compares the theoretically determined transition pressures with available experimental data [11].

Table 4.1: The comparison of theoretically determined phase transition pressures with experimental data.

Phase transition (GPa)	Theory (Present work)		Experimental
	From total energy	From enthalpy	
B1→B10	25.8	19	22.8[11]
B10→B2	169	169	--

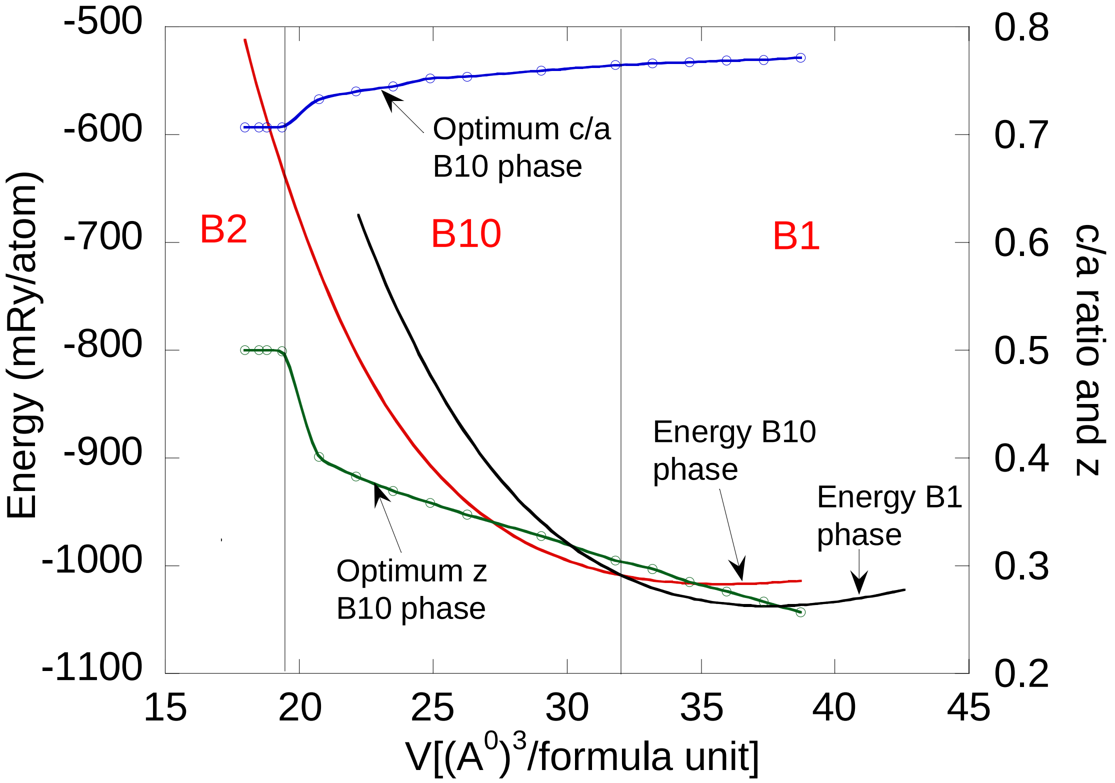

Figure 4.3: The total energy of B1 phase and tetragonal structure. The total energy at each volume for tetragonal structure is plotted for optimum c/a and z. For clarity, the optimized c/a and fractional coordinate z of tetragonal structure as a function of volume is also plotted. It may be noted that for V ≤ 19.44 (Å^3/formula unit), *i.e.*, pressure ≥ 169 GPa, the optimum c/a and z of tetragonal structure saturate at a value of ~ 0.707 and 0.5, respectively, indicating the transition of B10 phase to B2 structure.

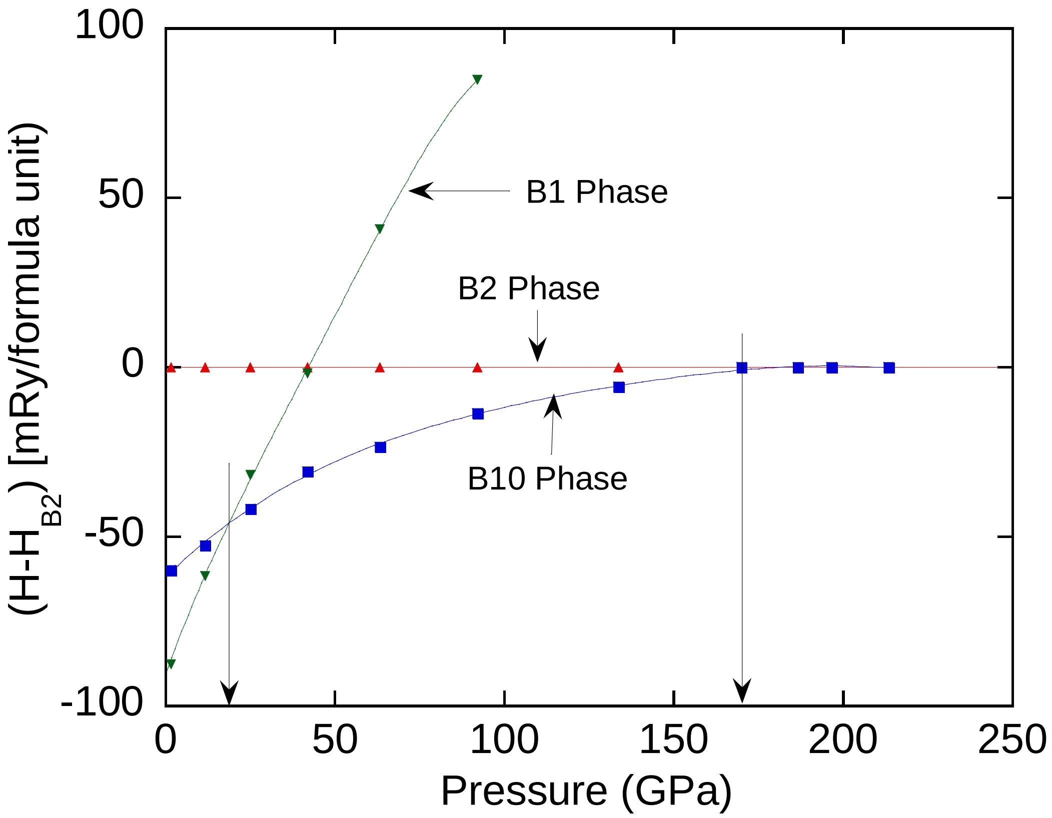

Figure 4.4: The comparison of enthalpy of the B1, B10 and B2 phases as a function of pressure.

The theoretical isotherm along with experimental data [11] is displayed in Fig. 4.5. As far as B1 phase is concerned, the agreement of theoretical isotherm is good with the experimental data [11], whereas, for B10 phase the theoretical isotherm is underestimated systematically as compared to the experimental data with maximum deviation of ~ 16% at experimental pressure of 60GPa (the maximum pressure in the experiment). The volume discontinuity determined theoretically at the B1 → B10 transition point is ~ 9% as compared to the experimental value of 11%. Theoretical isotherm shows no volume discontinuity at B10 → B2 phase transition indicating that this transition will be of second order in nature. Further, in Table 4.2, we have compared equilibrium volume, bulk modulus and its pressure derivative determined theoretically at ambient conditions with the available experimental data [11] and theoretical values reported in literature [6-9, 22]. The equilibrium volume shows excellent agreement with the experimental value, however, the bulk modulus and its pressure derivative agree with the experimental data within ~ 9% and ~ 32%, respectively. Further using B_0' in the Slater's definition [23], we have determined the value of Gruneisen parameter (γ) to be 1.52 (listed in Table 4.2).

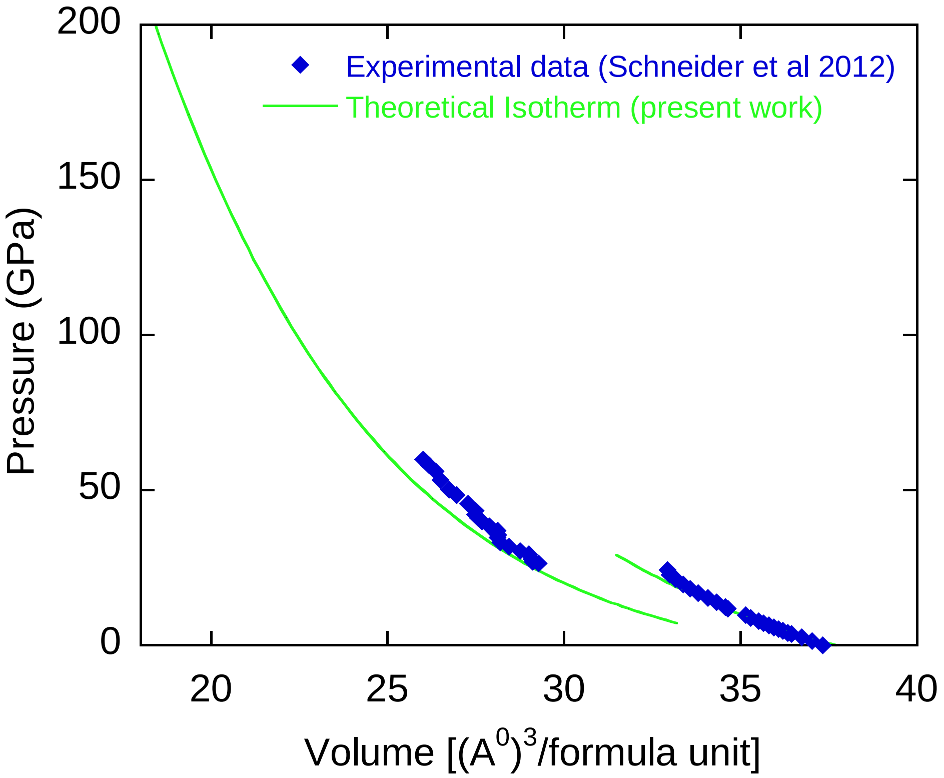

Figure 4.5: Pressure versus volume curve of LaN. The solid curves display the theoretical isotherm and the symbols correspond to the experimental data [11].

Table 4.2: Various physical quantities for B1 phase of LaN at zero pressure.

	Theory Present work	Experimental	Theory (other sources)
V_0 $(A^0)^3$/formula unit	37.53	37.32[11]	37.64[6], 34.3[7], 37.36[8], 36.85[9], 37.37[22]
B_0(GPa)	123.2	135.5[11]	148[6], 152[7], 117[8] 124.4[9], 152[22]
B_0'	3.38	5[11]	3.65[8], 4.48[9], 4.16[22]
C_{11}	208		213[8], 201[10], 221[22]
C_{12}	81		84 [8], 65[10], 118[22]
C_{44}	69		71[8], 49[10], 71[22]
θ_D(K)	318.1		
γ	1.52		

4.3.2 Stability of B10 phase: Symmetry Breaking Mechanism

In an attempt to understand the occurrence of low symmetry B10 structure before the stabilization of high symmetry B2 phase, we have analyzed the electronic band structure and DOS of B10 and B2 structure. To have a proper comparison, the B2 structure is also represented in tetragonal geometry and band structure and density of states are calculated in the tetragonal unit cell for both the B2 and B10 structure. Fig. 4.6 displays the band structure and corresponding DOS for B10 and B2 structure in the pressure regime where the B10 phase is stable. Along with the total DOS, the projected density of states is also plotted. The band structure plot displays that the band gap opens at Fermi energy for both the B10 and B2 structure. However, in B10 phase the opening is extended in all Brillouin zone directions, whereas the same is limited to only Z-R-A-M-X directions for B2 structure. Moreover, the amount of depression in energy bands is large for B10 structure as compared to that for the B2 structure. The total density of states plot displays that for B10 phase there are no states around the Fermi energy, however, that for B2 structure shows a density of ~ 0.5 states/eV at Fermi energy. These results suggest that relatively extended opening of the band gap and large depression of electronic bands near the Fermi energy in B10 as compared to that in B2 structure might have lowered the total energy low symmetry B10 phase and led the stabilization of this structure at lower pressures. The B2 phase due to its higher symmetry has high density of degenerate states (which are composed of *d* states of La and, *s* and *p* states of N hybridized near Fermi energy) near the Fermi energy. The energy of such a high symmetry structure can be lowered by lowering its symmetry as this lifts the degeneracy and pushes some of the states down in energy. It may be possible that the energy lowering caused by this symmetry breaking mechanism in the lower pressure region, is large enough to win over the high symmetry structure supporting Madelung energy term, leading to stabilization of B10 structure, which actually is a distortion of B2 structure. This kind of symmetry breaking mechanism also known Peierls distortion has been found to be even more pronounced in group IV d-electron metals Ti, Zr and Hf, where at lower pressure the low symmetry ω phase, which actually is a distortion of bcc structure occurs before the high symmetry bcc phase stabilizes at higher pressures [24-25]. Similarly, in light actinides the occurrence of low symmetry distorted structures even at ambient conditions has been associated to the lowering of total energy due to Peierls distortion

[26]. It has been argued that in case of group IV d-electron systems it is the narrow d bands pinned near Fermi level play a significant role in stabilizing the lower symmetry ω structure [24, 27], whereas in light actinide series the 5f bands are responsible for stabilizing distorted structures [28].

Additionally, the band structure and distribution of DOS indicates that the HP-LaN structure must be an insulator or semiconductor with a direct band gap of ~ 0.2 eV; however, the B2 phase must be a weakly metallic in character.

4.3.3 Elastic constants as a function of pressure

Further, we have examined the elastic stability of B1 phase under hydrostatic compression. For this purpose, we have calculated the elastic constants of B1 phase as a function of hydrostatic compression. To our knowledge, there are no experimental measurements available on elastic constants of this material. In Table 4.2, we compare the elastic constant of B1 phase at zero pressure calculated in the present work with those reported by other theoretical works [8, 10]. Values reported in the present work show very good agreement with those reported by Cifttci *et al.* [8]. Using these elastic constants, we have determined the zero pressure Debye temperature (θ_D) of LaN by following the procedure provided in Ref. (28-30). As listed in the Table 4.2, the value of θ_D is calculated to be 318.1 K. In Fig. 4.7, we have plotted the variation elastic moduli as a function of pressure. The bulk modulus and shear modulus C' increases monotonically with increasing pressure, however, the shear modulus C_{44} shows opposite trend with increasing pressure. It gets soften with pressure and vanishes at ~ 107 GPa i.e. much beyond the B1 → B10 phase transition pressure.

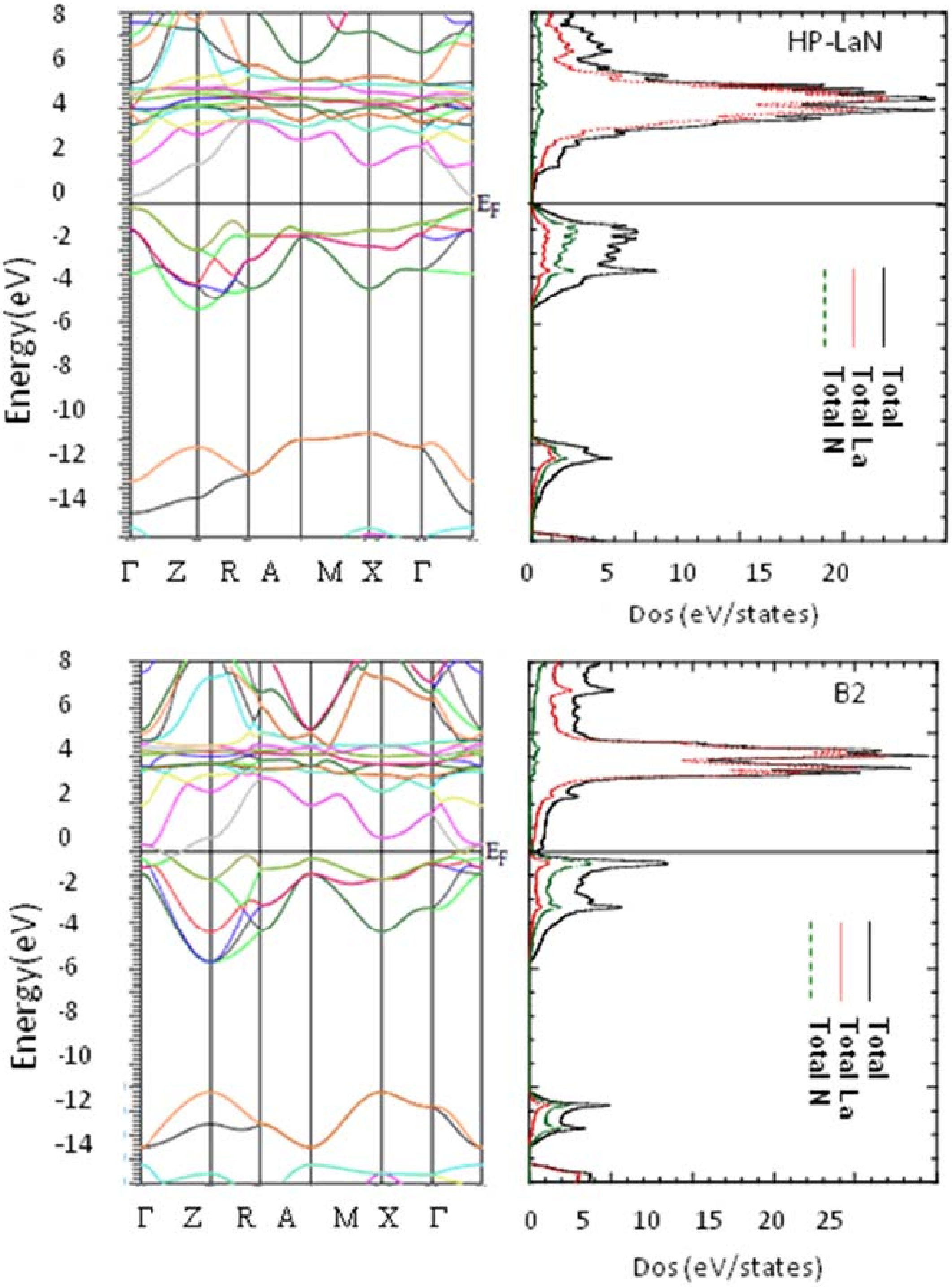

Figure 4.6: The electronic band structure and density of states of LaN in B10 and B2 structure at ~ 30 GPa i.e. in the regime of stability of B10 phase.

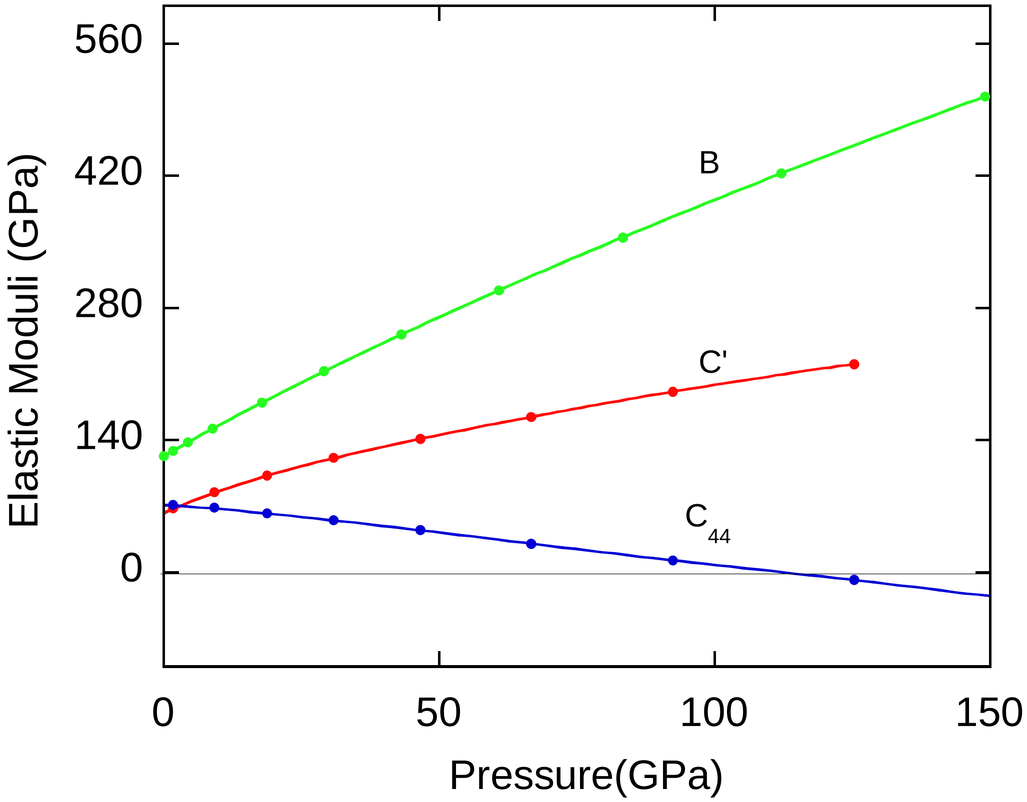

Figure 4.7: Theoretically determined elastic moduli of B1 phase of LaN as a function of pressure.

4.4 Summary

First principles electronic band structure calculations have been performed on LaN using FP-LAPW method with the aim to explore the possibility of existence of low symmetry B10 phase in the low pressure regime before the stabilization of high symmetry B2 phase at higher pressures. Present analysis predicts that the B1 phase of LaN will transform to this B10 primitive tetragonal structure (space group symmetry P4/nmm) at ~ 25.8 GPa as compared to the experimental value of 22.8 GPa [11]. Additionally, it has also been predicted that this structure will transform to B2 phase at higher pressure of ~ 169 GPa. Present analysis of band structure of B10 and B2 phases suggests that the occurrence of B10, which is a distortion of B2 structure, could be due to the Peierls distortion. The examination of elastic moduli as a function of pressure shows that the shear stability of B1 phase reduces monotonically due to decreasing C_{44} modulus. However, the B1 to B10 transition does not seem to be driven by shear instability. Finally, various physical quantities such as V_0, B_0, B_0' have been derived from present theoretical calculations and compared with the available theoretical and experimental data. The agreement of these quantities with experiment is reasonably good. The elastic constants could not be compared with the experimental data as, to our knowledge; there are no experimental measurements available on elastic constants. However, our theoretical values show good agreement with those of Cifttci *et al.* [8].

References

1. V. A. Gubanov, A. L. Ivanovsky, V. P. Zhukov, *Electronic Structure of Refractory Carbides and Nitrides* (Cambridge University Press, Cambridge, 1994).
2. X.-J. Chen, V. V. Struzhkin, Z. Wu, M. Somayazulu, J. Qian, S. Kung, A. N. Christensen, Y. Zhao, R. E. Cohen, H.-k. Mao, and R. J. Hemley, *PNAS* **102**, 3198 (2005).
3. F. Occelli, P. Loubeyre, and R. Letoullec, *Nat. Mater.* **2**, 151 (2003).
4. C. S. Yan, H. K. Mao, W. Li, J. Qian, Y. S. Zhao & R. J. Hemley, *Phys. Stat. Sol. A* **201**, R25 (2004).
5. P. Nesladek and S. Veprek, *Phys. Status Solidi B* **177**, 53 (2000).
6. C. Stampfl, W. Mannstadt, R. Asahi and A. J. Freeman, *Phys. Rev. B*. **63**, 155106-1 (2001).
7. G. Vaitheeswaran, V. Kanchana, M. Rajagopalan, *Solid State Commun.* **124**, 97 (2002).
8. Y. O. Ciftci, K. Colakoglu, E. Deligoz, H. Ozisik, *Mater. Chem. Phys.* **108**, 120 (2008).
9. M. Ghezali, B. Amrani, Y. Cherchab, N. Sekkal, *Materials Chem. and Phys.* **112**, 774 (2008).
10. S. D. Gupta, S. K. Gupta, P. K. Jha, *Comp. Materials Sci.* **49**, 910 (2010).
11. S. B. Schneider, D. Baumann, A. Salamat and W. Schnick, *J. Appl. Phys.* **111**, 093503-1 (2012).
12. A. Aid, R. Khenata, A. Bouhemadou, T. Seddik and Ali H. Reshak, *Advances in Condensed Matter Physics*, 2009: ISBN: 978-81-308-0336-4.
13. D. Varshneya, N. Kauravb, R. Kingea and R. K. Singh, *Phase Transitions: A Multinational Journal* **81**, 1(2008).
14. Y. Fei *et al.*, *Science* **266**, 1678 (1994).
15. H. Ozawa *et al.*, *Phys. Earth Planet. Inter.* **179**, 157 (2010).
16. H. Ozawa, *Phase transition in FeO and its implications for two-layered convection in Earth's outer core*, SPring – 8 Research Frontiers 2011**.**
17. P. Blaha, K. Schwarz, P. Sorantin and S. B. Trickey, *Comp. Phys. Comm.* **59**, 399 (1990).

18. P. Blaha, K. Schwarz and J. Luitz, WIEN2K (Technical University of Vienna).
19. J. P. Perdew, S. Burke and M. Ernzerhof, *Phys. Rev. Lett.* **77**, 3865 (1996).
20. T. W. Samuel, Y. K. Vohra, and A. L. Ruoff, *Phys. Rev. B* **33**, 4221 (1985).
21. F. Birch, *J. Geophys. Res.* 83(1978), 1257-1268.
22. A. T. A. Meenaatci, R. Rajeswarapalanichamy and K. Iyakutti, *Phase Transitions* doi: 10.1080/01411594.2012.713486 (2012), 1-15.
23. J. C. Slater, *Introduction to Chemical Physics* (MCGraw-Hill, New York, 1939)
24. S. C. Gupta, K. D. Joshi and S. Banerjee, *Metall. Mater. Trans.* **39A**, 1593 (2008).
25. D. Mukherjee, K. D. Joshi and S. C. Gupta, *Trans. Indian Inst. of Metals* **64**, 245 (2011).
26. P. Soderlind, *Advances in Physics* **47**, 959 (1998).
27. R. Ahuja, J. M. Wills, B. Johansson and O. Eriksson, *Phys. Rev. B* **48**, 16269 (1993).
28. P. Ravindran, F. Lars, P. A. Korzhavyi, B. Johansson, J. Wills and O. Eriksson, J. *Appl. Phys.* **84**, 4891 (1998).
29. O. L. Anderson, *J. Phys. Chem. Solids* **24**, 909 (1963).
30. E. Schreiber, O. L. Anderson, and N. Soga, *Elastic Constants and their Measurements* (McGraw-Hill, New York, 1973).

Chapter 5

Spall fracture and hardening of polycrystalline copper under shock loading

5.1 Introduction

Depending on the strain rates, the loading of the materials can be broadly categorized as quasi-static loading (strain rates $\leq \sim 10^{-3}$/s) and dynamic loading (strain rates can range from 10^{-3}/s to 10^{8}/s). The dynamic loading can further be classified as intermediate (strain rates ~ 10^{-3}-10^{0}/s), high (strain rates ~ 10^{0}-10^{4}/s) and ultrahigh (strain rates ~ 10^{4}-10^{9}/s) strain rate regimes [1-3]. In many applications materials are not only subjected to the condition of high stresses, but also the condition of high strain rates. Few examples of such conditions are blast and impulsive loading, contact stresses under high-speed bearings, high-speed machining, explosive forming and ballistics. As various mechanical properties such as the yield strength and fracture strength of materials depends not only on the amount of the applied stress but also on the strain rates rate [4-8] *i.e.* the rates at which these are applied, it is not sufficient to have knowledge of these properties only under quasi-static loading conditions. It has been demonstrated experimentally that the yield strength and fracture strength of materials at high strain rates, commonly referred as dynamic yield strength and spall strength, are higher than those measured in quasi static experiments [4-6, 9] and the reason for this overstressing has been associated to the inertia shown by material flaws to respond the rapid loading rates [5, 9]. In fact, in aluminum (Al) and copper (Cu), it has been found experimentally that that at ultrahigh strain rates $\geq 10^{8}$/s the spall strength approaches the ideal value governed solely by inter-atomic forces and corresponds to the maximum tensile stress achievable before spall fracture [9]. Apart from this, for a given material, it has also been demonstrated experimentally that the thickness of the target material also has strong effects on the spall strength [10-11]. Therefore, in order to ensure the suitability of a material for applications pertaining to high strain rates it is useful to measure the strength properties as a function of strain rate as well as thickness.

In past, measurement of dynamic yield strength and spall strength were limited due to unavailability of efficient experimental techniques to generate high tensile stresses at high strain rates and diagnostic techniques required for measurements. But significant advances made in techniques of producing [12-15] and measuring tensile stresses [16-17] at high strain rates in last two decades, have made it possible to generate data on dynamic yield strength and spall strength of many materials [5, 9-11, 18-24]. Apart from these continuum measurements, few advanced laboratories in the world have developed capabilities to carry out in-situ microscopy measurements at high strain rates which have facilitated the understanding of the mechanism of phase transitions or simple mechanical deformation in terms of the atomic level rearrangements [25-28]. The suitably configured shock loading experiments, *e.g.* plate impact experiments, are the one which not only can generate high compressive stresses but also high tensile stresses in target material at high strain rates varying from 10^4/s to 10^9/s. The detailed mechanism of generation of tensile stresses [29] in target material in plate impact experiments has been discussed in chapter 1. In brief, in a plate impact experiment, a planar shock wave propagates into the target material and reflects back as a release wave upon arrival at free surface. Similarly, a shock wave propagating into flyer plate in opposite direction also gets reflected as a rarefaction wave at flyer free surface. The interaction of these two opposite travelling release waves generates large tensile stress in the target which when exceeds the fracture strength causes spall fracture in the target material.

Recently, we have carried out plate impact experiments on commercially available 99.97% pure polycrystalline samples of copper and determined the yield strength and fracture strength at strain rates of ~10^4/s. Apart from this, we have performed the nanoindentation measurements on as received and shock treated sample and examined the effect of shock treatment on the mechanical properties such as hardness and Young’s modulus of the copper. Additionally, the shock recovery experiments have also been carried out on copper samples and analysis of recovered samples has been done using x-ray diffraction (XRD) technique. In order to compare the results on the yield strength and fracture strength at high strain rates with that under quasi-static loading conditions, the quasi-static tensile test have also been carried out on suitably prepared copper sample. This chapter of the thesis presents results on these measurements.

5.2 Experimental Method

5.2.1 Quasi Static Testing

A tensile test is a fundamental mechanical test on a carefully prepared specimen to determine the modulus of elasticity, elastic limit, proportional limit, tensile strength, yield strength, yield point and other tensile properties. The main outcome of a tensile test is load versus elongation data which is then converted to stress-strain curve. An ideal stress-strain curve for a ductile material appears as shown in Fig. 5.1. It has mainly three regions of importance. First portion of the curve is the linear elastic region where the Hooke's law is followed by the material and thus stress is proportional to applied strain. The proportionality constant is known as the modulus of elasticity or the Young's modulus. At some point, the stress-strain curve deviates from the linear relationship and after this point the material undergoes plastic deformation. This point is known as yield point and the corresponding stress is called the yield strength. The transition from elastic to plastic behavior is gradual and the exact point at which this transition occurs is hard to determine. For most of the engineering applications, yield strength is defined as the stress required for a small amount of plastic deformation which is known as offset yield strength. To determine this point a parallel line to the elastic part of the curve offset by some specified strain (0.2% offset) is drawn and the stress corresponding to the intersection of this line to the stress-strain curve gives the 0.2% offset yield strength (Fig. 5.1). After this yield point the material undergoes uniform plastic deformation and comes to a point where the stress is maximum which is known as ultimate tensile strength (UTS). After the ultimate stress, the cross-sectional area of the specimen begins to decrease in a localized region of the specimen, instead of over its entire length causing necking as the specimen elongated further. At the end, the specimen ruptures at that localized position and the corresponding stress is the fracture strength of the material.

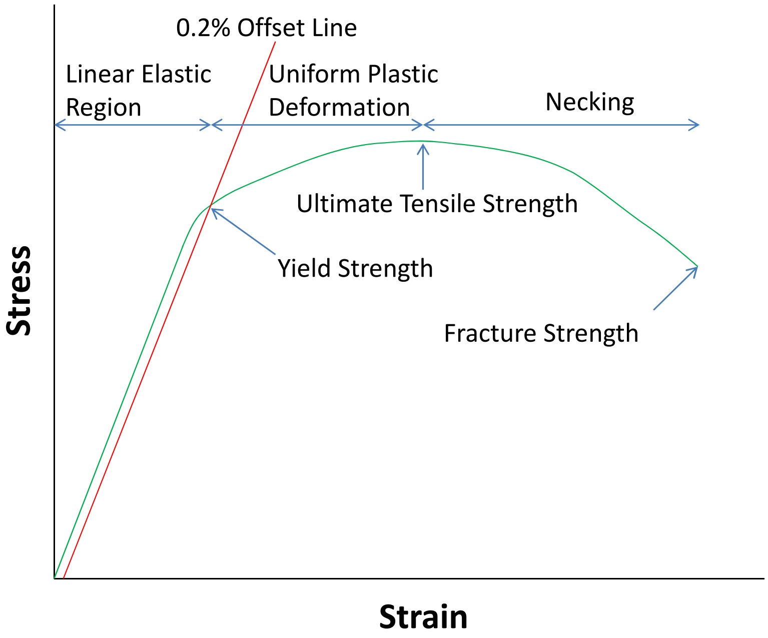

Figure 5.1: Ideal stress-strain relation for a ductile material. Three different region of this curve has been shown with horizontal arrow.

The tensile test of the as-received copper sample is carried out in the 100 kN screw-driven universal servo-hydraulic testing machine (Instron 1185 Machine). The schematic of this machine is shown in Fig. 5.2. Rectangular specimen of total length 85 mm and thickness 3.43 mm has been prepared for this purpose (Fig. 5.3). Gauge length of this specimen is 24 mm and gauge width is 6.14 mm. The holes in the sample are clamped between the crossheads of the machine. The crossheads are pulled apart by the screw driven hydraulic system with speed of the cross head kept at 0.10 mm/min.

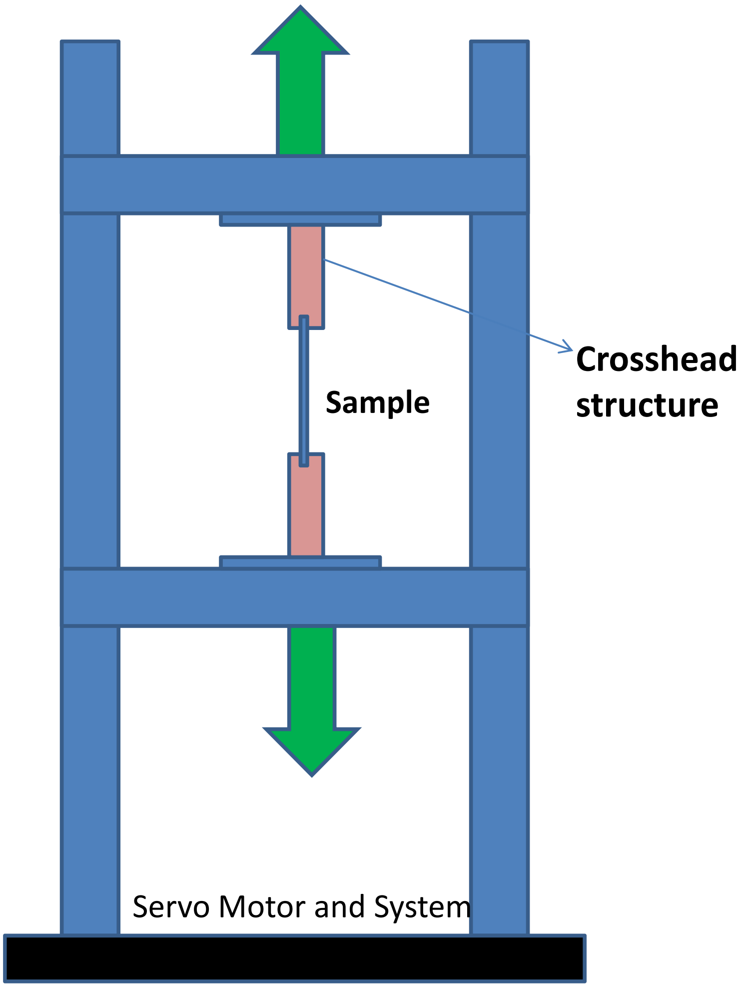

Figure 5.2: Schematic of servo-hydraulic universal testing machine.

Figure 5.3: Specimen of copper plate used for tensile test measurement.

5.2.2 Plate Impact Experiments

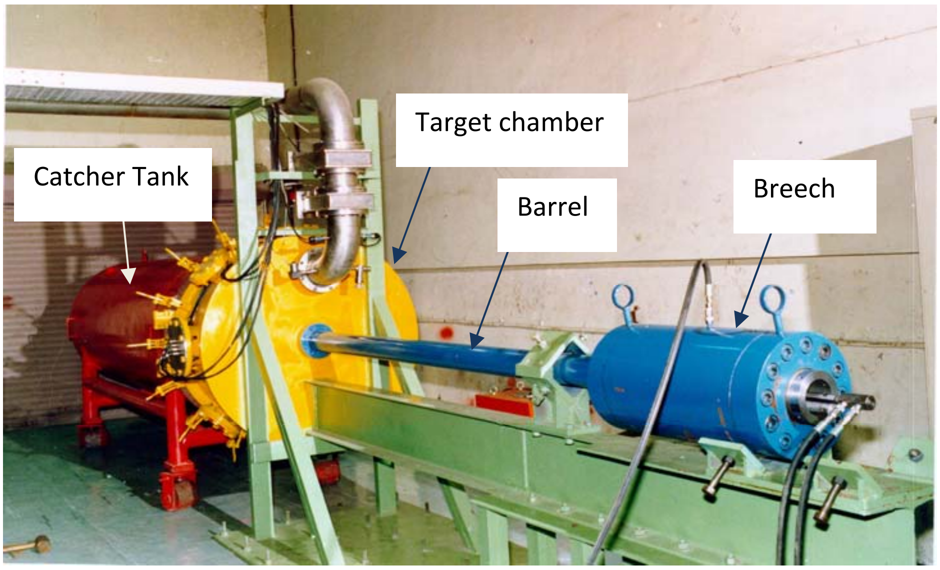

Figure 5.4: Gas Gun facility at Bhabha Atomic Research Centre, Mumbai [30] to conduct plate impact experiments.

The dynamic loading experiments have been conducted on polycrystalline copper samples in a 63 mm bore size single stage gas gun (Fig. 5.4) [30]. The gun has three main parts breech, barrel and target catch-up system (comprises target chamber and catcher tank). The breech is a vessel having capacity of 40 liters, which can hold gases compressed upto a pressure of ~ 420 bars. For plate impact experiment, the projectile consisting of an aluminium cylinder with a copper flyer plate of thickness 4.8 mm and diameter 57 mm attached to its nose was placed inside the projectile holder, residing at the central region of the breech and connecting to the barrel. In order to accelerate the projectile to a desired velocity the breech was filled with helium gas up to required pressure. A small amount of the high pressure gas was injected behind the projectile, causing it to move past the ports on the projectile holder and allowing the high pressure gas filled in the breech to rush behind the projectile. The projectile was accelerated to a desired velocity in a 3m long barrel before it impacted the target plate of the copper fixed in the Perspex target holder ring which was mounted on the target chamber at the muzzle end of the barrel (Fig. 5.5). As shown in the Fig. 5.5, to measure the impact velocity of the flyer plate, four pairs of electrical pins were kept known distance apart from each other in the path of the projectile which got sorted with the moving the projectile body. The impact velocity was then determined from measured time interval between successive electrical output pulses generated by pulse forming unit due to shorting of four pairs of the pins and known distance between successive pairs of the pins. The motion of the free surface of the 15mm thick copper target plate upon the arrival of the shock wave was monitored through optical interferometery technique known as velocity interferometer system for any reflector (VISAR) [31-32]. For this purpose the rear surface of the target plate was illuminated with the laser light (532 nm) and the laser reflected from the free surface of the target was collected back and fed to the interferometer to make fringe pattern. This interferometer which is basically a modified Michelson interferometer beat the two light signals reflected from the free surface of the target plate at two instants of time separated by a small interval of ~ few nanoseconds and corresponding fringe shift as a function time was recorded. This time dependent fringe shift was then utilized to derive the free surface velocity history which then was utilized to determine the dynamic yield strength and spall strength of copper plate.

The required target and flyer plate in the form of circular discs have been prepared from a large plate of the copper. The initial density (ρ_0) of the copper plates was measured to be 8.905 ± 0.005 g/cc. The shock pressure of 10.4 GPa is generated in the target plate by impacting it with a 4.8 mm thick and 57 mm diameter impactor plate made of the same material and accelerated to the peak velocity (V_p) of 0.52 km/s.

Additionally, a shock recovery experiment has also been carried out in the copper sample. The aim of this experiment was to see the post compression effect on copper sample under uniaxial strain compression conditions. A typical schematic of the target assembly for this experiment is displayed in Fig. 5.6. A circular sample of copper of 10 mm diameter and 1.2 mm thickness was fitted into a matching hole of stainless steel (SS304) plate of diameter 44mm and this plate is then fitted in a SS304 ring of inner diameter 44.05mm and outer diameter 85mm. The presence of this ring mitigated the affect of lateral release waves on uniaxial strain compression condition. This assembly is then emplaced into a steel capsule of 88 mm of inner diameter and

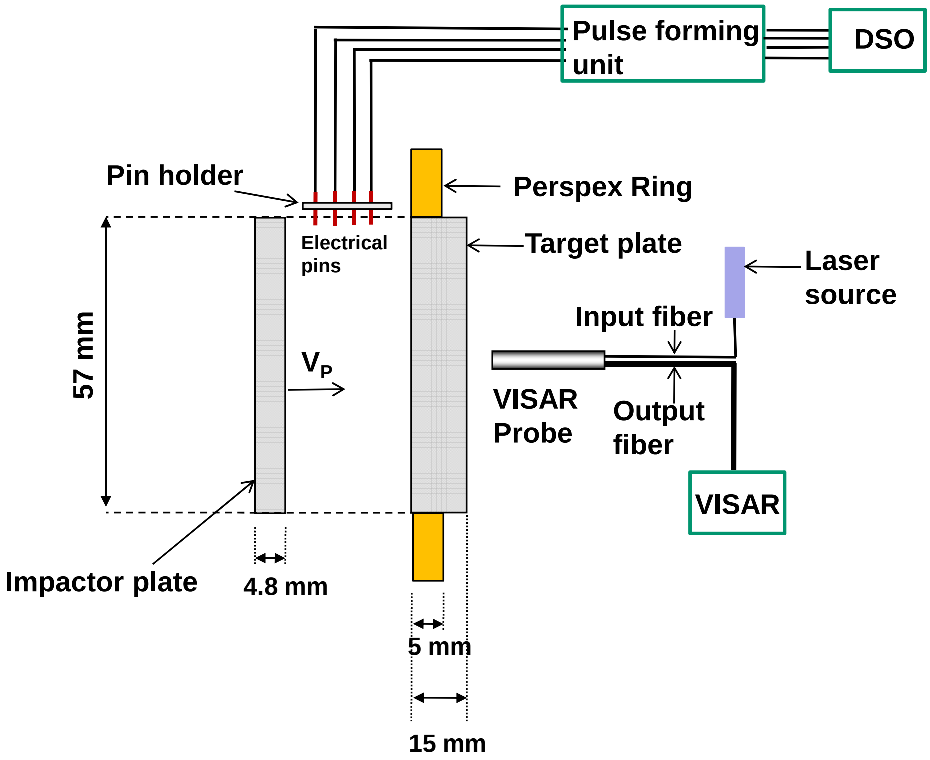

Figure 5.5: Typical schematic diagram of experimental layout for plate impact shock wave experiment on copper target. As shown in figure the target copper plate having thickness 15 mm and diameter 57 mm is fixed in Perspex target holder ring of thickness of 5 mm. A VISAR probe consisting of a single mode launching fiber and a multimode collection fiber is mounted with fiber ends at a distance of ~ 2 mm from the free surface with a suitable mounting arrangement. The output of the collecting fiber is fed to the interferometer system.

110 mm of outer diameter as shown in Fig. 5.6. The sample was covered by a 3mm steel cover plate and locked tightly by a locking nut. Two momentum trap plates of steel have been glued consecutively in the rear surface of the recovery fixture. The details of the working and momentum trapping mechanism have been discussed elsewhere (33). The catcher tank is used to arrest the target and projectile debris after the impact is taken place. The sample recovered after unloading from peak shock pressure of ~ 12 GPa has been analyzed through x-ray diffraction and nanoindentation method.

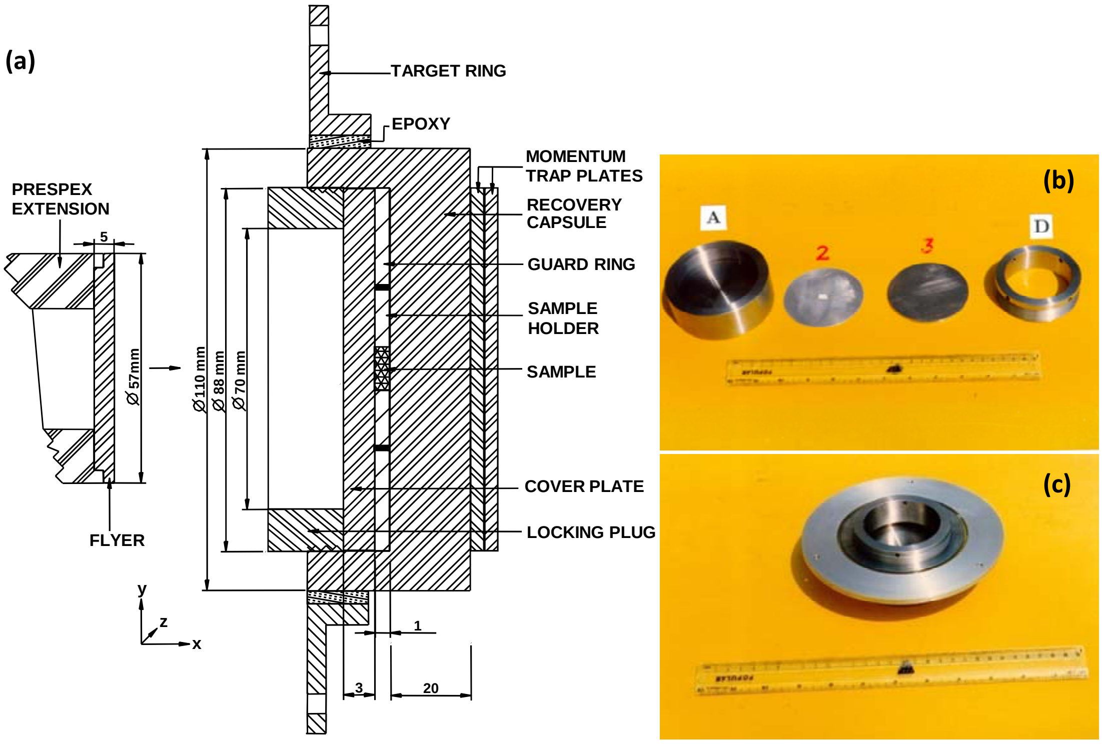

Figure 5.6: (a) Schematic diagram of the recovery fixture. (b) Picture of the different parts of the recovery fixture (upper picture) and (c) the assembled recovery fixture.

5.3 Method of Analysis of Experimental Data

5.3.1 The Analysis of Free Surface Velocity History

The impact of copper flyer plate on the stationary target plate generated planer shock waves propagating in forward direction in target plate and in backward direction in flyer plate (as discussed in chapter 1). The forward moving shock reached the free surface of the target and due to the impedance mismatch at the rear surface the shock wave reflected from target free surface as backward moving release wave. Similarly, the backward moving shock reflected from the flyer free surface as forward moving release wave. The interaction of these release waves in the target generated tensile stress and when this stress exceeded the strength of the material it spalled. The arrival of shock wave and the generation of release wave as well as spall fracture are manifested in the free surface velocity (U_{fs}) history of the impacted sample. To discuss the method of analyzing the free surface velocity history data, in

Fig. 5.7, an ideal free surface velocity profile of a material undergoing elastic to plastic transformation followed by phase transition and spallation has been displayed.

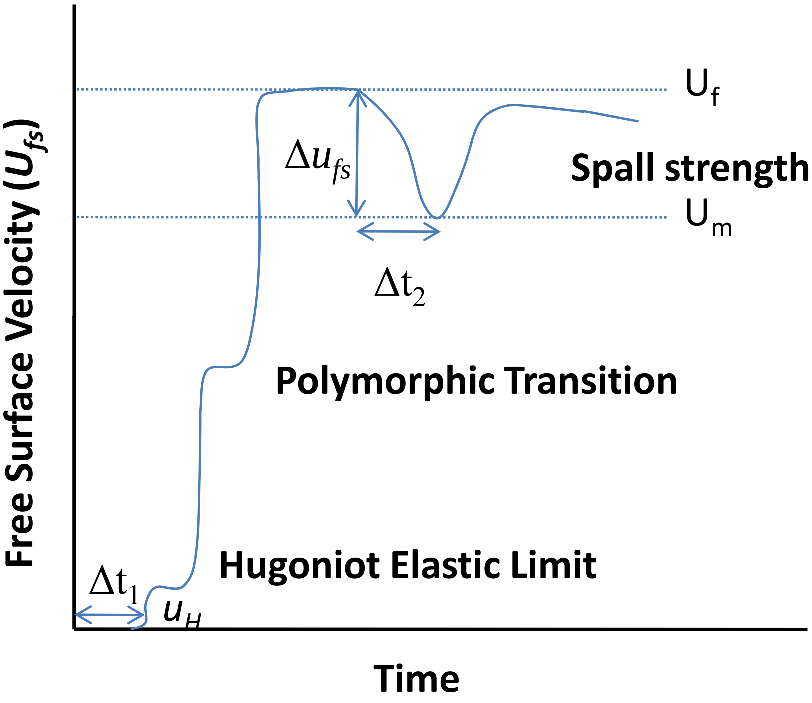

Figure 5.7: Ideal free surface velocity profile of material showing features corresponding to various phenomenons.

The first portion (i.e. from zero to peak velocity) corresponds to compressive stress, whereas, the later portion represents the tensile regime. The Huogoniot elastic limit (σ_{HEL}), strain rate ($\dot{\varepsilon}_c$) corresponding to σ_{HEL}, the spall strength (σ_s) and strain rate ($\dot{\varepsilon}_t$) corresponding to σ_s, are determined from this profile as follows [2-3, 26]:

$$\sigma_{HEL} = \frac{1}{2} U_H \rho_0 c_l \tag{5.1}$$

$$\dot{\varepsilon}_c = \frac{U_H}{2\Delta t_1} \frac{1}{c_l} \tag{5.2}$$

The dynamic yield Y from the σ_{HEL} is deduced using following expression:

$$Y = \sigma_{HEL} \frac{(1-2\sigma)}{(1-\sigma)} \tag{5.3}$$

$$\sigma_s = \frac{1}{2} \Delta U_{fs} \rho_0 c_b \tag{5.4}$$

$$\dot{\varepsilon}_t = \frac{\Delta U_{fs}}{2\Delta t_2} \frac{1}{c_b} \tag{5.5}$$

Here, U_H is free surface velocity at σ_{HEL}. The Δt_1 is the time taken for free surface to reach a velocity of U_H. The c_b, c_l and σ correspond to the bulk sound speed, longitudinal sound speed and Poisson ratio, respectively. The pull back velocity is defined as $\Delta U_{fs} = U_f - U_m$ where U_f is the peak free surface velocity and U_m is free surface velocity just ahead of spall pulse. The Δt_2 is the time taken by the free surface to retard from the peak velocity U_f to U_m.

5.3.2 Analysis of Nanoindentation Data

The nanoindentation measurements have been carried out on as-received and shock treated samples. The analysis of the nanoindentation data to determine the micromechanical properties, *e.g.* nanohardness and Young's modulus was carried out using well known Oliver-Pharr [34-35] model. The nanoindentation experiment were carried out using a nanoindentation machine (UNHT S/N: 50-00002) at a fixed maximum load (P_{max}) of 30 mN, with force and depth sensing resolutions of 0.2 μN and 0.1nm. Experiments were conducted using a load-time sequence. For each loading-unloading cycle, the loading and unloading rates were 60 mN/minute, *i.e.* the loading and unloading cycles each lasted 30s, respectively. During each test run, a personal computer collected and stored data for the load and displacement as the indenter was driven into the sample (loading segment) and then withdrawn from it (unloading segment). The raw data were then used to construct the load-displacement plot. The deformation during loading is assumed to be both elastic and plastic in nature, however, during unloading it is assumed that only elastic deformations are recovered [34-35]. The hardness (H) is estimated from the expression [34-35]:

$$H = \frac{P_{\max}}{A_r} \tag{5.6}$$

Here P_{max} is maximum load and A_r is the area of the residual indentation in the sample. The Young's modulus (*E*) is determined using the expression [34-35]:

$$\frac{1}{E'} = \frac{1-\nu^2}{E} + \frac{1-\nu_i^2}{E_i} \tag{5.7}$$

With E' is the effective Young's modulus and, E and E_i are Young's modulus of sample and indenter, respectively. The ν_i is the Poisson ratio of the indenter. The E' is related to the unloading stiffness and contact area with following expression [34-35]:

$$E' = \frac{S}{2\beta\sqrt{A_r}}\sqrt{\pi} \tag{5.8}$$

Here "*S*", which is obtained from the slope of the upper portion of the unloading curve, is called elastic unloading stiffness. The indenter geometry dependent constant β is 1.034 for Burkovich indenter [34-35].

5.4 Results and Discussions

5.4.1 Yield Strength and Fracture Strength from Quasistatic Test

Fig. 5.8 shows the stress versus elongation curve for as-received copper sample under quasistatic loading condition. The large strain hardening region of the stress-elongation diagram implies that copper is ductile in nature. Tensile strength at yield point (0.2% offset) has been found to be 130 MPa. The ultimate tensile strength is found to be 221 MPa corresponding to elongation of 11.802 mm.

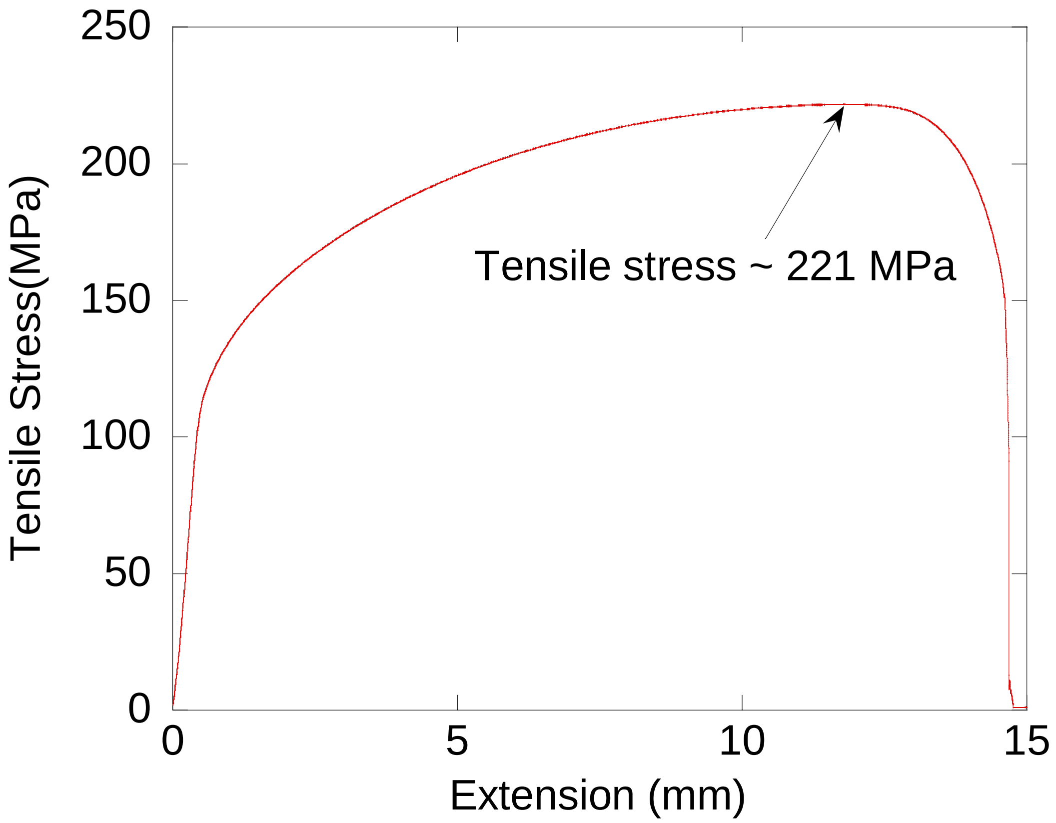

Figure 5.8: Stress versus elongation curve for the as received sample of copper.

5.4.2 Yield Strength and Fracture Strength from Plate Impact Experiment

Fig. 5.9 displays the free surface velocity history of Cu target plate recorded using VISAR. The peak free surface velocity of 0.51 km/s is very close to the impact velocity of 0.52 km/s measured by successive shorting of four pairs of electrical pins by the flyer plate just before the impact. This is expected as in the symmetric impact configuration, *i.e.* impactor and target made of same material, the maximum free surface velocity is almost equal to the impact velocity. As expected, there is not any signature of polymorphic phase transition in the free surface velocity profile. The U_H and ΔU_{fs} determined from the free surface velocity history are 0.014 km/s and 0.075 km/s with the time interval Δt_1 and Δt_2 of 0.3 μs and 0.6 μs, respectively. The c_l, c_b and ν are taken to be 4.76 km/s, 3.96 km/s and 0.34 from available literature [36, 37]. These quantities upon substitution in Eqn. (5.1) through (5.5) yielded the σ_{HEL} , $\dot{\varepsilon}_c$, Y

, σ_s and $\dot{\varepsilon}_t$ as listed in the Table 5.1. As shown in the Table 5.1, the yield strength and spall strength of copper measured at strain rates ~ 10^4/s in the present work is found to be 0.14 GPa and 1.32 GPa. The spall strength found from this dynamic compression experiment is higher by a factor of ~ 6 than the quasi static values, whereas, the yield strength measured at these high strain rates is marginally higher than the quasi static value. Further, as shown in Table 5.1, the spall strength measured in the present symmetric plate impact experiment agrees well with that measured by Moshe *et al* [9] in laser shock experiments and by Kanel *et al.* [38] in explosive driven asymmetric plate impact experiments. Additionally, the spall strength of 1.32 GPa measured in bulk polycrystalline copper in the present experiment is much lower than the 3.0 GPa measured in the nanocrystalline copper [24] and ~ 4.5 GPa measured in single crystal of copper along [100] direction [11, 38]. The reason for the higher spall strength of nanocrystalline copper than the polycrystalline bulk copper could be associated to the presence of relatively large number of grain boundaries [24]. However, the large spall strength exhibited by single crystal copper could be due to presence of relatively less number of damage nucleation sites in highly homogeneous single crystal of copper [11].

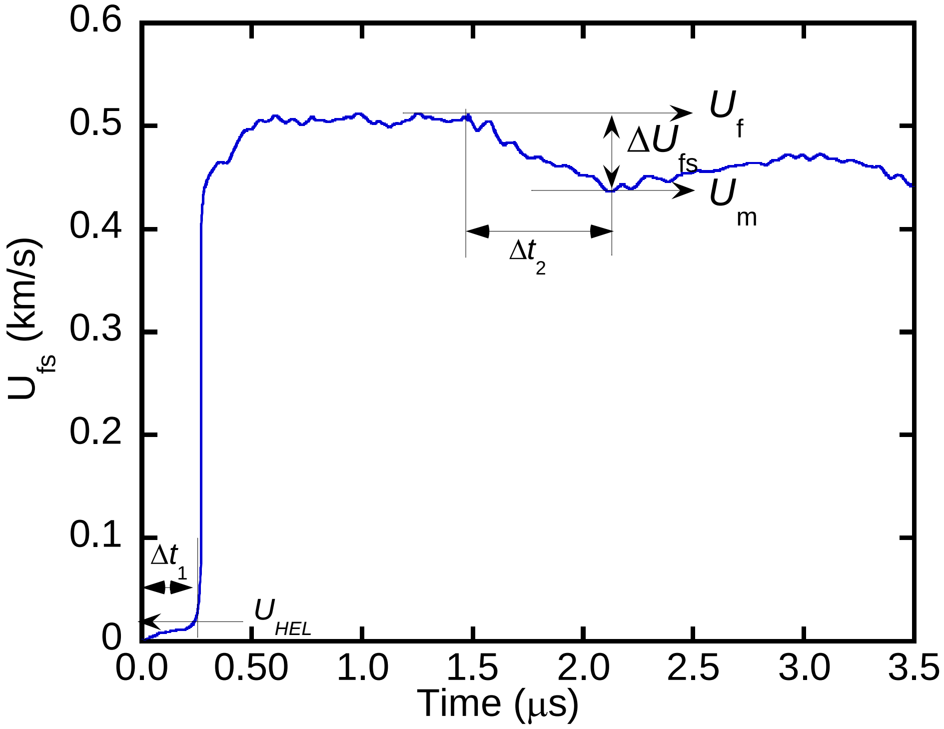

Figure 5.9: The free surface velocity history of shock loaded copper target recorded using VISAR.

Table 5.1: The dynamic yield strength, spall strength and corresponding average strain rates measured in the present work. A comparison also made with data measured under quasi static loading conditions.

Properties	High strain rate loading (present work)	High strain rate loading (other sources)	Quasi static loading (Present work)
σ_{HEL}(GPa)	0.29 ± 0.003	0.31[32]	
$\dot{\varepsilon}_c$ (s^{-1})	$4.90 \pm 0.060 \times 10^3$	7.90×10^3[32]	
Y(GPa)	0.14 ± 0.001	0.15[32]	0.13
σ_s(GPa)	1.32 ± 0.01	1.25[6],1.23[32]	0.22
$\dot{\varepsilon}_t$ (s^{-1})	$1.57 \pm 0.158 \times 10^4$	10^4[6],1.5×10^4[32]	

5.4.3 Nanoindentation Measurements

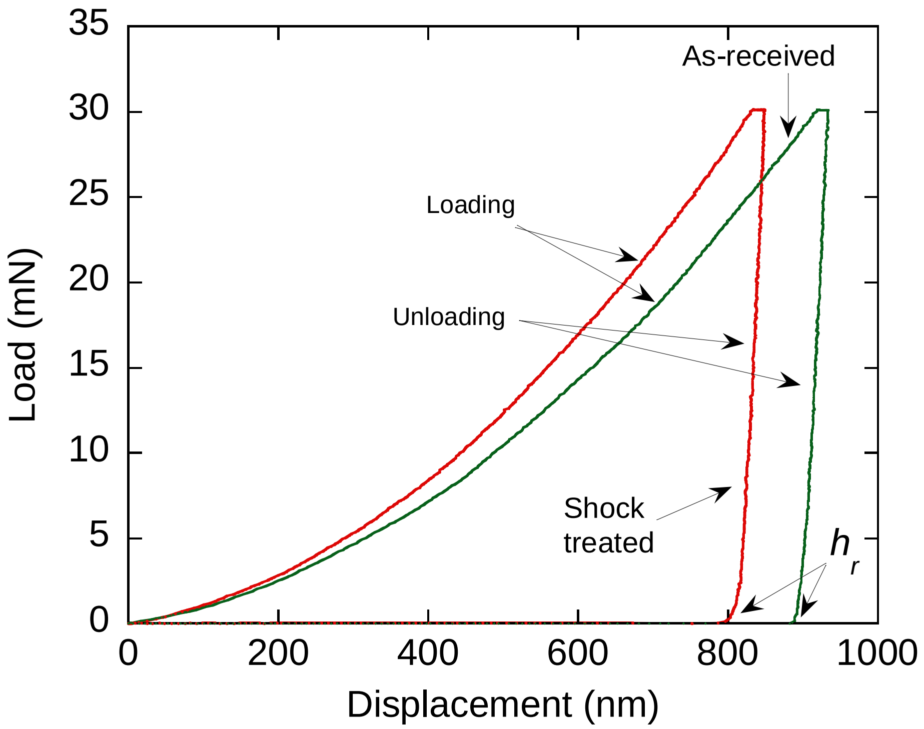

Figure 5.10: Indentation load-displacement curve of shock treated and as received copper sample.

In order to determine the hardness and elastic modulus of as received and shock treated polycrystalline copper sample the nanoindentation experiments using Berkovich indenter have been conducted at the maximum load of 30 mN. Fig. 5.10 displays indentation load-displacement diagram for loading as well as unloading cycle. As can be seen from this figure both the maximum depth of penetration and the permanent depth of penetration for the shock treated samples is less as compared to that for the as received Cu sample (Table 5.2), indicating the increase in hardness or stiffness of the Cu sample after shock treatment. Various parameters measured from nanoindentation experiments on the shock treated and as received Cu are listed in the Table 5.2. As shown in Table 5.2, the S parameter of shock treated sample is increased by ~ 14% as compared to that of the as received Cu. Finally, the hardness and Young's modulus of shock retrieved sample has increased by ~18% and ~29%, respectively. These results of nanoindentation experiments on shock treated and as received Cu samples suggest that the passage of the shock through Cu target plate has increased its hardness and Young's modulus.

Table 5.2: Various parameters measured from nanoindentation experiments.

Properties	As received Cu	Shock treated Cu
$h_{\max}$(nm)	933.09	849.69
S(mN/nm)	1.0316	1.1726
h_r(nm)	889.89	801.91
A_r(nm^2)	2.488×10^7	2.097×10^7
H(GPa)	1.207	1.433
E′(GPa)	177	219
E(GPa)	185	239

5.4.4 X-Ray Diffraction Measurements

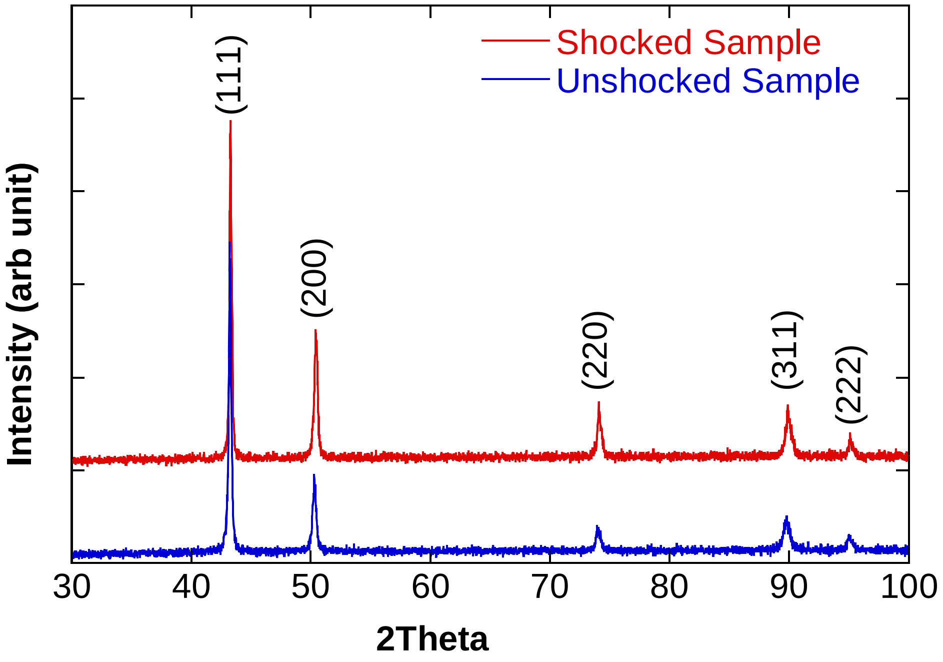

Figure 5.11: ADXRD patterns of shock treated copper sample. Also displayed is the diffraction pattern of initial unshocked sample for comparison.

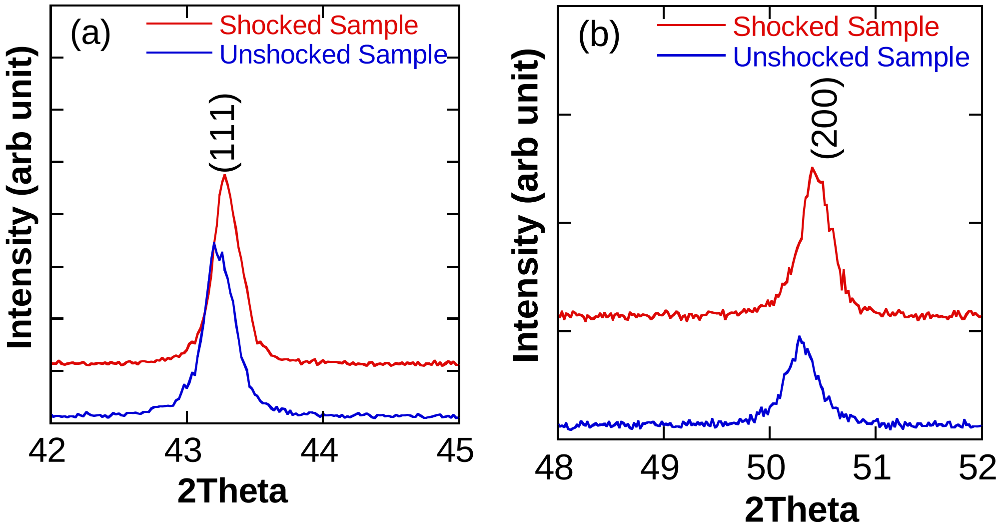

Figure 5.12: Most intense diffraction peaks (111) and (200) of the shock recovered sample and the as-received sample.

The sample recovered from peak shock pressure of ~ 12 GPa from shock recovery experiment has been analyzed through angle dispersive x-ray diffraction (ADXRD) technique. The x-ray diffractions of the copper sample are carried out in Ultima IV machine of Rigaku make. Continuous 2θ scanning mode is used with scanning speed of 2.000 deg/min and step width of 0.0200 deg. Scan (2θ) is done from 30 deg to 100 deg. The diffraction pattern of shock treated sample has been compared with that of the as received (unshocked) sample. Fig. 5.11 shows the diffraction patterns of the shocked as well as the initial unshocked sample. The diffraction peaks of both unshocked and shock treated samples are indexed for fcc structure. As is shown in Fig. 5.11, all the diffraction peaks of the shock treated copper sample are shifted towards higher angles as compared to those of as received sample. For more clarity the most intense (111) peak and (200) of shocked and as received samples are also displayed in Fig. 5.12(a) and 5.12(b). The percentage change in the *d*-spacing of different set of planes is listed in Table 5.3. These observations indicate that the shock treated copper sample has undergone a uniform compressive residual strain.

Table 5.3: Percentage fractional shift in d-spacing of various crystallographic planes measured from x-ray diffraction. Here d_0 and d_p are the *d*-spacing of various (hkl) planes of as received and shock retrieved Cu sample, respectively. $100\times(d_p-d_0)/d_0$ is the percentage shift in d-spacing of shock treated Cu.

(hkl)	*d*-spacing (Å)		Percentage shift in d-spacing ($100\times(d_p-d_0)/d_0$)
	d_0(Å)	d_p(Å)	
(111)	2.0929	2.0891	-0.18
(200)	1.8127	1.8085	-0.23
(220)	1.2806	1.2788	-0.14
(311)	1.0920	1.0903	-0.15
(222)	1.0449	1.0443	-0.05

5.5 Summary

To summarize, quasistatic and high strain rate tensile tests have been carried out in polycrystalline copper of purity 99.99%. The yield strength and fracture strength measured in quasi static loading conditions are 0.13 GPa and 0.22 GPa, respectively. The high strain rate loading in copper sample has been achieved in plate impact experiment carried out using single stage light gas gun. The average strain rates generated in the copper sample were ~ 10^4/s with impact velocity of ~ 0.52 km/s and peak shock pressure of ~ 10 GPa. The yield strength and spall (fracture) strength determined at these strain rates from measured free surface velocity history are 0.14 GPa and 1.32 GPa, respectively. The value of yield strength measured at these strain rates is marginally higher than that measured in quasi static test, whereas, the fracture strength increases by ~ 6 fold as compared to that at quasi static conditions. The spall strength measured in the present work agrees well with 1.25 GPa, that available from other source [9].

The nanoindentation measurements carried out in shock treated and unshocked copper sample reveal that the shock treatment has increased its hardness and elastic modulus by ~ 16% and ~29%, respectively. The comparison of the x-ray diffraction patterns of the unshocked and shock treated copper sample showed: (i) the shift towards higher angles in all diffraction peaks of the shock treated sample as compared to that of the unshocked sample. This shift could be due to a residual uniform compressive strain in the shock retrieved sample.

References

1. M. V. Zhernokletov, B. L. Glushak, *Material Properties under Intensive Dynamic Loading* (Springer 2006).
2. H. A. Colorado, A. Navarro, S. V. Prikhodko, J. M. Yang, N. Ghoniem, and V. Gupta, *J. Appl. Phys.* **114**, 233510 (2013).
3. K. T. Ramesh, *Springer Handbook of Experimental Solid Mechanics* (Ed.: Jr. W. N. Sharpe), pp 929-960 (2008).
4. N. Eliaz, E. Moshe, S. Eliezer, and D. Eleizer, *Metall. Mater. Trans. A* **31**, 1085 (2000)
5. G. I. Kanel, S. V. Razorenov, A. V. Utkin, V. E. Fortov, K. Baumung, H. U. Karow, D. Rusch, V. Licht, *J. Appl. Phys.* **74**, 7162 (1993).
6. K. D. Joshi, A. S. Rav, S. C. Gupta and S. Banerjee, *J. Phys. Conf. Series* **215**, 012149 (2010).
7. G. I. Kanel, *J. Mech. Phys. Solids* **46**, 1869 (1998).
8. G. I. Kanel, S. V. Razorenov, A. Bogatch, A. V. Utkin and D. E. Grady, *Int. J. Impact Engg.* **20**, 467 (1997).
9. E. Moshe, S. Eliezer, Z. Henis, M. Werdiger, E. Dekel, Y. Horovitz, S. Maman, I. B. Goldberg and D. Eliezer, *Appl. Phys. Lett.* **76**, 1555 (2000).
10. X. Chen, J. R. Asay, S. K. Dwivedi and D. P. Field, *J. Appl. Phys.* **99**, 023528-1 (2006).
11. G.I. Kanel, *Int. J. Fract.* **163**, 173 (2010). DOI 10.1007/s10704-009-9438-0 (and references therein).
12. W. J. Nellis, J. A. Morarity, A. C. Mitchell and N. C. Holmes, *J. Appl. Phys.* **82**, 2225 (1997).
13. A. Benuzzi, T. Löwer, M. Koenig, B. Faral, D. Batani, D. Beretta, C. Danson, and D. Pepler, *Phys. Rev. E* **54**, 2162 (1996).
14. Y. M. Gupta, *Shock Compression of Condensed Matter-1999*, (Eds. M.D. Furnish, L.C. Chhabildas and R.S. Hixson, AIP, 2000) p. 3.
15. J. R. Asay, *Int. J. Impact Engg.* **20**, 27 (1997).
16. M. D. Furnish, L. C. Chhabildas, and W. D. Reinhart, *Int. J. of Impact Engg.*, **23**, 261 (1999).
17. L. M. Barker and R. E. Hollenbach, *J. Appl. Phys.* **43**, 4669 (1972).
18. D. D. Bloomquist and S. A. Sheffield, *J. Appl. Phys.* **54**, 1717 (1983).

19. G. I. Kanel, S. V. Razorenov, K. Baumung and J. Singer, *J. Appl. Phys.* **90**, 136 (2001).
20. G. I. Kanel, S. V. Razorenov, E. B. Zaretsky, B. Herrman and L. Meyer, *Phys. Solid State* **45,** 656 (2002).
21. G. I. Kanel, S. V. Razorenov and V. E. Fortov, *J. Phys Cond. Matter* **16**, S1007 (2004).
22. P. B. Trivedi, J. R. Asay, Y. M. Gupta and D. P. Field, *J. Appl. Phys.* **102** 083513-1 (2007).
23. S. N. Luo, D. C. Swift, T. E. Tierney IV, D. L. Paisley, G. A. Kyrala, R. P. Johnson, A. A. Hauer, O. Tschauner and P. D. Asimow, *High Press. Res.* **24**, 409 (2004).
24. W. J. Murphy, A. Higginbotham, G. Kimminau, B. Barbrel, E. M. Bringa, J Hawreliak, R. Kodama, M. Koenig, W. McBarron, M. A. Meyers, B. Nagler, N. Ozaki, N. Park, B. Remington, S. Rothman, S. M. Vinko, T. Whitcher and J. S. Wark, *J. Phys.: Condens. Matter* **22**, 065404 (2010).
25. Y. Wang, H. He, M. Boustie, T. Sekine, *J. Appl. Phys.* **101**, 103528-1 (2007).
26. T. d'Almeida and Y. M. Gupta, *Phys. Rev. Lett.* **85**, 330 (2000).
27. B. J. Jensen and Y. M. Gupta, *J. Appl. Phys.* **100**, 053512-1 (2006).
28. S. J. Turneaure and Y. M. Gupta, *Appl. Phys. Lett.* **90**, 051905-1 (2007).
29. K. D. Joshi and S. C. Gupta, *High Press. Res.* **27**, 259 (2007).
30. S. C. Gupta, R. G. Agrawal, J. S. Gyanchandani, S. Roy, N. Suresh, S. K. Sikka, A. Kakodkar and R. Chidambaram, *Shock Compression of Condensed Matter* (Eds. S. C. Schmidt, R. D. Dick, J. W. Forbes and D. G. Taksar (Elsevir Science, 1992) p. 839.
31. L. M. Barker and R. E. Hollenbach, *J. Appl. Phys.* **43**, 4669 (1972).
32. D. H. Dolan, "*Foundations of VISAR analysis*", Technical Report No. SAND2006–1950 (2006).
33. N. Suresh, Thesis, Mumbai University.
34. W. C. Oliver and G M. Pharr, *J. Matter Res.* **7**, 1564 (1992).
35. W.C. Oliver and G M. Pharr, *J. Matter Res.* **19**, 3 (2004).
36. S.P. Marsh, *LASL Shock Hugoniot Data* (University of California Press, 1980).
37. Francois Cardarelli, *Materials Handbook, A concise Desktop Reference 2nd Edition*, (Springer, New York, London, 2005) p. 1187.

38. G. I. Kanel, S. V. Razorenov, A. V. Utkin and K. Baumung: *Shock Wave Profile Data*, (Russian Academy of Science, 1996) p. 57.

Chapter - 6

Summary and Future Scopes

The thesis has presented the *ab-initio* electronic band structure calculations to examine high pressure behaviour of binary systems LiH, MgO and LaN under pressure. Most of such binary systems have been reported experimentally/theoretically to undergo B1 to B2 structural transition under pressure [1-3]. In LiH and MgO, we also predict the B1 to B2 structural phase transition under pressure, however, unlike LiH and MgO, in LaN, the B1 phase is found to undergo a transition to lower symmetry B10 (which is a distortion of B2 phase) phase at ~ 25.8 GPa, which is in agreement with experimental observations of Schneider *et al* [4]. Further, we have predicted that the B10 phase will transform to B2 structure at pressures above 169 GPa, upon further compression. The occurrence of the low symmetry B10 structure before the stabilization high symmetry B2 phase has been explained by invoking the symmetry breaking mechanism. Apart from these theoretical studies, experimental shock compression study on elemental solid copper has also been presented in the thesis. The aim of this shock compression study was to determine the dynamic yield strength and spall strength of polycrystalline copper at strain rates of ~10^4/s. The main results of the studies conducted on these materials and presented in different chapters of the thesis are summarized below:

Total energy calculations on the binary system LiH, MgO and LaN have been carried out to investigate the possibility of B1 → B10 → B2 phase transition sequence under pressure. At ambient conditions, each of these systems exists in rocksalt type structure (B1 phase). For LiH and MgO, the theoretical analysis predicts the B1 to B2 (CsCl type structure) structural transition at a pressure of ~ 327 GPa and ~ 535 GPa, respectively, whereas for LaN, the B1 phase transforms to B10 (a tetragonal phase, which can be regarded as distortion of B2 phase) phase at ~ 25.8 GPa, in close agreement with the experimental value of 22.8 GPa [4]. The B10 phase is found to be stable upto ~ 169 GPa and beyond this pressure the B2 phase becomes favorable over the B10 phase. The stability of the low symmetry tetragonal phase in LaN has been associated to symmetry breaking mechanism induced lowering of total energy.

Further, adding thermal corrections to the first principles 0K energies at various hydrostatic compressions, the 300K isotherm have also been determined. Apart from this, the pressure dependent elastic moduli for B1 phase have also been calculated for LiH, MgO and LaN. Various thermophysical properties such equilibrium volume, bulk modulus, its pressure derivative, Debye temperature, elastic constants and Gruneisen parameter at zero pressure have been derived from these calculations and compared with the available experimental data.

In LiH apart from static lattice calculations, the lattice dynamic calculations have also been performed up to ~ 150 GPa and phonon spectra have been determined as a function of pressure. The phonon frequencies for different modes at various Brillouin zone points have been obtained as a function of pressure and compared with the experimental data [5,6]. Additionally, unlike that predicted by Zhang *et al.* [7] on the basis of their lattice dynamic calculations, we do not find any attenuation in the TA(X) phonon mode at ~ 200 GPa. *In-situ* high pressure Raman measurements upto pressures more than 200 GPa will be required to resolve this discrepancy.

For MgO, apart from investigations under hydrostatic compressions, the calculations have been extended to determine the ideal [001] compressive and tensile strength under two uniaxial loading conditions, namely “uniaxial strain condition” and “uniaxial stress condition”. The compressive strength is determined to be ~ -283 GPa and -115 GPa, respectively, for the two conditions. The ideal tensile strength is determined be ~ 20 GPa and 11 GPa, respectively, for the two loading conditions. There are further scopes to continue these kinds of studies in various other crystallographic directions such as [011], [111]. In addition to this the determination of ideal shear strength along different crystallographic directions of MgO single crystal is also an open question.

As far as prediction of crystal structure at high pressures in these binary solids is concerned only three structures B1, B2 and B10 have been taken for study, the possibility of any other high pressure structures may require testing of still more phases, specially for LiH and MgO, as there are no high pressure experiments on these materials up to the predicted B1 to B2 transition pressures. It is quite challenging to guess and perform total energy calculations for all the plausible structures to predict the high pressure phases of materials theoretically. For a new material (with only knowing the constituent atoms) without prior knowledge of its crystal structure, one has to carry out the total energy calculations as a function of pressure for all the possible candidate structures which may be the structures of analogous system or new structures guessed from chemical intuition. The plot of total energy versus pressure will show the structures which are lower in energy compared to other phases corresponding to particular compression and thereby the possibility of the stability of energetically higher structures can be cancelled out. In this way the ground state phase corresponding to the global minima as well as high pressure phases associated with the local minima and the corresponding structural transformation sequence with compression can be determined. But problem arises when some unexpected structure or hitherto unknown structure get stabilized at high pressure; as is the case for the high pressure B10 phase in LaN system. So, here, reliable structure prediction capabilities of computer simulation are necessary which will work without any prior knowledge, assumption or intuition of the system [8]. Simulated annealing [9-11], minima hopping [12] and metadynamics [13-15], evolutionary algorithm USPEX (Universal Structure Predictor: Evolutionary Xtallography) [16-18] etc. are some of the methods which have been applied in recent past to explore the stable crystal structure relaxing the randomly produced structures. These methods are implemented in the sophisticated simulation computer codes such as USPEX[19], CALYPSO[20], XtalOpt[21], to predict crystal structure.

Further, all these theoretical calculations are based on the DFT. Despite the improvements in various approximations in DFT, it has its own limitations. There are difficulties in using DFT to properly describe intermolecular interactions; charge transfer excitations; transition states, global potential energy surfaces and some other strongly correlated systems; and in calculations of the band gap of some semiconductors. The exchange-correlation potentials which are used in DFT calculations are not exact and these are some approximations to the true picture. This produces some inherent error in these calculations. The transition metals, the lanthanides, and the actinides has vacant inner orbital (the d - orbital and f - orbital are partially filled) and these atoms and their compounds are difficult to simulate theoretically and sometime give results which are away from the experimental observations.

In the experimental front, the yield strength and fracture strength of polycrystalline copper has been measured under both the quasistatic loading condition and high strain rate loading condition with strain rates ~ 10^4/s. The yield strength and fracture strength (maximum stress that the material can withstand before fracture) measured in quasistatic experiments is 0.13 GPa and 0.22 GPa, respectively. However, these quantities measured at strain rates of ~ 10^4/s generated in plate impact experiments are 0.14 GPa and 1.32 GPa, respectively. These results suggest that the yield strength of copper shows marginal increase with increasing strain rates up to 10^4/s, whereas the fracture strength increases by ~ 6 times as compared to that measured at quasi static condition. Further, the nanoindentation analysis of the as received and shock treated samples suggested that the effect of shock treatment is to increase the hardness of this material by ~20%.

Finally, the plate impact experiments carried out in copper to generate compressions as well as tensions at high strain rates using the Gas Gun facility are quite difficult as the rise time of pressure is of order of few tens of nanoseconds and duration pressure pulse in the material is extremely small (a few microseconds). All the measurements are to be completed successfully within this short time. In addition to this, the experiments are destructive in nature with most of the parts of the experimental assembly including various type of sensors need to prepared a fresh for each shot. This thesis reports the measurements of yield strength and fracture strength of polycrystalline copper under high strain rate conditions generated in shock wave experiments carried out using the gas gun facility. It will be interesting to perform similar investigations in single crystal copper subjected to shock loading along different crystallographic directions e.g. [100], [110] and [111], as above mentioned mechanical properties are expected to be dependent on the shock loading along a specific crystallographic axis.

Reference

1. O. Potzel, and G. Taubmann, *J Sol. Stat. Chem.* **184**, 5(2011).
2. A. Aid, R. Khenata, A. Bouhemadou, T. Seddik and Ali H. Reshak, *Advances in Condensed Matter Physics* (2009): ISBN: 978-81-308-0336-4.
3. D. Varshneya, N. Kauravb, R. Kingea and R. K. Singh, *Phase Transitions: A Multinational Journal* **81**, 1(2008).
4. S. B. Schneider, D. Baumann, A. Salamat and W. Schnick, *J. Appl. Phys.* **111**, 093503-1 (2012).
5. A. Lazicki, P. Loubeyre, F. Occelli, R. J. Hemley, and M. Mezouar, *Phys. Rev.B.* **85**, 054103-1 (2012).
6. A. C. Ho, R. C. Hanson, and A. Chizmeshya, *Phys. Rev. B* **55**, 14818 (1997).
7. J. Zhang, L. Zhang, T. Cui, Y. Li, Z. He, Y. Ma and G. Zou, *Phys. Rev. B* **75**, 1041151 (2007).
8. A. R. Oganov *et al.*, "Evolutionary Crystal Structure Prediction and Novel High-Pressure Phases." *High-Pressure Crystallography*. Springer Netherlands (2010), 293-323.
9. M. W. Deem, J. M. Newsam, *Nature* **342**, 260 (1989)..
10. J. Pannetier, J. Bassasalsina, J. Rodriguez-Carva jal, and V. Caignaert, *Nature* **346**, 343 (1990).
11. M. B. Boisen, G. V. Gibbs, M. S. T. Bukowinski, *Phys. Chem. Minerals* **21**, 269 (1994).
12. S. Gödecker, *J. Chem. Phys.* **120**, 9911 (2004).
13. R. Martonak, A. Laio, and M. Parrinello, *Phys. Rev. Lett.* **90**, 075503 (2003).
14. R. Martonak, A. Laio, M. Bernasconi, C. Ceriani, P. Raiteri, F. Zipoli, and M. Parrinello, *Z. Krist.* **220**, 489 (2005).
15. R. Martoňák, D. Donadio, A. R. Oganov, M. Parrinello, *Nature Materials* **5**, 623 (2006).
16. A. R. Oganov, C. W. Glass, S. Ono, *Earth Planet. Sci. Lett.* **241**, 95 (2006).
17. A. R. Oganov, C. W. Glass, *J. Chem. Phys.* **124**, 244704 (2006).
18. C. W. Glass, A. R. Oganov, N. Hansen, *Comp. Phys. Comm.* **175**, 713 (2006).
19. http://uspex.stonybrook.edu/

20. http://www.calypso.cn/

21. http://xtalopt.openmolecules.net/wiki/index.fcgi/